

Development of a Guided Wave EMAT Online Inspection
System for Al/Al-Sn/Al/Steel and CuSn/Steel Bimetal
Strip Bond Quality Control used in the Automotive
Industry

EngD Thesis

Philipp Johannes Tallafuss

DMEM

University of Strathclyde, Glasgow

February 14, 2019

This thesis is the result of the author's original research. It has been composed by the author and has not been previously submitted for examination which has led to the award of a degree.

The copyright of this thesis belongs to the author under the terms of the United Kingdom Copyright Acts as qualified by University of Strathclyde Regulation 3.50. Due acknowledgement must always be made of the use of any material contained in, or derived from, this thesis.

Signed:

Date:

Abstract

Cold roll bonded (CRB) Al/Al-Sn/Al/steel and sintered CuSnNi/steel bimetal strips are used in the automotive industry for the manufacture of engine bearings, bushes and thrust washers. Any defects such as delamination or porosity that occur in bimetal strips during manufacturing can cause problems at downstream production steps and if they remain undetected, could result in components failing in the field, which is a significant business risk. One way to reduce this business risk is to install a final inspection system on a continuous production line as the strip passes a fixed inspection point. In process control this could alert the operators to reject defective material and correct process parameters when the defect occurs. As this system requires 100% volumetric inspection, installing it has its challenges due to the harsh manufacturing environment in which the strip moves at up to 20 m/min in the processing lines at room temperature. A literature review and feasibility study on different non-destructive testing (NDT) techniques to inspect bond quality of CRBed Al/Al-Sn/Al/steel bimetal strips was conducted to assess technologies that could be developed for serial inspection. Guided waves generated using Electromagnetic Acoustic Transducers (EMATs) was identified as best suited for this application. Since this technology was not available off-the-shelf, significant research and experimental work was carried out to develop an automated prototype system. The system was successfully installed at a strip processing line and demonstrated the online bond inspection capability for Al/Al-Sn/Al/steel and CuSnNi/steel bimetal strips, which is the main achievement of this EngD project. For CuSnNi/steel strips, causes of defects and preventative control measures were studied and examined. Industrialisation of the inspection system will significantly reduce the company business risk and improve bond quality of bimetal strips.

Acknowledgements

University of Strathclyde

Dr Andrzej Rosochowski (Reader and Academic Supervisor): Your experience and support was essential for the completion of this EngD project.

Innerspec Technologies

Mr Peter Kowski (Project Manager), Mr Xavier Minguez (Application Engineer): Explained non-destructive testing of plates using guided waves generated with EMATs to me and provided technical support throughout this project.

Mr Huidong Gao (R & D Scientist): Used numerical models to obtain phase and group velocity curves in bimetal strips and finite element models to understand the wave interaction with defects to compare the theory against my experimental research.

Mr Antonio Romero (R & D Engineer), Mr Victor Garcia (General Manager): For supporting the publication of results of this EngD project.

MAHLE R & D, Operations and Global Technical Coordination

Ms Sylvia Campbell (Materials Development Engineer and Industrial Supervisor): Explained the cold roll bonding process to me and your support as industrial supervisor for this EngD project was invaluable.

Ms Janette Johnston (Process Development Engineer) and Mr Alistair Lindsay (Qual-

Chapter 0. Acknowledgements

ity Laboratory Manager): For explaining the sinter process and your countless support in the laboratory to prepare micrographs and discussing quality standards.

Mr Robbie Sinclair (Project Engineer), Mr Martin Robertson (Manufacturing Engineer), Mr David Williams (Controls Engineer) and Mr Ian Cochrane (Project Engineer): For your invaluable assistance during the installation of the prototype inspection system at the strip processing line and the electrical and mechanical trouble shooting.

Mr Matthias Langbein (Director Operations and Global Technical Coordination), Mr Charles Lorimer (Kilmarnock Plant Manager), Mr Jeff Carter (Director of R & D), Mr Falko Langbein (Head of Global Technical Coordination): For providing guidance in numerous stake holder meetings, challenging, supporting and motivating me during my EngD and the GTC support to develop a serial system technical specification.

Dedication

I dedicate this thesis to my family and friends for their support and unwavering belief in me to pursue my dreams and finish this dissertation.

Contents

Abstract	iii
Acknowledgements	v
Dedication	vii
List of Figures	xiii
List of Tables	xxiii
List of Abbreviations	xxix
List of Symbols	xxxix
1 Introduction	1
1.1 Background	1
1.2 Al/Al-Sn/Al/steel bimetal defects and testing	3
1.2.1 Quality assurance destructive testing	4
1.2.2 Defects	6
1.3 Aims of thesis	11
1.4 Publications to date arising as a result of thesis	12
1.5 Overview of thesis	13
2 Al/Al-Sn/Al/steel cold roll bonding process	17
2.1 Manufacturing process	17
2.1.1 Al-Sn alloy casting	17

Contents

- 2.1.2 Al/Al-Sn/Al cladding 18
- 2.1.3 Further rolling reduction 19
- 2.1.4 Cold roll bonding Al/Al-Sn/Al/steel 20
- 2.1.5 Solution heat treatment 20
- 2.1.6 Final inspection 21
- 2.2 Material and bond properties 22
 - 2.2.1 Aluminium bearing alloys 22
 - 2.2.2 Microstructural deformation effects in rolling aluminium and steel strips 23
 - 2.2.3 Roll bonding process 29

- 3 How guided waves using EMAT ultrasonic technology was selected in a feasibility study on different NDT techniques 37**
- 3.1 Reviewing the literature 38
 - 3.1.1 Radiography 38
 - 3.1.2 Magnetic particle inspection 38
 - 3.1.3 Dye penetrant testing 40
 - 3.1.4 Eddy current 41
 - 3.1.5 Thermography 42
 - 3.1.6 Shearography 43
 - 3.1.7 Ultrasound 44
 - 3.1.8 Guided waves using EMATs 46
 - 3.1.9 Conclusion 48
- 3.2 Experimental procedures 50
 - 3.2.1 Thermography 50
 - 3.2.2 Shearography 52
 - 3.2.3 Ultrasound 54
 - 3.2.4 Guided waves using EMATs 57
- 3.3 Results 59
 - 3.3.1 Thermography 59
 - 3.3.2 Shearography 61

Contents

3.3.3	Ultrasound	61
3.3.4	Guided waves using EMATs	67
3.4	Discussion	67
3.5	Conclusions	73
4	Guided waves generated with EMATs theory	75
4.1	Guided waves propagation	76
4.2	Analysis and simulation of Lamb waves	78
4.2.1	Analytical study of Lamb wave characteristics	79
4.2.2	Lamb wave dispersion curves in SAFE	80
4.2.3	Lamb mode selection	82
4.3	SAFE-FE coupling for defect and edge reflection	85
4.4	EMAT as guided waves ultrasonic generators and sensors	86
4.5	Lamb wave signal processing and feature extraction to find internal defects	88
4.6	Wave mode selection and system calibration	93
4.7	Optimising the guided waves EMAT-EMAT system	95
5	Detection of bond defects in cold roll bonded Al/Al-Sn/Al/steel plates	97
5.1	Experimental procedure	98
5.1.1	Wave propagation analysis	98
5.1.2	Sample preparation	100
5.1.3	Experimental set up	101
5.1.4	Sensor setup	102
5.2	Results and discussion	104
5.2.1	Lamb guided wave inspection	104
5.2.2	Wave interaction with defects	109
5.2.3	Effect of post rolling annealing on attenuation	111
5.3	Conclusions	113
6	Implementing an online bond quality inspection system for cold roll bonded Al/Al-Sn/Al/steel strips	115
6.1	General inspection system design	116

Contents

6.1.1	System requirements	116
6.1.2	General design of system	116
6.2	Experimental procedure	118
6.2.1	Guided wave propagation and analysis	118
6.2.2	Sample production	118
6.2.3	Clad Al lining adhesion peel-back test	120
6.3	Results and discussion	122
6.3.1	Data interpretation	122
6.3.2	Results	123
6.3.3	Determination of moving alarm threshold	128
6.3.4	Detectability of main bond defects	130
6.3.5	Improvements for serial system	131
6.3.6	Conclusions	132
7	Defects, causes and prevention controls in the continuous CuSn/steel bimetal strip sintering process	135
7.1	Introduction	136
7.2	The continuous bronze/steel bimetal sintering process	137
7.3	Liquid phase sintering mechanism	140
7.4	Experimental materials and procedures	141
7.5	Results and discussion	145
7.5.1	Delamination	146
7.5.2	Bronze lining structure defects	149
7.5.3	Bronze lining surface defects	153
7.5.4	Dimensional defects	156
7.6	Conclusion	157
8	CuSn/steel bimetal strip online inspection feasibility study	159
8.1	Introduction	160
8.2	Experimental procedure	160
8.2.1	Guided wave propagation analysis	160

Contents

8.2.2	Experimental set up	162
8.2.3	Sample preparation	163
8.3	Results and discussion	164
8.3.1	Wave mode selection	164
8.3.2	Wave mode optimisation using non-conformance samples	169
8.3.3	Online inspection	176
8.3.4	Serial inspection alarm threshold	178
8.4	Conclusions	179
9	Recommendations for the final inspection system	181
9.1	Place of installation	181
9.1.1	Required inspection line machine components	181
9.1.2	Criteria for selection of industrialisation scenario	182
9.1.3	Industrialisation scenarios	183
9.2	EMAT arrays and multi lane scrap marker to improve material yield	185
9.3	Robust mechanical integration	187
10	Summary and final conclusions	189
10.1	Main innovations	189
10.2	Industrial impact	192
10.3	Further work	192
	Bibliography	193
	Appendix	211

Contents

List of Figures

1.1	Application of bearings, bushings and thrust washers in the internal combustion engine	2
1.2	Schematic of bimetallic bearing	2
1.3	Schematic of bimetallic strip cold roll bonding	3
1.4	Lining adhesion peel back test ratings	5
1.5	Pareto analysis of defects that occurred over a period of three years in CRBed Al/Al-Sn/Al/steel bimetal strips	7
1.6	Foil to alloy bond defects (a) micrograph of sacrificial side, (b) blisters on bimetal strip surface, (c) micrograph showing oxides at bond, (d) micrograph showing porosity at bond and (e) micrograph showing tin at bond	8
1.7	Foil to steel bond defects (a) micrograph showing formation of aluminium iron, (b) steel debris bonded to foil	8
1.8	Delamination between intermediate bond foil and steel (a) in a narrow strand, (b) in a half shell bearing after oil groove milling and (c) in a half shell bearing after inner diameter boring	10
1.9	Microstructural defects in Al-Sn lining (a) porosity, (b) directionality and (c) stabilised tin stringers	10
1.10	Indents on steel backing material	10
1.11	Schematic diagram showing the main stages of the EngD project and how the individual work packages were published and are linked into sections of the final thesis	16

List of Figures

2.1	Schematic of continuous Al-Sn alloy twin belt casting process	18
2.2	Schematic of Al/Al-Sn/Al cladding process	19
2.3	Schematic of Al/Al-Sn/Al clad alloy rolling process	19
2.4	Schematic of cold roll bonding Al/Al-Sn/Al clad alloy to steel	21
2.5	Lattice structure (a) face-centred cubic and (b) body-centred cubic . . .	24
2.6	EBSD grain identification map from a rolled and bonded <i>Al-Sn-Si</i> alloy sample [12]	25
2.7	Schematics illustrating the more likely occurrence of slip in the (a) primitive cubic lattice compared to (b) lattice with smaller planar spacing .	26
2.8	Single edge dislocation	28
2.9	Screw dislocation [18]	28
2.10	Schematic of the rolling process [20]	30
2.11	Schematic illustration of the thin film theory showing fracture and extrusion of the stacked metal sheet surface layers during CRB [21]	31
2.12	SEM micrographs of Al-Sn alloy (a) cracking of the Al-Sn cover layer, (b) magnification of the same surface showing that the fracture is brittle, (c) finished low carbon steel after surface expansion showing cracking of the brittle cover layer [1]	32
3.1	Schematic illustration of (a) exposure arrangement for radiography, (b) resulting processed film [47]	39
3.2	Schematic illustration of (a) inspection set up for the detection of longitudinal defects using current flow through the material, (b) detection of transverse defects using an encircling coil [47]	40
3.3	Schematic illustration of (a) applying penetrant to the surface, (b) removal of excess penetrant from surface, (c) developer powder applied on surface to draw out penetrant and (d) attenuated indication of crack [47]	40
3.4	Schematic illustration of eddy current testing principle (a) circular pattern of eddy currents in material when no crack is present, (b) surface cracks cause distorted eddy currents that result in increased impedance [47]	42

List of Figures

3.5	Schematic of experimental set up for delamination detection in transient pulse thermography	52
3.6	Shearography experimental set up for a) thermal shock and b) vacuum technique	53
3.7	Schematic view of test set up showing the Al-Sn alloy/steel bimetal sample submerged in an immersion tank, stepper motor and the Data Acquisition System	55
3.8	C-scan colour code depending on Gate1/Gate2 amplitude ratio	56
3.9	Schematic diagram of scanning pattern in x-z plane of bimetal sample .	56
3.10	Experimental setup for online testing: (a) system installed at a position where the strip movement was kept to a minimum and access could be gained to the steel side of the bimetal strip (b) probe and bubbler head	57
3.11	Manufacturing of test samples with isosceles triangle shaped delamination applying (a) 80g/m ² gauge paper and (b) ink as contaminant . . .	58
3.12	Test setup (a) transmitter and receiver sensors arranged in through transmission mode, (b) sensor set up on test sample	59
3.13	Small spots with a few mm diameter present on (a) AT-NL sample, (b) AT-RR sample and (c) AT-RR sample with variation of analysis parameters that revealed surface effects	60
3.14	Good parts without specific defect signature but reflections due to curved surface	60
3.15	Image results for thermal testing: (a) normal bond conditions, (b) delamination, results for vacuum testing: (c) normal bond conditions, (d) delamination	62
3.16	3 consecutive tests with non-brushed / brushed samples showing a visible difference in the percentage of red, yellow and blue pixels	63
3.17	Effect of increasing the water fluid coupling temperature from 20°C to 23°C for non-brushed and brushed samples	65
3.18	Samples of variable bond quality (a), (b) and (d) passed the peel off test, (c), (e) and (f) failed the peel off test	66

List of Figures

3.19 Sample A-scan traces of (a) control sample, (b) 80g/m² gauge paper delamination sample and (c) ink delamination sample 68

4.1 Symmetric and anti-symmetric Lamb wave modes [104] 76

4.2 Shear horizontal (SH) mode in multilayered sheets [110] 77

4.3 Composite laminate dispersion curves obtained by transfer matrix method [115] 79

4.4 SAFE and analytical dispersion curves comparison for aluminum plate: (a) phase velocity, and (b) group velocity curves [112] 81

4.5 SAFE and analytical phase velocity dispersion curves for comparison between isotropic aluminum plate and unsymmetrical material arrangement with (a) 40% and (b) 10% thickness ratio between the layers with different Young’s modulus [112] 83

4.6 Coupling between SAFE-FE for Al/Al-Sn/Al/steel bimetal sheet at a defective position on the plate 86

4.7 Interaction between EMAT transducer and bimetal sample 87

4.8 Plan view of guided waves between EMAT transmitter and receiver, where (a) the bond interface between Al/Al-Sn/Al alloy and steel is without defect resulting in normal attenuation and reference A-scan amplitude, (b) delamination at the bond interface interfering with the guided waves sound path and resulting in attenuation and A-scan amplitude reduction, (c) foreign particles at the bond interface perpendicular to the EMAT coil that interact with the guided waves but may not be easily detectable because the attenuation in the A-scan amplitude is only moderate, (d) foreign particles parallel to the EMAT coil that should be easily detectable because of significant attenuation and A-scan amplitude reduction. 89

4.9 Cross section view of Al/Al-Sn/Al/steel bimetal and guided waves, where (a) the bond interface is without defect resulting in normal attenuation and reference A-scan amplitude, (b) delamination at the bond interface interfering with the guided waves sound path and resulting in attenuation. 90

List of Figures

4.10 Illustration of A-scan maximum amplitude trace, where (a) the bond interface between Al/Al-Sn/Al alloy and steel is without defect resulting in normal attenuation and reference A-scan maximum amplitude trace, (b) small delamination at the bond interface during inspection interfering with the guided waves sound path and resulting in significant attenuation and low A-scan amplitude for the length of the defect, (b) large delamination at the bond interface resulting in drop of A-scan maximum amplitude trace for the length of the defect. 91

4.11 Time domain signals at receiver location: A-scans showing transmitted frequency response of good and defective samples: (a)/(e) no frequency band width filtering, (b)/(f) +/- 0.3 MHz, (c)/(g) +/- 0.2 MHz and (d)/(h) +/- 0.1 Mhz frequency band width filtering around set wave mode frequency 93

5.1 (a) Phase velocity and (b) Group velocity dispersion curves with selected mode at 2.3 MHz marked for the sample described in Table 5.1 (supplied by Innerspec) 99

5.2 Samples with artificially implanted alumina and steel debris defects of different sizes 101

5.3 Schematic illustration of EMAT transducers used for generating and receiving guided waves propagating through artificial delamination . . . 102

5.4 Photographs of experimental set-up 103

5.5 Setup of sensors: (a) magnet and foam sponge, (b) coil wire, (c) metallic wear surface, (d) wear plate secured on transducer, (e) assembled transducer and plug-in connection, (f) bimetal clamped on transducers . 105

5.6 A-scan signal for (a) defect free and (b) defective location 106

5.7 A-scan maximum amplitude trace of reference samples: (a) prior and (b) post bimetal annealing, embedded 10x10 mm steel debris defect sample: (c) prior and (d) post bimetal annealing 106

5.8 Signal amplitude measured prior and post bimetal annealing for artificially implanted alumina defects in different sizes 108

List of Figures

5.9	Signal amplitude measured prior and post bimetal annealing for artificially implanted steel debris defects in different sizes	108
5.10	Optical micrographs: (a) reference sample, (b) artificial 5x5 mm delamination, (c) natural delamination, (d) artificial 5x5 mm embedded steel debris and (e) natural embedded steel debris	111
5.11	Optical micrographs: Al-Sn alloy (a) elongated structure in rolling direction and (b) flattened structure in transverse direction prior to annealing, (c) recrystallized structure in rolling direction and (d) transverse direction post annealing (Etchant: Wecks)	112
6.1	EMAT prototype inspection line for Al/Al-Sn/Al/steel strips	117
6.2	Temate software: (a) A-scan oscilloscope; (b) online A-scan maximum amplitude trace; (c) A-scan maximum amplitude recall panel	117
6.3	Defects in cold roll bonded Al/Al-Sn/Al/steel strips (a) 1x1 mm alumina, (b) 1x1 mm steel debris, (c) 5x5 mm alumina, (d) 5x5 mm steel debris, (e) run-off clad Al, (f) altered steel sanding, (g) rolled-in clad Al slivers, (h) rolled-in brush bristles, (i) altered clad Al brushing, (j) Al-1050 foil blisters on sacrificial side	121
6.4	Results-based illustration of A-scan maximum amplitude trace: (a) SP1-R1 320 m, (b) SP2-R2 390 m, (c) SP3-D 80 m strips, (d) AD samples	124
6.5	Boxplot of SP-R1, SP-R2 and AD strip samples showing central tendency and variability	125
6.6	Amplitude normal test plots	126
6.7	Relationship between false alarm rate and threshold for defect-free sample SP-R1	130
7.1	Difference in microstructure for (a) sintered CuPb10Sn10 and (b) cast CuSn4Bi lining on steel backed bimetal	136
7.2	Sintered bronze/steel bimetal continuous production process	139
7.3	Schematic illustration of sintered bronze/steel bimetal structure per process step	139

List of Figures

7.4	Cu-Sn phase diagram	140
7.5	Cross sectional view showing typical structures of (a) binary phase SB10 (b) single-phase SB20, (c) binary phase SB30 homogeneous sintered bronze/steel bimetal structure with a continuous lining to steel bond . .	142
7.6	Distribution of the investigated bronze/steel bimetal strips according to the bronze lining chemical composition	143
7.7	Technique applied for porosity measurement: (a) capture of section, (b) threshold setting, (c) areas selected for porosity measurement highlighted in colour	145
7.8	Percentage occurrence of (a) different defects, (b) location in bimetal . .	146
7.9	Fault tree analysis (FTA) of sintered bronze/steel bimetal strip defects .	147
7.10	SB10 with different lining to steel bond delamination length ratios (a) > 5 and \leq 10%, (b) > 10 and \leq 20%, (c) > 20%, (d) SB20 lining to steel bond delamination length ratio > 20%, (e) SB20 lining shear plane delamination ratio > 20% in the field of view of the micro sample	148
7.11	Different porosity SB10 (a) 1%, (b) 3%, (c) 5% and SB20 (d) 0.4%, (e) 2.0% and (f) 3.0%	150
7.12	SB10 Dual phase structure with CuSn matrix surrounding lead pools with different sizes (a) 5-50 μm , (b) up to 120 μm , (c) up to 150 μm and (d) eutectoid phase	151
7.13	SB10 with < 50% of their particle surface bonded (a) 0 RPs, (b) 5 RPs, (c) > 5 RPs and SB20 with different number of particles (d) 0 RPs, e) > 3 RPs	152
7.14	Bronze lead movement (a) no lead residue, (b) marginal lead residue, (c) increased lead residue, (d) excessive lead residue, (e) evidence of lead that was drawn back into lining by capillary action	154
7.15	Photographs (a) circular blowhole of approx. 10 mm diameter, (b) lining shrinkage cracks (c) scoring	155
7.16	(a) SEM image of particle ejected from blowhole, (b) EDAX showing presence of C, Ca, O2, Ti, Fe, Al, Si	156

List of Figures

8.1	Schematic of EMAT transducers generating and receiving guided waves in CuSn8Ni1/steel bimetal plates: (a) sound path; (b) interaction with material	161
8.2	A-scan for (a) defect free and (b) defective bronze/steel bimetal plates	162
8.3	Industrial strip processing line with installed prototype EMAT inspection system	163
8.4	Photographs of samples indicating the defective areas	165
8.5	Sample type I: (a) sintered bronze/steel bimetal phase velocity curve and (b) group velocity curve, (c) bare steel phase and (d) group velocity curve (supplied by Innerspec)	166
8.6	Sample type I: A_0 , S_0 , A_1 , S_1 , A_2 and S_2 wave modes in GQR-I, AWOL-I and BS-I samples	167
8.7	Sample type II: (a) sintered bronze/steel bimetal velocity curve indicating inspection points for wavelengths A, B and C, (b) group velocity curve for wavelength B (supplied by Innerspec)	170
8.8	Sample type II: S_1 mode with wavelength A, B and C (frequencies T, V and W) for samples GQR-II, NCS-II-P1, NCS-II-P2 and NCS-II-P3	171
8.9	Boxplot of measured amplitude for samples GQR-II, NCS-II-P1, NCS-II-P2 and NCS-II-P3 when scanned through the sensors for S_1 mode and different wavelengths A, B and C	172
8.10	GQR-II, NCS-II-P1, NCS-II-P2 and NCS-II-P3 micrographs	173
8.11	Relative amplitude of through transmission guided wave signal for sample ADT-II-100x20, S_1 mode and wavelength B	174
8.12	Sample ADT-II-100x20 micrographs at $h = 0, 20, 40, 60, 80$ and 100 mm comparing the actual and theoretical delamination width	175
8.13	Maximum A-scan trace for samples SPS-II-R and NCS-II-D online inspection trials	176
8.14	Scatter plot diagram of relative amplitude and delamination percentage for samples GQR-II and NCS-II-D	178
9.1	Continuous CRB line in Kilmarnock	184

List of Figures

9.2 SIC machine vision final inspection line in Kilmarnock 185

9.3 EMAT arrays and scrap marker that result in different material yield:
(a) 1-channel system and scrap marker with lowest yield in case of a
defect, (b) 3-channel system and multi-lane scrap marker with moderate
yield and (c) 4-channel system and multi-lane scrap marker optimised
yield 186

9.4 Bimetal strip one-side waviness leading to lift-off between material and
probe and resulting in false alarms 187

List of Figures

List of Tables

1.1	Evaluation method, sample size and frequency of bimetal product characteristic tests	4
2.1	Chemical composition (wt%) of Al-Sn alloys considered in this study . .	22
2.2	Chemical compositions (wt. %) and mechanical properties of low-carbon steel	22
2.3	Common slip planes {uvw} and directions <hkl> for fcc and bcc crystal lattice metals	27
3.1	Feasibility of NDT techniques to fulfil online Al/Al-Sn/Al/steel bimetal inspection requirements based on literature review	48
3.2	Test samples in relation to the applied NDT methods	50
3.3	Levels of ultrasound testing factors	62
3.4	P-values for two-way ANOVA of surface preparation and exposure time effect	64
3.5	P-values for two-way ANOVA of surface preparation and temperature effect	66
3.6	P-values for one-way ANOVA of peel off test result	67
3.7	Advantages and limitations of active thermography bond inspection of Al/Al-Sn/Al/steel bimetal strips	69
3.8	Advantages and limitations of shearography bond inspection of Al/Al-Sn/Al/steel bimetal strips	69

List of Tables

3.9	Advantages and limitations of ultrasound A-scan trace bond inspection of Al/Al-Sn/Al/steel bimetal strips	70
3.10	Advantages and limitations of guided waves using EMAT bond inspection of Al/Al-Sn/Al/steel bimetal strips	71
3.11	Feasibility of NDT techniques to fulfil online inspection requirements for Al/Al-Sn/Al/steel bimetal	71
5.1	Material properties and dimensions of four-layered Al/Al-Sn/Al/steel plate for wave propagation analysis	98
5.2	Statistical and RDR sample data	109
6.1	Material properties for Al/Al-Sn/Al/steel bimetal strips and employed guided wave modes	119
6.2	Al/Al-Sn/Al/steel strip samples for online inspection	122
6.3	Welch's ANOVA and Games-Howell Pairwise Comparison <i>post-hoc</i> results (Minitab 17.1.0 statistical software)	128
6.4	Comparison between clad Al lining adhesion peel-off and guided waves non-destructive testing results, considering 65% of the normal amplitude alarm threshold and 0.50% false alarm rate	131
7.1	Chemical compositions (wt. %) and mechanical properties of SB10, SB20 and SB30	142
7.2	Chemical compositions (wt. %) and mechanical properties of low-carbon steel	142
8.1	Material properties of sintered CuSn8Ni bronze/steel bimetal samples	161
8.2	Sintered bronze/steel bimetal samples for inspection	164
8.3	Phase and group velocity for modes A_0 , S_0 , A_1 , S_1 , A_2 , S_2 and wavelength A in sample type I bare steel and sintered bronze/steel bimetal sheets	168
8.4	Decision matrix for the selection of the most suitable wave mode for inspection (higher is better)	169

List of Tables

8.5 Phase and group velocity for mode S_1 and wavelengths A, B and C in sample type II	169
---	-----

List of Tables

List of Abbreviations

The following table describes the meaning of various abbreviations and acronyms used throughout the thesis.

AT	Active thermography
AD	Artificially implanted defect
ADT	Artificial delamination triangle
ANOVA	Analysis of variance
AWOL	Area of a disk without lining
bcc	Body centred cubic
BS	Bare steel
CRB	Cold roll bonding
DAQ	Data acquisition
DIO	Digital input/output
EBSD	Electron backscatter diffraction
EDAX	Energy dispersive X-ray analysis
EMA	Exponential moving average
EMAT	Electromagnetic acoustic transducer
fcc	Face centred cubic
FEM	Finite-element-method
FPGA	Field-programmable gate array
FTA	Fault tree analysis
GIM	Grain identification map
GQR	Good quality reference
GW	Guided waves

Chapter 0. List of Abbreviations

ID	Inner diameter
IR	Infrared
KTP	Knowledge transfer partnership
LL	Lower limit
MRD	Minimum resolvable distance
NCS	Non-conformance sample
NDT	Non-destructive testing
OM	Optical microscope
PFMEA	Process failure mode effects analysis
PLC	Programmable logic controller
RDR	Reference/defective sample amplitude ratio
RP	Residual particles
S	Shearography
SAFE	Semi-analytical finite element
SEM	Scanning electron micrograph
SH	Shear horizontal
SMA	Simple moving average
SNR	Signal-to-noise ratio
SP	Serial production
SPS	Serial production strip
TOF	Time-of-flight
TSR	Thermographic signal reconstruction
UL	Upper limit
UT	Ultrasound
WFE	Wave finite element
WMA	Weighted moving average
XRF	X-ray fluorescence

List of Symbols

b	Burgers vector
r_{red}	Rolling reduction ratio
t	Thickness
h	Plate thickness
k	Wave number / bandwidth depending constant
c_L	Longitudinal mode velocity
c_T	Transverse mode velocity
c_P	Phase velocity
ω	Wave circular frequency
U	Displacement field
ρ	Density
λ	Lame constant
μ	Lame constant
f	Frequency
c_G	Group velocity
A	Anti-symmetric Lamb mode
S	Symmetric Lamb mode
E	Young's module
n	Toneburst cycle number
l	Travel distance
T_{initial}	Wave-packet initial time duration

Chapter 0. List of Symbols

B	Magnetic field
J	Eddy currents
f	Lorentz force
t	Time
d	Distance
v	Velocity
H_0	Null hypothesis
H_a	Alternative hypothesis
μ	Mean value
p	P-value
α	Smoothing factor
h	Height
δ	Standard deviation

Chapter 0. List of Symbols

Chapter 1

Introduction

1.1 Background

Reciprocating engines are the most common type of internal combustion engines. These engines and their bearings are characterised by cyclic loading. Only sleeve type sliding bearings can support the moving parts and provide a distribution of the applied load over the running surface, which can withstand the loading conditions of internal combustion engines. Figure 1.1 illustrates typical bearing, bush and thrust washer applications in combustion engines. Bush applications are camshaft, balancer shaft and small end connecting rod assemblies. Connecting rod bearings connect the connecting rod and crankshaft. Main bearings are used to connect crankshaft and crankcase. Depending on the application, the components have different product features. Since the lower main bearing requires a higher load carrying capability compared to the upper main bearing, it is typically a plain bearing, while upper main bearings typically have oil hole or groove features. Connecting rod bearings are typically plain bearings. Thrust washers distribute the axial load of the crankshaft in the crankcase. In today's engine designs, increasing attention is paid to improving load resistance, wear reduction and increased conformability between bearings and shaft.

A full range of materials is available for applications in passenger car and commercial vehicle engines. These include aluminium-based two-layer bearings in which the alloy is bonded to the steel back, as well as bronze-based three-layer bearings with the

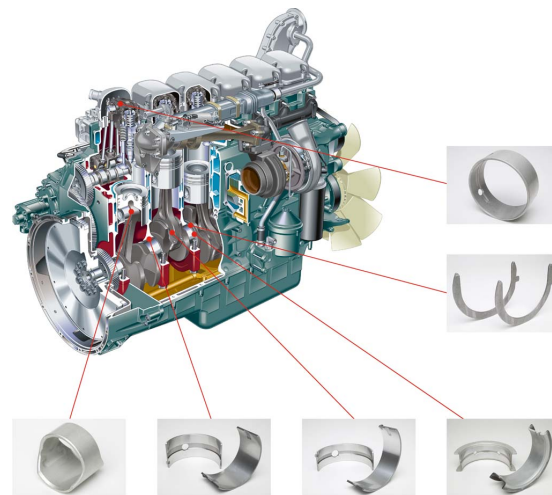


Figure 1.1: Application of bearings, bushings and thrust washers in the internal combustion engine

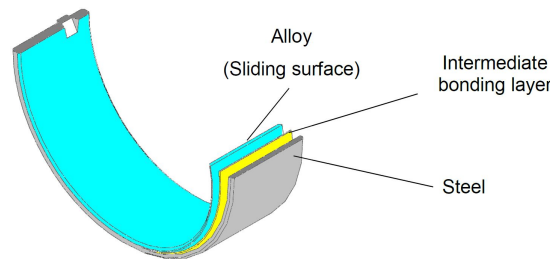


Figure 1.2: Schematic of bimetalllic bearing

bronze-alloy being cast or sintered to the steel back. The third layer, the overlay, can be applied by galvanic, sputter, or thermal spray processes. The majority of engine bearings are aluminium-based two-layer bimetall bearings. Aluminium-based alloys are used for engine bearings in the automotive industry due to the ideal hybrid properties of Al-Sn alloy and steel. The properties are wear and corrosion resistance as well as high anti-seizure properties. Figure 1.2 illustrates an aluminium-based bimetall bearing with the lining layer that is in sliding contact with the crankshaft, a technically pure Al-1050 intermediate bonding layer and steel backing layer to have sufficient strength to withstand the imposed loads and sufficient rigidity to maintain alignment.

Cold Roll Bonding (CRB) of aluminium-based alloys to steel is a key manufacturing process to produce bimetall strips for engine bearings. Figure 1.3 schematically illustrates the CRB process and shows a micrograph of the resulting four-layered Al/Al-

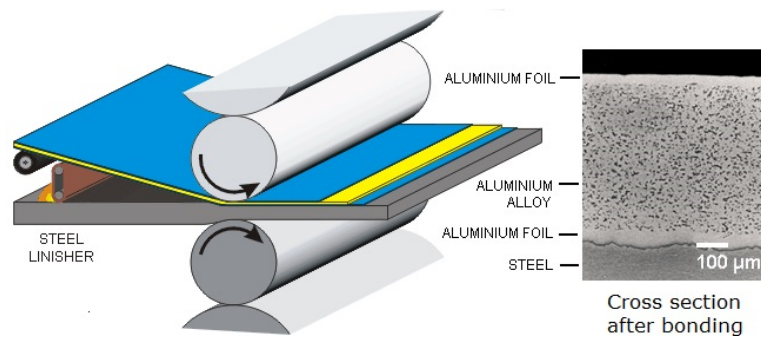


Figure 1.3: Schematic of bimetallic strip cold roll bonding

Sn/Al/steel structure. The cladding layers of the Al-Sn internal core are Al-1050 foil. The Al-Sn alloy has a nominal 6-20% tin content. The three-layered Al/Al-Sn/Al system is referred to as clad Al, which is CRBed onto steel free from aligned linear porosity or continuous oxides. The backing is made of a low carbon steel. In CRB, the solid state weld is achieved by a substantial and simultaneous plastic deformation of the metals at room temperature [1]. The disadvantage of the CRB process is the large number of secondary operations and high requirement for bonding surface preparation [2], which are critical to bond quality. In the MAHLE Kilmarnock Scotland plant, the internal Process Failure Mode Effects Analysis (PFMEA) of the continuous CRB production line, identified 171 different root causes for poor bond in the secondary and surface preparation operations.

1.2 Al/Al-Sn/Al/steel bimetal defects and testing

Despite permanent effort to prevent and minimise the occurrence of defects during manufacturing, it is near impossible to continuously yield a perfect product due to the many process and material related influencing factors that determine the final product quality. This section describes the destructive testing procedures that are applied in serial production for quality assurance and that were considered to correlate NDT results. The most significant defects that occur in serial production, which should be detected with the NDT technique, are introduced.

Table 1.1: Evaluation method, sample size and frequency of bimetal product characteristic tests

Product characteristics	Evaluation method	Sample size and frequency
Bimetal thickness	Micrometer	Sheet from start and end of each coil Edge / middle / edge of each sheet
Lining thickness	Optical microscope	Micro sample from start and end of each coil
Foil / alloy and foil / steel bond	Lining adhesion peel back test	Sheet from start and end of each coil Edge / middle / edge of each sheet
Lining and steel hardness	Vickers hardness test	One sample per coil
Microstructure	Optical microscope	Micro sample from start and end of each coil

1.2.1 Quality assurance destructive testing

The current practice in industry for strip inspection is destructive testing using a chisel test, peel test, shear test, Erichsen cup test or hot hammer test [1]. Although each technique has specific advantages and disadvantages, the major restriction for all of them is that only a minor proportion of the finished material is inspected. MAHLE has implemented a procedure based on various destructive tests to detect defects in serial production. From each produced bimetal coil, one bimetal sample sheet is taken from both ends. In the test section, the Al-Sn alloy to intermediate bonding layer and steel to bonding layer bond strength are assessed with a lining peel back test. The lining and steel hardness is tested using the Vickers hardness test. From each bimetal sheet, micro samples are also taken for examination in the quality control laboratory. In the laboratory, the microstructure, bond quality and lining thickness are tested. All test results are recorded in an electronic database. The occurrence frequency of the different defect types was based on three years data from the laboratory test database.

Table 1.1 provides an overview of the different evaluation methods, sample sizes and frequencies of tests that are used to access the various product characteristics of bimetal strips.

The lining adhesion peel back test is used as serial production test to assess the condition of the Al-Sn alloy to intermediate foil and foil to steel bond. The rolling direction is clearly identified on each sheet by an ink marked arrow. The peel back test is conducted at least three times per sheet, at the left edge, middle, and right edge of the sample sheet. The test procedure is that an incision through the Al/Al-Sn/Al

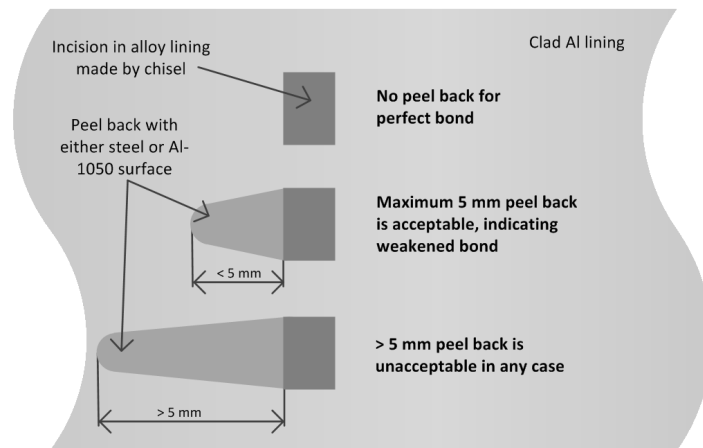


Figure 1.4: Lining adhesion peel back test ratings

lining is made with a sharp 13 mm wide chisel. The lining is then prised upwards until it can be gripped with a pair of round-nosed pincers. The lining is then peeled back in a rotational movement. In order to prevent premature fracture of the lining, it is continually re-gripped throughout the test. Once the lining fractured, the condition of the surface under the peeled lining is observed. A peel back with a clean steel surface, free of any lining material, indicates that the alloy-foil bond is stronger than the foil-steel bond. If lining material remains on the steel, it indicates that the foil-steel bond is stronger than the alloy-foil bond. If the lining fractures without any peel, it indicates that the alloy-foil as well as foil-steel bond is stronger than the Al-Sn alloy tensile strength. This method is based on the Gibbs free energy principle [3], which states that the fracture result is determined by the outcome that has the lowest delta G value and therefore requires the least amount of work and is the most thermodynamically favourable outcome.

Figure 1.4 schematically illustrates the different peel back failure ratings. The length of lining peel back prior to fracture is measured and used to rate the bond qualitatively. The peel back acceptability ratings were established empirically over many years and thousands of tests. No peel back indicates that the bond condition is optimal. A peel back up to 5 mm indicates that the bond condition is weakened, but acceptable. If the peel back is longer than 5 mm, it is unacceptable in any case.

The disadvantage of the test is that it is not rigorously scientific. Flawed aspects of

the test were described in [4]. When a hammer and chisel is used to create an incision through the lining, this results in work hardening of the clad Al lining material. Work hardening results in more brittle clad Al, which may fracture earlier than it would without work hardening. Furthermore the repeatability of the test is poor, because the applied force, impact angle, incision depth as well as the operator differ from test to test. Although the test is not accurate enough to evaluate subtle changes in bond conditions, it is time proven to detect clearly substandard bonding conditions with a high level of confidence. Since the objective of the online NDT technique is the identification of clearly substandard bonding conditions, the well established destructive peel back test is used to correlate the NDT results.

1.2.2 Defects

Figure 1.5 shows the frequency of defects that occurred in serial production over a period of three years. 71.2% of the defects were bond defects between intermediate bond layer and steel. 10.6% of the material was rejected because of substandard microstructure. The Al-1050 sacrificial foil to Al-Sn alloy bond accounts for 9.9% of the defects. Dimensional defects, either wrong lining to steel thickness ratio or total thickness, were found in 4% of all defective samples. 2.6% of the defects were related to substandard steel. 1.7% of the detected defects were not categorised. The sum of bond defects (intermediate bond foil to steel and Al-1050 foil to Al-Sn alloy) is 81.1%, which demonstrates that bond defects at the two interfaces are the most significant defects in CRBed Al/Al-Sn/Al/steel bimetal strips. At the same time, bond defects cause the largest risk that components fail in the field, because they are not visible at the surface and only a minor proportion of bimetal strips is inspected regarding the bond condition. In the following, the defects are described in more detail.

Figure 1.6 illustrates the different types of foil to alloy bond defects. In optimal bond conditions, the three-layered Al/Al-Sn/Al system is free from aligned linear porosity, tin or continuous oxides, as they may initiate the detachment of the foil from the alloy. Figure 1.6(a) shows the detached Al-1050 foil from the Al-Sn alloy caused by continuous oxides at the interface at the sacrificial side of the clad Al. Detached Al-1050 foil from

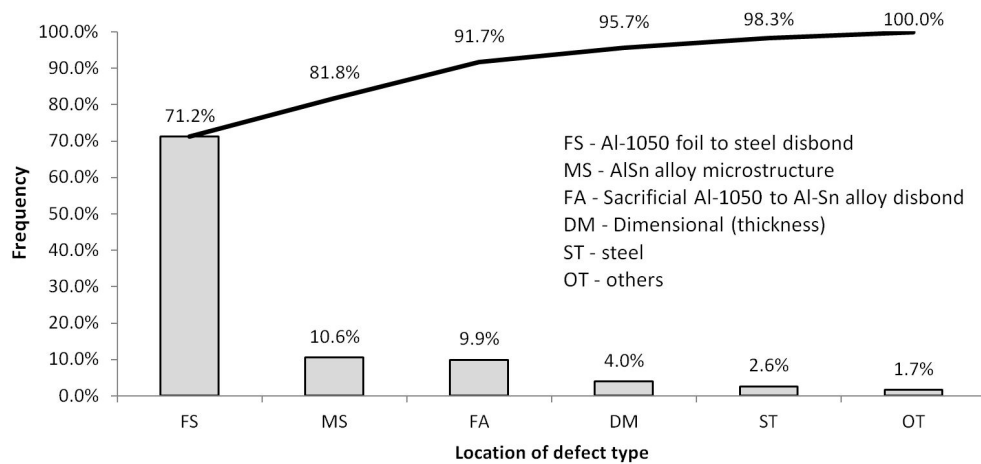


Figure 1.5: Pareto analysis of defects that occurred over a period of three years in CRBed Al/Al-Sn/Al/steel bimetal strips

the alloy at the sacrificial side is visible as blisters on the strip surface, which is shown in Figure 1.6(b). Figure 1.6(c) shows continuous oxides at the intermediate Al-1050 foil to Al-Sn alloy interface, which caused delamination. In Figure 1.6(d), the delamination between intermediate bond foil and Al-Sn alloy is caused by continuous porosity along the bond line. Continuous tin stringers, as shown in Figure 1.6(e), can also initiate delamination between intermediate bond foil and Al-Sn alloy.

Figure 1.7 illustrates the different types of intermediate bond foil to steel bond defects. If the solution heat treatment or annealing time is exceeded, there is the risk of the formation of a brittle intermetallic layer that forms at the bond line, as shown in Figure 1.7(a). Three intermetallic phases Al_2Fe , Al_5Fe_2 and $Al_{13}Fe_4$ exist when the steel diffuses into the aluminium layer, as Fe has a high solubility in Al [5]. Plant internal trials concluded that an intermetallic layer which is thicker than $3-5 \mu m$ is detrimental to the bond, which forms at enhanced solution heat treatment temperatures and/or times. Figure 1.7(b) shows steel debris along the bond line, which were bonded to the intermediate bond foil, but not to the steel. This is an initiation point for delamination. Debris at the bond line are typically caused by insufficient extraction of debris during the steel surface finishing operation.

If bond defects are not detected during strip manufacturing, there is a chance at downstream half shell bearing manufacturing operations at the internal customer to

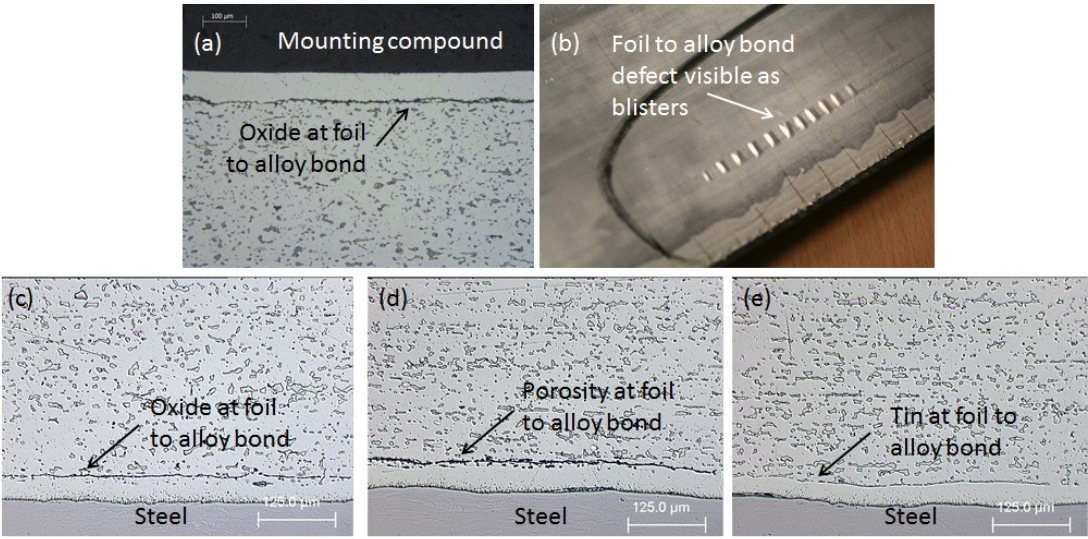


Figure 1.6: Foil to alloy bond defects (a) micrograph of sacrificial side, (b) blisters on bimetal strip surface, (c) micrograph showing oxides at bond, (d) micrograph showing porosity at bond and (e) micrograph showing tin at bond

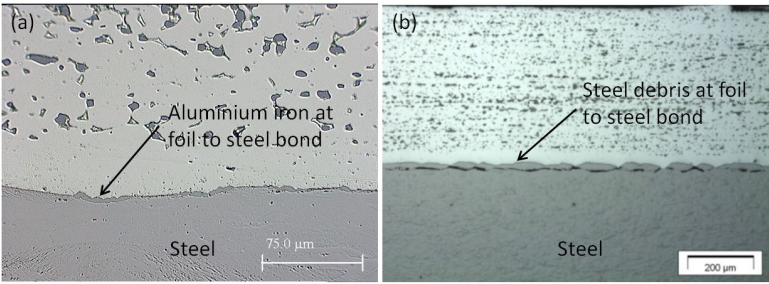


Figure 1.7: Foil to steel bond defects (a) micrograph showing formation of aluminium iron, (b) steel debris bonded to foil

detect bond defects. Figure 1.8 illustrates bond defects at the interface between intermediate bond foil and steel, which were only detected after further downstream processing. In the manufacturing of bearing components, bimetal strips are slit into multiple, more narrow strands. If the components are processed down-strip, then the strand width corresponds to the width of the component. If the components are processed cross-strip, then the strand width corresponds to the blank length of a component. Depending on the width of the bimetal strip and strand, one strip can be slit into two to 15 strands. Figure 1.8(a) shows a narrow down-strip strand after slitting, in which the clad Al completely detached from the steel. The steel surface appearance is relatively uniform, which indicates that the steel was not finished properly before bonding. The fact that the clad Al detached only after slitting, indicates that the processing issue was only local, because the clad Al did not detach from steel in adjacent strands. Once strips are slitted into strands, blanks are cropped from the strand. These blanks are then pressed into half shell bearings. At this stage, features are manufactured. Figure 1.8(b) shows a half shell bearing, in which the clad Al detached from the steel when the oil groove was milled. The forces during the milling operation exceeded the bond strength between foil and steel, indicating that the bond was weakened but not detected at earlier manufacturing and inspection steps. The inner diameter of the half shell bearings is finished with a high speed boring operation. Figure 1.8(c) shows a clad Al to steel delamination, which occurred when the shear forces exceeded the adhesion between the layers during inner diameter boring.

Figure 1.9 shows different lining microstructures that are unacceptable because of their detrimental effect on product performance. Figure 1.9(a) shows small areas of porosity in the Al-Sn alloy. A significant level of non-reticulated tin longer than 0.13 mm in rolling direction is shown in Figure 1.9(b). Figure 1.9(c) shows the occurrence of stabilised tin stringers.

Any point of contact between strip and machine (e.g. guided rollers, pinch units) can cause scoring or indents on the lining or steel side of bimetal strips. Figure 1.10 shows indents on the steel backing that were not acceptable.

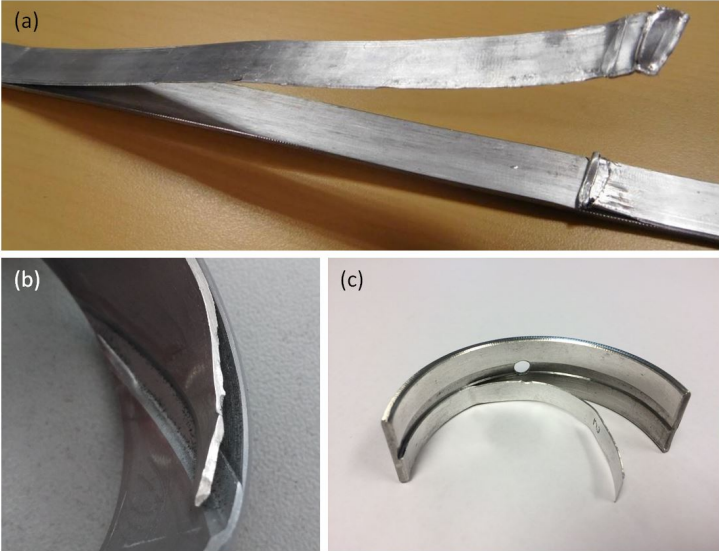


Figure 1.8: Delamination between intermediate bond foil and steel (a) in a narrow strand, (b) in a half shell bearing after oil groove milling and (c) in a half shell bearing after inner diameter boring

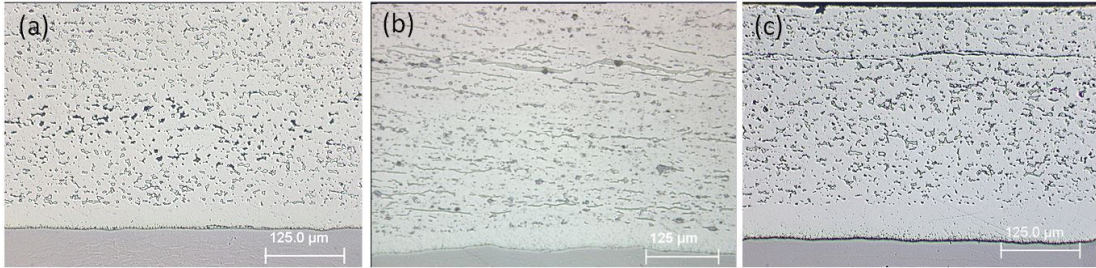


Figure 1.9: Microstructural defects in Al-Sn lining (a) porosity, (b) directionality and (c) stabilised tin stringers

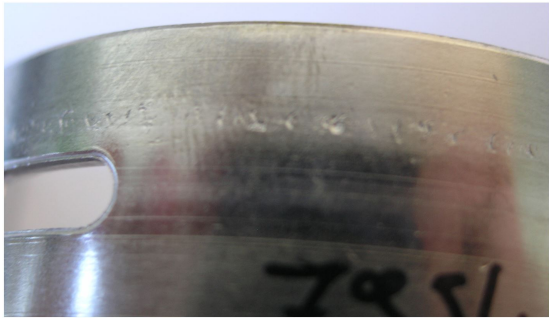


Figure 1.10: Indents on steel backing material

1.3 Aims of thesis

There are two bimetal strip manufacturing processes in the MAHLE Kilmarnock Scotland plant, CRB of aluminium-based alloy on steel and continuous sintering and rolling of CuSnNi bronze to steel. The objective of the NDT system is to detect sub-surface bond defects between the various interfaces. The main body of this thesis focuses on the development of an online NDT technique for Al/Al-Sn/Al/steel bimetal. A case study describes the development and application of the prototype system for CuSnNi/steel bimetal inspection, which was an additional validation of the developed technique. The overall aim of this thesis is to prevent bimetal strips being delivered to customers with bond defects. This can be achieved by reducing the occurrence of bond defects through the identification and implementation of defect prevention controls and developing from sampling to 100% volumetric online inspection. In order to achieve the overall aim of the thesis, the following objectives were concluded:

1. Establish what kind of defects occur in cold roll bonding and continuous sintering of bimetal strips.
2. Review the literature to identify suitable NDT techniques that could be employed for the bond inspection of CRBed Al/Al-Sn/Al/steel and sintered CuSn/steel bimetal strips.
3. Conduct an initial feasibility study on promising NDT techniques to detect bond defects.
4. Develop a system for final inspection and in-process control in serial production.
5. Identify root causes for defects in bimetal strips and implement prevention controls.

Findings from this research will contribute to the question; if a NDT technique can be developed and employed in the harsh bimetal strip manufacturing environment. Furthermore prevention controls will reduce the likelihood that defect occur in production.

1.4 Publications to date arising as a result of thesis

Journal publications

P. J. Tallafuss, A. Rosochowski and S. Campbell, "A feasibility study on different NDT techniques used for testing bond quality in cold roll bonded AlSn alloy/steel bimetal strips", *Manufacturing Review*, vol. 4, no. 4, pp. 1-18, 2017.

P. J. Tallafuss, V. Garca, P. Kowski and A. Romero, "Detection of bond defects in cold roll bonded Al/Al-Sn/Al/steel sheets using Lamb type guided wave EMATs (Spanish)", *Asociacion Espanola de Ensayos No Destructivos*, vol. 3, no. 80, pp. 32-40, 2017.

P. J. Tallafuss, A. Rosochowski, S. Campbell and X. Minguez, "Implementing an online bond quality inspection system for cold roll bonded Al/Al-Sn/Al/steel strips using guided wave EMATs", *Insight Non-Destructive Testing and Condition Monitoring*, vol. 60, no. 3, pp. 145-154, 2018.

P. J. Tallafuss and J. Johnston, "Defects, causes and prevention controls in the continuous bronze/steel bimetal strip sintering process", *Engineering Failure Analysis*, vol. 92, pp. 32-43, 2018.

P. J. Tallafuss, X. Minguez and A. Rosochowski, "Development of S_1 guided wave mode using EMATs for online inspection of porosity and delamination defects in CuSn/steel bimetal strip production", *Journal of Nondestructive Evaluation*, (under review).

Conference publications

P. J. Tallafuss, A. Rosochowski, S. Campbell and A. Camacho, "Detection of bond defects in cold roll bonded Al/Al-Sn/Al/steel sheets using Lamb type guided wave EMATs", in *Proceedings of the First World Congress on Condition Monitoring (WCCM 2017)*, p. 56, London, UK, 2017.

1.5 Overview of thesis

Figure 1.11 provides an overview of the EngD project. It schematically shows the logical progression of the project, how the individual work packages are linked to each other and were published in journal and conference articles.

After a major bearing component failure in the field caused by an undetected defect in the plant, MAHLE initiated the project to develop a serial online NDT system. Chapter 1 introduces the project background and aims of the thesis. The destructive quality tests and defects that occur in Al/Al-Sn/Al/steel bimetal are introduced. The most significant defects such as delamination and porosity that should be detected with the online NDT technique were identified.

Chapter 2 introduces the Al/Al-Sn/Al/steel manufacturing process and cold roll bonding mechanism.

A literature review was conducted to identify NDT techniques that exist and which could potentially be employed to detect delamination and porosity defects in bimetal strips. Based on the literature review, shearography, thermography, ultrasound and guided waves generated with EMATs were selected for a feasibility study. For this study, defects were artificially implanted into CRBed Al/Al-Sn/Al/steel samples and then tested with the different techniques. The result was that guided waves and EMATs was the most promising technique for bimetal strips bond NDT. The feasibility study is described in chapter 3.

After the technique using guided waves generated with EMATs was identified, an industrial development partner for the prototype inspection machine was selected. In chapter 4, the theoretical background about guided waves is summarised. It describes how a numerical model was used to obtain dispersion curves for Al/Al-Sn/Al/steel bimetal plates to identify potential guided wave modes for practical inspection and how guided waves interact with defects.

Subsequent experimental research presented in chapter 5 verified that the identified wave mode parameters can be used to detect bond defects in Al/Al-Sn/Al/steel plates. Samples with artificially implanted delamination, embedded steel debris and brittle

intermetallic Al-Fe diffusion bond layers were produced for this study. The result was an understanding of the system sensitivity to detect these significant defects. Furthermore it was found that the technique could work for in-process control and online final inspection.

A guided waves EMAT prototype inspection machine was designed and built in collaboration with the industrial partner. The system was installed at an industrial strip processing line for rigorous online inspection trials of full-length Al/Al-Sn/Al/steel strips to address the question, if online inspection under the harsh manufacturing conditions is possible. The EMAT prototype machine has successfully demonstrated the capability to detect bond defects online, which nowadays are only detectable with a destructive peel-off test. In addition, 100% volumetric inspection of the material can be achieved online instead of only spot-checks at the beginning and the end of strips. The experimental work that was done online on the industrial strip processing line is described in chapter 6.

Once trials with Al/Al-Sn/Al/steel samples were successfully completed, work was undertaken to also reduce the defects in CuSn/steel bimetal strips so that material would not fail in the field. Chapter 7 is a systematic analysis of defects that occur in CuSn/steel bimetal strips, root cause investigation and identification of defect prevention controls. Since to date no systematic review about strip defects originating from the manufacturing process existed in the public domain, research and examination was carried out in the MAHLE Kilmarnock plant to understand the defects that occur in serial production. It was identified that porosity and delamination are the most significant defects in CuSn/steel bimetal strips and that the NDT technique should be able to detect these defects.

Chapter 8 is a feasibility study to detect porosity and delamination defects in CuSn/steel bimetal strips. Dispersion curves were calculated to identify potential wave modes for practical inspection, which were then experimentally verified using the guided waves EMAT prototype machine and samples with artificially implanted defects. Online trials of full length non-conformance coils during production verified that the prototype system is also able to monitor CuSn/steel bimetal strips in the harsh manufacturing

Chapter 1. Introduction

environment.

Based on the project outcomes, it was decided to develop a serial machine concept and technical specification for industrialisation of the inspection technique. The concept was developed in collaboration with a 3rd party mechanical machine building partner. The concept considers the lessons learned from the extensive practical experimental research. Chapter 9 describes the key points that were considered for the industrialisation stage of the project.

Chapter 1. Introduction

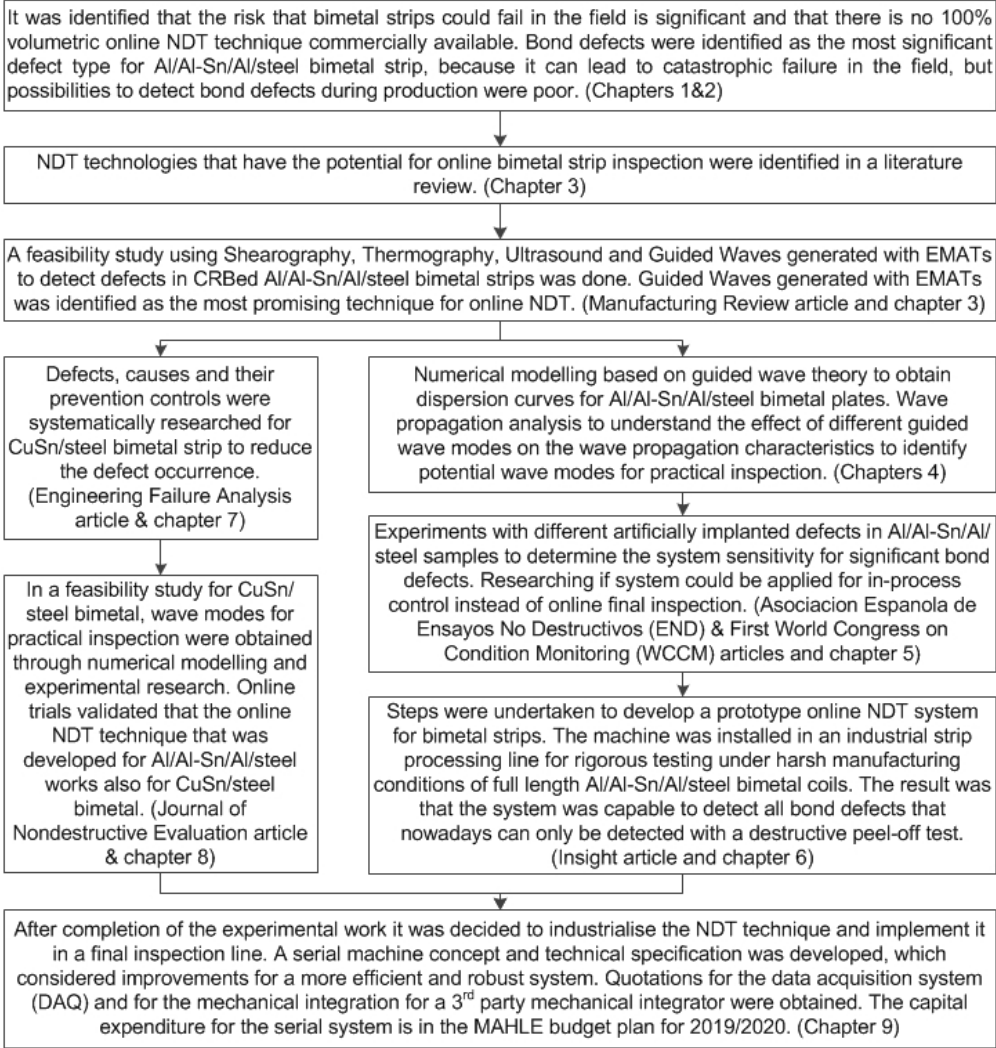


Figure 1.11: Schematic diagram showing the main stages of the EngD project and how the individual work packages were published and are linked into sections of the final thesis

Chapter 2

Al/Al-Sn/Al/steel cold roll bonding process

In this chapter the Al/Al-Sn/Al/steel bimetal CRB process is described. The NDT inspection system should be installed either as in-line process control or as a final inspection operation in this process. This manufacturing process was also used to produce sample sheets and strips for the NDT experimental research in this work.

2.1 Manufacturing process

2.1.1 Al-Sn alloy casting

Figure 2.1 schematically illustrates the casting process. A melting furnace with core-less crucible and helical copper coil is used to melt out initial and process residue material. The functional principle is to heat the charge by inducing alternating currents, which pass through the coil. Once the metal is liquid, the electromagnetic field, which is produced by the coil and the induced current in the material, creates a stirring effect that homogenises the chemical composition and temperature of the molten alloy. The crucible is tilted to transfer the melt into holding furnaces via launder segments. A critical process parameter is the temperature before transfer to ensure the melt reaches the holding furnaces at 770-790°C temperature. The crucible gas fired holding furnaces hold sufficient, small batches of melt at temperature available in front of the continuous

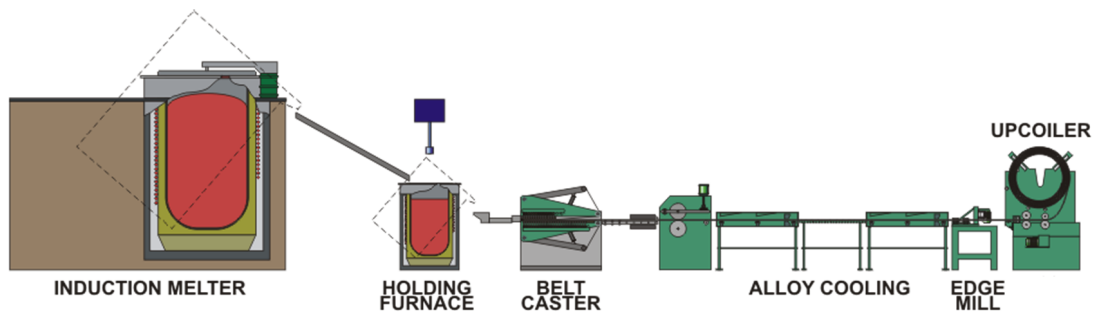


Figure 2.1: Schematic of continuous Al-Sn alloy twin belt casting process

horizontal twin-belt casting lines. A rotary degassing unit using N_2 purges the melt from impurities. This is required due to the high affinity of aluminium for hydrogen in order to prevent gas inclusions that could cause porosity in the cast coils. Al-Sn alloys for bearings are cast using a horizontal fibreglass twin-belt process. This technology can be traced back to US patent 3110941 filed in 1960 and assigned in 1963 to R.T. Fagg from American Metal Climax Inc. At present, the production of Al-Sn alloys is the only application of fibreglass twin-belt casting technology. The liquid Al-Sn alloy is poured from the holding furnaces into a tundish with a ceramic casting die between two rotating fibreglass belts. The belts are under tension using guided rollers. The molten metal solidifies between two water cooled copper plates, which are 16 mm apart from each other. The belts are sprayed with a graphite lubricant to prevent the metal sticking to the belt and are characterized by zero relative movement between belt and casting surface, which results in the desired surface quality for the next process step. A sample of the coil is analysed by XRF to confirm the correct chemical composition. Silicon containing alloys are annealed after casting to relieve stress and homogenise the alloy before cladding. Non-silicon containing alloy continue to the cladding process without annealing.

2.1.2 Al/Al-Sn/Al cladding

The Al-Sn cast coils are, depending on the final product, either clad with 1.2 mm or 1.5 mm thick Al-1050, Al-Cu, Al-Si or Al-Mn foil on either one or both sides in a cold rolling cladding operation. Due to the relatively soft tin phase in the Al-Sn alloy

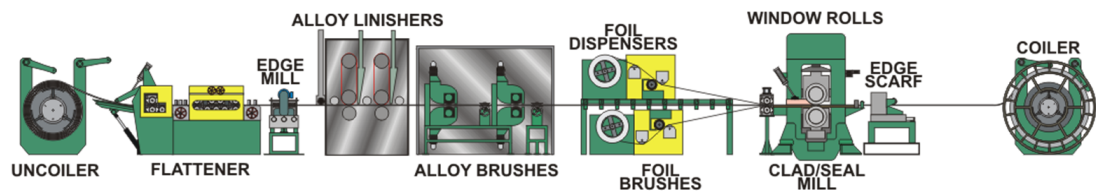


Figure 2.2: Schematic of Al/Al-Sn/Al cladding process

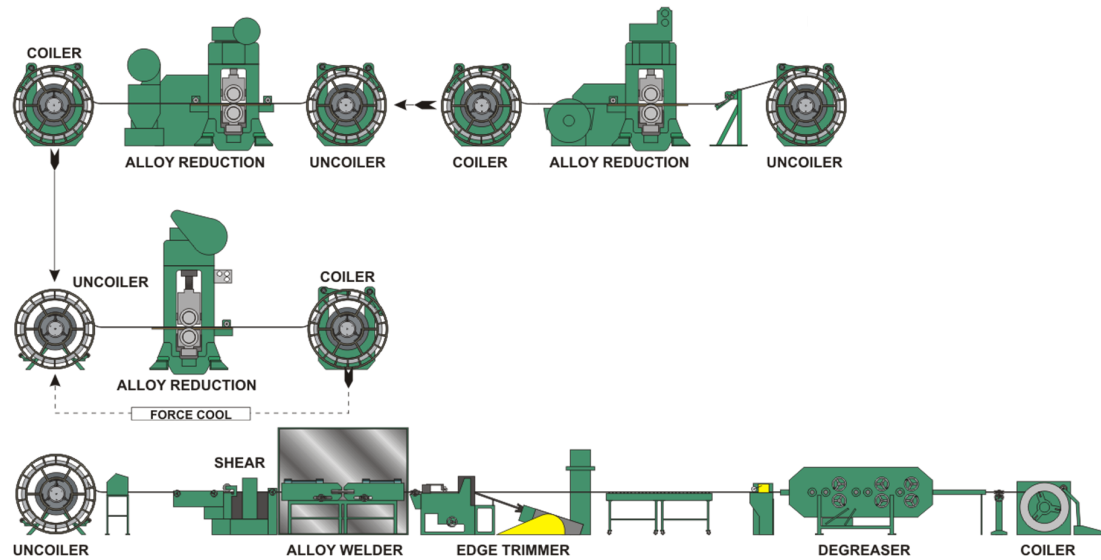


Figure 2.3: Schematic of Al/Al-Sn/Al clad alloy rolling process

that has an adverse bond effect, the cladding foil is required as bonding agent between Al-Sn alloy and steel to achieve the required adhesion at the bonding operation. The second clad foil layer is sacrificial and is machined at the downstream operation half shell bearing ID boring. The purpose of the sacrificial layer is to prevent tin bleeding at subsequent annealing operations. The Al-Sn cast coil surface is linished and brushed and the foil surface is brushed at their interfaces before all three layers enter the rolling mill simultaneously and the thickness is reduced by 63%. This process is shown in Figure 2.2.

2.1.3 Further rolling reduction

Figure 2.3 shows a sequence of rolling passes in which the Al/Al-Sn/Al clad alloy is rolled down from about 7.0 mm to 2.0 mm in a tandem mill stand. The first pass is

referred to as "sealing", as the first double pass has to take place within a certain time period to prevent the cladding foils from detaching from the alloy. Once at 2.0 mm thickness, the Al/Al-Sn/Al alloy is further rolled to the final thickness in another 3-4 passes at a stand-alone 4-high rolling mill with high tolerance control. A typical final rolling thickness is about 0.90 mm. Once at final thickness, the alloy is trimmed to the required width and to remove edge cracking and degreased before the clad alloy is sent to the bimetal bonding operation.

2.1.4 Cold roll bonding Al/Al-Sn/Al/steel

In cold roll bonding, a solid state weld is achieved at room temperature by the joint plastic deformation of the clad alloy and steel. Figure 2.4 illustrates the cold roll bonding process in the Kilmarnock plant. In order to run the process continuously, steel coils are welded together at the input side of the line. During the time that the steel input side of the plant has to stop for welding, steel is supplied from the input magazine to continue bonding. The steel coil is straightened and degreased in a high pressurised, high temperature water tank and then finished by rotating abrasive belts to activate the surface before the bonding operation. The clad alloy bond surface is brushed before bimetal bonding. Purpose of the surface preparation is the removal of contaminants and surface oxides, which would prevent an effective cold weld. The steel and clad alloy strips pass simultaneously through a 4-high mill with a 43% thickness reduction to bond the layers. After bonding, the bimetal strip is pulled through a bimetal exit magazine, which allows the operator to remove coils from the coiler while the bonding operation continues to run. The bimetal coils then undergo a post bonding annealing operation to alleviate any strain that was caused by cold working and to improve the bond.

2.1.5 Solution heat treatment

Some Si-containing materials are heat treated by processing the bimetal coils through a fluidised bed, which is a bed filled with sand that is kept at a constant temperature of about 475°C. The bed has approximately 4 m length and depending on the bimetal

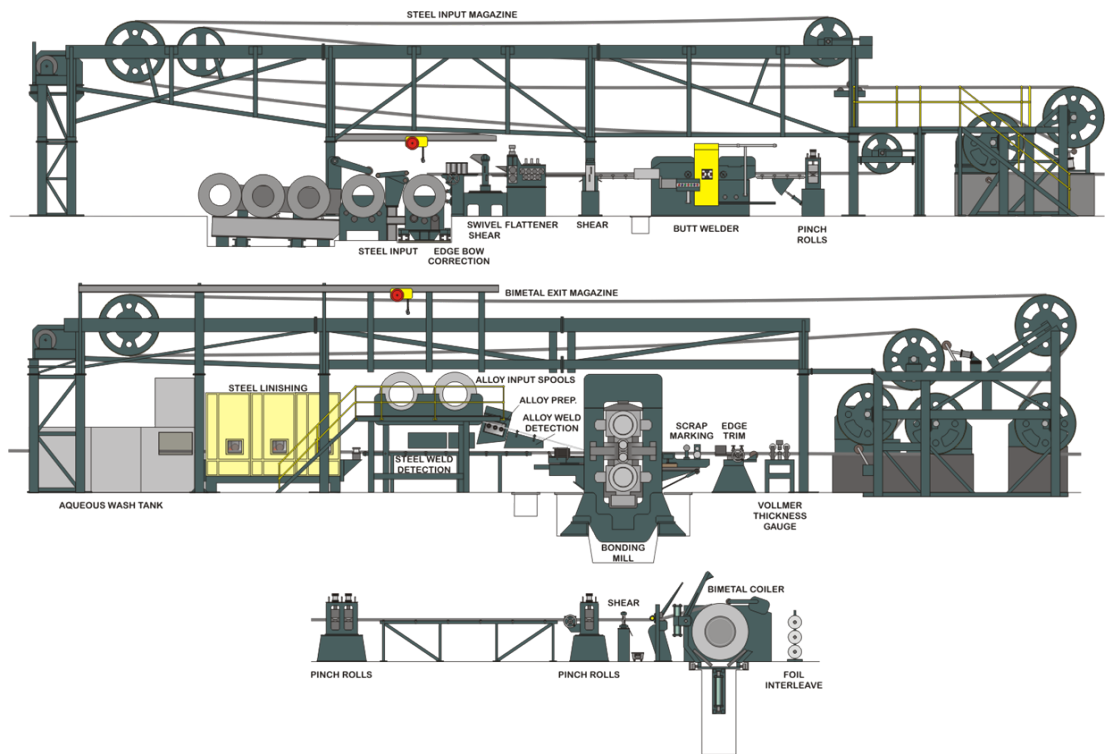


Figure 2.4: Schematic of cold roll bonding Al/Al-Sn/Al clad alloy to steel

thickness, the processing speed is between 4-5 m/min. In this process, precipitation hardening occurs which leads to a higher maximum load capability of the bearings made from this type of material. Exceeding the time at temperature at this process causes brittle Al_xFe_x intermetallics, which are the main cause for delamination between clad Al and steel for this type of material.

2.1.6 Final inspection

At the final inspection line, machine visual inspection (Cognex, 60 MHz compact digital camera nodes) is used for 100% volumetric inspection of the coil surface to find any previously unnoticed surface defects. Defects are scrap marked before packing the coils for delivery. Currently, only surface defects can be detected, but no subsurface or bond defects.

Table 2.1: Chemical composition (wt%) of Al-Sn alloys considered in this study

Alloy type	Sn	Cu	Si	Ni	Mn	V	Al
A11	6	1	-	1	-	-	Bal.
A15	20	1	-	-	-	-	Bal.
A16	20	1	-	-	0.25	-	Bal.
A104	10	1	4	-	-	-	Bal.
A19/A20	6	1	2.2	1	0.25	0.16	Bal.

Table 2.2: Chemical compositions (wt. %) and mechanical properties of low-carbon steel

Type	Fe	C	Mn	Si	Others total	Hardness
Low-carbon	Bal.	0.13% max.	0.60% max.	0.20% max.	0.20% max.	90 - 150 HV ₁₀

2.2 Material and bond properties

2.2.1 Aluminium bearing alloys

The aluminium lining material is made of *Al-Sn* and *Al-Sn-Si* alloys, which are the most widely used lining alloy type in today's bimetal bearing materials. Table 2.1 summarises the chemical composition of the alloys that are considered in this study. Table 2.2 shows a typical low-carbon steel used for bimetal strips.

Aluminium-Tin system

There are a large variety of *Sn* containing aluminium bearing alloys, with *Sn* content varying between 5% and 20%. *Sn* is contained in the aluminium bearing alloy for the bearing anti-friction properties, however microstructure and mechanical property improvements are achieved by adding further alloying elements. *Al* and *Sn* exhibit no solubility in each other, the proportions of the distinct phases depend on the cooling rate. Alloys that exceed 10% *Sn* content have a structure in which *Sn* envelopes surround *Al* grains. Solid solution hardening of the *Al* phase with the addition of up to 1% *Cu* greatly increases the strength of the *Al-Sn* alloy. Annealing is required after certain rolling reductions to recrystallize the *Al* grains due to the cold working. Since the annealing temperatures exceed the *Sn* melting point of 231.9°C, the *Sn* redistributes and therefore no longer isolates the *Al* grains from each other.

Aluminium-Tin-Silicon system

Although *Al-Sn* bearing alloys show good seizure resistance, they feature poor fatigue resistance under high engine loads. *Al-Si* alloys in contrary have excellent wear resistance, but only poor seizure resistance, especially under poor lubricating conditions that can occur in engine bearing applications [6]. The best set of material properties for bearing lining alloys can be achieved by the combination of the *Al-Sn* and *Al-Si* systems in an *Al-Sn-Si* system. The addition of *Mn*, *Ni*, *Cu* and *V* as alloying elements produces complex intermetallics that improve the strength and hardness of the alloy. The material properties of these intermetallic compounds are between metals and ceramics, with metallic and covalent bonds [7].

2.2.2 Microstructural deformation effects in rolling aluminium and steel strips

Aluminium and steel crystal lattice structure

Understanding the initial atomic structure and properties of aluminium and steel is essential to understand the formability behaviour during rolling. The crystal lattice is a regular, repetitive framework with ions at positions that are defined by the unit cell, which describes the atomic structure. Aluminium and austenitic steel have a face centred cubic (fcc) unit cell, while ferritic steel alloys usually crystallise with a body centred cubic (bcc) unit cell as shown in Figures 2.5(a) and 2.5(b) [8]. Both, fcc and bcc have ions that are located at the eight corners of the cube. The fcc unit cell has an additional ion located in the geometric centre of each of the cube faces, while the bcc only has one additional ion in the centre of the cube.

While aluminium always crystallises with a fcc lattice, the unit cell structure of steel alloys is dependent on the present iron phase and therefore more complex. Three phases exist, which are α -, γ -, and δ -iron [9]. However, low carbon steel that is subject in this work, can be considered as pure iron due to the very small weight % (approx. 0.005%) of carbon that is present in the alloy, which exists as the α -iron phase (ferrite) that crystallises as bcc unit cell and stays structurally stable up to a temperature of 910 °C,

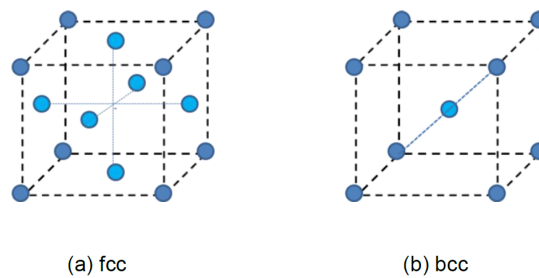


Figure 2.5: Lattice structure (a) face-centred cubic and (b) body-centred cubic [8]

which is not exceeded in the Al/Al-Sn/Al/steel bimetal manufacturing process. This phase is ferromagnetic [9].

Grain formation at microstructural level

Individual grains and their orientation, morphology and size of crystals determine the composition of a polycrystalline aggregate's microstructure. Grains are a volume of crystals that have a similar or same crystallographic orientation. These crystallographic grains play a significant role in the formability and mechanical properties of metals [10].

The extreme case of recrystallisation is when metal solidifies from a liquid state and grains start to grow. Formation of grains is initiated at random locations as small nuclei that are a focal source of grain growth, spread in all directions and form in the specific lattice structure of the metal. The orientation of the lattice relative to the other nuclei and the sample boundaries is random, since each nuclei develops independently. In an idealised scenario, each adjoining atom inherits the lattice structure and orientation of the initial grain nuclei, until eventually the individual grains meet and form grain boundaries [11]. Figure 2.6 illustrates an Electron backscatter diffraction (EBSD) Grain Identification Map (GIM) from a typical *Al-Sn-Si* bearing alloy. The colours are arbitrary and highlight the grains and their boundaries. The accumulation of grains is what is referred to as microstructure, which determines the physical material properties.

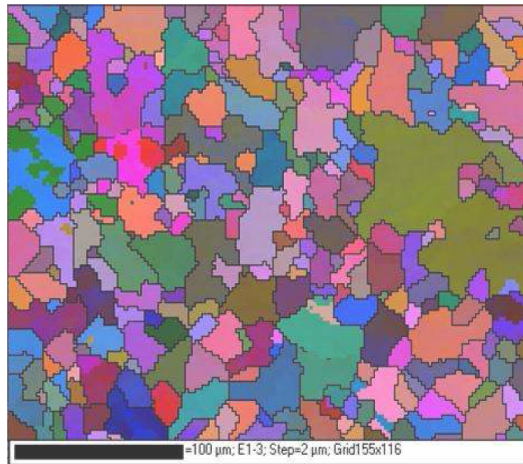


Figure 2.6: EBSD grain identification map from a rolled and bonded *Al-Sn-Si* alloy sample [12]

Microstructure deformation during rolling

The crystal lattice of the polycrystalline metal will either deform elastically or plastically [13], depending on the relation between applied load and yield strength of the metal [8].

Elastic deformation

Elastic deformation of the crystal lattice occurs when the applied load remains below the yield stress. Once the load is removed, the lattice returns to the initial state with the initial interatomic planar spacing, shape and size. The physical laws Hooke's law of elasticity and the materials Poisson's ratio describe the elastic deformation [8]. The elasticity of the crystal lattice is fundamental for the creation of ultrasound waves in the material that are used for inspection.

Plastic deformation

Plastic deformation is required to roll down the thickness of the *Al-Sn* or *Al-Sn-Si* bearing alloy and bonding on steel backing material. It can be described as flow-like behaviour of the metal, while the deformation alters the initial material properties [14]. The metal either *fractures* or *slips* when the yield strength is exceeded. During the

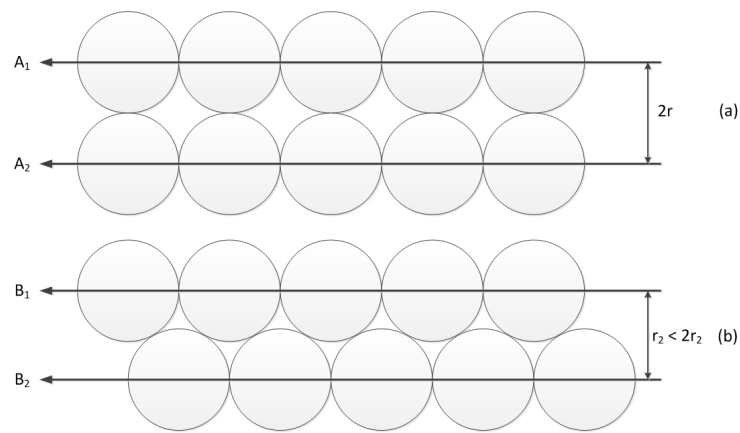


Figure 2.7: Schematics illustrating the more likely occurrence of slip in the (a) primitive cubic lattice compared to (b) lattice with smaller planar spacing

rolling of *Al-Sn* or *Al-Sn-Si* alloys, it is inevitable that fracture along the edges of the strips occurs, which is not desirable and is trimmed off during the process. Slip is the movement of atomic planes sliding over another and is the desired outcome of rolling the metal, as it creates a permanent and irreversible change in the shape and structure, while the polycrystalline volume is maintained.

Slip

The lattice structure for a metal determines the formation and direction of prevalent slip planes. Figure 2.7(a) shows a primitive cubic lattice that features planes along A_1 and A_2 , which are equal from all three Cartesian directions x , y and z . In these two planes, the atoms are exactly aligned with each other, which is characteristic for a primitive cubic lattice system. The inter-atomic planar spacing is equal to the diameter of one atom and each horizontal and vertical plane has the same, high atomic density. Figure 2.7(b) illustrates a lattice structure, in which the planes are defined by B_1 and B_2 , and the atomic separation is smaller compared to the primitive cubic lattice structure. Considering the 'least energy' argument, slip is more likely to occur between planes A_1 and A_2 than B_1 and B_2 [15].

Table 2.3: Common slip planes $\{uvw\}$ and directions $\langle hkl \rangle$ for fcc and bcc crystal lattice metals

Material	Primary slip system	Secondary slip system
fcc	$\{111\}\langle 1\bar{1}0 \rangle$	-
bcc	$\{110\}\langle \bar{1}10 \rangle$	$\{112\}\langle 11\bar{1} \rangle$ $\{123\}\langle 11\bar{1} \rangle$

Slip planes in bcc and fcc polycrystalline metals

Metal sheets such as *Al-Sn* or *Al-Sn-Si* alloys and low carbon steel are constructed of discrete grains (see Figure 2.6), therefore the simplified slip description is not adequate. Due to the fact that the individual grains have random lattice orientations relative to each other, the lattice structure is not homogeneous throughout the sheets, and consequently one slip system cannot propagate throughout the entire sheet [16]. Therefore plastic deformation in polycrystalline sheets involves multiple slip systems within the constituent grains that are involved in the forming process and their averaged mechanical properties determine when the yield point is exceeded, resulting in plastic deformation [8]. Table 2.3 summarises the common primary and secondary slip planes for fcc and bcc metals [17].

A defect in the lattice structure is defined as any interruption in the continuity of the crystal lattice. The type of defects that exist are either vacancies or extra interstitial atoms that are located within the crystal lattice. These defects manifest themselves either as point or line defects in the crystal lattice. It is the movement of line defects along the slip planes that initiate slip systems in polycrystalline systems. These line defects are referred to as dislocations, of which two primary types exist: edge and screw dislocations [10].

Edge dislocation

Figure 2.8 schematically illustrates shearing of a crystal by one atomic distance along the plane that leads to a single edge dislocation. If a dislocation propagates through the entire crystal lattice, it leads to an edge at the surface. Even though the edge is small and therefore difficult to detect, visible slip lanes are created when a number of

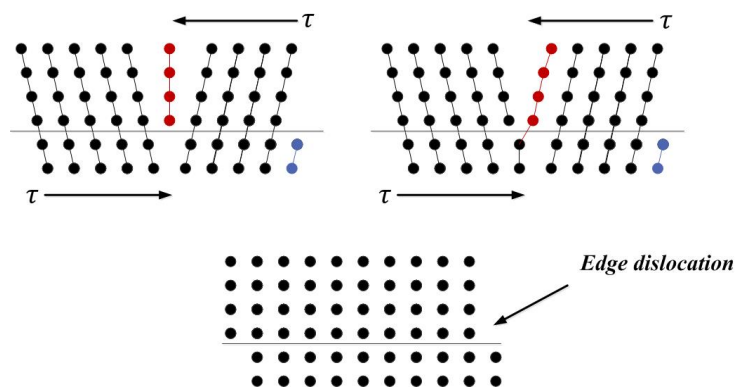


Figure 2.8: Single edge dislocation

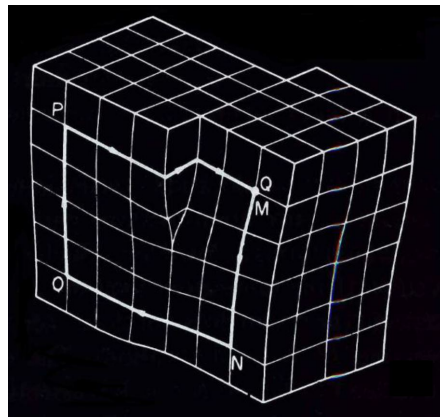


Figure 2.9: Screw dislocation [18]

edge dislocations accumulate along the same slip plane [10].

Screw dislocations

Screw dislocation is schematically shown in Figure 2.9. In contrary to the edge dislocation that propagates through the entire crystal, the screw dislocation is a helical-like defect that involves crystals from inter atomic planes adjacent to the slip plane. The direction of the screw dislocation is dependent on the planes that are involved [18], which is illustrated in Figure 2.9.

The Burgers vector, \mathbf{b} defines the order of magnitude and orientation of the edge or screw dislocation and corresponding lattice distortion. In case of the edge dislocation, the Burgers vector is orthogonal to the dislocation, while in the case of the screw ori-

entation, the Burgers vector is parallel to the dislocation [18]. The dislocation density is higher at grain boundaries, since grain boundaries prevent dislocations from propagating and therefore multiple dislocations accumulate at the grain boundaries. This accumulation of dislocations at grain boundaries is a significant influencing factor on ultrasound wave scattering [8].

2.2.3 Roll bonding process

During the rolling process the thickness of a metal, which is usually a strip, billet, bloom, plate or sheet, is plastically reduced, which results in an elongation of the material, while the material volume remains constant [19]. Rolling of sheets is a directional process, which means that the material properties become directional as well. On a micro structural level, this means that slip is introduced, which converts the isotropic into an anisotropic state, which affects the elastic behaviour of the cubic-crystallising metals [13].

CRB is the process of generating composite materials of dissimilar metals at room temperature. The metal sheets are stacked on top of each other and pass simultaneously through a rolling mill, in which both metals are subject to substantial reduction that facilitates a solid state bond [1]. The rolling as well as the roll bonding process can be done either above (hot rolling, hot roll bonding) or below (cold rolling, cold roll bonding) the recrystallisation temperature of the metals that are processed.

Figure 2.10 schematically illustrates the rolling process, in which two rolls rotate in opposite angular direction and apply load on the input material with initial thickness (t_1) to reduce the thickness of the material as it passes through the rolls. The resulting output material thickness (t_2) depends on the gap between the two work rolls. The elongation of the material implies that the angular roll velocity is greater than the material input speed, which is achieved by the substantial frictional forces to plastically reduce the thickness of the material [20]. The equation for the ratio of the rolling reduction that the materials experience as they pass through the rolls is given by Equation 2.1 [19]:

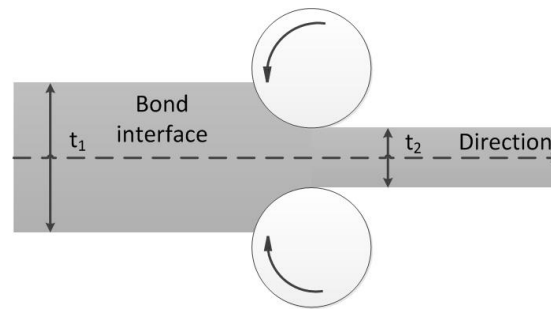


Figure 2.10: Schematic of the rolling process [20]

$$r_{red} = \frac{t_2}{t_1} \quad (2.1)$$

For high reduction levels like in this process in which alloy is reduced from 16 mm to 0.5 - 0.8 mm, i.e. $t_1 \gg t_2$, a sequence of multiple passes and/or rolling mill stands is used to achieve this substantial accumulated thickness reduction.

Mechanism of cold roll bonding

Although the complex interface that forms during roll bonding is not yet completely understood [21], there exist four theories to explain the mechanism of CRB and all four theories are believed to contribute to the bonding mechanism: 1. thin film [22–27], 2. energy barrier [22], 3. diffusion bonding [28] and 4. joint recrystallisation [29] theories. It is generally accepted that the thin film theory is the predominant mechanism of CRB [21, 30], since the rolling temperature is below the recrystallization temperature of the metals involved.

The thin film theory states that bonding between metals is achieved when surface deformation is severe enough to expose the uncontaminated metal from below the surface and the two layers get in contact with each other. Figure 2.11 schematically illustrates the thin film mechanism for two metal layers with brittle surfaces and covering layers that enter a mill simultaneously for bonding. The bond between the two metals develops in three stages:

1. The two brittle surfaces are brought into contact.
2. The contacting surfaces are activated by applying pressure via the rolling mills,

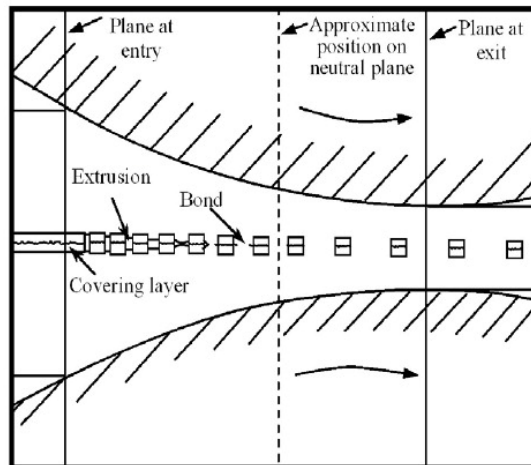


Figure 2.11: Schematic illustration of the thin film theory showing fracture and extrusion of the stacked metal sheet surface layers during CRB [21]

which results in surface area increase that cracks the brittle cover layers as well as reduces the thickness of the contaminant film.

3. Creation of the metallurgical bond by extruding uncontaminated metal that form cold welds that are interrupted by isolated islands of the brittle cover and contaminants layer.

The strongest bond is achieved when the areas of metallic bond and interruptions of brittle material are in a steady pattern [1]. The thin film theory was further developed by differentiating between two bond formation mechanisms within the thin film theory [31];

1. Brittle surface cover layers fracture as a result of the surface increase during rolling. In CRB these brittle, work hardened surface layers are achieved by scratch brushing and/or finishing the metal surfaces before bonding. The fractures open the metal surfaces that are bonded together so that the internal uncontaminated metal is extruded and their highest asperities form a metallic bond.
2. In metal surface areas where no brittle cover layer exist, the oxide, water and any other contaminant film is locally thinned until the uncontaminated metal

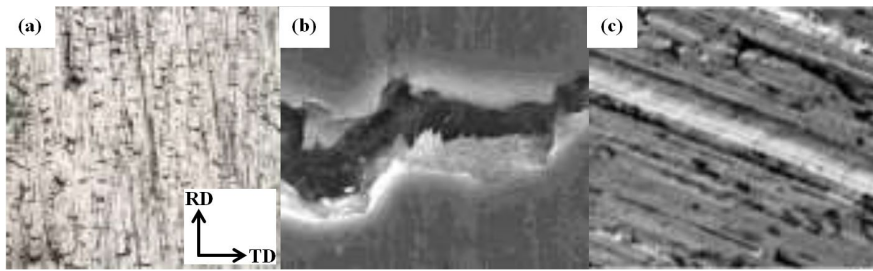


Figure 2.12: SEM micrographs of Al-Sn alloy (a) cracking of the Al-Sn cover layer, (b) magnification of the same surface showing that the fracture is brittle, (c) finished low carbon steel after surface expansion showing cracking of the brittle cover layer [1]

is exposed. In order to achieve this a threshold surface increase, the threshold reduction R_t during CRB is required.

Figure 2.12 shows Scanning Electron Micrographs (SEM) that confirm this mechanism, The SEM micrographs were taken from Al/Al-Sn/Al/steel bimetal samples. Figure 2.12(a) shows a SEM micrograph of the Al-Sn alloy surface after scratch brushing and surface expansion that led to cracking of the cover layer. Figure 2.12(b) is a magnification of the same Al-Sn alloy surface showing that the surface cracking is brittle. Figure 2.12(c) is a SEM micrograph showing the finished low carbon steel surface that exhibits cracking of the brittle cover layer.

For Al/Al-Sn/Al/steel bimetal strips in this thesis, the low carbon steel surface is finished and the clad alloy surface is scratch brushed to generate a brittle surface layer by introducing dislocations to the surface lattices [1] as required for the thin film theory mechanism. Metals with a cubic lattice structure, such as fcc for the the Al-Sn alloy and bcc for the low carbon steel, are more suited for CRB compared to metals with hexagonal lattice structure. Hexagonal lattice structures require a higher threshold deformation for bonding and feature lower maximum strength of the bond compared to cubic metals.

The proposed explanation for this behaviour is that for hexagonal metals, the oxide films break up independently from each other, while for the cubic metals, the oxide films crack coherently, which promotes bonding over a larger contact area for the two cubic metals [21].

The energy barrier theory suggests that a certain energy level is required to rear-

range atoms in the metal surface layer to achieve a boundary configuration as well as to disperse the surface contaminants layer, before bonding can take place [22, 24]. It is likely that the energy barrier is the barrier that is required to achieve recrystallization in the metals, since in experiments with clean surfaces no bonding occurred, until the required energy for recrystallization was achieved [29].

It is generally agreed that rolling creates an initial mechanical bond before a strong metallurgical bond develops. However, it is not clear whether the metallurgical bond already occurs during CRB or only during the post rolling annealing treatment [1].

Parameters affecting bond strength

In the following sections the process parameters are introduced, which affect bond quality and in the worst case can lead to catastrophic failure of engine bearing components in the field. Understanding the mechanism of CRB and its relationship with critical process parameters was systematically researched as part of a Knowledge Transfer Partnership (KTP) project between Glasgow Caledonian University and MAHLE Engine Systems UK Ltd. in Kilmarnock. The objective of the KTP project was to design-out delamination defects through process optimisation and control of critical process parameters. More details can be found in [4].

Surface preparation

As discussed in the thin film theory, a layer of contaminants and surface oxides can prevent the creation of nascent metal welds that are required to create effective cold welds. Studies reported [32, 33] that degreasing the bond surfaces and mechanically scratch brushing them shortly before the sheets enter the rolls, creates the strongest cold roll bonds, since the interfering cover layer is removed. An adequate surface roughness creates more surface asperities that enable localised sheer deformation, which breaks up the remaining, unavoidable surface oxide film [34]. It appears that the local sheer deformation additionally to the surface increase, also helps to break up the continuity of any contaminant film [35]. Results from bonding studies with various different metal combinations showed that each metal combination requires a specific surface prepara-

tion technique to achieve optimum bond quality [1]. For Al/Al-Sn/Al/steel bimetal strips, various studies [32,33], reported that finishing steel and scratch brushing clad alloy creates the strongest cold welds during CRB.

Effect of particles at interface

In general it was found that the presence of contaminant particles at the bond interface during CRB can result in bond failure. Therefore steps were undertaken to minimise the presence of any contaminants at the bond interface and in particular to minimise the aluminium oxide formation [36,37].

CRB reduction factor

Various studies reported that the thickness reduction of a bimetal during CRB is the most influential factor affecting bond strength [38,39] as it is directly related to the extrusion of uncontaminated metal by surface expansion [24]. The maximum bond strength is achieved when the shear bands, perpendicular to the rolling direction, become the same as the tensile strength of the weaker of the two bonding materials [40]. In the case of Al/Al bimetals, up to 60-70% thickness reduction was required to obtain weld strengths which were equivalent to solid metal [24].

Initial thickness

It was observed that increasing the initial thickness of bimetal strips during CRB results in decreased bond strength. This can be explained by pressure, i.e. increasing the thickness of the incoming sheets requires higher pressure to achieve the same reduction percentage [30,41].

Rolling speed

Kilmarnock plant studies from the 1970s trialled various CRB speeds with the result that increased speed did eventually result in poorer bond [1]. This is in line with other studies, which also report that this effect is more pronounced at higher thickness

reductions. It was concluded that this is due to a decrease in the contact time of the interfaces during bonding [42].

Friction coefficient

Studies reported that increasing the friction between work roll and strip increases the mean contact pressure, peel strength and therefore bond strength. Higher friction coefficient correlates to a lower thickness reduction to achieve the same bond strength [32, 41, 43, 44].

Annealing

Annealing is required in the CRB process to modify the hardness that is created by the required thickness reduction and to create strong metallurgical bonds. There are annealing operations that take place either prior or post rolling. Studies showed that in case of bonding aluminium to steel, the bond strength increases significantly if the steel is pre-heated because of the more similar flow characteristics of the metals [45]. In contrast, if the aluminium is pre-heated the bond strength decreases and results in only mechanical interlocking of the surface asperities [33]. The optimum post bonding annealing time depends on temperature and required energy for recrystallisation depending on the amount of deformation that the bimetal has experienced [1]. It was found that bonds, which were created at room temperature, require post rolling annealing to achieve bond strengths for which the shear strength is close to that of a parent material [46].

Chapter 3

How guided waves using EMAT ultrasonic technology was selected in a feasibility study on different NDT techniques

This chapter describes the results from four independent NDT studies, using active thermography, shearography, ultrasound and guided wave EMATs and samples with different artificially implanted defects to explore the feasibility to qualitatively indicate the presence of bond defects. The destructive peel off test was used to correlate the NDT results with known bond quality. The studies were done under laboratory conditions, and in case of ultrasound also online under production conditions. During the ultrasound online testing, the requirements that a NDT technique has to fulfil for online inspection of Al/Al-Sn/Al/steel bimetal strips were established. For active thermography, shearography and guided wave EMAT techniques, it was theoretically analysed, if the laboratory test results could be transferred to testing under production conditions. As a result, guided waves using EMATs, among the four tested methods, are best suited for online inspection of Al/Al-Sn/Al/steel bimetal strips. The content of this chapter is based on the article *A feasibility study on different NDT techniques used*

Chapter 3. How guided waves using EMAT ultrasonic technology was selected in a feasibility study on different NDT techniques

for testing bond quality in cold roll bonded Al-Sn alloy/steel bimetal strips (Tallafuss et al., 2017) that was published in the Manufacturing Review journal.

3.1 Reviewing the literature

The purpose of the evaluation of different NDT techniques is to identify a technology that is likely to be a suitable candidate for practical online NDT of Al/Al-Sn/Al/steel bimetal strip bond quality.

3.1.1 Radiography

In Radiography X-rays are generated electrically, while Gamma rays are emitted from radioactive isotopes. The principle is that the penetrating radiation is absorbed by the material through which it passes. The greater the thickness and the denser the material is, the greater is the absorption of the radiation. The X and Gamma rays convert, in proportion to the intensity of the radiation reaching the film or digital plate [47]. Internal defects like voids in material that is placed between the radiation source and the film are visible on the film as darkened areas, because more radiation reaches the film. This is schematically illustrated in Figure 3.1. The components of X and Gamma radiography systems consist of radiation monitors, film markers, image quality indicators, and darkroom equipment, which can be fully automatic processing units. Computerised tomography allow real time inspection, although more suitable for investigative purposes than in production inspection [47]. Radiography is not suitable for online applications mainly due to possible health hazards and because X-ray images get blurred when parts move, therefore it is not further considered in this feasibility study.

3.1.2 Magnetic particle inspection

Magnetic particle inspection is used to inspect magnetic material, mainly ferritic steel and iron, for the detection of surface and near surface defects. The functional principle is that magnetic flux is generated in the material. If there is no defect, the flux lines are

Chapter 3. How guided waves using EMAT ultrasonic technology was selected in a feasibility study on different NDT techniques

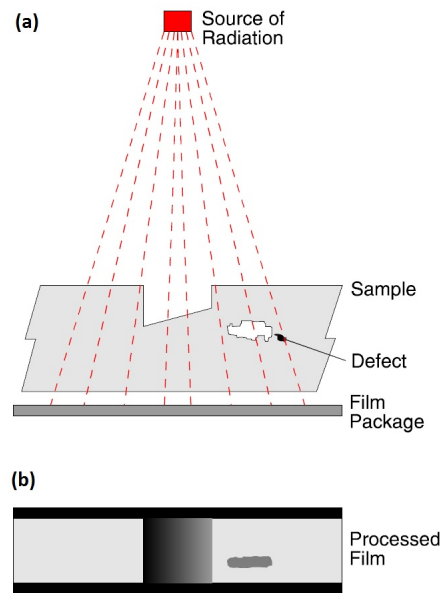


Figure 3.1: Schematic illustration of (a) exposure arrangement for radiography, (b) resulting processed film [47]

parallel to the surface of the material, but if there is a discontinuity, the flux lines stray out and magnetic attractive poles are generated at the defect boundaries. Particles suspended in a liquid that provides mobility for the particles on the surface of the test material are required for inspection. Typically these particles are iron oxides between 20 to 30 microns size. The magnetic poles at the defect attract the particles, which indicates the presence of a defect. The most simple and often used technique to apply magnetic flux in the material is to apply a permanent magnet to the surface, however the disadvantage of this technique is that it cannot be controlled accurately because of indifferent surface contact and deterioration in magnetic strength. In modern equipments, the magnetic field is generated electrically. Figure 3.2 schematically illustrates the inspection set up for bar-shaped material. In order to ensure that the material is flawless, it is necessary to magnetise it in at least two directions, in order to make sure that the magnetic flux flow is at least once orthogonal, either in case of longitudinal or transverse orientated defects.

It is possible to automatise the technique to suit production inspection to the extent of loading, magnetising, inking and unloading. However, the indicating ink systems

Chapter 3. How guided waves using EMAT ultrasonic technology was selected in a feasibility study on different NDT techniques

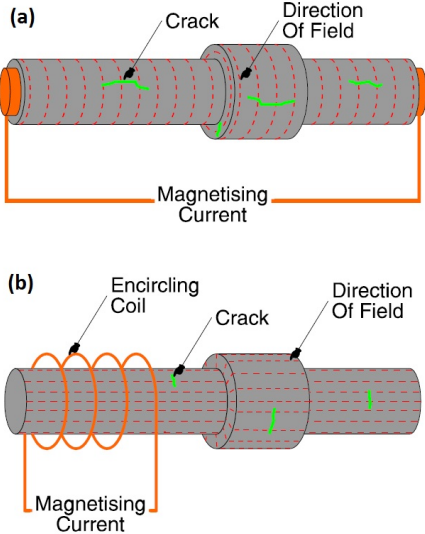


Figure 3.2: Schematic illustration of (a) inspection set up for the detection of longitudinal defects using current flow through the material, (b) detection of transverse defects using an encircling coil [47]

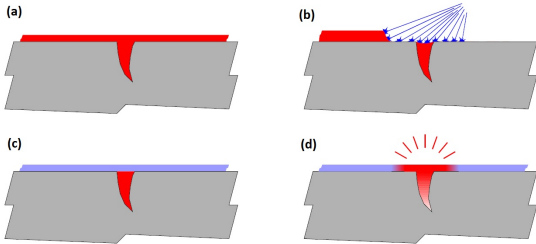


Figure 3.3: Schematic illustration of (a) applying penetrant to the surface, (b) removal of excess penetrant from surface, (c) developer powder applied on surface to draw out penetrant and (d) attenuated indication of crack [47]

with recirculating fluid are restricted to smaller test pieces. In partly automatised systems, the material still has to be viewed by eye to indicate the presence of a defect [47]. Since magnetic particle inspection is restricted to ferromagnetic materials, has a limited degree of possible automation for moving parts and is restricted to surface or near surface defects, this technique is not further considered in the feasibility study.

3.1.3 Dye penetrant testing

Dye penetrant testing is typically used to detect surface breaking flaws in non-ferromagnetic materials [47]. The functional principle is that a penetrant is drawn into cracks by cap-

Chapter 3. How guided waves using EMAT ultrasonic technology was selected in a feasibility study on different NDT techniques

illary action, which indicates in good contrast to the background the presence of a crack. Figure 3.3 schematically illustrates the dye penetrant testing procedure. Figure 3.3(a) illustrates the thin oil penetrant that is dyed with a fluorescent colour, which is applied to the material surface and is drawn into the crack by capillary action. Figure 3.3(b) shows the removal of surplus penetrant from the surface and (c) applying a thin surface coating of powdered chalk, which after a certain development period draws the dye out of the crack and (d) visualises the crack magnified in width and in good contrast to the background. Although the principle always remains the same, it is possible to automate the process with large sophisticated tanks, spraying and dyeing equipment, but the detection cannot be automatised and still requires viewing by eye [47]. Since dye penetrant testing is restricted to surface defects and cannot be fully automated for moving parts, it is not considered in the feasibility study.

3.1.4 Eddy current

Eddy current testing is a well established technique in industry for surface and sub-surface flaw detection, conductivity measurement and coating thickness measurement [47]. Eddy currents that are generated by passing alternating current through coils can be produced in any conducting material. The functional principle is that any change in material or geometry is detected by the excitation coil as a change in the coil impedance. When a defect, such as a crack, occurs in the material surface, the eddy current must travel further around the crack, which is detected by the impedance change. Figure 3.4(a) schematically illustrates the circular eddy current pattern when no defect is present. Figure 3.4(b) shows a surface crack in the plate, which distorts the eddy current and is indicated by the increased impedance. Eddy current is one of the most widely used NDT techniques in industry, because it is suitable for total automation at high-speed testing up to 150 m/s and under harsh operating conditions [48] where other techniques cannot be used. Although eddy current can perform a wide variety of inspections, delaminations that lie parallel to the probe coil winding and probe scan direction are undetectable [49]. Since delamination between aluminium clad lining and steel in Al/Al-Sn/Al/steel bimetal strips is the most significant defect type, eddy

Chapter 3. How guided waves using EMAT ultrasonic technology was selected in a feasibility study on different NDT techniques

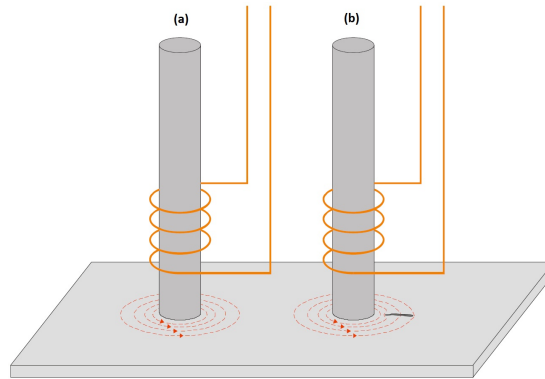


Figure 3.4: Schematic illustration of eddy current testing principle (a) circular pattern of eddy currents in material when no crack is present, (b) surface cracks cause distorted eddy currents that result in increased impedance [47]

current testing is not further considered in the feasibility study.

3.1.5 Thermography

Temperature is one of the most common indicators of the structural health of components. Typical examples are damaged machineries, corroded electrical connections and damaged material components, which cause an abnormal temperature distribution. Recently thermography became a widely accepted NDT technique in industry, which uses the abnormal temperature distribution to detect flaws [50]. Thermography is widely used to inspect buildings and civil structures [51], in the automotive and aerospace industry in numerous applications for flaw detection, bonding integrity assessment and composite structure evaluation [52–54] and diverse other applications such as pressure vessel evaluation [55], pipeline inspection [56] and micro-crack inspection [57]. The transient pulse heating technique has proven to be the most suitable method for bond integrity testing for adhesive bonds, e.g. for panel frame structures or the bonnet of a car, because the adhesive bond is usually close to the surface of the material [58]. This is the reason for selecting the transient pulse thermography technique for the bond inspection of Al/Al-Sn/Al/steel bimetal sheets, in which the clad Al to steel delamination is close to the surface of the sample. The functional principle in active thermography is that heat is transferred into the material that causes an instantaneous thermal excitation and the materials heat-transfer response is measured. It is a fast technique

Chapter 3. How guided waves using EMAT ultrasonic technology was selected in a feasibility study on different NDT techniques

allowing real-time inspection, provides 100% check and is a non-contact technique to inspect the material [58]. Flaws are revealed by searching anomalous hot-spots that are caused by the flaws after thermal excitation. As thermography is a thermal radiation measurement technique, flaws cause spatial variations in the observed surface temperature pattern [58]. While in passive thermography only the variation of surface radiation is measured, a controllable thermal source to excite the material and reduce environmental influences is used in active thermography to inspect the material. Common active thermography techniques are transient pulse, step heating, periodic heating as well as thermal mechanical vibration [58]. The harsh production environment of Al/Al-Sn/Al/steel bimetal strips with varying ambient conditions (vibrations, temperature and light conditions) is a challenge to apply Thermography for online inspection. However, recent developments such as the Thermographic Signal Reconstruction (TSR) method can enhance the analysis of thermographic sequences by creating a noise reduced replica of each pixel, which allows improved analysis over unprocessed image data [59]. Since promising reference applications for the detection of sub-surface defects exist for thermography, this technique is considered in the feasibility study.

3.1.6 Shearography

Shearography is a technique that is already well established in industry for NDT [60]. It has been successfully employed for adhesive bonding integrity inspection for multi-layered composites, e.g. GLARE panels, honeycomb structures and glass (or carbon)-fibre-reinforced plastics [61]. Other shearography applications are measurement of specific surface strains, residual stresses, 3D shapes and vibration modes and leakage detection [62]. All these applications have in common, that the samples are usually static. Bond defects in composites are detected by applying a known external excitation that leads to deformation of the material, which enables NDT of the samples as the basic principle of this technique is based upon the response of the flaw to the applied stress. The techniques include: pulse thermography [63], lock-in thermography [64], thermosonics [65] and digital shearography [66]. Digital shearography has a broad application field to provide information about flaws in materials such as discontinuities

Chapter 3. How guided waves using EMAT ultrasonic technology was selected in a feasibility study on different NDT techniques

and separations, dimensions, as well as stress and dynamic response. Displacement and displacement-derivatives are considered to measure the surface deformation. Flaws are revealed by comparing flawless deformation areas to flaw containing deformation anomalies, after the material is stressed. Analysis of the fringe patterns and backwards calculations are used to detect the flaw. Typical methods for material deformation that are non-contact and cause small rigid-body movement are pressurisation, partial vacuum, acoustics as well as thermal-shock excitation [58]. In an ideal case, the applied stress is similar to the service stress. This way only flaws that are critical in service are detected and cosmetic flaws are ignored [60]. Furthermore it is a fast technique allowing real-time inspection, provides 100% check and is a non-contact technique to inspect the material [58].

A limitation for online NDT using shearography is the presence of higher disturbances, especially vibrations, which introduces unknown phase deviations in the shearographic images, which makes bond defect detection impossible. Recently a new approach to improve the quality of shearographic phase maps that are acquired in a harsh environment was presented, which combines the N-dimensional Lissajous algorithm and the concept of phase of differences, to improve the quality of phase maps [67]. This progress could facilitate the application of digital shearography for the online inspection of Al/Al-Sn/Al/steel bimetal strips. Shearography is considered in the feasibility study.

3.1.7 Ultrasound

Ultrasonic testing is considered as the most efficient inspection method in all major industries, such as electrical and electronic components manufacturing, metallic and composite material production, structures fabrication like airframes, piping and pressure vessels, ships, bridges, motor vehicles, machinery and jet engines [68]. Ultrasonic testing methods are the most applied methods in non-destructive testing of multi-layered composites [69]. In ultrasound inspection, sonic energy is used to locate and identify surface and subsurface flaws. In the ASM handbook [70], the pulse-echo method is presented as the most widely used configuration, in which the ultrasound

Chapter 3. How guided waves using EMAT ultrasonic technology was selected in a feasibility study on different NDT techniques

pulse is reflected from a discontinuity. The functional principle is that waves travel in a straight line and at a constant speed until they encounter an anomaly in the material, which reflects the ultrasound wave. The reflected signals from the flaw surface that the sound beam encounters are differently attenuated. Flaws such as cracks, holes, delaminations, slags, cavities, porosities, bursts, lack of fusion or flakes that have sharp boundaries, are easily detected and identified by ultrasonic testing [71].

A typical ultrasound amplitude representation technique is a C-scan, in which an attenuation map of the scanned area of the part is shown. The flaw depth, which is dependent on the ultrasound time of flight, is usually not recorded, but can be controlled accurately by setting inspection gates. A limitation of C-scans is that the interpretation can be misleading due to noise; however the development and use of advanced transducers and the advancement in digital signal processing improved the effectiveness of using ultrasonic testing for composite materials [69].

A limitation of ultrasound is that it requires a two-dimensional scan to cover the entire material volume, which makes it difficult to inspect material online at high speed [72]. Wang et al. [73] reported the development of an phased array ultrasonic system for composite flaw detection. The advantage of phased array ultrasonic probes compared to single-element probes is that it can focus and sweep the beam electronically instead of moving the probe. This results in improved sensitivity and coverage. In order to increase the range and accuracy of inspection, plane beams, steered angled beams and focused beams are often used [74, 75]. Furthermore recent development of two-dimensional arrays reduce the requirement of a two-dimensional scan for single-element probes to a one-dimensional scan to obtain a three-dimensional, 100% volumetric scan of components [76–78]. The principle of ultrasonic arrays is to emulate monolithic transducers. Multiple independently controlled, parallel transmission circuits enable staggered activation of transducer elements in order to steer, translate or focus the physical wave front in the material. The inspection system presented in [73] was tested at laboratory level with the result that a clear visual representation of cracks in composite parts and determination of the size and location of defects is possible with phased array.

Chapter 3. How guided waves using EMAT ultrasonic technology was selected in a feasibility study on different NDT techniques

The limitation is that the phased array transducer and the sample have to be immersed in liquid to transmit the ultrasonic waves. Also piezoelectric ultrasound transducers require a coupling media to transmit the ultrasonic sound from the probe into the material to prevent an air gap with significant impedance mismatch between the probe and the material. Coupling is either achieved by immersion testing [79], typically for smaller test specimens, or by using water jet probes for larger components [80] and smaller components [79]. This coupling media requirement can restrict ultrasound inspection for certain applications, in which no coupling media can be applied on the sample.

Devices that are used for evaluation of rails could provide a potential solution to remove the need for coupling media. Ultrasonic rail track inspection is typically performed either manually, using push-trolleys with integrated portable ultrasonic equipment or special high-speed test vehicles carrying ultrasonic probes [81]. The principle of ultrasound rail inspection is the same as for defect detection in components, using the amplitude of any reflection to provide information about the location and type of defect in the rails under inspection [82]. In so called roller search units or sled carriers, the transducers are contained in a liquid filled tyre [83, 84] and the inspection speed achieved is up to 80 km/h. Variations in the speed of sound within fluid-filled tyres that act as the primary transmission medium between the transducer and the rail head may create widely varying ultrasonic inspection results. A new patent by Sperry Rail, Inc. [85] describes a rolling search unit including an ultrasonic device and a heat exchanger mounted within a fluid-filled tire. The heat exchanger maintains the temperature of the fluid within the tire to standardise the results of testing regardless of the ambient temperature in the environment [85]. Another recent development is that some manufacturers have started inspecting in this area using linear phased array transducers [86]. Since promising reference applications for the detection of sub-surface defects exist for ultrasound testing, this technique is considered in the feasibility study.

Chapter 3. How guided waves using EMAT ultrasonic technology was selected in a feasibility study on different NDT techniques

3.1.8 Guided waves using EMATs

EMATs belong to the group of noncontact ultrasonic transducers [87]. Typical applications are the inspection of pipes to detect corrosion or cracks [88], the condition of rails [89], weld defect detection [90], adhesive bond inspection in composites [91] and metal plates [72, 92, 93].

EMATs are capable to emit and receive ultrasound on conductive metals and they are in particular suitable when the application requires a contactless inspection. Typical cases are if the sample is hot, moving, or otherwise not suitable for a transducer to be directly in contact with the material, or when no coupling media or surface preparations are possible to use [93–95]. Most of these criteria apply for the online inspection of Al/Al-Sn/Al/steel bimetal, which is moving, contact should be avoided to not damage the surface and carry over of the coupling media into the material is not desired. Although EMAT is in theory a contactless technique, close proximity is required. The maximum possible lift-off between the EMAT probe and material depends on the EMAT design, material properties, and the acoustic wave frequency [96]. Studies report that due to the requirement of a reasonable signal-to-noise ratio (SNR), the lift-off is typically restricted to below 3 mm [48].

EMAT sensors typically have a built in neodymium-iron-boron (Nd₂Fe₁₄B) sintered permanent magnet that provides a static magnetic field and a coil of wire to induce eddy currents at the skin depth of the sample. The ultrasound generation and reception between sample and probe is an electromagnetic mechanism due to the Lorentz force and can involve magnetostriction, as well as the magnetisation force between the oscillating magnetic field of the probe and the static magnetic field of the ferromagnetic material [97–99].

EMATs are relatively inexpensive to produce, however they are less efficient at generating or detecting ultrasound compared to piezoelectric transducers [100]. An advantage compared to the pulse-echo or through transmission ultrasound technique is that a conventional two-dimensional scan is reduced to a one-dimensional scan, which increases inspection speed [72]. Furthermore guided waves that can be generated using EMATs are well suited for thin plate inspection. The technique was already successfully

Chapter 3. How guided waves using EMAT ultrasonic technology was selected in a feasibility study on different NDT techniques

Table 3.1: Feasibility of NDT techniques to fulfil online Al/Al-Sn/Al/steel bimetal inspection requirements based on literature review

NDT techniques	Automation possible	Is the technique non-contact?	Suitable for moving parts	Suitable for internal defects	Suitable for material properties	Consideration in feasibility study	Other limitations
Optical							
Human visual inspection	No	Yes	Yes	No	Yes	No	
Machine camera	Yes	Yes	Yes	No	Yes	No	
Laser shearography	Yes	Yes	No	Yes	Yes	Yes	
Thermal							
Thermography	Yes	Yes	Yes	Yes	Yes	Yes	
Electromagnetic							
Eddy currents	Yes	Yes	Yes	Yes	Yes	No	Delaminations parallel to coil undetectable
Ultrasonic testing							
Immersion UT	Yes	No	Yes	Yes	Yes	Yes	
Contact UT	Yes	No	Yes	Yes	Yes	Yes	
Phased Arrays	Yes	No	Yes	Yes	Yes	No	
Roller search units	Yes	No	Yes	Yes	Yes	No	
EMATs	Yes	Yes	Yes	Yes	Yes	Yes	
Others							
Dye penetrant	No	No	No	No	Yes	No	
Magnetic flux leakage	Yes	No	No	No	No (aluminium)	No	
X or Gamma rays	No	Yes	No	Yes	Yes	No	

applied in the inspection of three-layered clad of brass/copper/brass material for coin stock [72]. A recent development in the guided wave inspection of metallic plates is to attempt to accurately determine the size and shape of defects instead of only detecting the defects, which is possible by using an array of transducers to transmit and receive guided waves from all directions [92]. Due to the promising reference applications that exist for guided waves online detection of sub-surface defects, this technique is considered in the feasibility study.

3.1.9 Conclusion

The literature was reviewed to identify which NDT methods fulfil the theoretical minimum requirements to be considered in a feasibility study to detect artificially implanted defects in Al/Al-Sn/Al/steel bimetal sheets. Table 3.1 summarises the results of the literature review. The following minimum requirements were considered:

- Possibility for full automation: since the inspection application is high-volume production for automotive components, it is desired to exclude any human interaction to detect defective material in order to guarantee 100% volumetric inspec-

Chapter 3. How guided waves using EMAT ultrasonic technology was selected in a feasibility study on different NDT techniques

tion and good material.

- Non-contact technique: it is a strip production line design objective to minimise the contact points between strip surface and machine, since each contact point is a potential root cause to score the strip surface. Although it is desired that the technique is contactless, this objective is not definite.
- Online inspection: some NDT techniques can only be used for components or there are other reasons that prevent online inspection, such as health hazards, considerable consumption or carry-over of consumables into the material or too low inspection speed.
- Sub-surface defects: the most significant defects in bimetal strips are sub-surface defects, since they entail the risk not to be detected and can lead to engine failure in the field.
- Material properties: the functional principle of some NDT techniques require certain material properties, such as electrical conductivity for eddy current testing or ferromagnetic materials for magnetic particle testing, which are not fulfilled by some alloys.
- Other limitations: Eddy current testing cannot detect sub-surface defects which are in the same plane as the coil winding. Delamination between clad Al lining and steel is in the same plane as the coil winding and therefore would not be detectable.

The techniques that fulfil all theoretical requirements are laser shearography, thermography, ultrasonic testing (immersion and contact), and guided waves generated with EMATs. The literature review identified applications in which these NDT techniques were already successfully employed to detect sub-surface defects in composite materials. In the following chapter, the NDT feasibility study results for the selected techniques and Al/Al-Sn/Al/steel bimetal plates with artificially implanted defects are presented.

Chapter 3. How guided waves using EMAT ultrasonic technology was selected in a feasibility study on different NDT techniques

Table 3.2: Test samples in relation to the applied NDT methods

#	NDT technique	Ident.	NOM comp.	Clad Al THK	Steel THK	Red. Sheet DIM	Surface preparation	Peel back
1	Active thermography	AT-R	AlSn20CuMn	0.67 mm	1.96 mm	43% 280x171x2.63 mm	Reference	no peel
2	Active thermography	AT-NL	AlSn20CuMn	0.52 mm	2.13 mm	43% 280x171x2.65 mm	No linishing	13 mm
3	Active thermography	AT-RR	AlSn20CuMn	0.63 mm	2.00 mm	30% 280x171x2.63 mm	Rolling reduction 30%	9 mm
4	Shearography	S-R	AlSn20CuMn	0.53 mm	1.22 mm	43% 280x171x1.75 mm	Reference sample	no peel
5	Shearography	S-SP	AlSn20CuMn	0.53 mm	1.22 mm	43% 280x171x1.75 mm	80g/m ² sheet paper	> 5 mm
6	Ultrasonic testing	UT-R	AlSn20CuMn	0.53 mm	1.22 mm	43% 280x171x1.75 mm	Reference sample	no peel
7	Ultrasonic testing	UT-NB	AlSn20CuMn	0.53 mm	1.22 mm	43% 280x171x1.75 mm	No brushing	2 mm
8	Guided wave EMAT	GW-R	AlSn20CuMn	0.53 mm	1.22 mm	43% 800x171x1.75 mm	Reference sample	no peel
9	Guided wave EMAT	GW-PT	AlSn20CuMn	0.53 mm	1.22 mm	43% 800x171x1.75 mm	80g/m ² paper triangle	> 5mm
10	Guided wave EMAT	GW-IT	AlSn20CuMn	0.53 mm	1.22 mm	43% 800x171x1.75 mm	Ink polluting agent	1 mm

3.2 Experimental procedures

3.2.1 Thermography

Sample preparation

Table 3.2 summarises the samples that were used in the active thermography feasibility study. Sample AT-R is produced under normal production parameters and is used as reference sample. The peel-off test confirmed sound Al-1050 foil to steel bond as there was no peel back in the test that was done according to the procedure described in section 1.2.1. This sample is made of 0.67 mm thick clad Al and 1.96 mm thick steel sheets after 43% thickness reduction in CRB. The sample dimensions are 280 mm long and 171 mm wide and have a total thickness of 2.63 mm.

For the AT-NL sample no linishing was applied to the steel surface. Various studies [32,33] reported that steel linishing is essential to establish an effective cold weld during CRB because it removes contaminants and surface oxides that could interfere with the creation of nascent metal. It has been reported that localised shear deformation to break unavoidable surface oxide films is promoted by a larger amount of surface asperities, which are created by steel surface linishing [101]. MAHLE plant trials substantiate that there is a negative effect on the bond integrity, if the steel surface is not linished before CRB. The AT-NL sample prepared in this specific way failed the peel back test, as the peel back was about 13 mm. This sample is made of 0.52 mm thick clad Al and 2.13 mm thick steel sheets after 43% thickness reduction in CRB. The sample dimensions are 280 mm long and 171 mm wide and have a total thickness of 2.65

Chapter 3. How guided waves using EMAT ultrasonic technology was selected in a feasibility study on different NDT techniques

mm. For sample AT-RR, the same process like for sample AT-R was used, except for the thickness reduction during CRB which was only 30% instead of the standard 43% thickness reduction. The thickness reduction in bimetal CRB is the most influencing factor on the bond strength [38]. This is because of the direct relation between thickness reduction, surface expansion and extrusion of uncontaminated metal [24]. The AT-RR sample prepared in this specific way also failed the peel back test, since the peel back was about 9 mm. This sample is made of 0.63 mm thick clad Al and 2.00 mm thick steel sheets after 30% thickness reduction in CRB. The sample dimensions are 280 mm long and 171 mm wide and have a total thickness of 2.63 mm.

Experimental set up

Figure 3.5 is a schematic of the transient pulse thermography experimental setup. Thermal radiation in the reflection mode of the one-time transient pulse excitation technique was used in this experiment. This technique has the advantages of fast inspection speed, full-field interrogation, as well as being contactless. Short exposure time (approx. 3 ms) and transient light sources with large power (approx. 9.6 kJ) excited the material. The samples were placed horizontally in a stable position on a measurement table throughout the measurement process to keep the bimetal samples perfectly aligned with the two flash lamps and the infrared camera. The clad Al surface was facing the lighting source to heat it up with a short and spatially uniform light pulse. Delamination areas are identified by an infrared (IR) camera that is connected to a PC, which monitors and analyses the time-dependent sample surface temperature response relative to the thermal pulse.

The delaminated areas in the bimetal sample obstruct the transient heat flow from surface into the sample interior during the thermal excitation, because the vacuum between the layers acts as a lagging. This produces an increase in the local transient temperature of the alloy surface, directly above the delamination. These anomalous hot-spots are revealed with time. The material depending characteristic diffusivity and delamination depth that is dependent on the clad Al and steel sample thickness and their influence on the transition time were taken into consideration when the model was

Chapter 3. How guided waves using EMAT ultrasonic technology was selected in a feasibility study on different NDT techniques

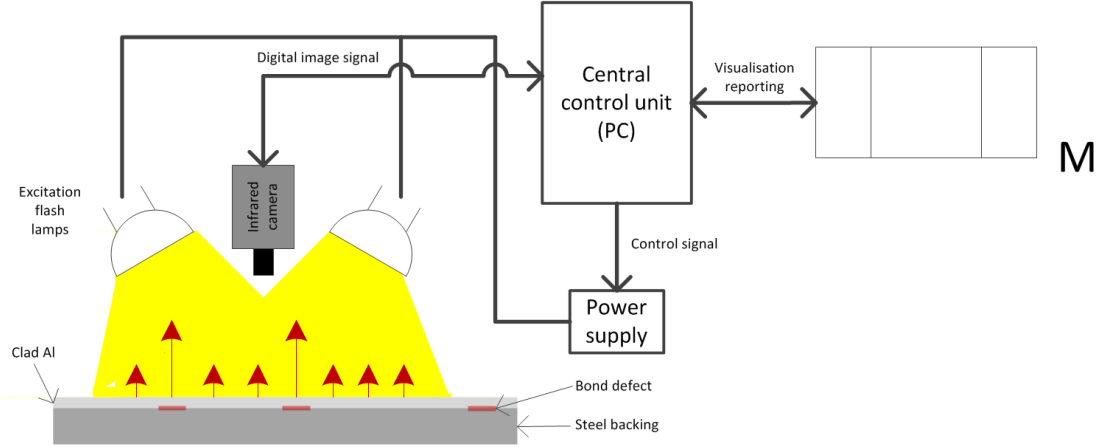


Figure 3.5: Schematic of experimental set up for delamination detection in transient pulse thermography

setup. The sequential data sets were considered as independent time histories of the temperature at each pixel, which were described and analysed with a one-dimensional diffusion model. In this model, the surface temperature depends only on time. Sample variables in the model are thermal conductivity, density and the specific heat. The inspection set-up variables are input energy per unit area. For a defective sample, the temperature slope deviates from the characteristic slope of a defect-free sample. Focusing on the deviation of a single pixel on the surface identifies delaminations that interrupt the heat flow without reference to their neighbours.

3.2.2 Shearography

Sample preparation

Table 3.2 provides an overview of the two samples that were used in the digital shearography feasibility study. Sample S-R is the reference sample that was produced under normal production parameters. Good bond was confirmed with the peel-off test. S-SP is the test specimen with artificially implanted delamination, in which 140x45 mm 80g/m² gauge paper was inserted between the clad Al and the steel sheets before CRB. The S-SP sample failed the peel off test, since the gauge paper created a defined gap between clad Al and steel. The destructive test result was more than 5 mm peel off and only ended due to fracture of the clad Al. This sample preparation method is also

Chapter 3. How guided waves using EMAT ultrasonic technology was selected in a feasibility study on different NDT techniques

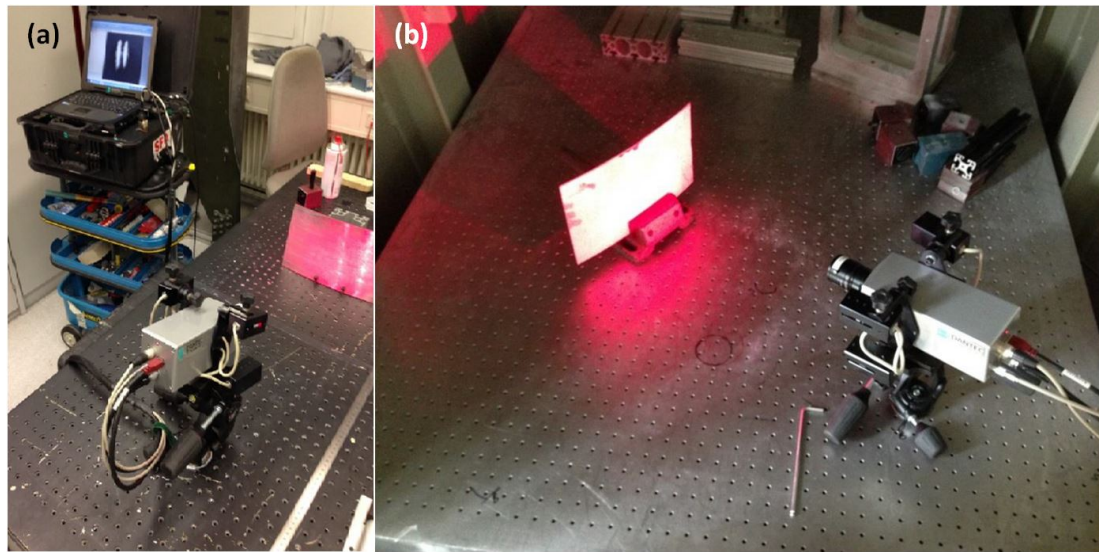


Figure 3.6: Shearography experimental set up for a) thermal shock and b) vacuum technique

used in other studies to create a delamination, as it does not affect the adjacent bonded interface [102]. Both samples were 280 mm long and 171 mm wide and were made of 0.53 mm thick clad Al and 1.22 mm thick steel sheets after 43% thickness reduction during CRB.

Experimental set up

Two different excitation methods, vacuum and thermal shock loading, were tested in the shearography feasibility study. Vacuum loading has already been successfully tested on laboratory samples of aluminium-CFRP panels, which had artificially implanted delaminations [58]. A drawback of this technique is that it is limited to delaminations with enclosed boundaries. If the delamination in Al/Al-Sn/Al/steel bimetal strips are at the edge of the strip, it would have an open boundary. Thermal shock loading overcomes this drawback and is therefore more suitable in open panels. Thermal shock excitation can be achieved by using hot air jet, heat lamp, and high power argon laser or recently developed high power Xenon flash lamps. This technique successfully revealed flaws under laboratory conditions for subsurface cracks that were engineered in aluminium panels [58].

Chapter 3. How guided waves using EMAT ultrasonic technology was selected in a feasibility study on different NDT techniques

The feasibility testing was carried out using the Dantec Dynamics Digital Shearography NDT System Q-800. Figure 3.6(a) illustrates the thermal testing set up that was used. The Q-800 system was mounted on the same table as the samples, approximately 450 mm away from each other. A 230V/750W heat lamp was positioned 30 mm away from the sample with the alloy side facing to the heat lamp. First a reference specklegram was captured without loading the sample. The illumination duration was 30 seconds. Then heat energy was delivered to apply a thermal stress to the sample. Due to the thermal heat excitation, the gas inside the delamination expands, creating an internal pressure in the sample. Then another series of specklegrams was captured. Due to the temperature difference between the relatively cool interior of the specimen and the exposed surface, a thermally induced bending moment is caused. Delaminations lead to locally reduced rigidity close to the delamination, which causes localized out-of-plane deformation anomalies. These anomalies were captured as fringe condensation, which reveals the delamination.

Figure 3.6(b) shows the vacuum test set up. For vacuum testing, the same Q-800 system and the samples were placed in an airtight chamber 450 mm apart from each other and an air pump produced a 100 mbar partial vacuum in the chamber between the material surface and the enclosed space. As the test piece was uniformly stretched by the negative pressure difference, delamination areas bulged and caused fringe anomaly.

3.2.3 Ultrasound

Sample preparation

Two samples were manufactured for the ultrasound testing feasibility study that are summarised in Table 3.2. Sample UT-R is the reference sample that was produced under normal conditions. The peel off test confirmed sound Al-1050 foil to steel bond, since there was no peel back in the peel back test that was done according to the procedure in section 1.2.1. For the UT-NB sample, the alloy surface was not brushed prior to CRB to prevent an effective cold weld during CRB. It has been shown in other studies that the oxide film thickness that is present on the alloy if it is not brushed prior to CRB, does markedly decrease the bond integrity between Al-1050 foil and steel [1].

Chapter 3. How guided waves using EMAT ultrasonic technology was selected in a feasibility study on different NDT techniques

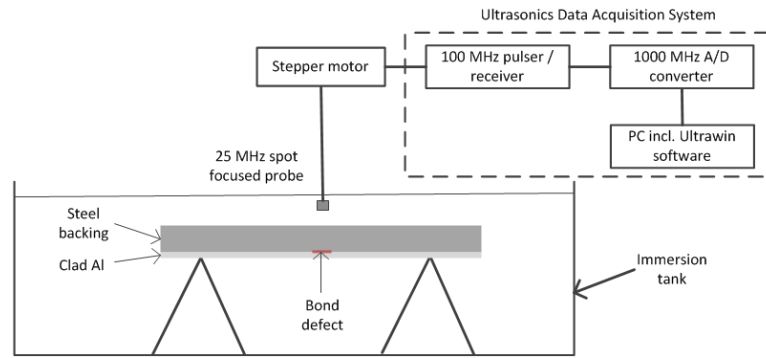


Figure 3.7: Schematic view of test set up showing the Al-Sn alloy/steel bimetal sample submerged in an immersion tank, stepper motor and the Data Acquisition System

Poor bond between Al-1050 foil and steel for the UT-NB sample was confirmed with the peel off test, in which the peel back was about 2 mm, which indicates weakened bond according to the acceptability criteria in section 1.2.1. The samples were 280 mm long and 171 mm wide and were made of 0.53 mm thick clad Al and 1.22 mm thick steel sheets after 43% thickness reduction during CRB.

Laboratory experimental set up

The pulse echo technique was used in the laboratory experiment. The system was supplied by Physical Acoustics Ltd. It had a 25 MHz spot focused probe, stepper motor and a Data Acquisition System comprising of a 100 MHz pulser / receiver, 1000 MHz A/D converter with dual gates and a PC with Ultrawin software.

Figure 3.7 shows a schematic of the scanner ultrasonic inspection system set up in the laboratory. The pulse-echo scanner was submerged in the immersion tank and a stepper motor was used to scan the specimen. The ultrasonics data acquisition system was positioned next to the water tank. The system recored 100 pulses per second and a moving average of 100 pulses (1 second) was used to monitor the signal. The probe was transmitting and receiving from the steel surface and was focused onto the bond line. Two signal gates were set to receive the echo from the bond line (Gate 1) and from the alloy backwall (Gate 2). The output from the returned signal is displayed as percentage of the signal strength returned by Gate 1 divided by the signal strength returned by Gate 2. The stronger the signal returned from the bond line is, the stronger

Chapter 3. How guided waves using EMAT ultrasonic technology was selected in a feasibility study on different NDT techniques

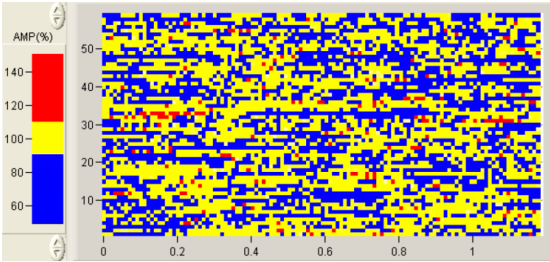


Figure 3.8: C-scan colour code depending on Gate1/Gate2 amplitude ratio

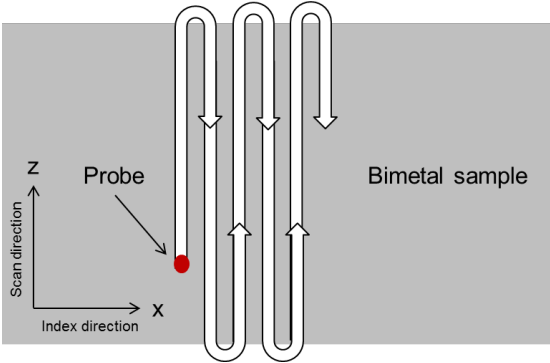


Figure 3.9: Schematic diagram of scanning pattern in x-z plane of bimetal sample

is the reflector and consequently weaker is the bond. Therefore the Gate1/Gate2 ratio is higher for weaker bonds. Figure 3.8 shows the C-scan colour code that was used for the received signal strength. Values of Gate1/Gate 2 ratio greater than 110% are coded red, ratio between 90% to 110% yellow and ratio below 90% blue.

Figure 3.9 shows the probe scanning pattern on the x-z plane of the bimetal sample. Only one probe was used for the pulse-echo inspection in the immersion tank. Scanning the material is necessary in order to cover 100% volume of the material. This is required as the ultrasound pulse-echo technique is by nature limited to a one dimensional measurement across the thickness normal to the plane surface of the bimetal sample.

Online experimental set up

The equipment for the online trials was the same as for the laboratory feasibility study supplied by Physical Acoustics Ltd. (PAL) with a 25 MHz high resolution focussed ultrasonic probe. The position of the probe in the online trial was between a rolling mill exit accumulator and a coiler, where the strip movement is kept to a minimum

Chapter 3. How guided waves using EMAT ultrasonic technology was selected in a feasibility study on different NDT techniques

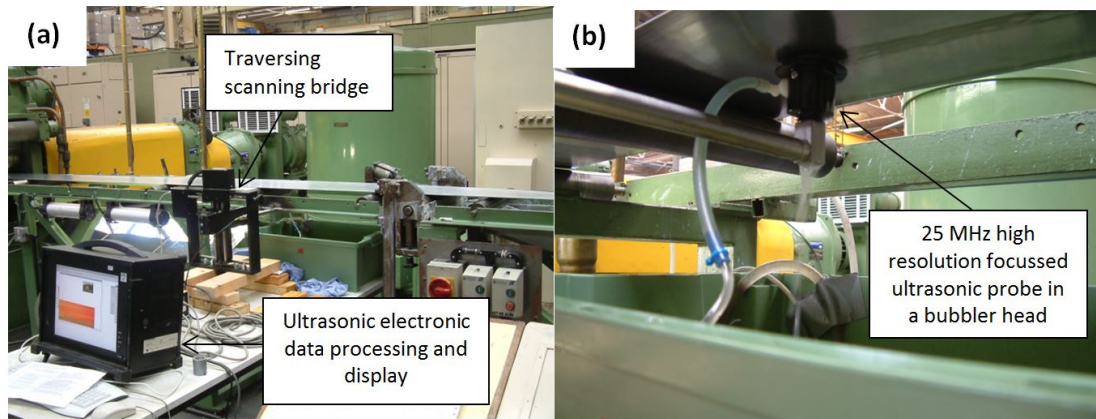


Figure 3.10: Experimental setup for online testing: (a) system installed at a position where the strip movement was kept to a minimum and access could be gained to the steel side of the bimetal strip (b) probe and bubbler head

and the steel side could be accessed. Figure 3.10(a) shows the position where the traversing scanning bridge and electronic inspection equipment was set up. Figure 3.10(b) shows the bubbler head, which repeatedly traversed over a 150 mm width of the bimetal strip to scan the material. In order to avoid significant water carryover, a bubbler head instead of an immersion tank for the water fluid coupling medium was used during online trials. A pump in the water container reservoir forced a column of water through the probe, which transmitted the ultrasonic signal to the steel underside of the bimetal strip. During the trials, the line ran at a constant speed of about 12 m/min.

3.2.4 Guided waves using EMATs

Sample preparation

As outlined in Table 3.2, three samples were used for the EMAT feasibility study. Sample GW-R was manufactured under normal conditions and used as reference sample, for which good bond was confirmed with the peel off test, as there was no clad Al peel back. The artificially implanted delamination in the test samples were produced in the shape of an isosceles triangle. The reason for the isosceles triangle shape is that a cyclic behaviour of the received ultrasound signal strength in the through transmission mode

Chapter 3. How guided waves using EMAT ultrasonic technology was selected in a feasibility study on different NDT techniques

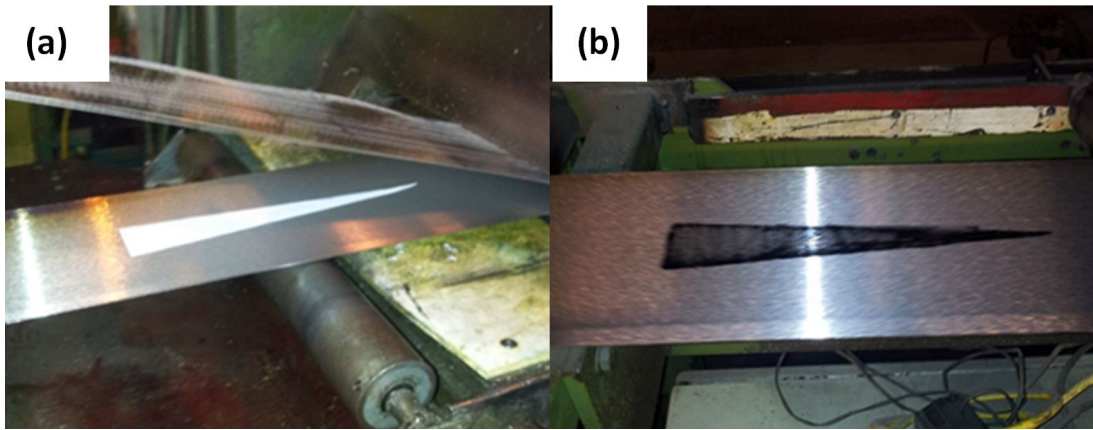


Figure 3.11: Manufacturing of test samples with isosceles triangle shaped delamination applying (a) 80g/m² gauge paper and (b) ink as contaminant

was observed in a bond inspection application for three-layered brass/copper/brass sheets, depending on the delamination width [72]. Contaminants to create the delamination were 80g/m² gauge paper in the GW-PT sample and ink in the GW-IT sample, which created a clean and precise delamination area. This method does not affect the adjacent bonded interface [102]. The size of the delamination in the shape of an isosceles triangle with two sides of equal length was approx. 500 mm height and 114 mm width after CRB. The GW-PT sample had a clad Al peel back of more than 5 mm that only ended due to fracture of the clad Al. This is a bond fail according to the peel off procedure in section 1.2.1. Sample GW-IT peel back was about 1 mm, which is weakened bond. The samples were 800 mm long and 171 mm wide and were made of 0.53 mm thick clad Al and 1.22 mm thick steel sheets after 43% thickness reduction during CRB.

Figure 3.11(a) shows the manufacturing of the GW-PT sample and Figure 3.11(b) the GW-IT sample immediately before the clad Al and steel sheets entered the CRB mill.

Experimental set up

Figure 3.12 shows the guided wave EMAT test setup. The probes shown in Figure 3.12(a) were arranged in the through transmission set up with one transmitter and

Chapter 3. How guided waves using EMAT ultrasonic technology was selected in a feasibility study on different NDT techniques

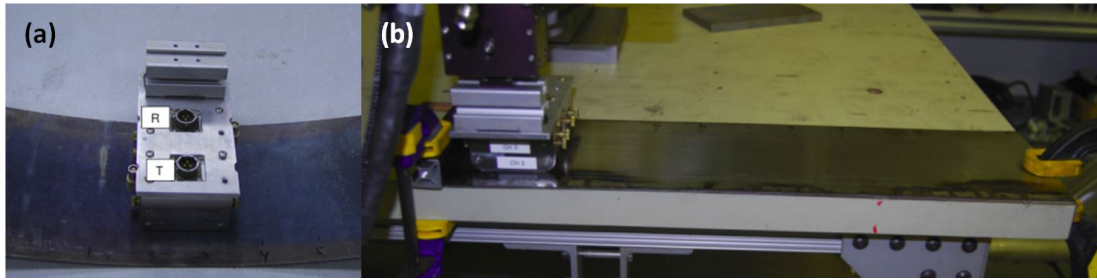


Figure 3.12: Test setup (a) transmitter and receiver sensors arranged in through transmission mode, (b) sensor set up on test sample

one receiver. Ultrasound was generated on the steel surface. The wave was reflected at the steel and alloy boundaries and propagated along the plate. The samples were clamped on a table as shown in Figure 3.12(b) to obtain a plain sample surface to prevent sensor lift-off. The samples were scanned with the two sensors in a uniform motion along the length of the sample. An Innerspec PowerBox H hand held, battery operated instrument with embedded PowerUT H software was used to process the data and display A-, B- and C-scans.

3.3 Results

3.3.1 Thermography

Figure 3.13(a) presents active thermography results obtained by inspection of the AT-NL sample. The sample presents a high density of clearly visible small spots with a diameter of few mm, which are likely delamination spots that weaken the bond and reduce the transferable load. These delamination spots were caused by not finishing the steel surface before CRB in the AT-NL sample and reducing the rolling reduction to only 30% in the AT-RR sample. The darker area is the region that is well bonded, which cooled faster because the heat could flow through the bond. Due to the small size of the delamination spots, the area that was peel off tested comprised multiple delamination spots at the same test sample. The AT-NL and AT-RR samples were peel back tested before the thermography inspection. The peel back of the clad Al lining for the AT-NL samples was 13 mm, and for the AT-RR sample 9 mm respectively, as shown in

Chapter 3. How guided waves using EMAT ultrasonic technology was selected in a feasibility study on different NDT techniques

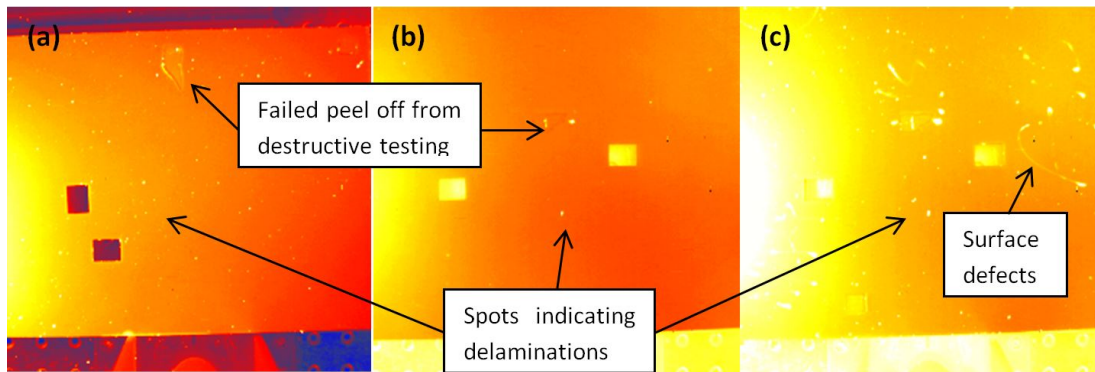


Figure 3.13: Small spots with a few mm diameter present on (a) AT-NL sample, (b) AT-RR sample and (c) AT-RR sample with variation of analysis parameters that revealed surface effects

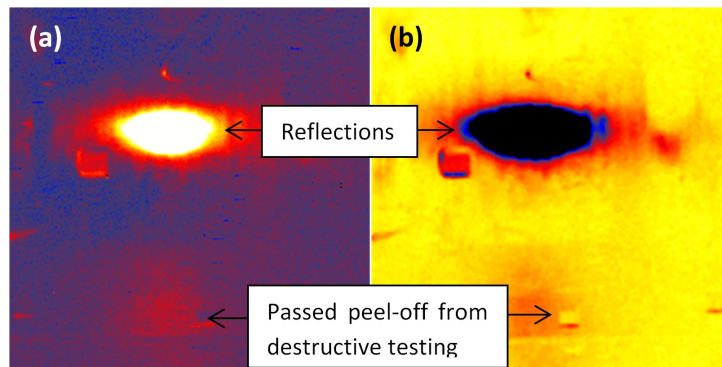


Figure 3.14: Good parts without specific defect signature but reflections due to curved surface

Figure 3.13. According to the procedure and acceptability ratings described in section 1.2.1, this is a fail test result. Figure 3.13(b) shows the results for the AT-RR sample with the same analysis parameters like for AT-NL sample. In a direct comparison, the AT-RR sample presents less, but still clearly visible heat spots. Figure 3.13(c) shows thermography results with a variation of analysis parameters for the AT-RR sample, which showed up additional defects on the surface. This is caused by the in-homogenous surface due to indentations and scores. Although these surface defects can be countered by adaption of the measurement set up, a continuous system adjustment for moving strips is an issue and poses the risk to miss flaws.

Figure 3.14 shows the AT-R sample without the specific delamination defect structure that was observed on samples AT-NL and AT-RR. The AT-R sample was peel

Chapter 3. How guided waves using EMAT ultrasonic technology was selected in a feasibility study on different NDT techniques

back tested and passed without peel back. However, it became apparent that the samples have a challenging surface for inspection, which is illustrated in Figure 3.14. The Al/Al-Sn/Al/steel bimetal sheets feature curvature that can result in reflections depending on the orientation of the two flash lamps and the infrared camera relative to the clad Al surface. The curvature of bimetal strips results from rolling, annealing and coiling. All test samples that were placed horizontally on the measurement table during inspection did exhibit an upwardly directed curvature. In Figure 3.14(a) the normal scale and in Figure 3.14(b) the inverted scale was used for inspection.

3.3.2 Shearography

Figure 3.15 shows the fringe patterns of the S-R and S-SP samples that were tested. Figure 3.15(a) is the fringe pattern of the S-R sample, which was tested with thermal shock loading. As expected, the reference sample did not show any visible signs of delamination. Figure 3.15(b) shows the fringe pattern of the S-SP sample under the same thermal loading conditions. The delaminated area is clearly visible. It appeared as if there were four definable, parallel delaminations within a clear common-defined central 140x45 mm area through the centre of the sample where the 80 g/m² gauge paper was inserted. However, only one piece of 80 g/m² gauge paper was inserted. Figure 3.15(c) shows the fringe pattern of the S-R reference sample that was tested under partial vacuum loading. Again as expected, the S-R sample did not show any visible signs of delamination. Figure 3.15(d) is the fringe pattern of the S-SP sample under partial vacuum loading, in which the common-defined central 140x45 mm area through the centre of the sample where the 80g/m² gauge paper was inserted is still clearly visible, but the partial vacuum loading showed a less defined, interconnected delamination area.

3.3.3 Ultrasound

In order to observe the influence of the three control factors sample bond surface preparation, interval between c-scan tests and coupling medium temperature, different levels of these factors were tested. Table 3.3 summarises the c-scan inspection parameters.

Chapter 3. How guided waves using EMAT ultrasonic technology was selected in a feasibility study on different NDT techniques

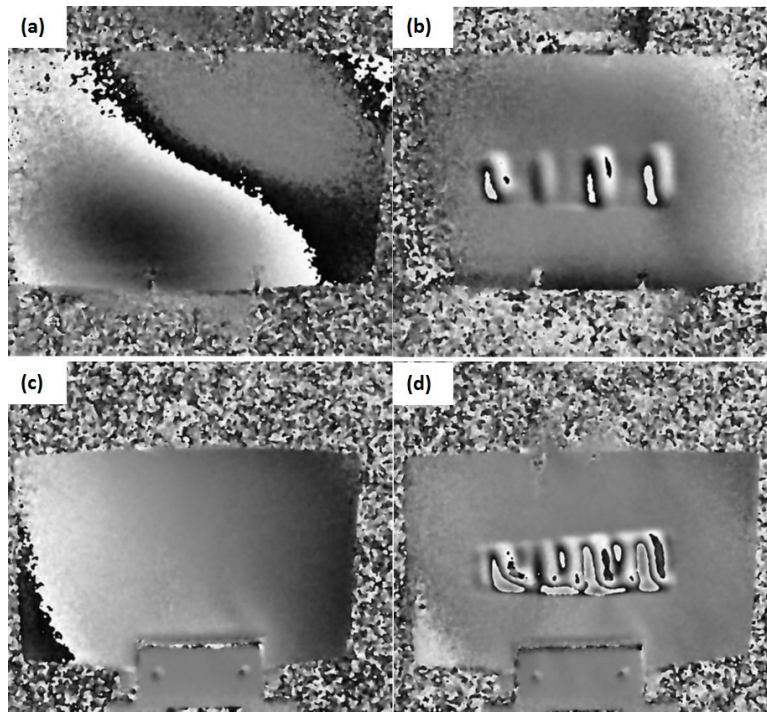


Figure 3.15: Image results for thermal testing: (a) normal bond conditions, (b) delamination, results for vacuum testing: (c) normal bond conditions, (d) delamination

Table 3.3: Levels of ultrasound testing factors

Control factor	Level 1	Level 2	Level 3
(S) Surface preparation	brushed	not brushed	-
(I) Interval	24h	48h	72h
(T) Temperature	20°C	23°C	-

The bond surface preparation and temperature factors had two levels and the interval between the tests had three levels. A two-way analysis of variance (ANOVA) was done for the two different categorical independent variable combinations surface preparation and interval as well as surface preparation and temperature to examine the influence on the dependent variable ultrasound signal amplitude.

Influence of time interval between consecutive c-scans

Figure 3.16 illustrates maps of the reflected amplitude ratio and its variation across the surface for various samples. This was done to test the time control factor on the c-scan ratio and it became evident that there is a variation in the amplitude ratio with

Chapter 3. How guided waves using EMAT ultrasonic technology was selected in a feasibility study on different NDT techniques

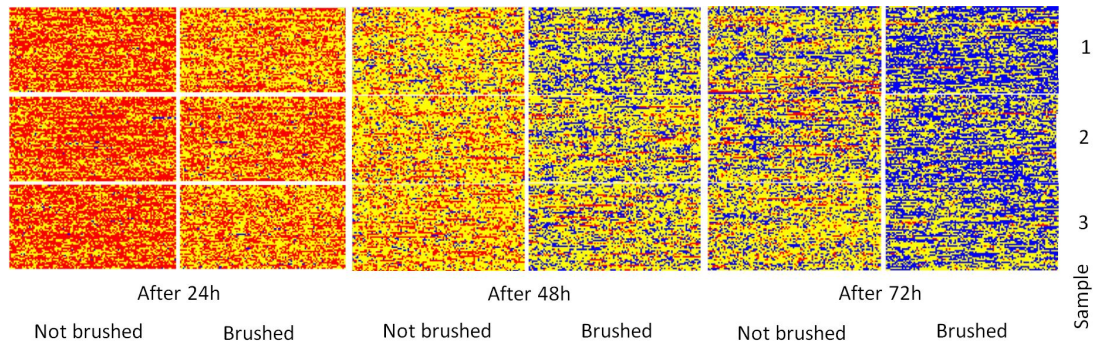


Figure 3.16: 3 consecutive tests with non-brushed / brushed samples showing a visible difference in the percentage of red, yellow and blue pixels

time. Three consecutive tests repeated in a 24h interval for three brushed and non-brushed samples were done. The water temperature was kept constant at 20°C during all three days with no alterations to the system. At each time interval, the brushed samples could be clearly differentiated from the non-brushed samples. After 24h, the brushed samples showed significantly more yellow pixels than red pixels compared to the non-brushed samples. After 48h, the brushed samples showed significantly more blue and less red and yellow pixels than the non-brushed samples. After 72h, the brushed samples showed significantly more blue and almost no red pixels, compared to the non-brushed samples. If the non-brushed samples after 48h or 72h were compared to the brushed samples after 24h, then the non-brushed samples would appear to have better bond.

Table 3.4 summarises the statistical analysis of the measurement data. The null hypothesis states that the response means that the main effects of surface preparation and exposure time and their interaction are equal. A significance level of 5% was considered. The p-value for surface preparation for the percentage of red pixels for poor bond and blue pixels for good bond is 0, which indicates that the surface preparation is associated with the bond strength. The p-value for the time interval between the tests is also 0, indicating that also the interval between the tests is associated with the measured bond strength. Both effects are statistically significant. This confirms that if the samples, for which the Al/Al-Sn/Al alloy surface was not brushed before bonding, at the 72h interval are compared to the brushed samples at the 24h interval,

Chapter 3. How guided waves using EMAT ultrasonic technology was selected in a feasibility study on different NDT techniques

Table 3.4: P-values for two-way ANOVA of surface preparation and exposure time effect

Analysis of Variance	DF	% red	% yellow	% blue
Surface preparation	1	0.000	0.603	0.000
Interval of 24 hours	2	0.000	0.000	0.000
Surface preparation*interval	2	0.049	0.000	0.001

the bond quality of the non-brushed samples appears to be better than the brushed samples, although the samples did not physically change. Since the interaction effect between surface preparation and interval is statistically significant, the bond cannot be inspected without considering the interaction effect. It was found that the reason for amplitude variation over time was caused by the water quality. As in serial production inspection conditions it is not practical to consider the interval between tests, the water quality would have to be controlled.

Temperature influence on c-scan amplitude ratio

In order to test the effect of the water temperature control factor on the c-scan ratio, an extra colour band was introduced to better differentiate between the echo for brushed and non-brushed material. Values of Gate1/Gate 2 ratio greater than 110% are coded red, ratio between 100% to 110% yellow, between 90% to 100% green and ratio below 90% as blue. Figure 3.17 shows the reflected amplitude ratio map for the non-brushed and brushed samples at 20°C and 23°C. At 20°C the samples can be clearly differentiated, as the non-brushed sample shows significantly more red pixels and the brushed sample shows more blue pixels. When the temperature was increased to 23°C, this significantly affected the received signal and it could not be differentiated between brushed and non-brushed samples anymore. If the non-brushed sample at 23°C were compared to the brushed sample at 20°C, then the non-brushed sample would appear to have better bond.

Table 3.5 summarises the statistical analysis of the measurement data for the temperature influence test. The null hypothesis states that the response means for the main effects surface preparation and water temperature in the tank and their interaction are equal. A significance level of 5% was considered. The surface preparation p-values for

Chapter 3. How guided waves using EMAT ultrasonic technology was selected in a feasibility study on different NDT techniques

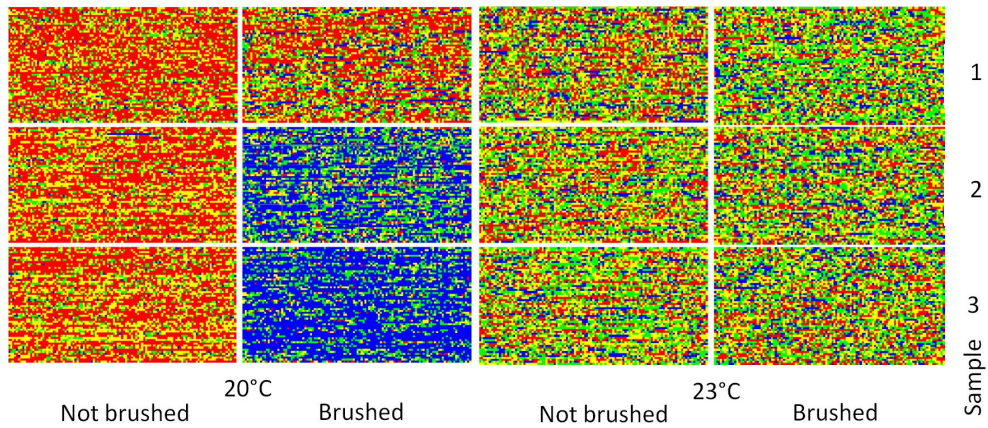


Figure 3.17: Effect of increasing the water fluid coupling temperature from 20°C to 23°C for non-brushed and brushed samples

the percentage of red, yellow, green and blue pixels were below 0.05, which indicates that the surface preparation is associated with the bond strength. The time interval p-values for the percentage of yellow and green area is below 0.05, indicating that also the coupling medium temperature is associated with the ultrasound signal. However, for the percentage of red and blue pixels there is no statistical evidence to substantiate this. This could be due to the chosen range of the buckets, which determines if the received Gate1/Gate 2 amplitude ratio falls either into the category good, weak or unacceptable bond. More trials would be necessary to determine the correct bucket size and back up that they match up with the peel off test results. If the non-brushed sample results at 23°C are compared to the brushed sample results at 20°C, then the bond quality of the non-brushed samples appears to be better than for the brushed samples, although the samples did not physically change. Since the interaction effect between surface preparation and temperature is statistically significant, independent of the chosen buckets, the bond cannot be inspected without controlling the coupling medium temperature, which is a challenge considering online inspection in a production environment with environmental influence on the temperature as well as a wide temperature range of the strips itself.

Chapter 3. How guided waves using EMAT ultrasonic technology was selected in a feasibility study on different NDT techniques

Table 3.5: P-values for two-way ANOVA of surface preparation and temperature effect

Analysis of Variance	DF	% red	% yellow	% green	% blue
Surface preparation	1	0.016	0.015	0.002	0.030
Temperature	1	0.191	0.034	0.000	0.342
Surface preparation*temperature	1	0.037	0.038	0.045	0.046

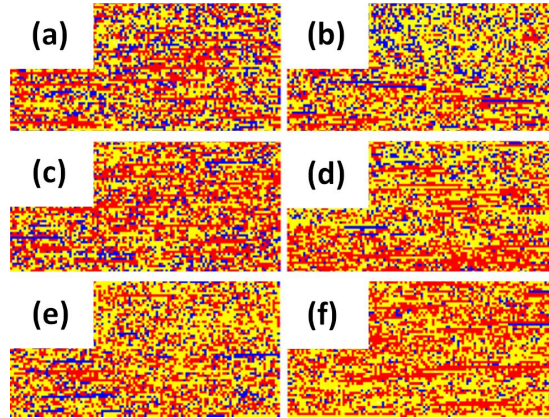


Figure 3.18: Samples of variable bond quality (a), (b) and (d) passed the peel off test, (c), (e) and (f) failed the peel off test

C-scan amplitude ratio for samples without known reason for weakened bond

Samples were taken from serial production that had poor bond, which was detected in the production peel off test. For these samples it was not possible to identify what caused the poor bond. The reflected amplitude ratio map for these samples is shown in Figure 3.18. All measurements were done at 20°C and without delay between each test. Figure 3.18(a), (b) and (d) show amplitude ratio maps of samples that passed the peel off test. Figure 3.18(c), (e) and (f) are samples that failed the peel off test. It appears that samples that failed the peel off test have less blue pixels and are predominantly yellow and red indicating a poor bond. Samples that passed the peel off test tend to have more blue pixels indicating a better bond. However, the difference of the reflected amplitude ratio map is too low to differentiate between the samples unambiguously.

Table 3.6 shows the statistical analysis of the measurement data, which substantiates the qualitative results, that the samples cannot be differentiated based on the amplitude ratio map. A one-way ANOVA was done to compare the percentage of red,

Chapter 3. How guided waves using EMAT ultrasonic technology was selected in a feasibility study on different NDT techniques

Table 3.6: P-values for one-way ANOVA of peel off test result

Analysis of Variance	DF	% red	% yellow	% blue
Peel off test	2	0.211	0.146	0.335

yellow and blue pixels on the amplitude ratio map for the production samples. The p-value for the percentage of red, yellow and blue pixels is more than 0.05. This result indicates that the received ultrasound signal for the different samples is not statistically significant. The production samples that failed the bond peel off test cannot be differentiated from samples with good bond with the pulse-echo ultrasound inspection technique.

3.3.4 Guided waves using EMATs

Figure 3.19 shows the obtained A-scans that were plotted along the sample scan. For sample GW-R, the received signal amplitude in Figure 18(a) has only minor variations along the scan. The drop at the end of the scan is where the bimetal sample ended. Figure 18(b) shows the A-scan trace for the GW-PT sample. The amplitude has a periodic oscillation. Despite the oscillation, the maximum amplitude of the artificial delamination is significantly below the amplitude for normal bond condition. Figure 18(c) shows the A-scan trace of the GW-IT sample, which has the same characteristics like the GW-PT sample. The test results show that the selected guided wave mode is sensitive to detect delamination in Al/Al-Sn/Al/steel bimetal strips.

3.4 Discussion

The advantages and limitations of the four NDT techniques tested are summarised in Tables 3.7 to 3.10. Active thermography did detect the artificially implanted poor bond areas. The thermal image showed unambiguously small spots of delaminated areas. Active thermography could likely keep up with the desired online inspection speed of 12 m/min, since a large area is inspected at the same time. The Al/Al-Sn/Al/steel bimetal samples had a reflective surface, which turned out to be a challenge for active thermography inspection. It is likely that reflections, oil and/or indents that

Chapter 3. How guided waves using EMAT ultrasonic technology was selected in a feasibility study on different NDT techniques

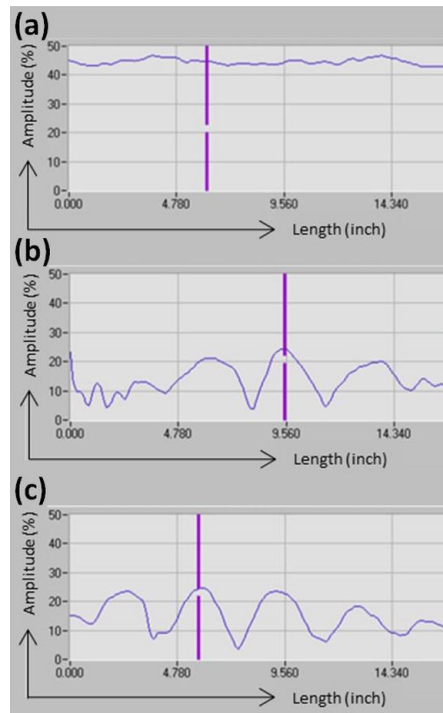


Figure 3.19: Sample A-scan traces of (a) control sample, (b) 80g/m² gauge paper delamination sample and (c) ink delamination sample

are not affecting the bond, but are present on strips in serial production, can cause local variations in surface emissivity, which can be misinterpreted as defects. The major limitation for active thermography to be used for online inspection is that the data acquisition of thermography needs to be consistent with the speed of the material loading method, which is challenging considering the varying strip tension, vibration and inspection line speed. Furthermore it is a challenge to reduce the temperature environmental influence in a rough production environment for continuous production, which would be required for online inspection.

Thermal and vacuum shearography testing did clearly detect the artificially implanted delamination. The samples with the artificial flaw showed a clear area of delamination through the centre of the sample and the reference sample showed no visible sign of defects. The surface irregularities of Al/Al-Sn/Al/steel bimetal strips were no issue for inspection with the shearography technique. The maximum inspection area of the used Q-800 system can reach up to 1.2 m² within 20 seconds, which is

Chapter 3. How guided waves using EMAT ultrasonic technology was selected in a feasibility study on different NDT techniques

Table 3.7: Advantages and limitations of active thermography bond inspection of Al/Al-Sn/Al/steel bimetal strips

Advantages	Limitations
Full-field inspection	Potential to miss flaws due to diffuse and/or reflecting surface
Contactless inspection	Highly skilled and/or experienced operator required
Revealing flaws in seconds	Signal interpretation can be ambiguous
Information about criticality of flaw	

Table 3.8: Advantages and limitations of shearography bond inspection of Al/Al-Sn/Al/steel bimetal strips

Advantages	Limitations
Full-field inspection	Difficulty to apply mechanical loading without rigid-body movement in-line / limited to laboratory
Contactless inspection	Potential to miss flaws due to matt and/or reflecting surface
Revealing flaws in seconds	Highly skilled and/or experienced operator required
Information about criticality of flaw	Signal interpretation can be ambiguous

equivalent to 12 m/min for 0.3 m wide strips. Therefore the maximum inspection speed matches the desired inspection line speed. The major drawback of shearography is the limitation of tolerance to rigid-body motion. This limitation requires loading methods such as thermal or vacuum technique that were used in the laboratory feasibility study. These loading methods are working well under laboratory conditions and for small samples, but their applicability is limited for online inspection due to the varying strip tension and vibrations. This aspect limits the applicability of shearography for the online inspection of Al/Al-Sn/Al/steel bimetal strips, because the movement causes de-correlation of speckle patterns and deterioration of fringe visibility and therefore make flaw detection difficult.

Ultrasound testing is a well-established NDT technique in industry for composite materials and it has been shown that the technique can detect poor bond that is created by not brushing the clad Al before CRB. However, serial production samples that failed the peel off test due to an unknown root cause were not detected. There are practical limitations since the temperature and water quality have to be controlled, because these factors have a significant influence on the measurement result. The same equipment

Chapter 3. How guided waves using EMAT ultrasonic technology was selected in a feasibility study on different NDT techniques

Table 3.9: Advantages and limitations of ultrasound A-scan trace bond inspection of Al/Al-Sn/Al/steel bimetal strips

Advantages	Limitations
Ultrasound directly interrogates and interacts with delamination	Time consuming and costly scanning required to inspect 100% of the material
Well established technique in industry	Poor reproducibility & repeatability
No mechanical loading required	Requirement for coupling media or immersion bath (difficult for in-line continuous testing)
Slow automated inspection possible	Significant water / coupling media carry over
	High calibration effort
	Highly skilled and/or experienced operator required
	Difficulties to focus probe when material is moving

from the laboratory tests was used for online trials to determine the online suitability. During the trials, a series of practical handling issues were encountered. The required water fluid coupling medium was significantly carried over into the bimetal coil, which causes corrosion. Furthermore, the strip shape deviations cause difficulties to focus the probe on the bond line whilst strips are moving. The received ultrasound signal variation with water temperature and quality that was observed in laboratory tests was also observed in the online tests. In regards to 100% volumetric material inspection, a computer controlled scanner can maximise inspection speed and minimise human intervention, hence automation is possible, but scanning of the entire material is too slow for 0.3 m wide strips to keep up with a typical inspection line speed of about 12 m/min. Furthermore ultrasound requires time consuming and costly calibration, because for each alloy type and lining/steel thickness combination of bimetal strips, a calibration sample is required, as the ultrasonic wave propagates differently. In summary, although ultrasonic testing did detect poor bond that was artificially implanted under laboratory conditions, there are many practical issues that obstruct the application of this technique for online inspection of Al/Al-Sn/Al/steel bimetal strips.

Guided waves EMAT is an emerging NDT technique in industry [103] and the non-contact ultrasound generation is the major advantage over conventional ultrasound testing. Based on the set of criteria to be suitable for online inspection and in a direct comparison between all tested NDT techniques, the EMAT technology using guided waves is the most promising technique for inspection of the bond between clad Al and

Chapter 3. How guided waves using EMAT ultrasonic technology was selected in a feasibility study on different NDT techniques

Table 3.10: Advantages and limitations of guided waves using EMAT bond inspection of Al/Al-Sn/Al/steel bimetal strips

Advantages	Limitations
Ultrasound directly interrogates and interacts with delamination	Rigid mechanical integration required to avoid any lift offs between test specimen and probe
High reproducibility & repeatability, not depend on operator	High calibration effort
No requirement for coupling media or immersion bath	No commercial system exists, need to be adapted for AlSn alloy/steel bimetal strip
Material surface irregularities do not affect the test results	Can act as an antenna and therefore requires excellent earthing
No mechanical loading required	Debris and swarf sticks to probes
100% volumetric inspection due to guided waves	Wear plates of probes wear
Low Signal-to-Noise ratio possible	
Fast automated inspection possible	

Table 3.11: Feasibility of NDT techniques to fulfil online inspection requirements for Al/Al-Sn/Al/steel bimetal

NDT technique / criteria	Delamination detection capability	Inspection speed for in-line application >12m/min	Compatibility with AlSn alloy/steel bimetal material properties	Surface irregularities: scratches, oil, specular and matt appearance	Strong rigid-body motion and vibration	Ambient conditions changes: light/temperature
Thermography	✓	✓	✓	X	X	X
Laser Shearography	✓	✓	✓	X	X	X
Ultrasound	✓	X	✓	✓	✓	✓
Guided wave EMATs	✓	✓	✓	✓	✓	✓

steel. It uses the advantages of ultrasound testing and overcomes its weaknesses as it does not require a coupling medium or scanning of the material. In an application for inspection of material used for coin dollars, a scanning speed of up to 360 m/min for 0.3 m wide strips was reported [72], which is faster than the 12 m/min online inspection speed requirement for Al/Al-Sn/Al/steel bimetal strips. Scanning as required for conventional ultrasound methods is eliminated because for guided waves, the two-dimensional scan is reduced to a one-dimensional scan, which allows 100% volumetric inspection at high speed. Furthermore, EMATs work at elevated temperatures and are insensitive to misalignment [87]. A disadvantage of EMAT is that it requires time consuming and costly calibration similar to ultrasound testing.

During the laboratory test it was established that in addition to detect the delamination itself, the potential technique needs to be able to cope with specular and matt

Chapter 3. How guided waves using EMAT ultrasonic technology was selected in a feasibility study on different NDT techniques

strip surface, thin oil films up to 5.4 g/m^2 and samples that have surface irregularities such as small indents or scratches. During the installation of the ultrasound inspection equipment for the online tests, the following requirements for online strip inspection were established:

- 100% of the material volume must be inspected at room temperature at an inspection speed of up to 12 m/min for strips with a cross section of up to 4.25x300 mm
- The technique must be able to operate with constantly changing strip tension, which results in vibration and sudden strong movements
- Automation of the inspection and defect detection is required
- Handling of the equipment must be appropriate in such a way that machine operators can unmistakably distinguish between good and bad material
- High technical availability of the machine and availability of spare parts
- Strip shape deviations that are observed in the Al/Al-Sn/Al/steel production that make inspection challenging are coil set, cross bow, torsion, wavy edges, one-sided wavy edges, coil breaks and central buckles. The NDT technique must be able to cope with these shape deviations.

Table 3.11 summarises the suitability of the tested NDT techniques for online inspection, based on the established requirements. Among the four tested NDT techniques, EMAT is most suited for online inspection of Al/Al-Sn/Al/steel bimetal strips. The demonstrated measuring sensitivity is adequate for the typical delamination sizes that are expected in Al/Al-Sn/Al/steel bimetal strips. Studies report good repeatability and reproducibility as well as the high inspection speed for 100% volumetric material inspection [72]. Since no coupling medium is required, guided waves generated with EMATs is a suitable technique for online NDT of Al/Al-Sn/Al/steel bimetal strips.

Chapter 3. How guided waves using EMAT ultrasonic technology was selected in a feasibility study on different NDT techniques

3.5 Conclusions

A case study of thermography, shearography, ultrasound and guided wave EMAT testing of the bond integrity of Al/Al-Sn/Al/steel bimetal strips is given in this chapter. In order to test the feasibility of these techniques to detect delamination, a number of laboratory experiments were done with samples that had different artificially implanted flaws. It was demonstrated that each NDT technique is capable to detect delamination between clad Al and steel layers under laboratory conditions, but has specific advantages and limitations. The limitations are particularly relevant in regards to online inspection, in which a NDT technique needs to meet more requirements compared to inspecting the bond under laboratory conditions. Active thermography and shearography are both practical enough for inspection under laboratory conditions, but the key issues that prevent an online application are the excitation methods and the environmental influences in the harsh serial production environment, which are not suited for these inspection techniques. Ultrasound testing is well established in industry to inspect the bond of laminates, but these applications are usually for components which are either inspected only point by point, or when it is acceptable that scanning the complete component is time consuming. Due to the one-dimensional beam and the scanning requirement, the technique is too slow for an online application at elevated speed. Furthermore there are practical issues associated with the requirement for a coupling medium. Guided waves inspection using EMATs was identified as a promising technique for online NDT of Al/Al-Sn/Al/steel bimetal strips. EMAT has all advantages of ultrasound testing without the limitations that are caused by the conventional ultrasound coupling medium requirement. However, no EMAT inspection system for Al/Al-Sn/Al/steel bimetal strips is currently commercially available.

Chapter 3. How guided waves using EMAT ultrasonic technology was selected in a feasibility study on different NDT techniques

Chapter 4

Guided waves generated with EMATs theory

Defects in bimetal strips can be detected using guided waves generated with EMATs. In guided waves EMAT technology, an EMAT transducer generates ultrasonic guided waves that propagate through the lining as well as steel backing material. Another EMAT probe is positioned at the opposite side of the strip to receive the guided waves ultrasound signal. In case of Al/Al-Sn/Al/steel bimetal, the transducers were positioned at the steel side. The empirical relationship between bond defects and guided waves in the experiments in this study was that when guided waves encounter a bond defect, the defect causes either mode conversion or destructive interference which converts incident wave energy into radiation energy in all directions, which results in dispersion. The remaining wave energy that propagates to the receiving EMAT transducer decreases, which is measured and shown as a lower signal amplitude in the A-scan. In this chapter, the theoretical considerations for the development of the NDT technique are introduced.

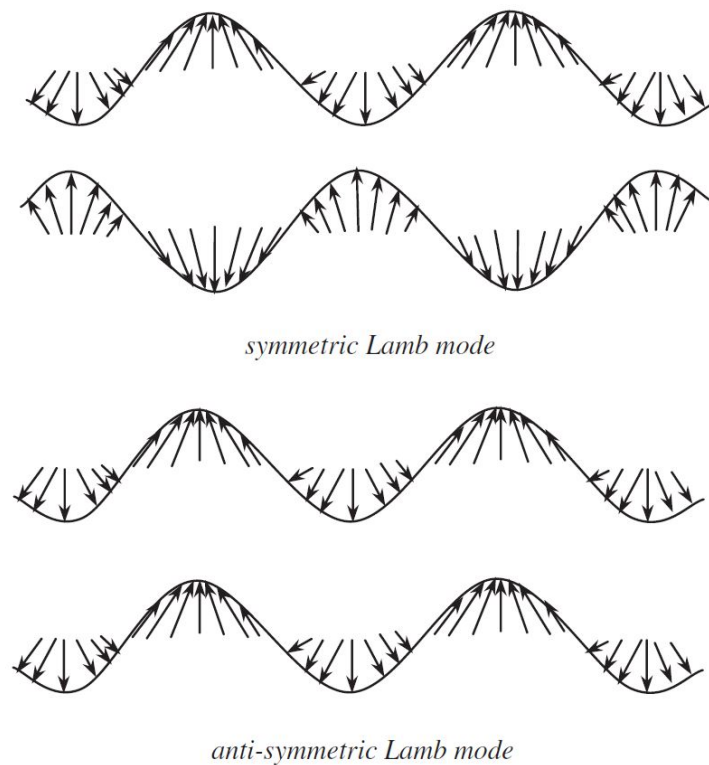


Figure 4.1: Symmetric and anti-symmetric Lamb wave modes [104]

4.1 Guided waves propagation

Fundamentals of Lamb wave

Lamb waves consist of a superposition of longitudinal and shear modes. They exist in thin plates. The entry angle, excitation and structural material geometry determine their propagation characteristics [104]. Figure 4.1 illustrates the symmetric and anti-symmetric Lamb modes that exist.

Equations 4.1 for symmetric modes and Equation 4.2 for anti-symmetric modes correlate the propagating velocity and its frequency, in which h , k , c_L , c_T , c_P and ω are the plate thickness, wave number, velocities of longitudinal and transverse modes, phase velocity and wave circular frequency [105]. Lamb wave velocity depends on frequency regardless of the mode.

$$\frac{qh}{ph} = -\frac{4k^2qp}{(k^2 - q^2)^2} \quad (4.1)$$

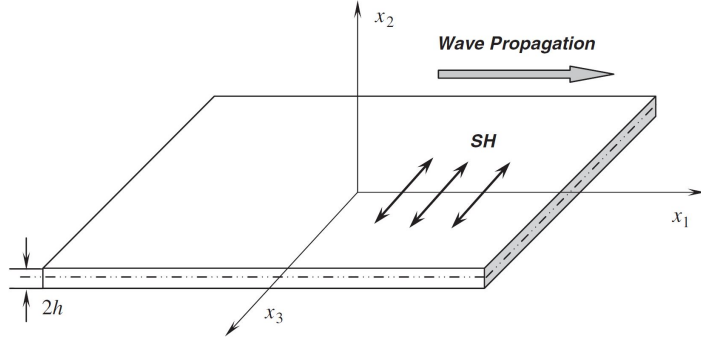


Figure 4.2: Shear horizontal (SH) mode in multilayered sheets [110]

$$\frac{qh}{ph} = -\frac{(k^2 - q^2)^2}{4k^2qp} \quad (4.2)$$

$$p^2 = \frac{\omega^2}{c_L^2} - k^2, \quad q^2 = \frac{\omega^2}{c_T^2} - k^2 \quad \text{and} \quad k = \omega/c_p$$

Another wave mode that is used in some plate inspection applications [106, 107], namely the *shear horizontal* (SH) mode, is employed together with Lamb modes. The SH mode has a transverse shear motion, which is different from normal shear waves that have a vertical shear motion. Figure 4.2 illustrates the transverse shear motion of the SH mode perpendicular to the plane of wave travel. This mode was first discovered between layers of laminate by Love in 1911 [104] and was later confirmed by experimental work [108] and finite element simulation [109].

Multilayered plates consisting of different materials have anisotropic properties which add complex phenomena to wave propagation [104], like speed depending on direction and difference between phase and group velocities. Lamb waves in an N -layered composite laminate can be described with its displacement field u and satisfying Navier's displacement equations (4.3) where ρ^i is the density and λ^i, μ^i are Lamé constants for the i -th layer [110].

$$\mu^n \nabla^2 u^n + (\lambda^n + \mu^n) \nabla(\nabla \cdot u^n) = \rho^n \frac{\delta^2 u^n}{\delta t^2} \quad (n = 1, 2, \dots, N) \quad (4.3)$$

Dispersion, meaning attenuation in magnitude, variation in propagating velocity and change in wave number is commonly observed in Lamb waves. Additionally, surface

coatings may cause significant damping and consequently attenuation [111]. Despite dispersion, Lamb waves are able to propagate relatively long distances [104]. Adding boundary conditions at $N - 1$ interfaces and free surfaces to Equation 4.3, results in a comprehensive *dispersion* equation 4.4 [110]. For any given material (λ^n, μ^n), the Lamb wave frequency (ω) is related to the wave number (k) and plate geometry (h_n). The dispersive curves of Lamb modes are indefinite according to the implicit expression of the dispersion equation with infinite roots. This leads to specific challenges when employing Lamb waves for damage identification [104]. These challenges are further discussed in the following sections.

$$| A(\omega, k, \lambda^n, \mu^n, h_n) | = 0 \quad (4.4)$$

4.2 Analysis and simulation of Lamb waves

The complexity of Lamb waves in real world applications is well known. Numerical simulation helps to understand these complex Lamb wave behaviours. Recent advancements are to not only simulate dispersion curves, but also the Lamb wave propagation inside the plate itself. This allows to obtain the induced Lamb wave signals from the actuators, their interactions with defects and the resulting signals at the receiving sensors. The FEM is the most robust numerical simulation tool for this purpose [112]. The disadvantage of FEM simulations is that even with today's computers, still a lot of computational resources are required [113]. For the reduction of the model size, symmetrical boundary conditions between the layers have been introduced. In order to remove the complexity of wave reflections from actuator simulations, infinite boundaries are needed, which requires special types of elements [112]. The simulation of Lamb wave problems can be categorised into three main subject areas [104]:

1. Calculation of dispersion curves
2. Lamb wave interaction with irregularities
3. Simulation of actuator/sensor coupled systems

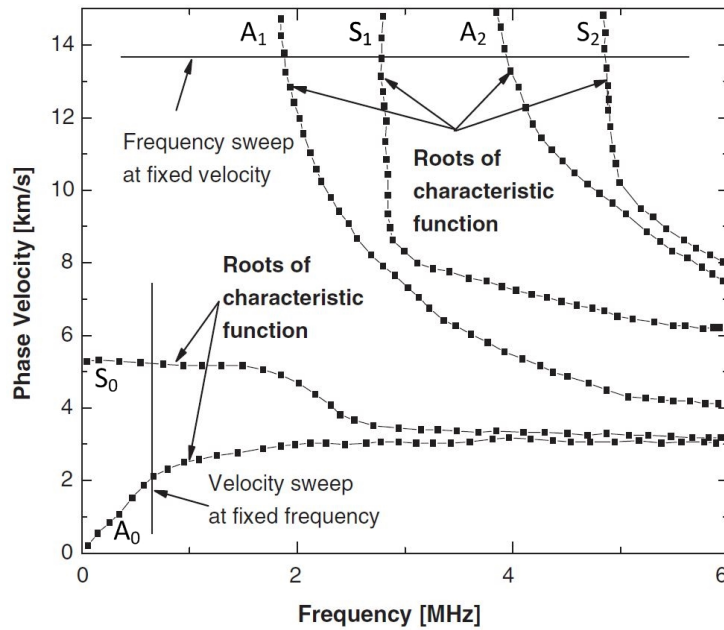


Figure 4.3: Composite laminate dispersion curves obtained by transfer matrix method [115]

4.2.1 Analytical study of Lamb wave characteristics

Dispersion curves for composite plates can be calculated in two different theoretical approaches, the exact solution approaches and approximate solution approaches [114]. The most important tools for exact dispersion curve analysis are the *transfer matrix* approach (Thomson-Haskell method) and *global matrix* approach [115]. For any given frequency, infinite wavenumbers exist that mathematically satisfy Equations 4.1, 4.2 and 4.4 which are obtained by an iterative root-finding method (like Newton-Raphson), in which the root loci of the equation are the dispersive curves of different modes [110]. In the transfer matrix method, it is assumed that four waves exist at each layer of a multi-layered laminate, which all share the same frequency and spatial properties at their interfaces [115]. Under this assumption, the intermediate interface equations eliminate each other and the boundary condition is a relation between wave frequency and wave number, which is established in the form of matrices. Solving the matrices results in the set of dispersion curves [115].

Figure 4.3 illustrates a set of dispersion curves for a composite laminate that was

obtained using the transfer matrix method. The disadvantage of this method is that it gets ill-conditioned and unstable, if the plate thickness (d) is large and the frequency (f) is high, which is referred to as '*large fd problem*'. The *global matrix* method directly addresses this disadvantage by directly assembling a single matrix to seek for root loci. As a result, the method is numerically robust for any range of fd values. However, it involves larger matrices and has a slower convergence. In regards to approximate solutions, the guided waves dispersion curves can be obtained by FEM. Homogenised material properties are used in anisotropic composite plates at each material layer. The existing modelling approaches are [112] *time domain modelling, mode shape of short wave guides*, *Wave Finite Element* (WFE) method and the *Semi-Analytical Finite Element* (SAFE) method.

4.2.2 Lamb wave dispersion curves in SAFE

The SAFE method was used for analytically studying the propagation characteristics of Lamb waves in this thesis. Among all FEM techniques, the SAFE approach is the most efficient one [116]. In the SAFE approach, the wave propagation is described analytically in the wave propagation direction and is therefore able to cope with high frequency propagation. Furthermore, the small element size requirement in the FEM analysis does not significantly affect the method [112]. Applying the theory for multi-layered plates [117], the method calculates approximate solutions of plate dispersion curves. A disadvantage of the SAFE method is that the necessary elements are not readily available in commercial FEM packages and therefore need to be developed by the user.

Phase and group velocity curves

The phase velocity curves can be calculated based on the relationship $c_p = \frac{\omega}{k}$. The wavenumber k is obtained by solving the eigenvalue problem that was described in the previous chapter. The group velocity (wave packet velocity) can be obtained from the relationship $c_g = \frac{d\omega}{dk}$, in which \vec{k} is the wave propagation direction. The unit vector in x direction is \vec{x} , hence the wave vector for guided wave propagation in x direction

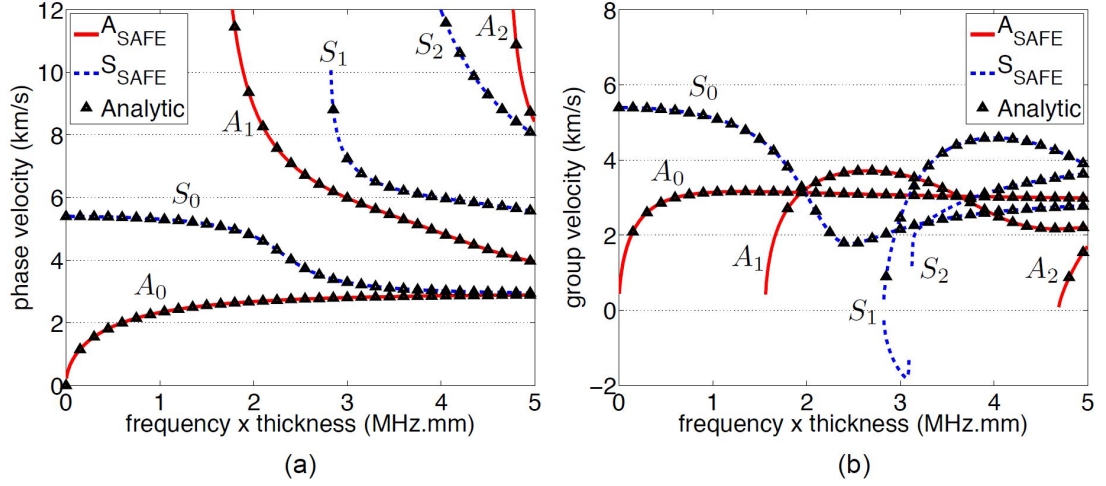


Figure 4.4: SAFE and analytical dispersion curves comparison for aluminum plate: (a) phase velocity, and (b) group velocity curves [112]

is $\vec{k} = k \vec{x}$ [112]. The group velocity is given by Equation 4.5. The group velocity curves in the SAFE method can be directly calculated from the SAFE method results, while in Equation 4.5 the phase velocity curves need to be differentiated to obtain the group velocity curves [118].

$$c_g = \frac{dw}{d\vec{k}} = \frac{dw}{d(\frac{w}{c_p})} = \frac{c_p^2}{c_p - w \frac{dc_p}{dw}} = \frac{c_p^2}{c_p - f \frac{dc_p}{df}} \quad (4.5)$$

Verification of dispersion curves

Lamb wave dispersion curves for an aluminium plate with Young's modulus of 70 GPa, Poisson's ratio of 0.33 and density of 2700 kg/m² were calculated in [112] using the SAFE method and ten 1D quadratic elements to model the plate thickness. The results were compared to the analytical solution from [119]. Both sets of velocity curves were plotted in Figure 4.4. It shows that a good agreement between the SAFE and analytical solution can be obtained.

In order to increase the accuracy of the SAFE method solution, either a higher number of elements or higher order interpolation functions can be used [120]. Comparisons between different number of elements in SAFE for the first four modes A_0 , S_0 , A_1 , and S_1 and the analytical solution for the dispersion curves in the aluminium plate

were made in [112]. It was shown that when the number of elements exceeds three, then the SAFE dispersion curves match almost exactly the analytical solutions.

The so far discussed SAFE dispersion curves were for isotropic aluminium plates. However, the Al/Al-Sn/Al/steel plates considered in this study are made of multiple isotropic aluminium alloy and steel layers in an unsymmetrical arrangement. In the following, the unsymmetrical material arrangement effect on dispersion curves is discussed.

Ahmad (2011) considered 1 mm thick plates and two Young's modules, E_1 and E_2 , where $E_1 = E_{aluminum}$ and $E_2 = 0.5E_{aluminum}$. For both materials a Poisson's ratio of 0.33 and a density of 2700 kg/m^3 were used. Figure 4.5(a) shows an unsymmetrical material arrangement with 40% thickness ratio between the top layer (E_2) and bottom layer (E_1). Figure 4.5(b) illustrates an unsymmetrical material arrangement with the same material properties as in Figure 4.5(a), but a 10% thickness ratio between the top and bottom layer. It can be seen in Figure 4.5(a) that the first and second mode in the dispersion curves separate as a result of the unsymmetrical material arrangement, which was marked by the red circle. When comparing this to the case with unsymmetrical arrangement and 10% thickness ratio, it can be seen that the effects on the dispersion curves are small, if the top layer is less than 40% of the plate thickness. In plates with unsymmetric material properties, the symmetric and anti-symmetric Lamb modes cannot be differentiated, hence both modes exist at the same time. The Al/Al-Sn/Al/steel bimetal plates that are considered in this study have a typical thickness ratio of 25% for the lining clad Al layer. Thus, based on the reviewed literature, it is expected that Lamb modes are quasi symmetrical and quasi anti-symmetrical and that the first and the second mode are slightly separated.

4.2.3 Lamb mode selection

The ideal Lamb mode for inspection should have the following properties: (1) non-dispersive, (2) low attenuation, (3) high sensitivity, (4) easy excitability, (5) good detectability and (6) tool-less selectivity [121]. It was found in various applications with different modes and frequencies in thick and thin plates that using a narrow bandwidth

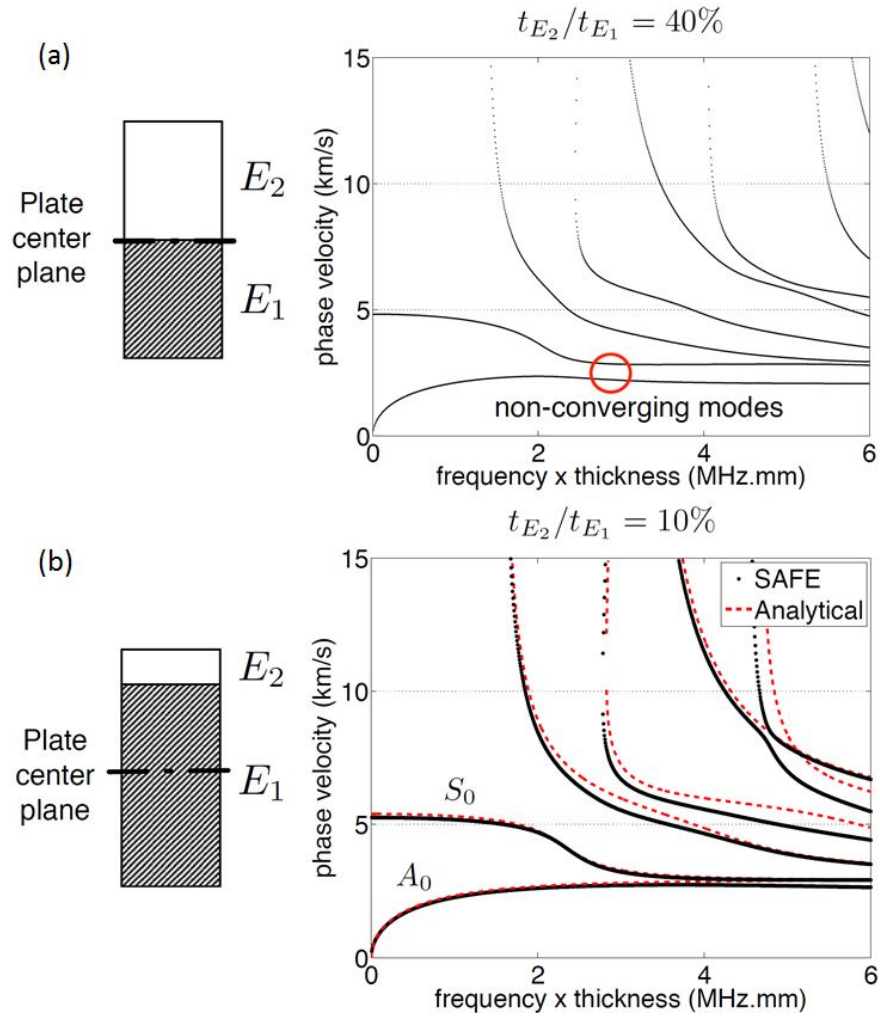


Figure 4.5: SAFE and analytical phase velocity dispersion curves for comparison between isotropic aluminum plate and unsymmetrical material arrangement with (a) 40% and (b) 10% thickness ratio between the layers with different Young's modulus [112]

input signal effectively prevents wave dispersal. Therefore windowed toneburst instead of pulse is often employed as Lamb signal for inspection. The available frequency range $[f_{\min}, f_{\max}]$ can be calculated by Equation 4.6, where the toneburst cycle number is n , excitation frequency is f_0 and k is a bandwidth depending constant [121]:

$$f_{\min} = f_0(1 - k/n) \quad f_{\max} = f_0(1 + k/n) \quad (4.6)$$

As per Equation 4.6, increasing the number of cycles reduces the bandwidth, causing less dispersion. However, when a large cycle number is used for a small inspection sample, different wave components like incident and reflected waves can overlap. An alternative approach to determine the most suitable cycle number and frequency for a Lamb mode is the *minimum resolvable distance* (MRD) approach [122], in which l and d are wave propagation distance and plate thickness; v_0 , v_{\min} and v_{\max} are the input wave-packet group velocity at central frequency, minimum and maximum velocities in the wave-packet to travel through the distance of l ; and T_{initial} is the wave-packet initial time duration [122].

$$MRD = \frac{v_0}{d} \left[l \left(\frac{1}{v_{\min}} - \frac{1}{v_{\max}} \right) + T_{\text{initial}} \right]_{\min} \quad (4.7)$$

In general it was observed that the smaller the MRD value is, the more suitable is the frequency and cycle number and therefore the better is the resolution. It was found [122] that S_0 and A_0 typically have very low MRD values. Furthermore, it was found that S_0 has reasonable defects sensitivity anywhere throughout the sample thickness. In contrary, A_0 is more sensitive to surface cracks or corrosion, but at the same time has higher attenuation ratio and therefore may not be suitable for long-distance propagation and inspection.

Other research [123] proposed as best frequency selection technique to consider the maximum response amplitude for a range of potential frequencies depending on different sample structures and damage types. This is the approach that was used in this thesis. Regarding waveform selection, pure sinusoidal shapes excite Lamb wave harmonics more efficiently than parabolic shapes and the bandwidth can be narrowed and energy

centralised with a windowed sinusoidal signal [123]. It was also found [124, 125] that modes are most effective to identify defect types, if the existence of a defect causes a higher stress level for a specific wave mode than others. Defects that cause a change in interface stiffness, are best found using wave modes which produce a large shear stress at the interface defect position [124, 125].

In practice, the basic symmetric mode (S_0) and anti-symmetric mode (A_0) are mostly employed for inspection. In various studies [126–130] it was reported that A_0 is highly effective for delamination and transverse ply crack inspection. A_0 has a shorter wavelength, which is required to detect smaller defects. S_0 is the preferred mode in the majority of studies [106]. Lamb waves interact with damages, actuators and sensors.

4.3 SAFE-FE coupling for defect and edge reflection

Lamb wave reflection and transmission by damage strongly depends on the Lamb wave frequency and the defect size [131]. There exist two-dimensional and more complex three-dimensional FEM models to simulate the Lamb wave scattering characteristics [104]. It was shown in a 2D FEM model with absorbing boundary conditions [132] that when waves interact with delamination, then the incident wave energy is partially converted to radiate energy in all directions and surface waves can occur around the cavity. Furthermore, complex mode conversion can occur when guided waves interact with defects. Various studies [133, 134] showed that at fine FEM mesh with at least 10 nodes per Lamb wavelength are required for good precision. However, such a fine mesh quickly requires too much computational power for large structures.

The coupled SAFE-FE method [135] can be used to study how defects in the plate influence the Lamb wave reflection and transmission. In this technique, the defective plate region is modelled in FEM, while the SAFE technique is used to model the infinite plate regions before and after the defects. Ahmed (2011) described how continuity of displacements between the SAFE and FE region is preserved by considering the same interpolation functions and number of nodes at the boundary between the two regions, as well as how to best verify the obtained results.

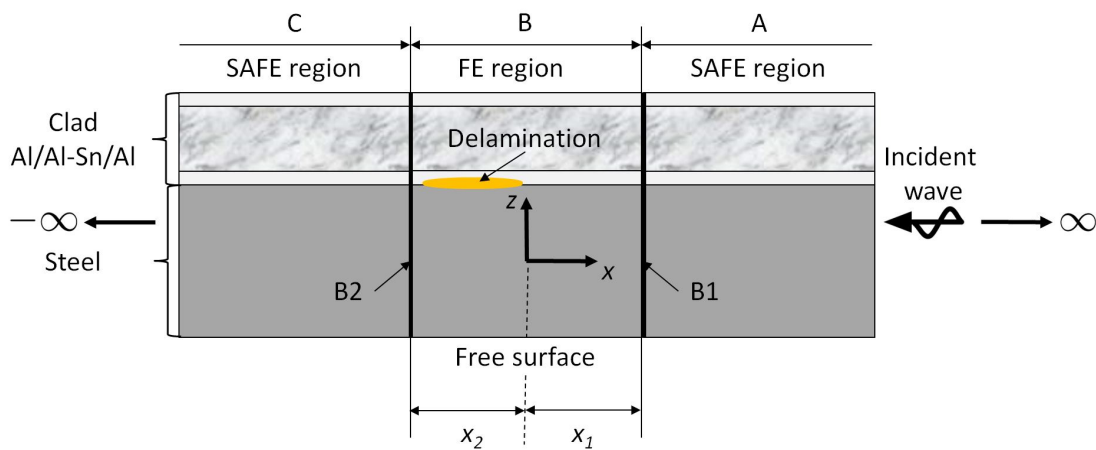


Figure 4.6: Coupling between SAFE-FE for Al/Al-Sn/Al/steel bimetallite sheet at a defective position on the plate

Figure 4.6 illustrates how the region with a delamination defect is modelled using the FEM, while the SAFE method is used to model the infinite plate regions before and after the defect. The regions A, B and C denote the infinite plate region before the defective region, the defective region, and the infinite plate after the defective region. B1 indicates the boundary between regions A and B and B2 between B and C. In region A, in which $x \geq x_1$, the Lamb waves are reflected due to the defect. In region B, where $x \leq x_2$, the Lamb waves are transmitted [112].

In addition to interaction with damages, Lamb waves reflect at the plate edges. The different cases are reflection by a vertical plate edge and general plate edges. The different boundary conditions are either fully free or fully fixed edges. The boundary conditions of the vertical plate edge problem can be defined easily in the SAFE method, as the condition is homogeneous for all points along the plate edge. For general plate edge geometries, the conditions at the edge need to be formulated in the FEM that is coupled with the SAFE method.

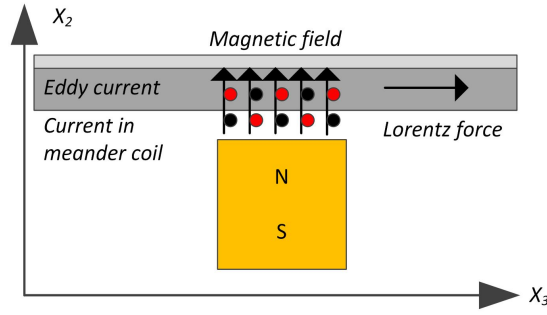


Figure 4.7: Interaction between EMAT transducer and bimetal sample

4.4 EMAT as guided waves ultrasonic generators and sensors

Any force that can be decomposed into point forces is considered in the force response analysis in the FEM and SAFE method. Approaches which model general 2D external forces acting on a plate are described in a 2D point force response simulation in [136]. There are a variety of means to actively excite and collect Lamb waves in plates. Su et al. (2006) grouped them into the five categories ultrasonic probes, lasers, piezoelectric elements, interdigital transducers and optical fibres. Non-contact EMATs that are used in this study belong to the ultrasonic probes category.

Figure 4.7 is a schematic of the EMAT transducer that was used in this study and its interaction with the bimetallic sample. The transmitting and receiving transducers each have a magnet in the housing and a meander coil over the magnetic pole. Above the magnetic pole, the magnetic field (B) is mainly in the X_2 direction. Eddy currents (J) are induced by the meander coil in the X_1 direction. The Lorentz force (f) acts on particles and creates ultrasound in the sample. It is the result of the interaction between the magnetic field (B) and eddy currents (J), which is given by Equation 4.8:

$$f = JxB \quad (4.8)$$

Since the current sent along the meander coil is periodically distributed, the corresponding eddy currents in the steel surface of the bimetallic sample generate periodically distributed loading. When the guided wave propagates above the receiving EMAT, the

horizontally polarized stress field that it produces interacts with the magnetic field, thus generating currents in the meander coil, which is placed between the bimetallic sheet and the magnet.

4.5 Lamb wave signal processing and feature extraction to find internal defects

The recorded Lamb wave signals must be interpreted to find defects that are buried below the strip surface. Under the harsh manufacturing conditions, extraction of key features is challenging due to signal contamination from noise, natural structural vibration, existence of multiple wave modes and bulkiness of the inspection data. In the following section, the feature extraction technique that was used in this study is introduced.

Guided waves can be reflected at the edges of the bimetal. In order to avoid superposition of guided wave signals, the EMAT transmitter and receiver are oriented slightly angled as can be seen in the plan view in Figure 4.8. For bimetal strips without bond defect along the Al/Al-Sn/Al alloy and steel interface, guided waves propagate without interference from the EMAT transmitter to the receiver as shown in Figure 4.8(a). The system sensitivity depends on the defect size. Figure 4.8(b) illustrates when the delamination is larger than the guided wave length, the defect causes destructive interference that results in attenuation, which reduces the remaining wave energy that propagates to the receiving EMAT transducer. The system is optimally sensitive when the EMAT meander coil is approximately parallel to the defect. Figure 4.8(c) illustrates a foreign particle at the bond interface, which is perpendicular to the EMAT meander coil. Since the size of the particle that is acting as reflector is minimal in this orientation, the reflected wave energy and attenuation is small. Therefore it is not easily distinguishable from background noise in defect free bimetal and might be difficult to detect. However, if the same foreign particle is oriented parallel to the EMAT meander coil, then the reflector area is large, which results in strong attenuation. This case when the system is optimally sensitive is shown in Figure 4.8(d). Ideally the machine would have an

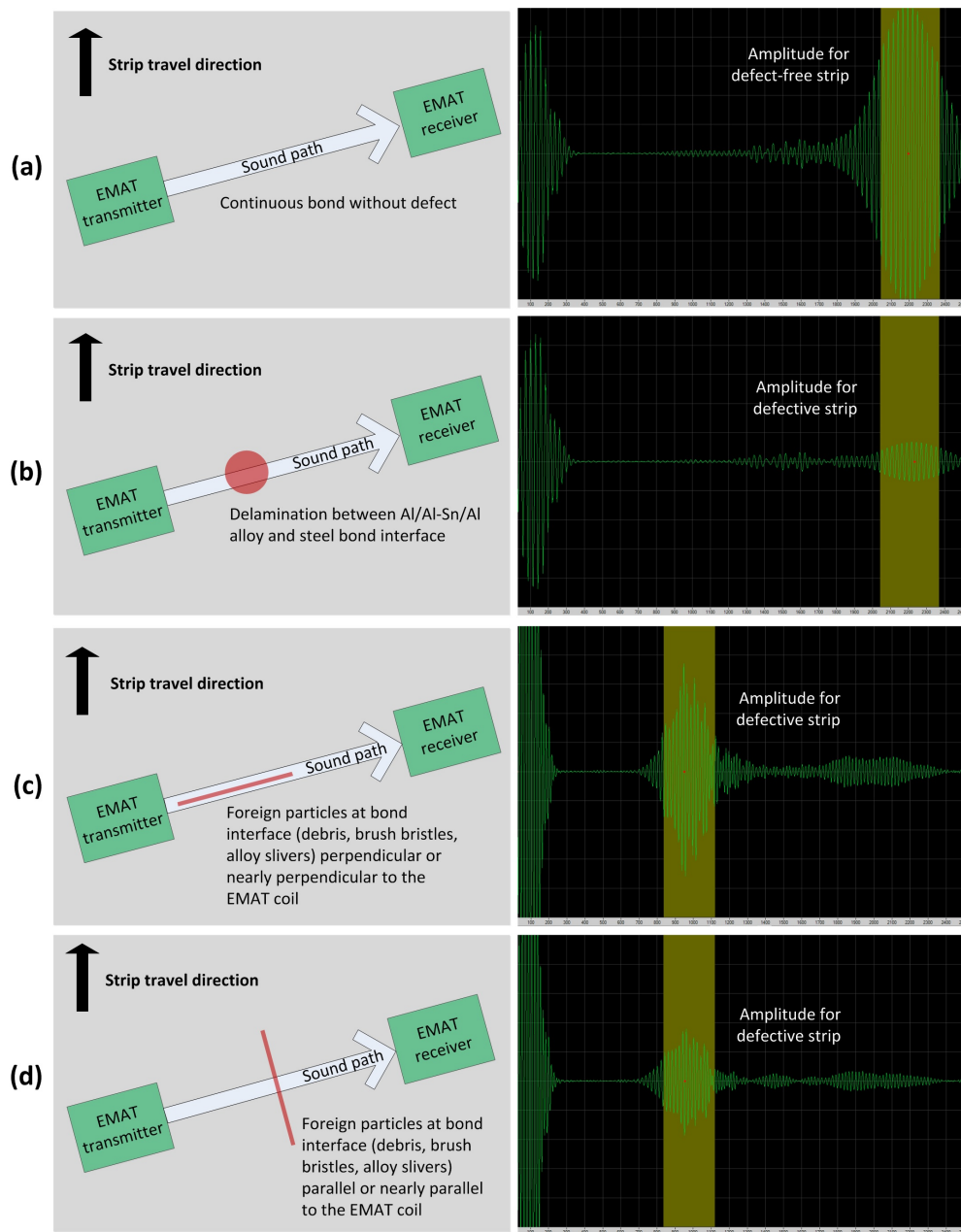


Figure 4.8: Plan view of guided waves between EMAT transmitter and receiver, where (a) the bond interface between Al/Al-Sn/Al alloy and steel is without defect resulting in normal attenuation and reference A-scan amplitude, (b) delamination at the bond interface interfering with the guided waves sound path and resulting in attenuation and A-scan amplitude reduction, (c) foreign particles at the bond interface perpendicular to the EMAT coil that interact with the guided waves but may not be easily detectable because the attenuation in the A-scan amplitude is only moderate, (d) foreign particles parallel to the EMAT coil that should be easily detectable because of significant attenuation and A-scan amplitude reduction.

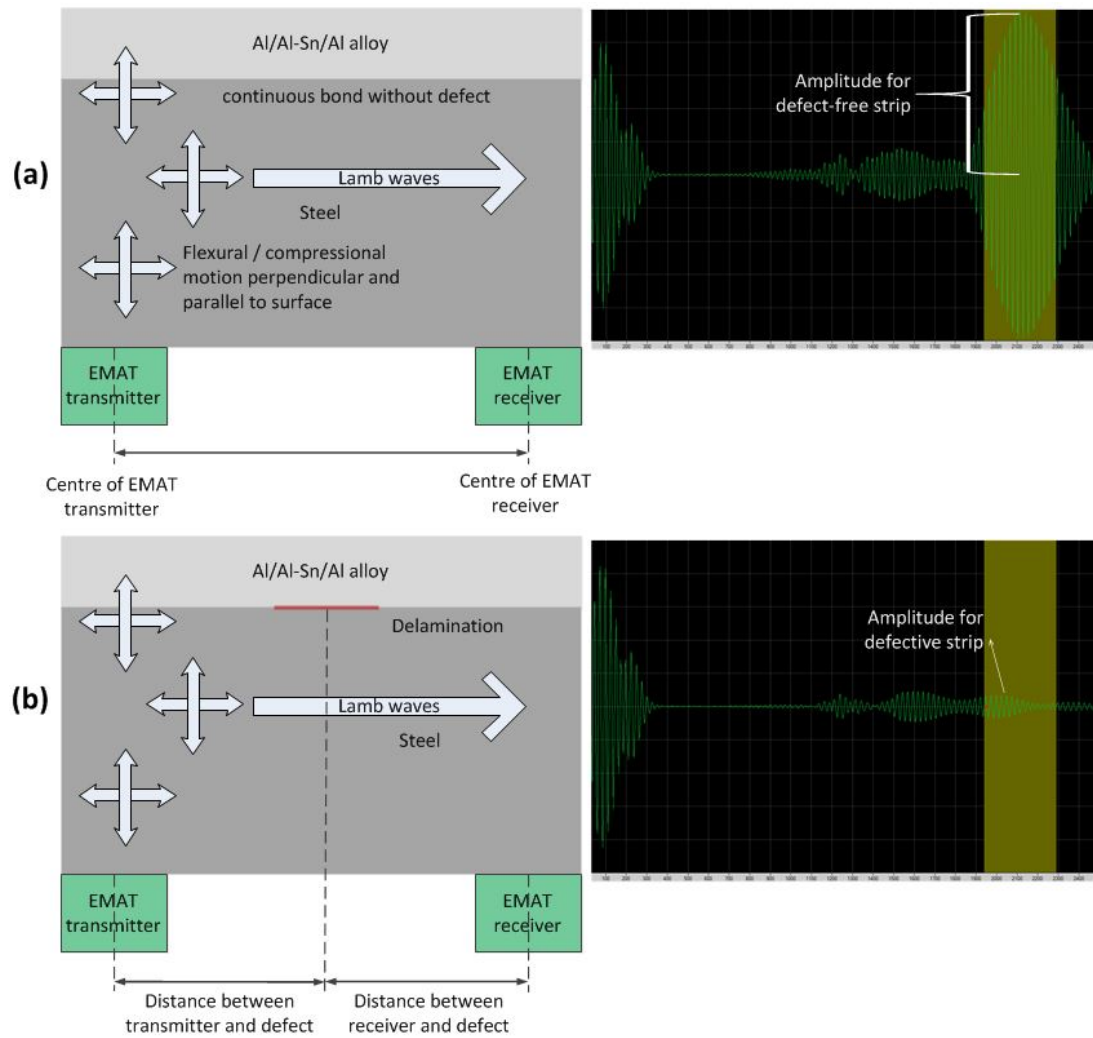


Figure 4.9: Cross section view of Al/Al-Sn/Al/steel bimetal and guided waves, where (a) the bond interface is without defect resulting in normal attenuation and reference A-scan amplitude, (b) delamination at the bond interface interfering with the guided waves sound path and resulting in attenuation.

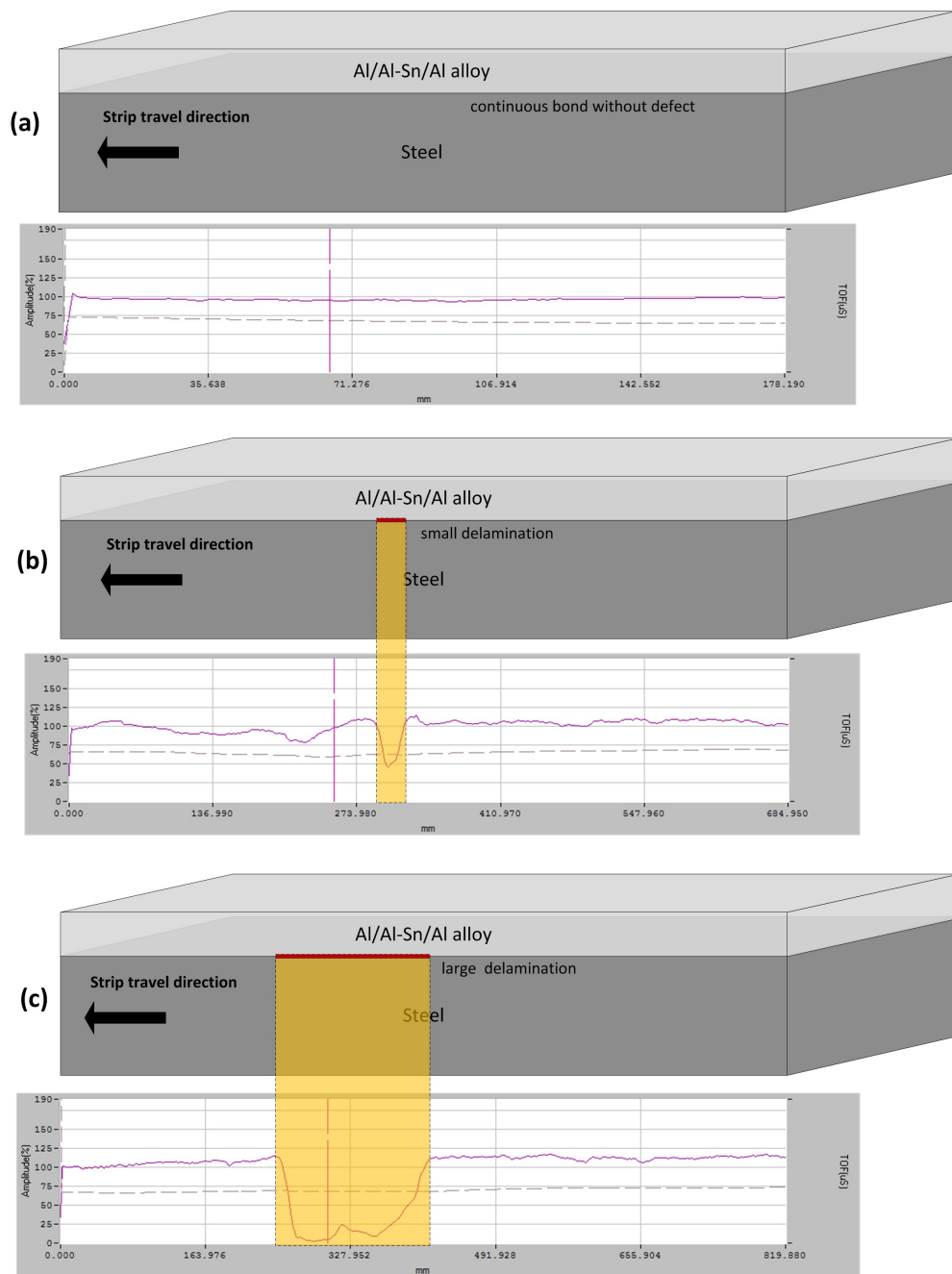


Figure 4.10: Illustration of A-scan maximum amplitude trace, where (a) the bond interface between Al/Al-Sn/Al alloy and steel is without defect resulting in normal attenuation and reference A-scan maximum amplitude trace, (b) small delamination at the bond interface during inspection interfering with the guided waves sound path and resulting in significant attenuation and low A-scan amplitude for the length of the defect, (b) large delamination at the bond interface resulting in drop of A-scan maximum amplitude trace for the length of the defect.

EMAT array, in which transverse as well as longitudinal defects could be found. The EMAT meander coil and sound path in this system is oriented diagonal across the strip width to allow 100% volumetric inspection. Sensor arrangement considerations for the final system are further discussed in section 9.2.

Figure 4.9 shows the relative distance between the EMAT transmitter and receiver in a bimetal cross section view. In Figure 4.9(a) the sound path of the Lamb wave is not obstructed by any defect. The time of flight of the Lamb wave can be calculated by $t = d/v$, where t is time, d is distance between EMAT transducer and receiver, and v is the Lamb wave velocity. The inspection gate is set at the observed Lamb wave arrival time for the defect free sample. Figure 4.9(b) illustrates delamination between the Al/Al-Sn/Al alloy and steel layers, which is obstructing the sound path of the Lamb wave between EMAT transmitter and receiver. Depending on the employed wave mode, attenuation and/or mode conversion occurs when the guided wave interacts with the defect. As a result, the maximum amplitude in the set inspection gate drops and in case of mode conversion arrives earlier or later than the inspection gate, which qualitatively indicates the presence of a defect. Figure 4.9(b) shows attenuation due to destructive interference as a result of the guided wave interaction with delamination that acts as reflector. The amplitude ratio between a reference and defective sample signal, defined as *R/D amplitude ratio (RDR)* in this thesis, is the ratio of the wanted signal from a defect-free signal relative to the signal received at the same TOF from a defective sample. Figure 4.9 shows the amplitudes that were used to calculate the RDR, which is used to extract features and find internal defects in this thesis. In order to reduce signal noise, signal frequency band width filters were used to filter only the wave mode of interest for inspection. This is further explained in the next section.

Figure 4.10 illustrates A-scan maximum amplitude traces that are used to inspect full length coils. Each trace is the maximum amplitude from the inspection time filter that is set in the A-scan and plots it relative to the position of the inspected bimetal strip. The A-scan maximum amplitude trace in Figure 4.10(a) is for a bimetal coil without defect at the interface between Al/Al-Sn/Al/steel and therefore the maximum amplitude is relatively stable at about 100% relative amplitude. In case of a delami-

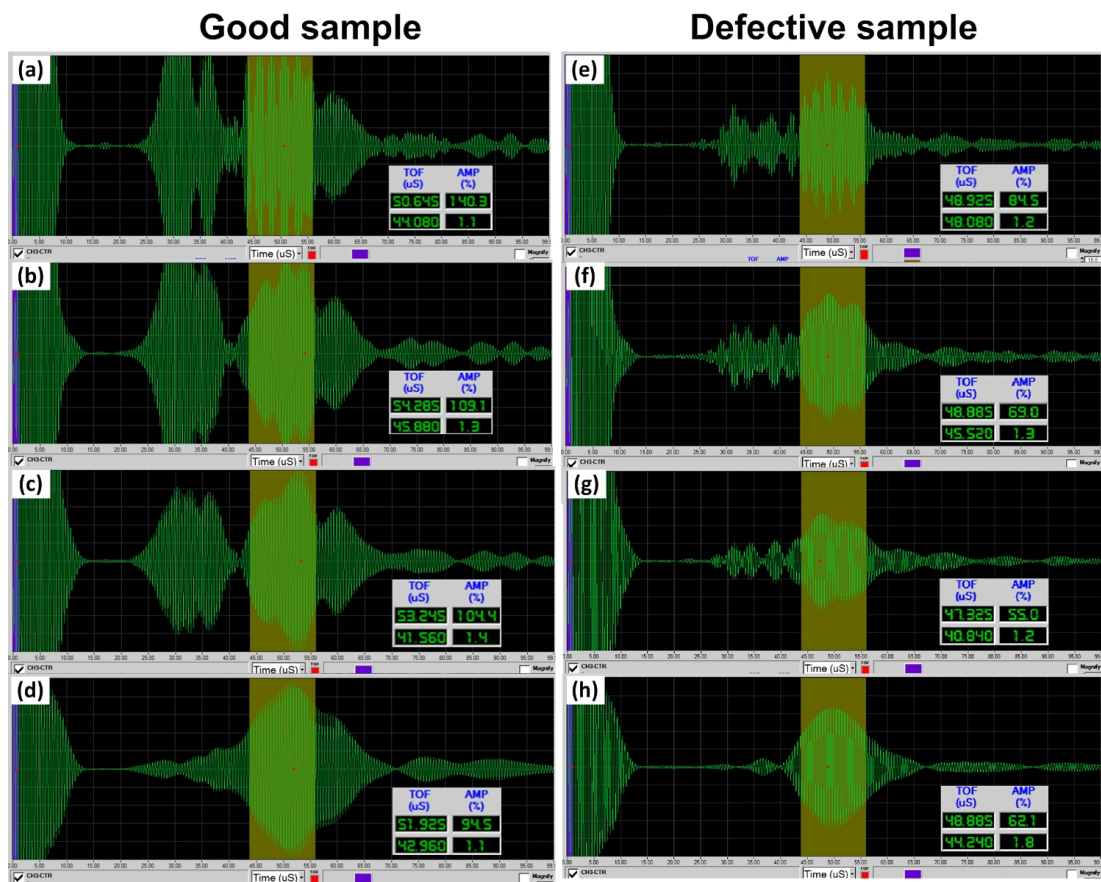


Figure 4.11: Time domain signals at receiver location: A-scans showing transmitted frequency response of good and defective samples: (a)/(e) no frequency band width filtering, (b)/(f) ± 0.3 MHz, (c)/(g) ± 0.2 MHz and (d)/(h) ± 0.1 MHz frequency band width filtering around set wave mode frequency

nation at the bond line, the A-scan maximum amplitude drops at the beginning of the defect and then returns again to 100% relative amplitude. At 60% relative amplitude a dashed line marks an arbitrary alarm threshold. The length of bimetal strips for which the A-scan maximum amplitude traces is below a defined threshold, is categorised as defective. Figure 4.10(c) shows that the A-scan maximum amplitude trace is recording the defect size according to the physical size of the defect.

4.6 Wave mode selection and system calibration

The methodology described below was used to select wave modes and to calibrate the system before measurements were taken.

1. For calibration, two samples with identical dimensional and material characteristics were used, one sample without defect and the other sample with known, artificially implanted defect. In order to start calibration, the good quality sample was used first.
2. The EMAT construction provides mode selectivity in the frequency domain, thus the ability to precisely select the wave mode of interest. The wave modes were selected from dispersion curves for Al/Al-Sn/Al/steel plates that were calculated in the SAFE method.
3. Multiple modes are excited at a set frequency as explained in section 4.2. As the different modes travel at different speeds, their signal is received at different times and with different amplitude, which is shown in the measured time/amplitude domain response in Figure 4.11. The different modes were identified based on their time of arrival at the receiver and the velocity from the group velocity curve.
4. In order to verify that the excited wave modes is the same as the wave mode in the dispersion curves, the frequency was adjusted up and down from the set point until the frequency with the maximum amplitude response was found.
5. Filters were used to filter only the wave mode of interest for inspection. Figure 4.11 shows how the time/amplitude domain response changes for (a)/(e) no frequency band width filtering, (b)/(f) ± 0.3 MHz, (c)/(g) ± 0.2 MHz and (d)/(h) ± 0.1 Mhz frequency band width filtering around the set wave mode frequency.
6. Once the frequency maximum response amplitude was obtained and the frequency band width filter was set, the gain (dB) was adjusted till the amplitude was as

close as possible to 1 arbitrary unit (AU) or 100%. This amplitude is referred to as *good quality, reference* or *normal* amplitude.

7. The set wave mode with normalised amplitude was then tested with the defective sample regarding wave mode sensitivity. The more the amplitude for the defective sample drops within the set inspection time gate, the better is the wave mode suited for practical inspection.
8. If the set wave mode was not sensitive to the specific defect, then steps 3 to 7 were repeated until a wave mode with high defect sensitivity was found.
9. Steps 1 to 8 were repeated for every different sample structure and defect type. Every selected wave mode and corresponding sample structure was systematically recorded so that the same wave mode could be used again for future inspection.

4.7 Optimising the guided waves EMAT-EMAT system

There is a set of factors that influence the performance of the inspection machine. It is a balancing act to consider all different factors to optimise the system as a whole and obtain the best possible inspection data. The influencing factors, which were considered to optimise the system are:

- The type of EMAT coil used and the dimensions of the coil to transmit and receive Lamb waves (e.g. meander coil, number of coil turns, overall coil width, magnetic field strength, wire diameter, gap between transducer and material).
- The type of EMAT amplifier that is used to convert the low-voltage electrical signal into a high-power pulse train, which is required to drive the transmitting EMAT and produce a good SNR.
- Remote electronics signal conditioning box that connects the EMAT sensors, tone burst amplifier and Digital Input/Output (DIO) interface for signal conversion and extraneous noise filtering from the ultrasonic waveform.

Chapter 4. Guided waves generated with EMATs theory

- Material characteristics (density, Young's modulus, Poison's ratio) of the different Al-Sn alloys as well as dimensional characteristics of the bimetal (lining thickness, steel backing thickness, lining/steel ratio).
- Selection of wave mode (frequency, speed, dispersion).
- Practicalities concerning how to position the probe for inspection and for maintenance.
- Being able to save the data for later interpretation if required.
- Ability to mark the position of any defect on the strip.

Chapter 5

Detection of bond defects in cold roll bonded Al/Al-Sn/Al/steel plates

In this chapter, multi-layered samples were produced with artificially implanted delamination, embedded steel debris and a brittle intermetallic Al-Fe diffusion bond layer defects at the interface between clad Al and steel. Experiments were done to determine the sensitivity of the S_1 guided wave mode to qualitatively indicate the presence of defects based on signal attenuation caused by defects. EMATs were used to generate and detect the guided waves in the pitch and catch technique. Signals were measured in the as rolled and post rolling annealed state to determine the influence of the altered material properties on attenuation and RDR. Results show good sensitivity of the S_1 wave mode for delamination and embedded steel debris detection and a relation between attenuation, defect type, size and annealing state. However, detection of the presence of the brittle intermetallic Al-Fe diffusion layer was not possible due to the sensitivity to the clad Al and steel thickness relative to the thin intermediate bond layer thickness and their similar material properties. Micro sections of all samples were examined to explain the observations. The results suggest a promising use of the S_1 Lamb guided wave mode for online detection of bond defects in serial production of Al/Al-Sn/Al/steel bimetal strips. The content of this chapter is based on the First

Table 5.1: Material properties and dimensions of four-layered Al/Al-Sn/Al/steel plate for wave propagation analysis

Characteristics	Clad Al/Al-Sn/Al layer			Backing layer
Material	Al-1050	AlSn20CuMn	Al-1050	CR steel
Height (mm)	0.04 +/- 0.01	0.51	0.04 +/- 0.01	1.080
Width (mm)	211	211	211	211
Density (g/cm ³)	2.71	3.11	2.71	7.8
Young's modulus (GPa)	70	70	70	203
Poison's ratio	0.33	0.33	0.33	0.293

World Congress on Condition Monitoring conference publication *Detection of bond defects in cold roll bonded Al/Al-Sn/Al/steel sheets using Lamb type guided wave EMATs* (Tallafuss et al., 2017).

5.1 Experimental procedure

5.1.1 Wave propagation analysis

The objective of wave propagation analysis is to understand which wave mode at which frequency and wavelength can be efficiently excited in Al/Al-Sn/Al/steel bimetal plates and what their propagation characteristics (dispersion, phase and group velocity) are. The dispersion curves provide the propagation properties for each different wave mode. The numerical simulation to obtain velocity curves was done by the development partner Innerspec. Table 5.1 summarises the dimensions, density, Young's modulus and Poison's ratio that were considered as input for the numerical simulation. The numerical model was developed in the SAFE method according to section 4.2.2 and is based on the general theory of elastodynamics [105], represented by Navier's displacement equation (4.3) that was introduced in section 4.1.

The obtained phase and group velocity dispersion curves are plotted in Figure 5.1. Figure 5.1(a) shows the mode separation for a range of frequencies. It can be seen that the first two modes A_0 and S_0 are non-converging modes, which means that both modes exist at the same time (quasi symmetrical and quasi anti-symmetrical). This is due to the unsymmetrical material arrangement, in which the three-layered clad Al is approximately 35% of the total plate thickness. Figure 5.1(b) plots the group velocity

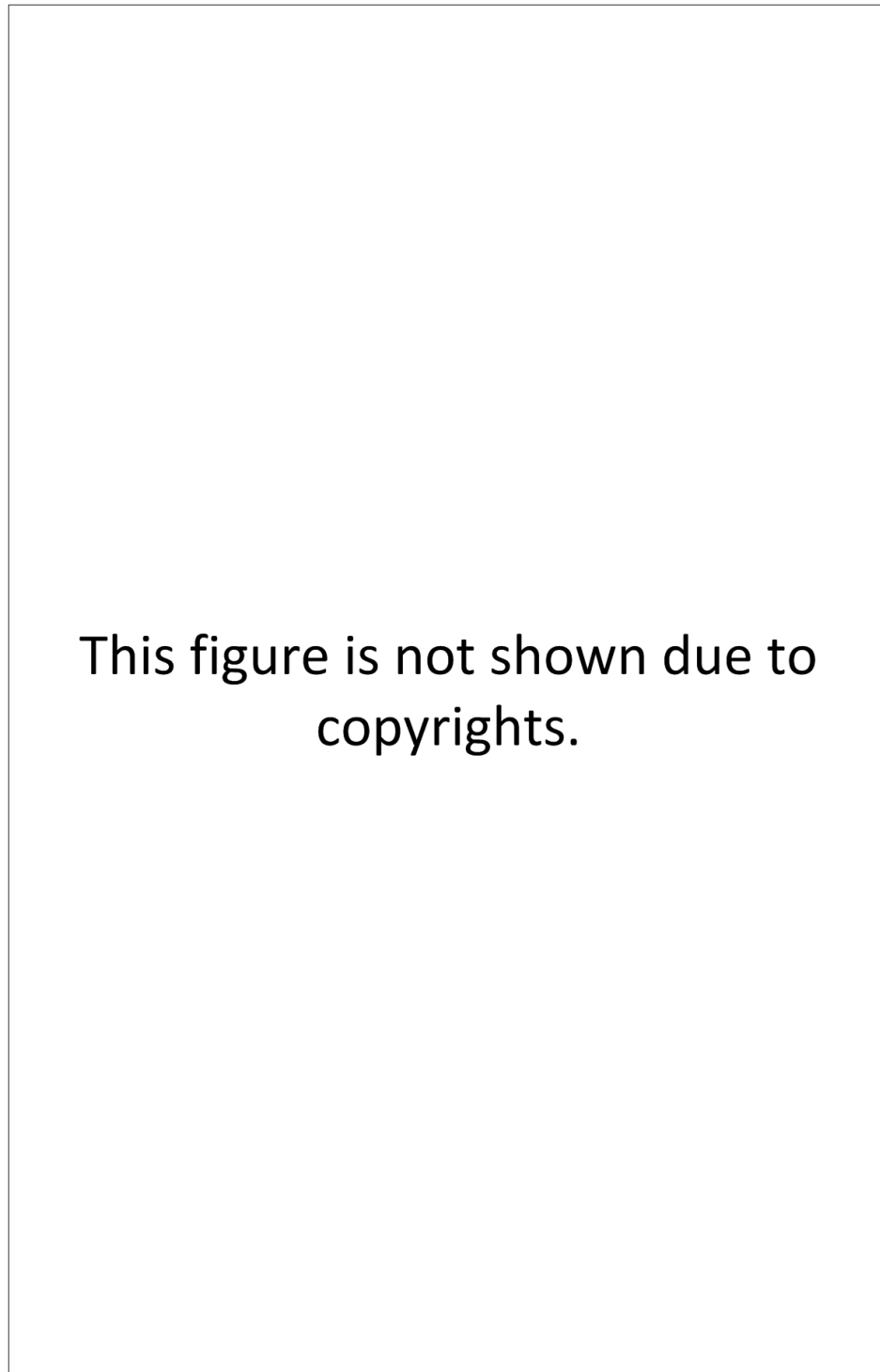


Figure 5.1: (a) Phase velocity and (b) Group velocity dispersion curves with selected mode at 2.3 MHz marked for the sample described in Table 5.1 (supplied by Innerspec)

dispersion curve for the bimetal plate, which provides information about how each mode travels in time depending on frequency.

Each combination of frequency and phase velocity on the dispersion curve represents a possible test mode. From the infinite wave modes, the S_1 wave mode with 2.3 MHz was selected for the experiments. The wave mode was selected according to the procedure described in section 4.6.

5.1.2 Sample preparation

In total 9 test samples were produced for this study. The material properties and dimensions are summarised in Table 5.1. The 1.55-1.65 mm thick bimetal sheets are made of 0.52 mm thick clad Al and 1.08 mm steel layers after 43% reduction during CRB. The width of the samples was 211 mm. The samples were produced in a continuous process as strip and then cut into individual pieces, each approximately 800 mm in length. The test samples production process was identical to serially produced material, except that a specific defect was artificially implanted immediately before CRB, which is shown in Figure 5.2(a) to (h). A template and sieve were used to spread a defined quantity of contaminants in a thin and even layer on the finished steel surface. Figure 4(a) to (d) show Al_2O_3 alumina powder and (e) to (h) steel debris that was implanted. The elongation factor in rolling direction during the CRB reduction was taken into account, thereby the theoretical 2D defect size in the X1-X3 bimetal plate plane after CRB were approximately 1x1 mm, 5x5 mm, 10x10 mm and 15x15 mm size. Alumina was applied to create an artificial delamination, as it was reported that surface oxides interfere with the creation of nascent metal welds, which establish an effective cold weld [32]. Steel debris was implanted, as it is the most frequently detected impurity in serial production that impairs the bond quality as described in chapter 1.2. One sample without artificial defect was produced as a control sample. After all measurements were taken, micrographs of the defects were examined to compare the defect structure with the NDT results.

Micrographic specimens of 15 mm length were punched from the sheet samples using a flywheel press. The micro samples for assessment were hot mounted using Bakelite.

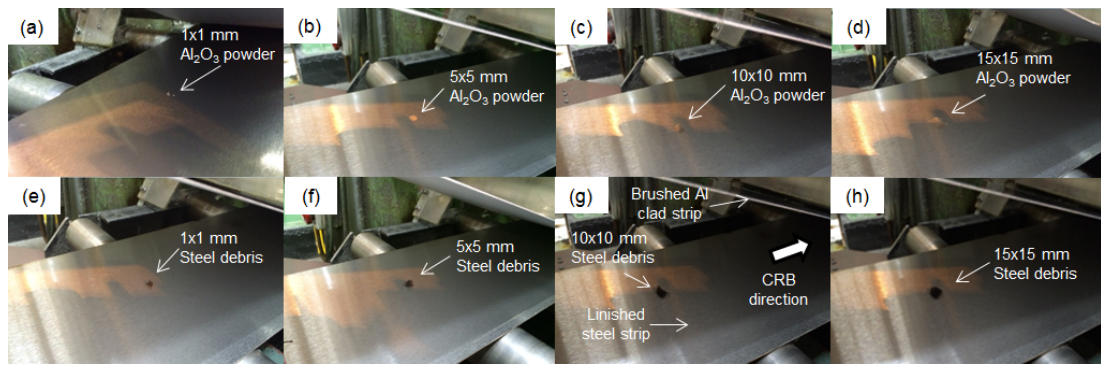


Figure 5.2: Samples with artificially implanted alumina and steel debris defects of different sizes

Al/Al-Sn/Al/steel samples were mounted in the rolling and transverse directions for examination. A thin slice was cut off of the micro block using a disk cutter machine and discarded to remove any deformed areas from specimen pressing. Initial wet grinding was carried out by hand using increasingly finer silicon carbide grinding papers (240, 600, 1200 and 2500 grit). The final grinding operation was always carried out using 2500 grit paper. A good water supply was used at all times to remove all grinding debris. The samples were mechanically polished on automated equipment, using 3 micron diamond suspension for 5 minutes followed by non crystallising colloidal silica, 0.04 micron, for 6 minutes. After each step, the micro block was removed from the pad and washed with clean running water and dried. Optionally, some samples were etched after polishing using Weck's reagent (KMnO₄ 4g, NaOH 1,5g, H₂O to 100ml). Samples were immersed for approximately 30 seconds at room temperature and then washed with clean running water and dried. Metallographic analysis was carried out using standard bright field microscopy at magnifications up to x1000.

5.1.3 Experimental set up

The guided wave experiment was set up in the pitch and catch configuration as shown schematically in Figure 5.3. The transducers were positioned at the steel side. Both transducers were placed so that the wave path propagated along a direction with shallow angle from normal to the edge of the sheet, in order to eliminate the influence of edge reflection.

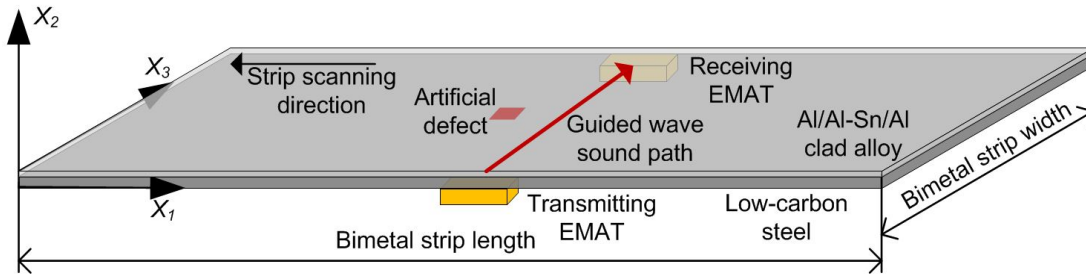


Figure 5.3: Schematic illustration of EMAT transducers used for generating and receiving guided waves propagating through artificial delamination

A data acquisition Pentium-based personal computer (PC) running the Windows XP operating system with temate® software and a field-programmable gate array (FPGA) card with high-speed waveform digitizer was used to generate the excitation signal (Figure 5.4(a)). This signal is sent to a DIO interface, which receives trigger signals from the signal conditioning box and FPGA card and distributes them to the tone burst amplifier (Figure 5.4(b)). In Figure 5.4(c), a temate 2-CH tone burst amplifier with 10KW power is shown that is used to convert the low-voltage signal into a high-power pulse train, which is required to drive the transmitting EMAT to produce a good signal-to-noise ratio. A remote electronics signal conditioning box (Figure 5.4(d)) connects the EMAT sensors with the tone burst amplifier and to the DIO interface. It has an analogue-to-digital converter for signal conversion. A specific holder shown in Figure 5.4(e) was used for all measurements to keep both EMATs perfectly aligned and at a constant distance apart from each other.

5.1.4 Sensor setup

The system was set up and calibrated in a standard procedure before any measurements were taken. The machine setup consists of following steps:

1. Cleaning of transducer from any contaminants such as steel debris or oil from previous inspection. Steel debris acts as ferromagnetic conductors and their magnetostriction produces additional stresses that enhance the signals to higher levels than could be obtained by the Lorentz force alone and should therefore be avoided.

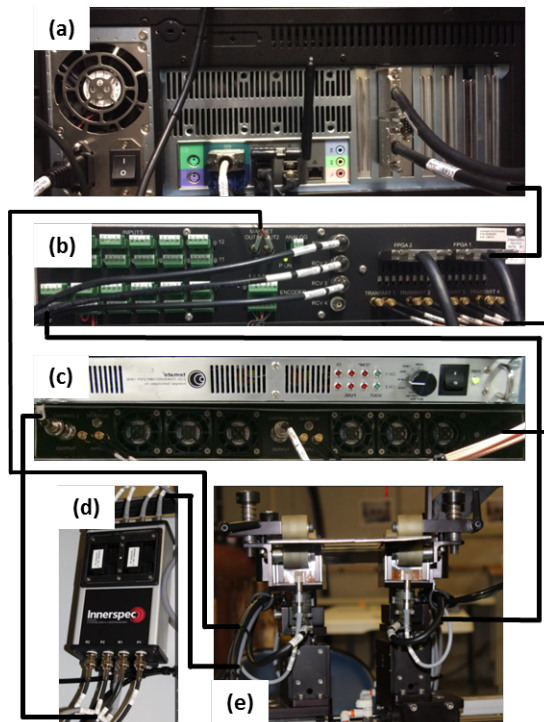


Figure 5.4: Photographs of experimental set-up

2. EMAT transducers consist of a coil wire and a magnet. Putting a foam sponge between magnet and electrical coil provides a constant stand-off between magnet and coil wire so that the alternating electrical currents inducing surface currents (Eddy currents, J) are placed in a uniform magnetic field (B) at a constant distance. Figure 5.5(a) shows the foam sponge placed on top of the magnet. Figure 5.5(b) shows the coil wire placed on top of the foam sponge.
3. A metallic wear surface is placed on top of the coil wire to protect the transducer and prevent any relative movement between material and coil wire. The wear surface is made of a non-magnetic, high wear resistant alloy. The wear plate is shown in Figure 5.5(c).
4. Knurled-head screws (Figure 5.5(d)) were used to secure the wear plate on either side of the transducer.
5. The transducers were connected to the tone burst amplifier by means of cable and plug-in connections as shown in Figure 5.5(e).

6. The same setup was done for transmitting and receiving transducer.
7. Once both sensors were setup, the bimetal was placed on top of the transducers with the steel side facing the wear surface. A clamping mechanism with rollers was used to keep the bimetal plate (or strip) and transducers aligned. This is shown in Figure 5.5(f).
8. Steps 1 to 7 were repeated for every different sample structure and defect type before inspection.

5.2 Results and discussion

5.2.1 Lamb guided wave inspection

An inspection gate was set between 42 and 46 μs to monitor the amplitude changes of the through transmission signal. Figure 5.6(a) shows the A-scan for a defect free location, for which the gain was adjusted so that the reference amplitude was approximately 100%. When the selected S_1 guided wave encounters a delamination or embedded steel debris between the clad Al and steel layer, incident wave energy is converted into radiation energy in all directions, which results in attenuation. As a result, the wave energy that reaches the receiving EMAT transducer at the set inspection gate decreases, which is displayed as lower signal amplitude. Figure 5.6(b) shows an example of a defective sample with embedded 10x10 mm area steel debris for which the sound wave that arrives at the inspection gate between 42 and 46 μs reduced to 30% amplitude due to the wave reflection at the defect. For the selected S_1 mode and the type and size of the artificial defects tested in this study, only signal attenuation was observed. However, mode conversion may occur for other wave modes in the same bimetal plates.

The CRBed samples were tested twice, prior and post annealing. This was done to determine if inspection could take place in-line at the CRB production line, or only after bimetal annealing as final inspection. Figure 5.7(a) shows the A-scan maximum amplitude trace of the defect free sample prior to annealing. Once the gain was set for the un-annealed reference sample to obtain approximately 100% relative amplitude,

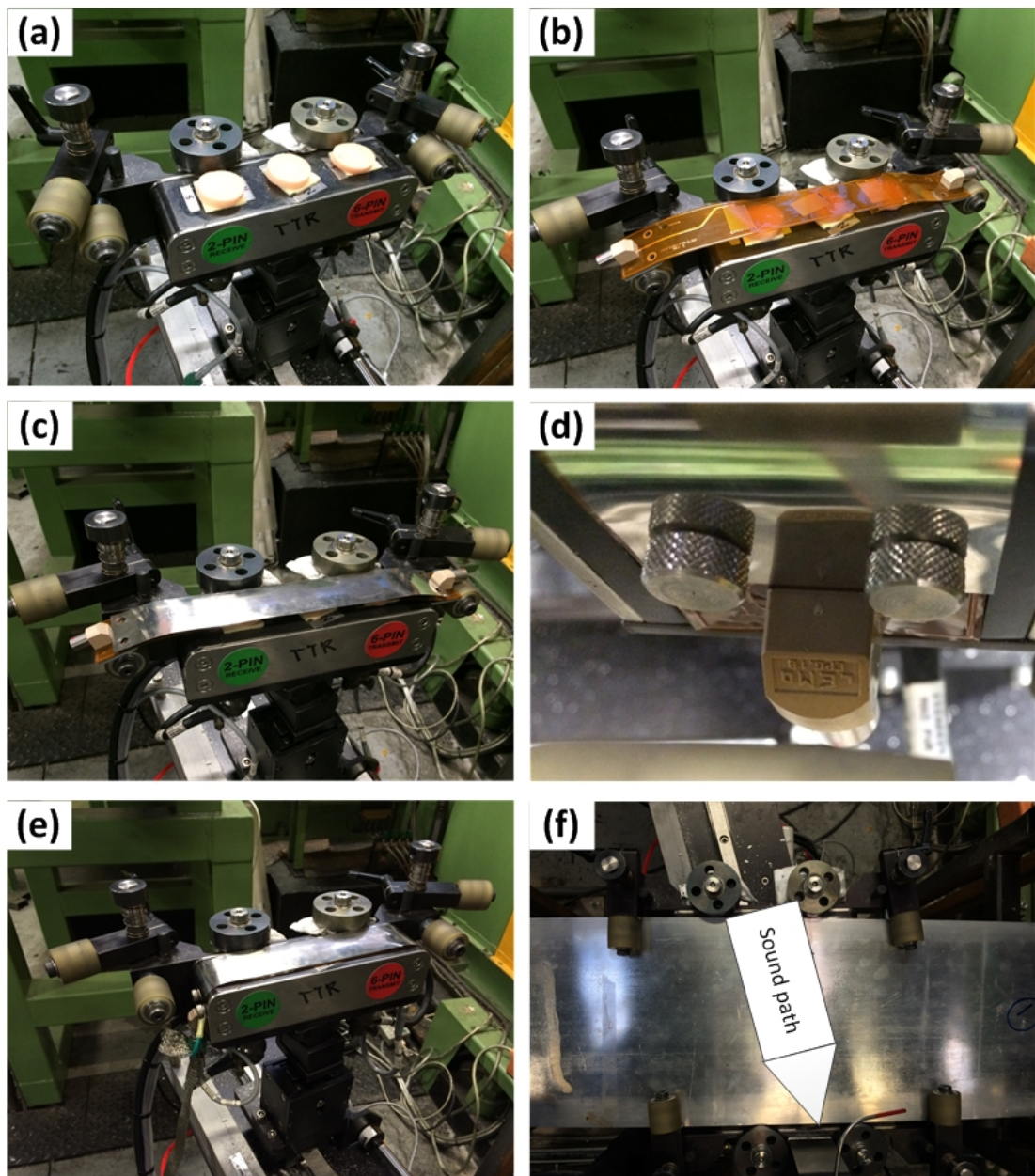


Figure 5.5: Setup of sensors: (a) magnet and foam sponge, (b) coil wire, (c) metallic wear surface, (d) wear plate secured on transducer, (e) assembled transducer and plug-in connection, (f) bimetal clamped on transducers

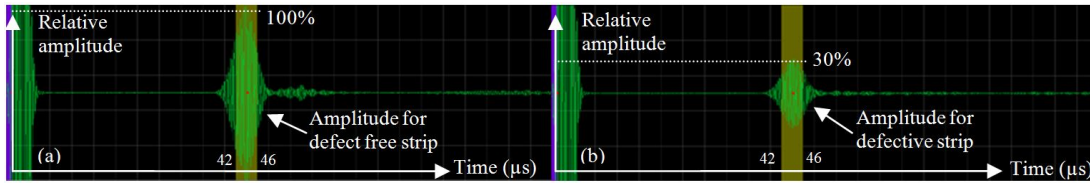


Figure 5.6: A-scan signal for (a) defect free and (b) defective location

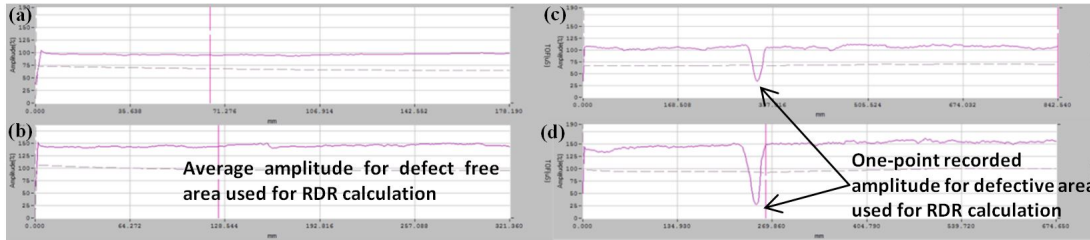


Figure 5.7: A-scan maximum amplitude trace of reference samples: (a) prior and (b) post bimetal annealing, embedded 10x10 mm steel debris defect sample: (c) prior and (d) post bimetal annealing

the inspection parameters were kept the same for all other measurements. Figure 5.7(b) shows the A-scan maximum amplitude trace of the same defect free sample after annealing. Figure 5.7(c) shows the A-scan maximum amplitude trace of the embedded 10x10 mm steel debris defect prior to annealing and in Figure 5.7(d) post annealing. For the reference sample, 175 measurement points were recorded along the sample scan. For the defective samples, the scan was repeated ten times and in each scan the lowest amplitude was recorded.

Figure 5.8 and Figure 5.9 plot the median, the quartiles, and outliers of the amplitude prior and post bimetal annealing that was measured for the reference and all defective samples. Figure 5.8 shows the alumina delamination defect results. There is a correlation between defect size and amplitude drop. The larger the defect size of the delaminations is, the less wave energy arrives at the receiving EMAT. For the smallest 1x1 mm area delamination defect prior annealing, the amplitude dropped by 75% from the 97% mean amplitude for the reference sample to 24%. For the 5x5 mm alumina delamination defect, the amplitude dropped by 90% to 10%, for the 10x10 mm defect by 96% to 4% and for the 15x15 mm defect by 97% to 3% prior annealing. For the reference sample, the amplitude post annealing increased by 49% from 97% to 144% compared

to the un-annealed state, suggesting that post rolling annealing results in lower attenuation. The same relation was observed for most alumina delamination defects, though with a different magnitude. For the 1x1 mm area defect, the post annealing amplitude remained at 24%. For the 5x5 mm area defect, the amplitude increased by 90% from 10% to 19%. For the 10x10 mm area defect, the amplitude increased by 50% from 4% to 6%. However, for the 15x15 mm area defect, the amplitude dropped by 44% from 2.5% to 1.4%. This could be due to electrical noise considering the low magnitude of the received signal strength. For all measurements, prior and post rolling annealing, the RDR increases for larger defects.

Figure 5.9 plots the measured amplitude for samples with embedded steel debris. It was again observed that there is a correlation between defect size and amplitude drop. The larger the defect size of the embedded steel debris is, the less wave energy arrives at the receiving EMAT. For the smallest 1x1 mm area embedded steel debris defect prior annealing, the amplitude dropped by 28% from the 97% mean amplitude for the reference sample to 70%. For the 5x5 mm embedded steel debris defect, the amplitude dropped by 56% to 43%, for the 10x10 mm defect by 62% to 31% and for the 15x15 mm defect by 97% to 3% prior annealing. The same reference sample was considered, for which the amplitude post annealing increased by 49% from 97% to 144% compared to the un-annealed state. Also for embedded steel debris defects the same relation was observed with a different magnitude, except for the 10x10 mm area defect. For the 1x1 mm area embedded steel debris defect, the post annealing amplitude increased by 33% from 70% to 93%. For the 5x5 mm area defect, the amplitude increased by 28% from 43% to 55%. For the 10x10 mm area defect, the amplitude remained at 30%. For the 15x15 mm area defect, the amplitude increased by 270% from 2.5% to 9.3%. Due to the low magnitude of the received signal strength, this could be caused by electrical noise. For all measurements for embedded steel debris, prior and post rolling annealing, the RDR increases for larger defects. Table 5.2 summarises the measurement results and RDR.

For automatic online strip inspection, it is necessary to set an alarm threshold, which classifies the material as defective if the amplitude falls below a certain thresh-

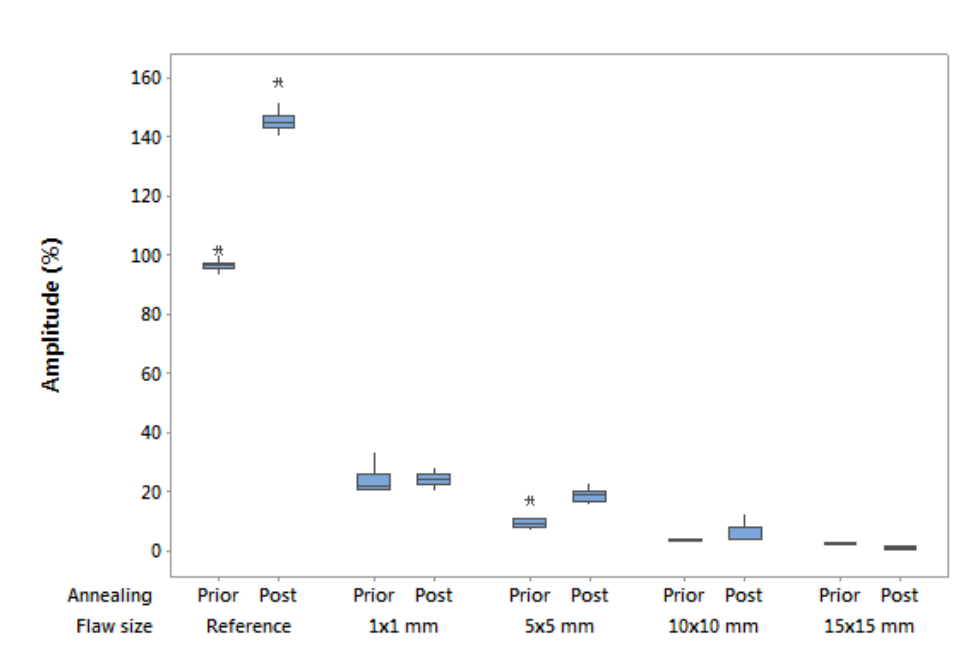


Figure 5.8: Signal amplitude measured prior and post bimetal annealing for artificially implanted alumina defects in different sizes

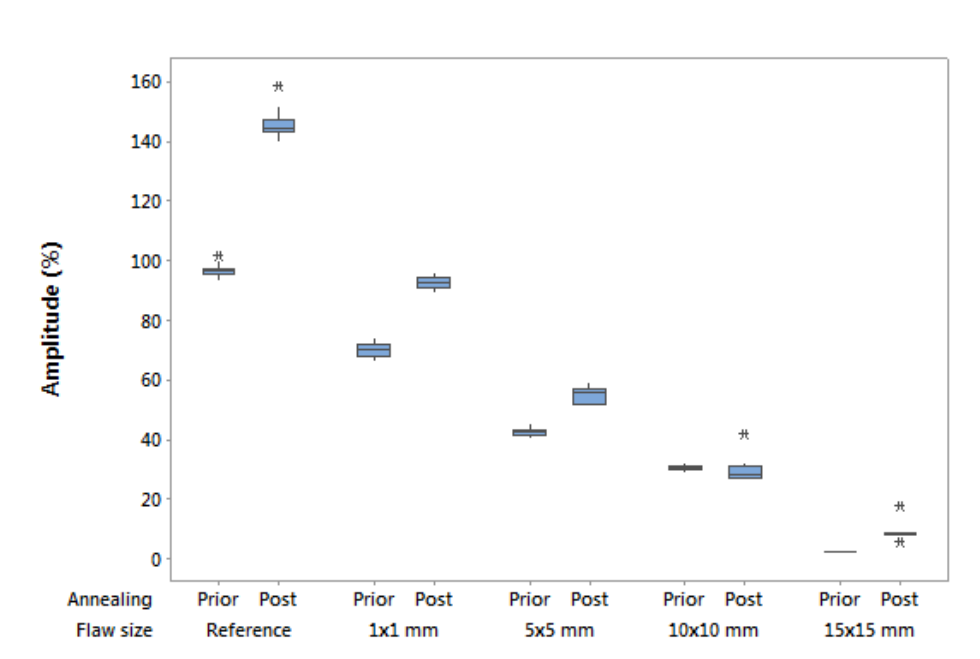


Figure 5.9: Signal amplitude measured prior and post bimetal annealing for artificially implanted steel debris defects in different sizes

Table 5.2: Statistical and RDR sample data

Measurement	Reference		Delamination defect								Embedded steel debris defect							
			1x1 mm		5x5 mm		10x10 mm		15x15 mm		1x1 mm		5x5 mm		10x10 mm		15x15 mm	
Size	-	-	1x1 mm		5x5 mm		10x10 mm		15x15 mm		1x1 mm		5x5 mm		10x10 mm		15x15 mm	
Annealing	prior	post	prior	post	prior	post	prior	post	prior	post	prior	post	prior	post	prior	post	prior	post
N	175	175	10	10	10	10	10	10	10	10	10	10	10	10	10	10	10	10
Mean (μ)	96.7	144.1	23.9	24.3	9.9	18.9	3.9	6.1	2.5	1.4	70.1	92.7	42.7	55.1	30.6	30.1	2.5	9.3
std(X)	2.0	2.9	4.2	2.4	2.9	2.3	0.6	3.3	0.2	0.4	2.6	2.2	1.5	2.8	0.9	4.7	0.3	3.3
RDR	-	-	4.0	5.9	9.7	7.6	25.1	23.8	38.2	106.7	1.4	1.6	2.3	2.6	3.2	4.8	38.1	15.5

old. Any variation in signal amplitude due to local material property changes, external factors or noise should not cause false alarms. The required RDR for this application needs to get established in online experiments. In the only known industrialised online EMAT guided waves inspection system for brass/copper/brass three-layered composites to date, an alarm threshold of 65% of the normal amplitude was used [72]. The calculated RDR values prior and post annealing for the delamination and embedded steel debris defects are summarised in Table 5.2. Considering a 65% alarm threshold and the obtained measurement data under laboratory conditions, all delamination type defects would be detectable with the inspection system, prior as well as post bimetal annealing. For embedded steel debris defects, all sizes would be detectable prior and post bimetal annealing, except for the smallest 1x1 mm area defect, for which the amplitude dropped by only 28% prior annealing. Post annealing, the amplitude for the smallest 1x1 mm defect dropped to 64% of the normal amplitude. The results suggest that online inspection can be done either prior or post annealing to qualitatively indicate the presence of delamination or embedded steel debris defects, with the only exception being the 1x1 mm area embedded steel debris defect prior annealing, which would not be detectable. However, the percentage of normal amplitude as alarm threshold that is required for this application needs to be verified in experiments, in which the prototype inspection system is installed online.

5.2.2 Wave interaction with defects

Microsections of the test samples were taken to ascertain that the nature of the artificial defects is similar to real defects in regards to the defect type, location, size and orientation, which influences the amount of sound energy that is reflected, when the

guided wave sound path encounters the defect. Furthermore, the different attenuation for delamination and embedded steel debris defects need to be explained. An optical microscope with 100x and 200x magnification was used to inspect the bond line. The cross sections were taken in the X1-X2 rolling direction plane. Figure 5.10(a) is a micrograph of the reference sample, which was used to obtain the reference amplitude. The bond line is free from aligned linear porosity, continuous oxides and delamination, which confirms that the reference amplitude corresponds to a flawless sample. The Al-1050 to steel delamination in Figure 5.10(b) is caused by a thin alumina layer while Figure 5.10(c) illustrates a real delamination from serial production. In both cases, the continuous delamination spreads about 800 μm in rolling direction and has a similar volume and shape that acts as sound reflector. Figure 5.10(d) shows embedded steel debris between the Al-1050 and steel layer, which was artificially implanted. In Figure 5.10(e), embedded steel debris that was found in serial production is shown. In both samples, the length of the embedded steel debris exceeds 1000 μm in the rolling direction. It appears that in both cases the steel debris is bonded to the Al-1050 foil, but not to the steel layer. When comparing the embedded steel debris and delamination defects, the void volume of the delamination defect is significantly larger. The defect volume of the embedded steel debris defect that acts as reflector can be described as the volume of the debris itself, but there is no void between the debris and the clad Al layer, only between debris and steel layer. This explains why the reflected ultrasound wave energy is higher for the delamination defect compared to the embedded steel debris defect. When the ultrasonic guided wave counters the boundary of the delamination void, the defect acts as reflector due to the different density, Young's modulus and Poisson's ratio of the void compared to the clad Al and steel. This causes destructive interferences, which results in attenuation and amplitude drop. Regarding the embedded steel debris defect, for which the layers are mostly physically in contact and almost no void exists, only a relatively small proportion of the ultrasound wave energy is reflected when the sound wave encounters the defect, because the embedded steel debris material properties are similar to the steel layer itself. The microscopic assessment of the samples suggests that the artificially implanted and real defects, which were randomly found

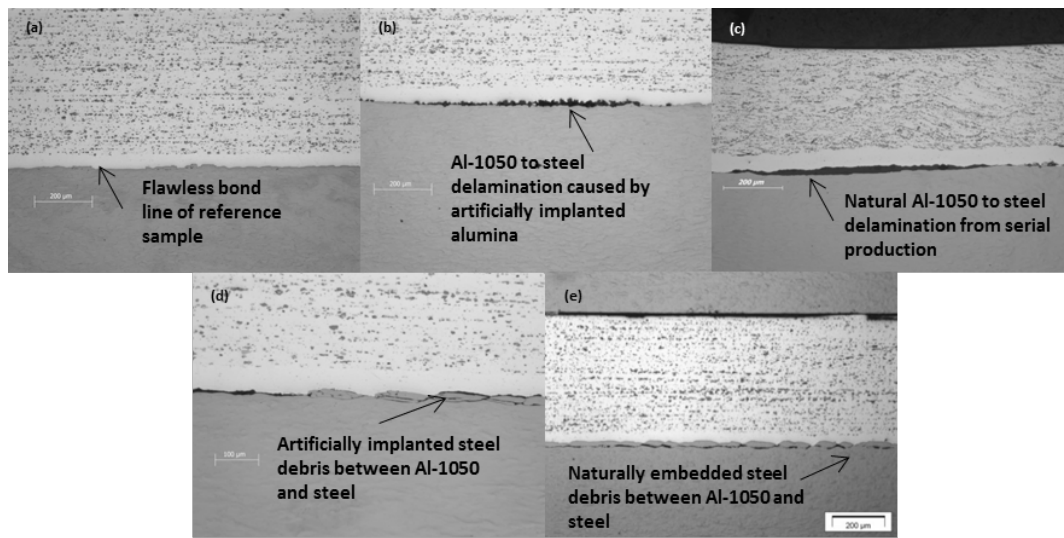


Figure 5.10: Optical micrographs: (a) reference sample, (b) artificial 5x5 mm delamination, (c) natural delamination, (d) artificial 5x5 mm embedded steel debris and (e) natural embedded steel debris

in serial production, have similar characteristics and therefore their ultrasound wave reflector properties are representative for real defects.

5.2.3 Effect of post rolling annealing on attenuation

The reference sample amplitude increased by 49% due to post rolling annealing. Analysing the structural changes in the material provides an explanation. During rolling, the grains become elongated and flattened, which changes the grain aspect ratio. Figure 5.11(a) shows the elongated grain structure in the rolling direction, and Figure 5.11(b) the flattened grain structure in the transverse direction. These micrographs were captured prior to annealing. The elongated grain boundaries cause reflection of the ultrasound sound wave and therefore increased attenuation [8]. During post rolling annealing, the grain structure of the work hardened clad Al is recrystallized and diffusion between the steel and Al-1050 layer takes place to enhance the metallurgical bond. Figure 5.11(c) shows the recrystallized grain structure in the rolling, and Figure 5.11(d) in transverse direction, which were captured post rolling annealing. The difference in the grain structure is apparent. The recrystallized grain structure reduces the elastic scattering because of a smaller surface of the reflector, hence the transmitted energy of

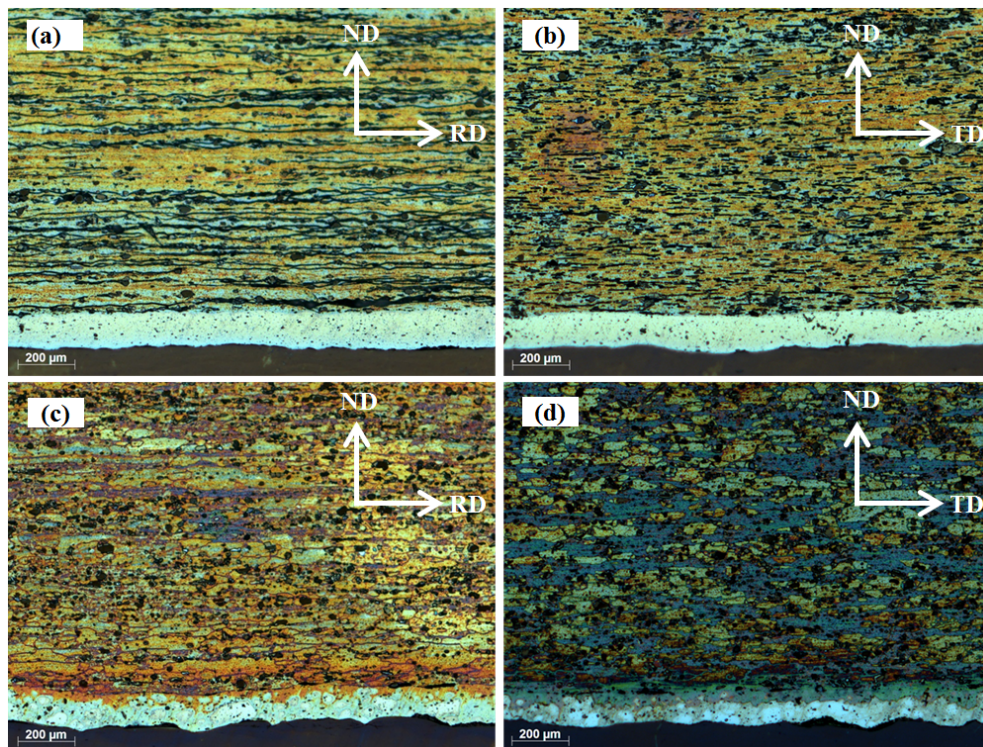


Figure 5.11: Optical micrographs: Al-Sn alloy (a) elongated structure in rolling direction and (b) flattened structure in transverse direction prior to annealing, (c) recrystallized structure in rolling direction and (d) transverse direction post annealing (Etchant: Wecks)

the ultrasound wave increases, which explains the amplitude increase post annealing. During CRB, the grain structure of the steel is also elongated, however the annealing temperature is too low to recrystallize the steel grain structure and therefore steel post rolling annealing does not affect signal attenuation in the bimetal system.

If the solution heat treatment or annealing time is exceeded, there is the risk of the formation of a brittle intermetallic layer that forms at the bond line. Three intermetallic phases Al_2Fe , Al_5Fe_2 and $Al_{13}Fe_4$ exist when the steel diffuses into the aluminium layer, as Fe has a high solubility in Al [5]. Plant internal trials concluded that 3-5 μm thick intermetallic layer is detrimental to the bond, even though this thick layer only forms at enhanced solution heat treatment temperatures and/or times. A sample with about 5 μm thick Al-Fe intermetallic layer was produced and inspected with the same experimental setup. As a result, the guided wave that interrogates the entire

plate could not detect the presence of the brittle intermetallic layer, as there was no measurable amplitude difference compared to a normally solution heat treated bimetal sample without Al-Fe intermetallic layer. Lowe et al. [137] studied the bond inspection of diffusion bonded titanium sheets, which have no evidence of a bond line in the perfect bonding case, but if oxygen or nitrogen is present at the bond line during the high-temperature bonding process, an unwanted brittle titanium phase layer forms. Their study was concerned with the detection of the presence of the unwanted layer. It was concluded that the Lamb wave technique was not applicable for the detection of the unwanted intermetallic layer, due to the strong sensitivity to the material properties and thickness of the parent materials and insensitivity to the bond line layer. The same explanation applies for Al/Al-Sn/Al/steel bimetal. The dispersion curves and sound propagation behaviour is practically only influenced by the properties of the clad Al and steel material layers and is insensitive to the embedded layer, because the volume of the embedded layer is insignificant compared to the lining and steel layer thickness. Additionally, the Al-Fe density, Young's modulus and Poisson's ratio are relatively similar to the parent materials Al-Sn and steel compared to a void. This leads to the conclusion that diffusion between the clad Al and steel, such as the 5 μm thick brittle Al-Fe intermetallic layer, has no measurable influence on the sound attenuation. Therefore the amplitude increase post annealing can be primarily attributed to the recrystallization of the Al-Sn alloy.

5.3 Conclusions

Lamb wave modes for Al/Al-Sn/Al/steel bimetal were calculated with the SAFE method. The S_1 mode (2,300 kHz frequency, 2.54 mm wavelength) that is efficiently excited in the Al/Al-Sn/Al/steel bimetal system was first selected based on FEM simulation and then verified in an empirical study, using defect free and defective samples. A sample production technique was developed to produce artificially implanted defects, which have ultrasound properties that are comparable to real defects. The selected S_1 wave mode is reasonably sensitive to the artificial defects and measurement results showed good repeatability. An explanation for the attenuation decrease in defect free sam-

ples post rolling annealing was provided, which is that quasi equiaxed grains produced by post rolling annealing cause less elastic scattering than elongated grains that are present in the clad Al prior to rolling annealing. It was also found that Lamb waves are insensitive to diffusion between the clad Al and steel layers. It was observed that amplitude attenuation depends on the type and size of the bond defects. Based on a 65% of normal amplitude alarm threshold, the results suggest that delamination defects with approximately 1x1 mm area can be detected prior and post rolling annealing, embedded steel debris with 1x1 mm area can be detected post annealing and 5x5 mm area embedded steel debris can be detected prior to rolling annealing. Therefore bond inspection could be done either during production prior rolling annealing based on the detectable defect size, or as final inspection post rolling annealing. Further research is required to verify the alarm threshold percentage when the inspection system is installed online in a continuous strip inspection line and to confirm that the guided wave inspection technique is capable of inspecting 100% material volume at the required line speed. The study results provide encouraging signs that the investigated inspection technique can be employed in serial production of Al/Al-Sn/Al/steel bimetal strips.

Chapter 6

Implementing an online bond quality inspection system for cold roll bonded Al/Al-Sn/Al/steel strips

In this chapter a prototype online bond inspection system for Al/Al-Sn/Al/steel strips is introduced to detect bond defects that occur in the CRB process of strips. The transmitting and receiving EMAT probes inspect 100% material volume whilst strips are processed continuously. The inspection signals are processed in real time and stored for post-processing. Serial production strips with good bond as well as those with defects along the bond line were inspected for rigorous testing of the prototype machine. The inspection results were statistically analysed to determine an alarm threshold for serial inspection. The most important result is that the guided waves are sensitive enough to use practical NDT with only 0.5% false alarm rate to detect all bond defects, which nowadays can only be detected with a destructive peel-off test. Previously, the detection of all kinds of bond defects would have lead to unreasonable levels of scrap due to false alarms. The application of this prototype EMAT inspection system to an industrial strip processing line shows that online detection of significant defects in

Chapter 6. Implementing an online bond quality inspection system for cold roll bonded Al/Al-Sn/Al/steel strips

CRBed Al/Al-Sn/Al/steel strips in a harsh serial production environment is possible. Improvements are proposed to address the issues that occurred during inspection trials and to aid in the design of a more robust mechanical machine for the industrialisation of an EMAT inspection system. The content of this chapter is based on the journal publication *Implementing an online bond quality inspection system for cold roll bonded Al/Al-Sn/Al/steel strips using guided wave EMATs* (Tallafuss et al., 2018) published in *Insight Non-Destructive Testing and Condition Monitoring*.

6.1 General inspection system design

6.1.1 System requirements

The system must meet the following performance characteristics for online inspection:

1. Industrial CRB capability (rolling speed: 5 m/min to 15 m/min and a harsh manufacturing environment, for example vibrations and shape deviations during processing)
2. Ability to detect serial production bond defects
3. Maximum strip width: ~ 300 mm
4. Minimum strip width: ~ 170 mm
5. Maximum strip thickness: ~ 4 mm
6. Minimum strip thickness: ~ 1.5 mm
7. Display and export of historic records.

6.1.2 General design of system

Figure 6.1 shows the strip processing line used for the experiments. The pneumatic brake disc uncoiler provides back tension. The roller table avoids strip oscillation. A rolling mill guides strips to the EMAT probes. The transmitting and receiving probes, remote signal conditioning boxes, pneumatic and electrical components are mounted

Chapter 6. Implementing an online bond quality inspection system for cold roll bonded Al/Al-Sn/Al/steel strips

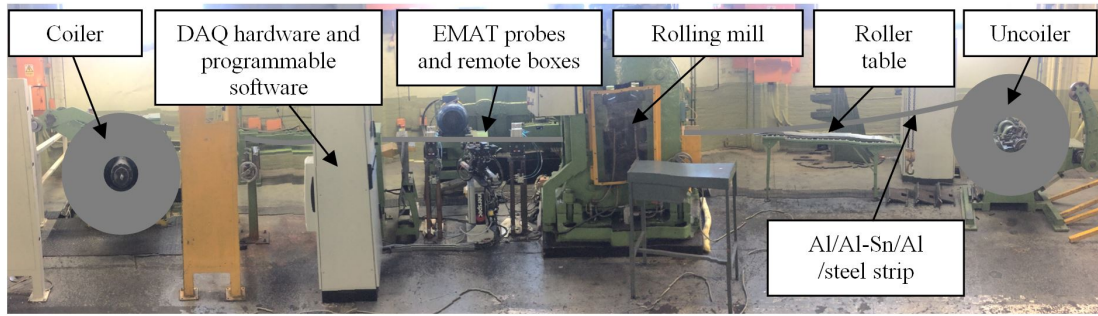


Figure 6.1: EMAT prototype inspection line for Al/Al-Sn/Al/steel strips

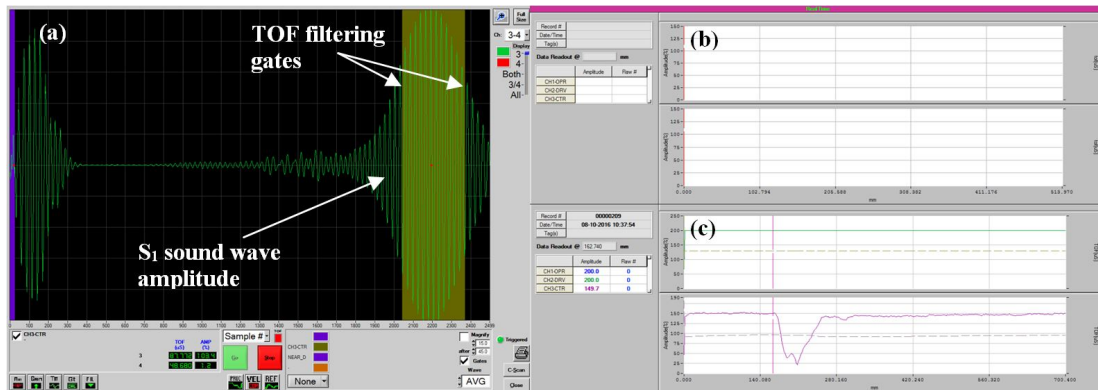


Figure 6.2: Temate software: (a) A-scan oscilloscope; (b) online A-scan maximum amplitude trace; (c) A-scan maximum amplitude recall panel

onto a probe assembly frame, which is positioned directly below the strip. Pneumatics provide passive compliance between probes and moving strip. Wear plates that are in sliding contact with the steel cover the probes. Remote signal conditioning boxes process and connect the probes to the Data acquisition (DAQ) hardware and computer with programmable temate® software. A coiler provides front tension and coils strips after inspection.

Signals are processed and displayed in real time. Figure 6.2 shows the interface of the temate software. Figure 6.2(a) illustrates the A-scan oscilloscope that is used to verify the selected wave mode, adjust gains and set signal inspection gates. Figure 6.2(b) represents the maximum amplitude within the TOF filtering gates along the strip in real time during inspection. Once inspection is completed, the results can be retrieved in the recall panel (Figure 6.2(c)). In these modes, measurement locations, signal amplitude, indication of the pass/fail status depending on alarm threshold and

Chapter 6. Implementing an online bond quality inspection system for cold roll bonded Al/Al-Sn/Al/steel strips

current strip identification data can be analysed. The ultrasound signals are measured in voltage and are displayed as relative amplitude as a percentage of the reference amplitude for a defect-free sample. The gain remains unchanged for all measurements.

6.2 Experimental procedure

6.2.1 Guided wave propagation and analysis

The inspection experiments were set up in the pitch and catch configuration using the same DAQ hardware as introduced in section 5.1.3. The physical principle of the guided wave inspection was introduced in chapter 4. The empirical relationship between bond defects and guided waves in all experiments was when guided waves encounter a bond defect, the defect causes destructive interference which converts incident wave energy into radiation energy in all directions, which results in attenuation. The remaining wave energy that propagates to the receiving EMAT transducer decreases, which is measured and shown as a lower signal amplitude in the A-scan. During inspection, the maximum amplitude within the TOF filtering gates is used to indicate defective material with the attenuation method. Table 6.1 details the dimensional and material characteristics of the samples that were used for the online feasibility study. The Lamb phase and velocity curves for these samples were calculated with the SAFE method according to chapter 4 and the wave modes were selected according to the procedure in section 4.6. Since the prototype system will be industrialised as a commercial product, the wavelengths and frequencies of the selected S_1 wave modes are not revealed. The wavelength was controlled by the period of the meander coil.

6.2.2 Sample production

All Al/Al-Sn/Al/steel strip samples in this study were produced on the CRB production line at MAHLE Kilmarnock, Scotland according to the manufacturing process described in chapter 2. Table 8.2 summarises the test samples in this study. SP-R1 and SP-R2 are serial production reference samples that were produced without defects. SP-D is an 80 m long serial production strip with Al-1050 sacrificial side foil blisters. Artificial

Chapter 6. Implementing an online bond quality inspection system for cold roll bonded Al/Al-Sn/Al/steel strips

Table 6.1: Material properties for Al/Al-Sn/Al/steel bimetal strips and employed guided wave modes

Material type	Characteristics	Clad Al/Al-Sn/Al			Backing material	Employed wave mode
I	Material	Al-1050	AlSn20CuMn	Al-1050	CR steel	S_1
	Height (mm)	0.04 +/- 0.01	0.64	0.04 +/- 0.01	2.06	
	Width (mm)	206	206	206	206	
	Density (g/cm ³)	2.71	3.12	2.71	7.8	
	Young's modulus (G)	70	70	70	203	
	Poison's ratio	0.33	0.33	0.33	0.293	
II	Material	Al-1050	AlSn6Si2CuNiMnV	AlMnSi	CR steel	S_1
	Height (mm)	0.04 +/- 0.01	0.52	0.04 +/- 0.01	1.58	
	Width (mm)	279	279	279	279	
	Density (g/cm ³)	2.71	2.82	2.73	7.8	
	Young's modulus (G)	70	70	70	203	
	Poison's ratio	0.33	0.33	0.33	0.293	
III	Material	Al-1050	AlSn10Si4Cu	Al-1050	CR steel	S_1
	Height (mm)	0.04 +/- 0.01	0.91	0.04 +/- 0.01	2.19	
	Width (mm)	206	206	206	206	
	Density (g/cm ³)	2.71	2.90	2.71	7.8	
	Young's modulus (G)	70	70	70	203	
	Poison's ratio	0.33	0.33	0.33	0.293	
IV	Material	Al-1050	AlSn6Si2CuNiMnV	Al-1050	CR steel	S_1
	Height (mm)	0.04 +/- 0.01	0.65	0.04 +/- 0.01	1.45	
	Width (mm)	227	227	227	227	
	Density (g/cm ³)	2.71	2.82	2.71	7.8	
	Young's modulus (G)	70	70	70	203	
	Poison's ratio	0.33	0.33	0.33	0.293	

Chapter 6. Implementing an online bond quality inspection system for cold roll bonded Al/Al-Sn/Al/steel strips

defects (ADs) were implanted in the AD strip. The AD-T sample is the first 28 m in the AD strip, which were bonded when the mill roll temperature was only 42°C compared to the required temperature of above 100°C. Once at temperature, the next 28 m were bonded under normal process parameters to obtain a good bond reference sample (GBR). Samples AD-1x1D and AD-5x5D contain artificially implanted 1x1 mm and 5x5 mm area delaminations (D), by spreading a thin alumina powder layer on the steel surface before CRB. Steel debris (SD) was artificially implanted in samples AD-1x1SD and AD-5x5SD. The clad Al and steel strips were misaligned when entering the CRB mill to produce a sample with run-off alloy (ROA) on one edge of the strip and bare steel on the other side. The steel surface finishing before CRB in sample AD-ASS was intermittent due to a removed 50 x 150 mm area location in the rotating finishing belt, which produced locally altered steel sanding (ASS) parameters. Rolled-in alloy slivers (RAS) and rolled-in brush bristles (RBB) were artificially implanted between the clad Al and steel in the AD-RAS and AD-RBB samples. In order to obtain altered clad Al brushing (ACB), 50 mm of the wire brush width were deactivated across the circumference by bulging the bristles so as not to mechanically activate the clad Al surface. For reduced rolling reduction (RRR), the CRB thickness reduction was set to only 30% instead of the standard thickness reduction of >40%. For each sample in the AD strip, approximately 0.5 m length of the clad Al before and after each defect was ball-indented to mark scrap and locate the position of the artificial defect. When the bonding production process stops with strip between the roll gap, this causes an imprint in the strip, which is also scrap. This imprint is present in the AD strip whenever the line was stopped to implant an artificial defect. These roll mill stops (RMS) were also inspected. In between each artificial defect segment, approximately 10 m good bond strip was produced to keep the work rolls at temperature. The production of the artificially implanted defects immediately before CRB is shown in Figure 6.3.

6.2.3 Clad Al lining adhesion peel-back test

The clad Al adhesion peel-back test was used to obtain pass/fail measurement data for the test samples in this study to compare the results with the guided wave inspection.

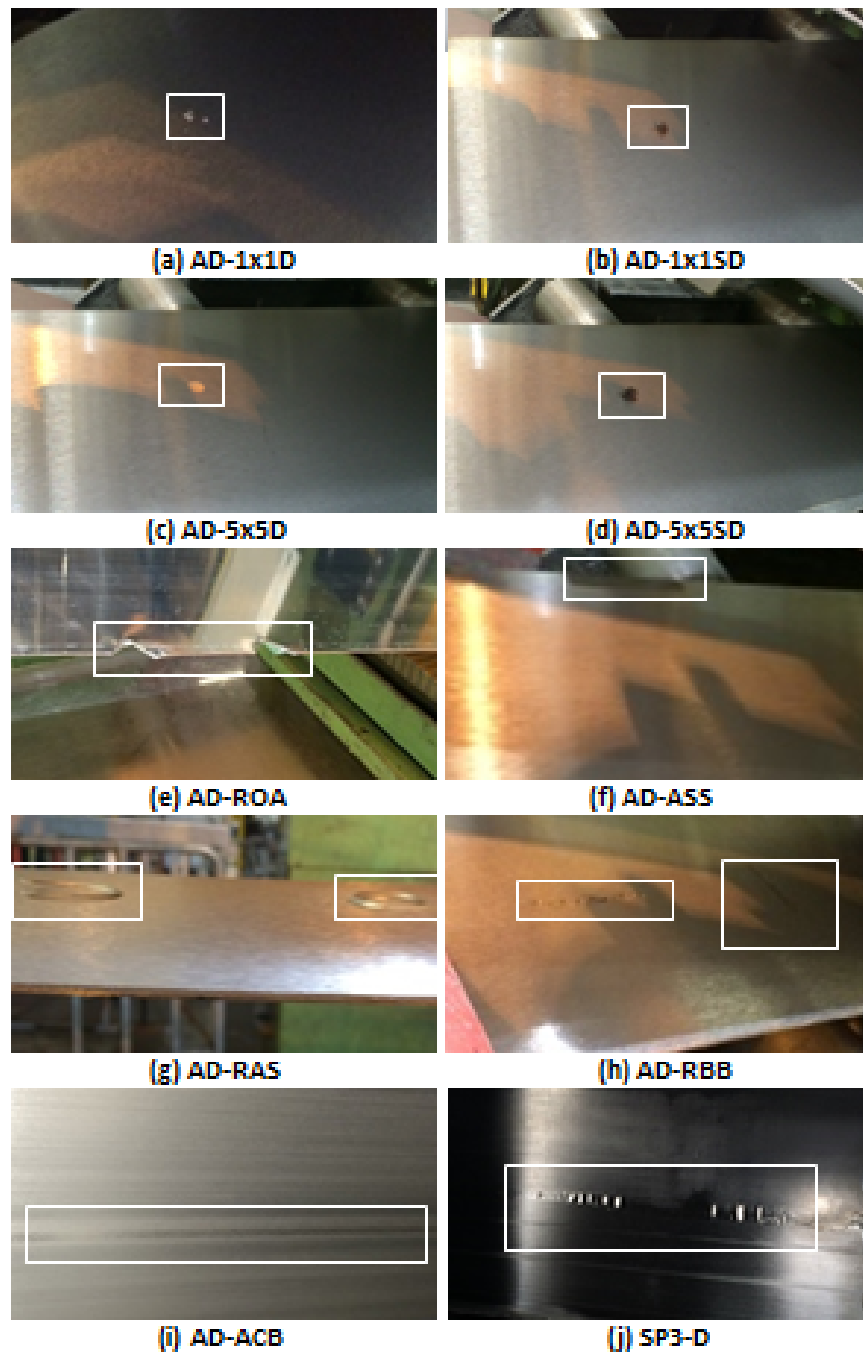


Figure 6.3: Defects in cold roll bonded Al/Al-Sn/Al/steel strips (a) 1x1 mm alumina, (b) 1x1 mm steel debris, (c) 5x5 mm alumina, (d) 5x5 mm steel debris, (e) run-off clad Al, (f) altered steel sanding, (g) rolled-in clad Al slivers, (h) rolled-in brush bristles, (i) altered clad Al brushing, (j) Al-1050 foil blisters on sacrificial side

Table 6.2: Al/Al-Sn/Al/steel strip samples for online inspection

Strip	Sample #	Sample reference	Nominal alloy composition	Dimensions (clad Al/steel/width) (mm)	Strip length (m)	Approx. position from start (m)	Sample preparation
SP1	1	R1	AlSn20CuMn	0.64/2.06/206	320	-	Serial production reference 1
SP2	2	R2	AlSn6Si2CuNiMnV	0.52/1.58/279	390	-	Serial production reference 2
SP3	3	D	AlSn10Si4Cu	0.91/2.19/206	80	continuous	Serial production defect: Al-1050 blisters
AD	4	AD-T	AlSn6Si2CuNiMnV	0.65/1.45/227	160	0	Roll temperature 42°C
AD	5	AD-GBR	AlSn6Si2CuNiMnV	0.65/1.45/227	160	28	Good bond reference
AD	6	AD-1x1D	AlSn6Si2CuNiMnV	0.65/1.45/227	160	55	1x1 mm area delamination
AD	7	AD-5x5D	AlSn6Si2CuNiMnV	0.65/1.45/227	160	68	5x5 mm area delamination
AD	8	AD-1x1SD	AlSn6Si2CuNiMnV	0.65/1.45/227	160	81	1x1 mm area steel debris
AD	9	AD-5x5SD	AlSn6Si2CuNiMnV	0.65/1.45/227	160	90	5x5 mm area steel debris
AD	10	AD-ROA	AlSn6Si2CuNiMnV	0.65/1.45/227	160	100	Run off alloy
AD	11	AD-ASS	AlSn6Si2CuNiMnV	0.65/1.45/227	160	103	Altered steel sanding parameters
AD	12	AD-RBB	AlSn6Si2CuNiMnV	0.65/1.45/227	160	116	Rolled in brush bristles
AD	13	AD-RAS	AlSn6Si2CuNiMnV	0.65/1.45/227	160	117	Rolled in alloy slivers
AD	14	AD-ACB	AlSn6Si2CuNiMnV	0.65/1.45/227	160	140-142	Altered clad Al brushing parameters
AD	15	AD-RRR	AlSn6Si2CuNiMnV	0.65/1.45/227	160	144	Reduced rolling reduction to 30%
AD	16	AD-RMS	AlSn6Si2CuNiMnV	0.65/1.45/227	160	various	Rolling mill stop during bonding

The destructive test was introduced in section 1.2.1.

6.3 Results and discussion

6.3.1 Data interpretation

Figure 6.4 illustrates the measurement data interpretation approach in this study. The complete strip length of samples SP1-R1, SP2-R2 and SP3-D was scanned in one maximum amplitude trace without stopping the processing line. This is schematically illustrated in Figure 6.4(a) to (c). The same procedure was applied for samples AD-GBR, AD-T, AD-ASS, AD-ACB and AD-RRR, since the artificially implanted defects for these samples are several metres long.

For all other AD sample defects, which were artificially implanted at just a single position, one maximum amplitude trace was gathered per defect segment. Each segment consisted of approximately 10 m strip with good bond as reference and a 0.5 m ball indentation scrap marking to indicate the beginning of the artificial defect, followed by the artificially implanted defect and ending with 0.5 m ball indentation. Within each maximum amplitude trace, the artificially implanted defect scan was repeated 50 times to test the repeatability of the inspection system. The AD samples maximum

Chapter 6. Implementing an online bond quality inspection system for cold roll bonded Al/Al-Sn/Al/steel strips

amplitude trace in Figure 6.4(d) shows 100 amplitude drops at the position of the artificially implanted defect, since recording continued whilst the strip was reversed. Only the measured amplitude in the forward direction was used for statistical analysis, to control the strip front tension and eliminate any influence of lift-off between EMAT probe and strip. Before every measurement, the system was calibrated according to the procedure in section 4.6.

A lower threshold of the normal amplitude level must be defined to detect bond defects. This threshold must avoid false alarms due to electrical noise and local material property variation, but still detect all potential defects. Therefore, the mean amplitude for defects must be statistically significantly different from the good bond amplitude. If the amplitude intervals overlap, then no unambiguous differentiation between defective and good material is possible. In this case, setting the level of the threshold is a trade-off between not detecting real defects and reducing the false alarm rate. Sample SP3-D in Figure 6.4(c) shows that the signal amplitude drops below the alarm threshold at the location where the Al-1050 foil detached from the AlSn alloy, which indicates the presence of defects. Since the exact locations and quantities of delamination spots in the serial production sample SP3-D were unknown, it was not considered in the statistical analysis.

6.3.2 Results

Figure 6.5 shows a boxplot of the SP and AD strip samples to compare the central tendency and variability of the measured amplitude for various defects. The interquartile range (IQR) from the first quartile (Q1) to the third quartile (Q3) shows that the middle 50% measurement points of all defects have a narrow spread. The IQR of the reference samples R1, R2 and GBR overlap. This was expected, since the reference samples were used to calibrate the system. All of the other measured amplitudes are normalised as the same gain was used to inspect the reference and defective samples. The range of the reference samples from the smallest to the largest amplitude value, including outliers, is from about 55% to 120% normalised amplitude. It can be seen that the combined interval of samples R1 and R2 completely contains the amplitude

Chapter 6. Implementing an online bond quality inspection system for cold roll bonded Al/Al-Sn/Al/steel strips

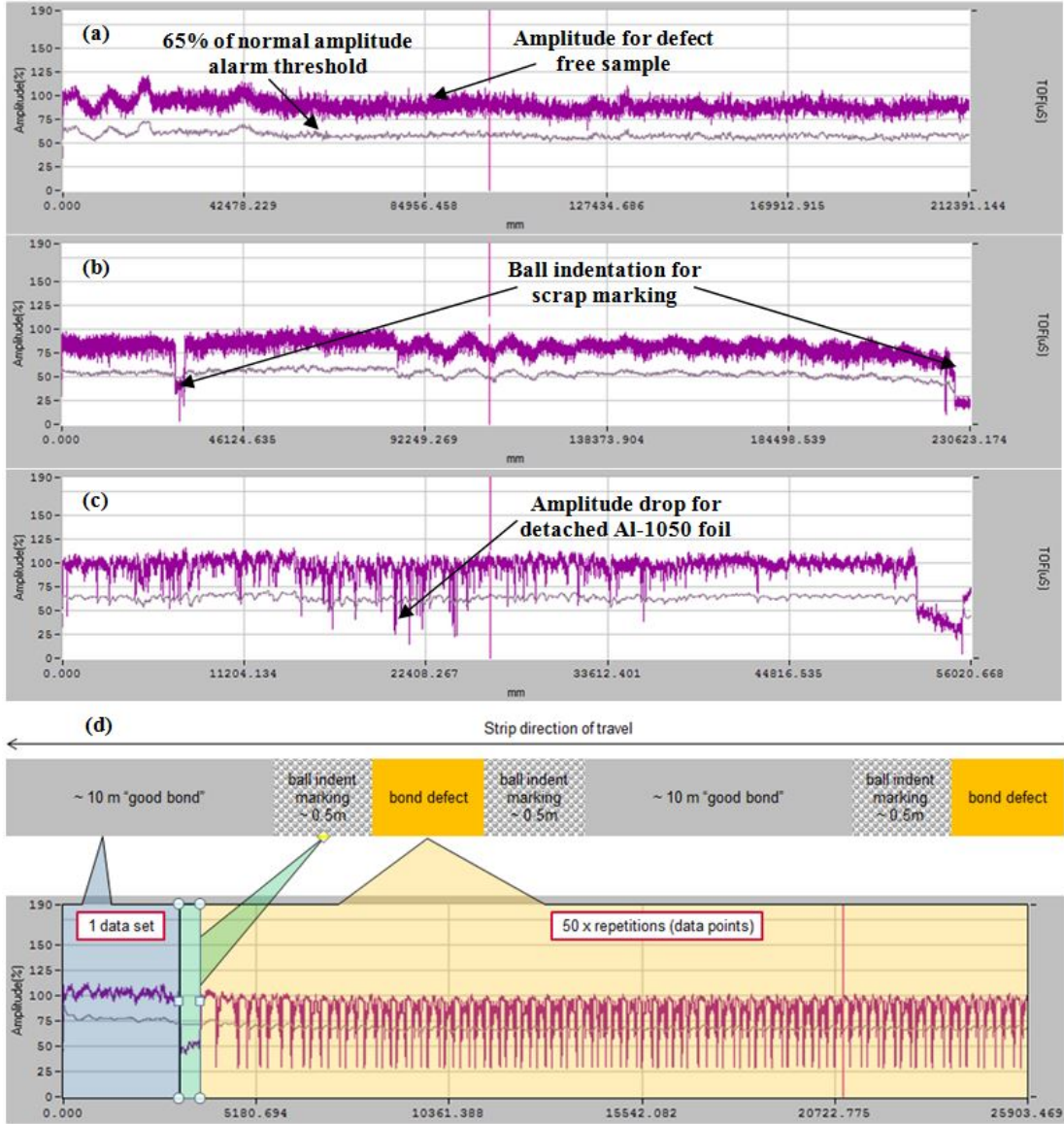


Figure 6.4: Results-based illustration of A-scan maximum amplitude trace: (a) SP1-R1 320 m, (b) SP2-R2 390 m, (c) SP3-D 80 m strips, (d) AD samples

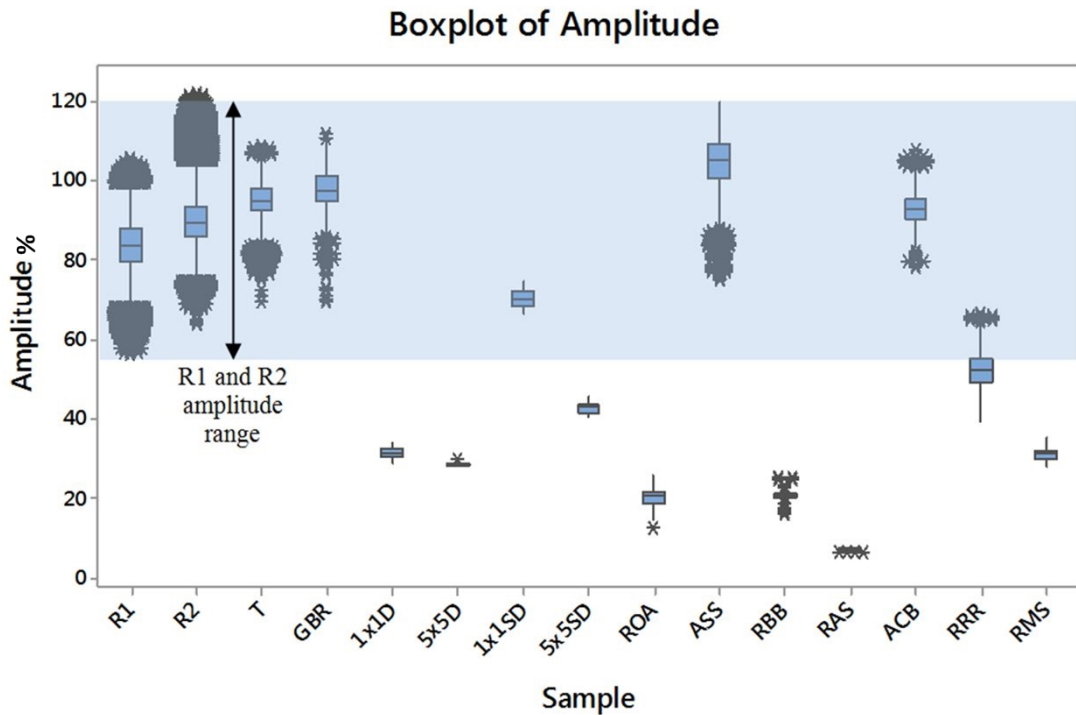


Figure 6.5: Boxplot of SP-R1, SP-R2 and AD strip samples showing central tendency and variability

intervals of defective samples ASS, T, ACB and 1x1SD. These samples can therefore only be detected by accepting a significant false alarm rate. The sample RRR amplitude interval partly overlaps with the combined R1 and R2 interval, hence detection with a reduced false alarm rate is possible. Samples 5x5D, RMS, 1x1D, 5x5D, RBB, ROA and RAS amplitude intervals do not overlap with the combined R1 and R2 interval; therefore, detection without false alarms is possible. The boxplot shows that the variances of the various samples are different.

Analysis of Variance (ANOVA) was used to analyse if the various bond defects could be differentiated by their mean amplitude. An alarm threshold of the normal amplitude was determined based on statistical analysis of the measurement data. Welch's ANOVA was identified as the applicable ANOVA test in this study, since it can be used for samples with normal distribution and unequal variances. Normal probability plots were generated, as shown in Figure 6.6, to check the normal distribution of the measurement data. The x -axis is transformed to plot a cumulative normal density function in a

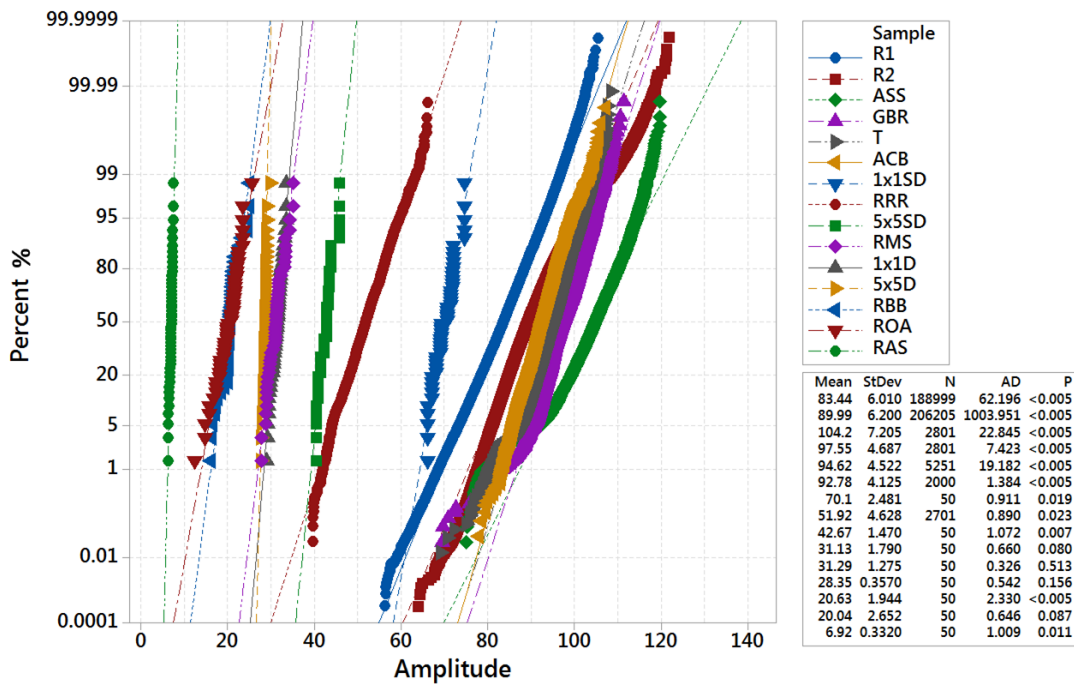


Figure 6.6: Amplitude normal test plots

straight line. The measurement data is plotted and transformed to standard normal values by using the mean and standard deviation of the measurement data. The data is normally distributed when the samples fall along the normal line. It is recognisable that samples T and ASS are right skewed. This can be explained by the way the samples were made. The roll temperature was cold at the beginning of CRB when sample T was produced and then gradually increased to the operating temperature, hence the bond quality along sample T is different. For sample ASS, as shown in Figure 6.3(f), the unlinished area at the edge of the strip is not continuous along the length of the strip but intermittent, since only parts of the rotating linishing belt were removed to alter the linishing parameters. Therefore, the local un-linished areas, with different signal amplitude, were measured repeatedly, which skewed the sample data distribution. ANOVA is insensitive to the normality assumption for large sample sizes, which applies for samples ASS and T. It can be seen that all samples fulfil either the normal distribution or large sample size criterion and therefore Welch's ANOVA can be used.

Chapter 6. Implementing an online bond quality inspection system for cold roll bonded Al/Al-Sn/Al/steel strips

Levene's test was used to test the homogeneity of variance of the samples. The null hypothesis (H_0) states that the variances are the same for all defects. The alternative hypothesis (H_a) states that at least one of the defective samples has a significantly different variance. The p -value is 0.000, hence H_0 must be rejected and the variances are significantly different. This is in line with the box plots in Figure 6.5, in which the different box lengths and whiskers for each sample indicate different variances. Welch's ANOVA test can be used for samples with different variances.

The null hypothesis (Equation 6.1) for Welch's ANOVA is that all sample means are the same ($\mu =$ defect mean):

$$H_0 = \mu_{R1} = \mu_{R2} = \mu_D = \mu_T = \mu_{GBR} = \mu_{1x1D} = \mu_{5x5D} = \mu_{1x1SD} = \mu_{5x5SD} = \mu_{ROA} \\ = \mu_{ASS} = \mu_{RBB} = \mu_{RAS} = \mu_{ACB} = \mu_{RRR} = \mu_{RMS} = \mu_k \quad (6.1)$$

The Welch's ANOVA results are Welch's $F(14,461.175) = 315281.13$, $p = 0.000$, which is summarised in Table 6.3. The p -value = 0.000 means that H_0 must be rejected and the alternative hypothesis (H_a), that there are at least two defect means that are statistically different from each other, has to be accepted. Therefore, the Games-Howell pairwise comparison *post-hoc* test [138] can be used to determine which specific samples are different from each other. This test can be used with unequal variances and unequal sample group sizes. The grouping results are summarised in Table 6.3. Differences between the means that share a letter are not statistically significant and cannot be differentiated. This is the case for samples RMS and 1x1D, which share the letter E, as well as the samples ROA and RBB, which are both in group I. All other samples do not share a letter, hence their means are statistically significantly different and can be differentiated from each other.

The result of the Welch's ANOVA and Games-Howell pairwise comparisons *post-hoc* test is that all samples, except for pairs 1x1D and RMS, as well as ROA and RBB, have statistically significantly different means and can be differentiated. The disadvantage of this analysis is that it can only be carried out after inspection of the

Table 6.3: Welch's ANOVA and Games-Howell Pairwise Comparison *post-hoc* results (Minitab 17.1.0 statistical software)

Welch's ANOVA results					
Source	DF Num	DF Den	F-Value	P-Value	
Sample	14	461.175	315281.13	0.000	

Games-Howell Pairwise Comparisons post hoc results					
Sample	N	Mean	StDev	95% CI	Grouping
R1	188999	83.438	6.0102	(80.7404, 80.8163)	A
R2	206205	89.9866	6.2004	(89.9597, 90.0132)	B
T	5251	94.6202	4.5219	(94.3724, 94.8680)	C
GBR	2801	97.5498	4.6867	(97.2105, 97.8891)	D
1x1D	50	31.29	1.275	(30.928, 31.652)	E
5x5D	50	28.352	0.357	(28.2505, 28.4535)	F
1x1SD	50	70.1	2.481	(69.395, 70.805)	G
5x5SD	50	42.67	1.47	(42.252, 43.088)	H
ROA	50	20.042	2.652	(17.503, 22.581)	I
ASS	2801	104.238	7.205	(103.971, 104.505)	J
RBB	50	20.042	2.652	(19.288, 20.796)	I
RAS	50	6.92	0.332	(6.8257, 7.0143)	K
ACB	2000	92.7775	4.1255	(92.5966, 92.9584)	L
RRR	2701	51.9228	4.6282	(51.7482, 52.0974)	M
RMS	50	31.132	1.79	(30.623, 31.641)	E

complete strip. In order to qualitatively indicate the occurrence of bond defects in real time, the attenuation method that was introduced earlier can be used. In this method, defects are qualitatively indicated when the amplitude falls below a threshold of the normal amplitude, but the limitation of this technique in finding faults is that no unambiguous differentiation between defect types is possible. The criterion for the optimal threshold level is to minimise the false alarm rate and maximise the number of defect types that can be detected. Signal variation can be caused by stand-off between probes and material, electrical noise and local material property changes. In order to to minimise the false alarm rate, a moving alarm threshold can be used. This is explained in the following section.

6.3.3 Determination of moving alarm threshold

The relationship between false alarm rate and threshold of the normal amplitude to detect defects was investigated to determine a reasonable threshold. A comparative

Chapter 6. Implementing an online bond quality inspection system for cold roll bonded Al/Al-Sn/Al/steel strips

study of a simple exponential moving average (EMA) (Equation 6.2), a weighted moving average (WMA) (Equation 6.3) and a simple moving average (SMA) (Equation 6.4) was carried out. The EMA indirectly takes all previous measurement points into account and a smoothing factor $\alpha = 0.25$ was used. For WMA, $m = 10$ weights ($w_1 = 1/55$, $w_2 = 2/55$, $w_3 = 3/55$, $w_4 = 4/55$, $w_5 = 5/55$, $w_6 = 6/55$, $w_7 = 7/55$, $w_8 = 8/55$, $w_9 = 9/55$, $w_{10} = 10/55$) were assigned to the ten most recent measured amplitude values. For SMA, $m = 50$ previous measured values were considered. The purpose of the moving average alarm threshold is to filter outliers and consequently reduce or avoid the false alarm rate. The same sample data from above was used for this study. The following equations were used:

$$\hat{y}_{t+1|t} = \alpha y_t + (1 - \alpha)\hat{y}_{t|t-1} \quad (6.2)$$

$$\hat{y}_i = (w_m y_{i-m} + \dots + w_1 y_{i-1})/m \quad (6.3)$$

$$\hat{y}_i = \frac{1}{m} \sum_{j=i-m}^{i-1} y_j = (y_{i-m} + \dots + y_{i-1})/m \quad (6.4)$$

Figure 6.7 plots the SP-R1 sample false alarm rate depending on the alarm threshold for the different averaging techniques. The false alarm rate is calculated as the number of occurrences in which the calculated amplitude value based on the averaging technique falls below the defined alarm threshold, divided by the total number of measured amplitude values per sample. This calculation is based on the assumption that the good bond reference sample SP-R1 is free of defects. The criterion for the selection of the averaging technique is to minimise the false alarm rate. The SMA technique offers the smallest false alarm rate. Considering that a false alarm rate of 0.50% is reasonably acceptable, then the alarm threshold should be defined as 65% of the normal amplitude level for the SMA technique. This point P(65.3%/0.50%) for the SMA technique is marked on the graph. For the same 65% alarm threshold, the WMA false alarm rate is 1.23%, EMA is 1.58% and for the unchanged data set it is 1.69%.

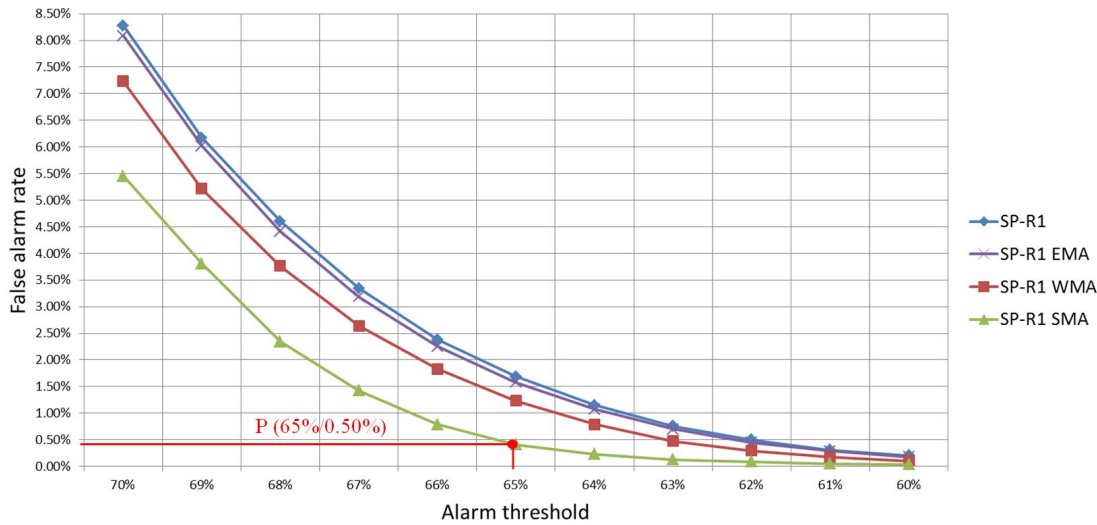


Figure 6.7: Relationship between false alarm rate and threshold for defect-free sample SP-R1

Therefore, the measurement data should be processed with the SMA technique during inspection to reduce the amount of rejected material due to false alarms.

6.3.4 Detectability of main bond defects

The detectability of defects depends on the alarm threshold. Table 6.4 summarises the defects that are detectable in serial inspection with the attenuation method if a 65% alarm threshold is used. Samples SP-D, AD-5x5D, AD-5x5SD, AD-ROA, AD-RBB, AD-RAS and AD-RMS can be detected online with guided waves as well as with the destructive peel-off test. Samples AD-1x1D and AD-RRR can be detected online with guided waves but are likely to remain undetected with the destructive peel off test, because the peel-off is still below the fail rating. Defects AD-T, AD-GBR, AD-1x1SD, AD-ASS and AD-ACB cannot be detected with the 65% alarm threshold, but the same defects cannot be detected with the destructive peel-off test either. Based on a 65% alarm threshold, online inspection with guided waves offers the detection of more defect types than with the destructive peel-off test and, at the same time, 100% material volume online inspection.

Chapter 6. Implementing an online bond quality inspection system for cold roll bonded Al/Al-Sn/Al/steel strips

Table 6.4: Comparison between clad Al lining adhesion peel-off and guided waves non-destructive testing results, considering 65% of the normal amplitude alarm threshold and 0.50% false alarm rate

Sample #	Sample reference	Defect	Guided waves detectability	Peel off tets detectability	Peel off (mm)	Test correlation
1	SP-R1	Serial production reference 1	x	x	1	✓
2	SP-R2	Serial production reference 2	x	x	1	✓
3	SP-D	Serial production defect: Al-1050 blisters	✓	✓	visual	✓
4	AD-T	Roll temperature 42°C	x	x	1	✓
5	AD-GBR	Good bond reference	x	x	1	✓
6	AD-1x1D	1x1 mm area delamination	✓	x	2-3	x
7	AD-5x5D	5x5 mm area delamination	✓	✓	>5	✓
8	AD-1x1SD	1x1 mm area steel debris	x	x	1	✓
9	AD-5x5SD	5x5 mm area steel debris	✓	✓	>5	✓
10	AD-ROA	Run off alloy	✓	✓	visual	✓
11	AD-ASS	Altered steel sanding parameters	x	x	1	✓
12	AD-RBB	Rolled in brush bristles	✓	✓	visual	✓
13	AD-RAS	Rolled in alloy slivers	✓	✓	visual	✓
14	AD-ACB	Altered clad Al brushing parameters	x	x	1-2	✓
15	AD-RRR	Reduced rolling reduction to 30%	✓	x	1	x
16	AD-RMS	Rolling mill stop during bonding	✓	✓	visual	✓

6.3.5 Improvements for serial system

Rigorous testing of the guided wave prototype inspection machine revealed that various machine modifications are necessary before the machine is capable of serial CRB inspection. A frequently occurring issue was lift-off between strip and the EMAT probe. Huang et al [92] reported that lift-off between EMAT probes and samples are typically restricted to below 3 mm due to the requirement of a reasonable SNR. In this study, lift-off up to 20 mm occurred, in particular when the strip showed one-side waviness. In a serial system, the lift-off must be controlled to prevent false alarms. This could be achieved with a more flexible probe assembly design that is capable of maintaining a defined gap, or a strip guidance system such as a three-roll steering stand to correct the strip movement without deflection of the strip.

A further limitation of the current prototype system is that the position of the defects across the width of the strips cannot be localised, which results in a low yield because the full width of the strips has to be scrap marked. It is common practice in engine bearing manufacturing that strips are slit into multiple strands in downstream

Chapter 6. Implementing an online bond quality inspection system for cold roll bonded Al/Al-Sn/Al/steel strips

processes. If the system resolution could be improved to locate the exact position of the defect, the yield could be improved by scrapping only the lane that contains the defect. A recent development in guided wave inspection of metallic plates is to attempt to accurately determine the location, size and shape of defects instead of only detecting the presence of defects. This is possible by using an array of transducers to transmit and receive guided waves from all directions [92]. This would be an improvement compared to the current system, which only uses one sound path across the width of the strip. Strip irregularities, such as notches, steel and clad Al weld seams, can damage the EMAT probes if they remain undetected. A potential solution could be to integrate the bond inspection equipment into a machine visual inspection line that detects surface flaws. The machine visual inspection system could provide a signal to the bond inspection system to remove the sensor probes from the material when an irregularity arrives to prevent any damage. The current system uses different wave modes for strips with different dimensional characteristics. This requires EMAT meander coils with different coil periods. As a result of the different required inspection set-ups, time is required for the changeover from one part to another before inspection can begin. Further work is required to reduce the number of different wave modes for inspection of the complete product portfolio.

6.3.6 Conclusions

An online bond inspection system with a high degree of automation, using guided waves generated with EMATs, has been applied and researched under harsh industrial conditions in an industrial strip processing line for CRBed Al/Al-Sn/Al/steel strips. The EMAT equipment has successfully demonstrated the online detectability of bond defects. The amplitude means of the defective samples were statistically significantly different from the control samples. It was found that, based on a 0.5% false alarm rate, the alarm threshold should be set at 65% of the normal amplitude. Based on this threshold, more defects were detectable with the online inspection system than are nowadays detectable with the destructive clad Al peel-off test. In addition, 100% of the material volume is inspected online instead of only samples at the beginning and

Chapter 6. Implementing an online bond quality inspection system for cold roll bonded Al/Al-Sn/Al/steel strips

the end of strips. The limitation of the system is that no unambiguous differentiation between defects is possible with the real-time attenuation method. A more complex measurement data analysis method that considers the time of flight could be considered for quantitative defect detection in future work. The implementation of a serial inspection system will result in a significant business risk reduction that engine bearings fail in the field.

Chapter 6. Implementing an online bond quality inspection system for cold roll bonded Al/Al-Sn/Al/steel strips

Chapter 7

Defects, causes and prevention controls in the continuous CuSn/steel bimetal strip sintering process

Continuous sintering of CuSn/steel bimetal strips is another manufacturing process in the MAHLE Kilmarnock plant. CuSn/steel strips are used to manufacture bearings and bushes for the internal combustion engine, typically for applications with higher load compared to Al/Al-Sn/Al/steel. Since the business risk that CuSn/steel bimetal components fails in the field is considered too high, it was decided to work on two streams to reduce the risk of defects. The first stream was the systematic identification of all defects that occur in the CuSn/steel manufacturing process, getting to their root causes and to implement prevention controls. Since to date no systematic review about strip defects originating from the manufacturing process existed in the public domain, research and examination was carried out in the MAHLE Kilmarnock plant to understand the defects that occur in serial production. The second stream was to attempt to employ the developed guided waves EMAT inspection system also for CuSn/steel bimetal defect inspection. This would reduce the manufacturing cost, business risk

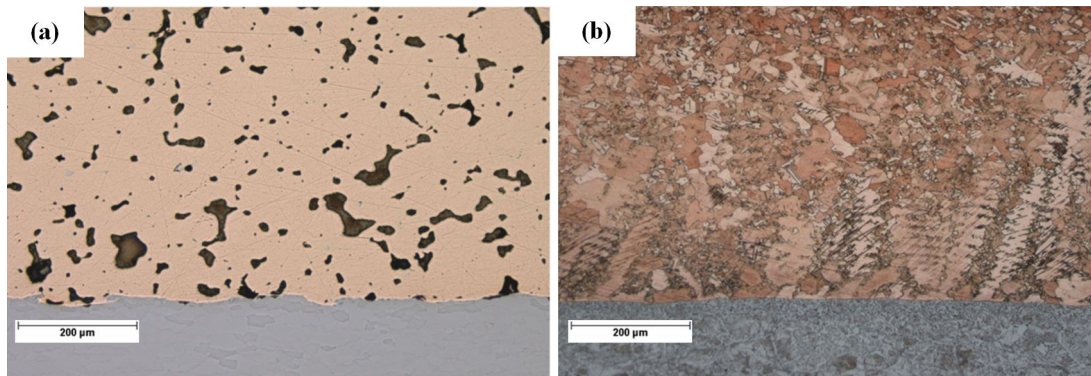


Figure 7.1: Difference in microstructure for (a) sintered CuPb10Sn10 and (b) cast CuSn4Bi lining on steel backed bimetal

and verify that the inspection technique works in similar applications. In this chapter, the defects, causes and prevention controls in CuSn/steel bimetal production were researched. The content of this chapter is based on the journal publication *Defects, causes and prevention controls in the continuous bronze/steel bimetal strip sintering process* (Tallafuss et al., 2018) published in Engineering Failure Analysis.

7.1 Introduction

Bronze is either cast on to the steel or applied by a powder-metallurgy technique to produce bimetal strips. The advantage of the powder-metallurgy technique is that it confers a more isotropic structure and distribution of second phases independent of their lining thickness, though porosity exists. Figure 7.1(a) shows CuPb10Sn10 that was sintered onto steel. Figure 7.1(b) shows cast bronze CuSn4Bi with characteristic tree-like structure, called dendrite, in which crystal growth occurs faster along energetically favourable crystallographic directions resulting in consequences for lining material properties. For cast as well as sintered bronze/steel bimetal, the bond interface between the constituents is critical. When comparing the bond between sintered and cast bronze/steel bimetal, no significant difference can be observed as shown in Figure 7.1. In both processes, diffusion between bronze and steel is extrinsic. Sintering is more economically viable compared to the casting process [139].

Both leaded and lead-free bronzes are considered in this study. Tightened environ-

Chapter 7. Defects, causes and prevention controls in the continuous CuSn/steel bimetal strip sintering process

mental regulations have resulted in an increasing demand for lead-free materials with equivalent or superior properties to their lead-containing counterparts [140]. Many publications document damages and failures in plain bearings, while only a small number deal with defects and their occurrence in strips. Papers dealing with plain bearings focus on damage and failure classification and appearance [141,142], their possible root causes [143,144], corresponding corrective actions [145,146], effect of lubricants [147], diagnostics and examination tests [148], as well as the frequency of wear defect types in diesel engines based on field data [149]. Strip related papers describe sintering copper-based alloys to steel through various stages of manufacture [150], mechanical and wear properties as well as fatigue crack defects [139], and investigate the influence of sintering and rolling reduction process parameters on the adhesion of bronze to steel [151]. However, to date papers have not focussed on strip defects originating from the manufacturing process, despite this being the process stage at which the detection and prevention has the greatest opportunity to reduce cost and business risk. This paper presents all defect types that took place in an industrial production site in a logical structure, analyses the critical process parameters and material characteristics to quality, and discusses control measures to prevent those defects from occurring.

7.2 The continuous bronze/steel bimetal sintering process

Figure 7.2 shows a schematic of the process, which was used to manufacture the materials examined in this study. Steel strip is uncoiled, straightened and washed in a hot alkali solution to remove surface contamination and preservative oil. The bonding surface is finished using abrasive rotating belts, and then it is up-coiled and ready for powdering. Bronze powder is evenly spread over the steel surface using an adjustable powder die. The loose powder thickness is calculated based on the ratio between apparent density of the powder and theoretical density of the alloy, including an allowance for elongation of the strip during rolling. The bronze powder is sintered on to steel in a muffle type continuous sintering furnace at temperatures between 800-900°C. Hydrogen (H₂) and Nitrogen (N₂) created by dissociating gaseous anhydrous Ammonia (NH₃) in the reaction $2\text{NH}_{3(g)} \rightarrow \text{N}_{2(g)} + 3\text{H}_{2(g)}$ [152] is used as reducing atmosphere inside the

Chapter 7. Defects, causes and prevention controls in the continuous CuSn/steel bimetal strip sintering process

furnace during sintering. The hydrogen atmosphere prevents the bronze and steel from oxidising into the metallic state according to the reaction $\text{CuO}_{(s)} + \text{H}_{2(g)} \rightarrow \text{Cu}_{(s)} + \text{H}_2\text{O}_{(g)}$. This enables the de-oxidised particles which are physically in contact with each other and the steel surface to bond together due to mutual diffusion of their atoms and become a continuous network of bronze particles bonded to the steel backing. The density of the bronze lining after first sintering is higher than in the loose powder state, but still retains 20 to 30% porosity. Sintering is either performed in a gas fuelled or electrical induction muffle type continuous sintering furnace. During first sintering, the powder layer thickness shrinks by 12-20% depending on powder type. The bimetal strip is cooled by radiation and convection processes in a long cooling section comprised of an enclosed water jacket and containing a reducing atmosphere. The bronze/steel bimetal strip is rolled using a 2 high mill, in order to compact the bronze layer and reduce porosity. In the resintering process, the new particle interfaces formed during the rolling process are bonded together as a result of mutual diffusion of their atoms, forming a solid layer with higher strength. Resintering process parameters are similar to sintering. Ideally there would be zero residual porosity, but for components which do not require plating, up to 5% porosity is considered acceptable. Any non-alloying second phase (Pb or Bi) shall be homogeneously distributed throughout the bronze matrix as fine pools of around 25-50 μm cross sectional area between the bronze grains. Some bronze alloys of certain dimensional characteristics may require a third sintering pass to achieve the desired material structure. After the final sintering pass, a further cold rolling operation may be performed to work harden the bronze lining and steel back. Figure 7.3 schematically illustrates the structure of the sintered bronze/steel bimetal per process step.

Process parameters which are critical to quality are line speed, temperature, reducing atmosphere, rolling pressure and the time between first sintering and resintering. Material characteristics which are critical to quality are powder layer thickness, particle size distribution and chemistry, especially phosphorous and oxygen level. The sintering time is governed by the steel and lining thickness, chemical composition of the bronze lining, process stage (sintering or resintering) as well as furnace type (gas fuelled or

Chapter 7. Defects, causes and prevention controls in the continuous CuSn/steel bimetal strip sintering process

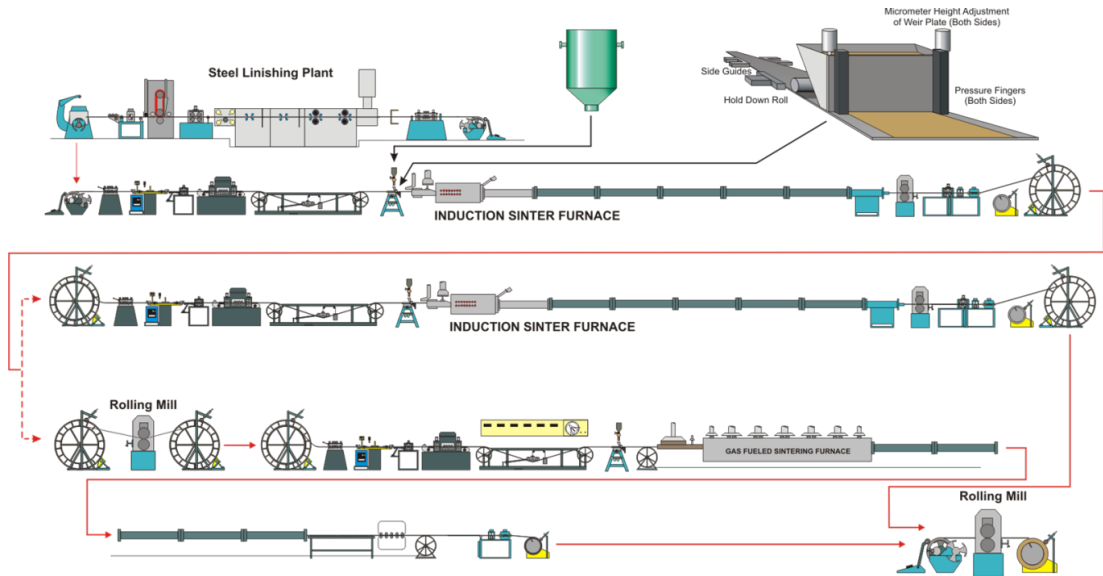


Figure 7.2: Sintered bronze/steel bimetal continuous production process

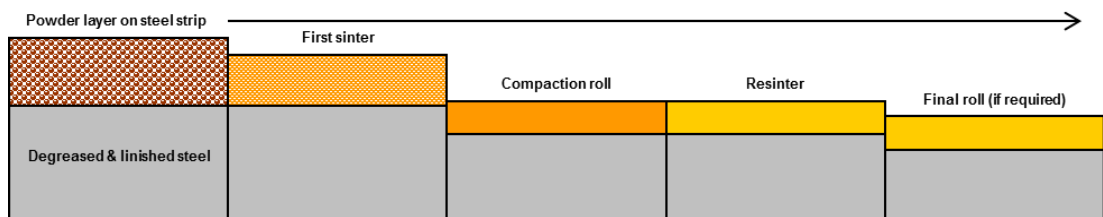


Figure 7.3: Schematic illustration of sintered bronze/steel bimetal structure per process step

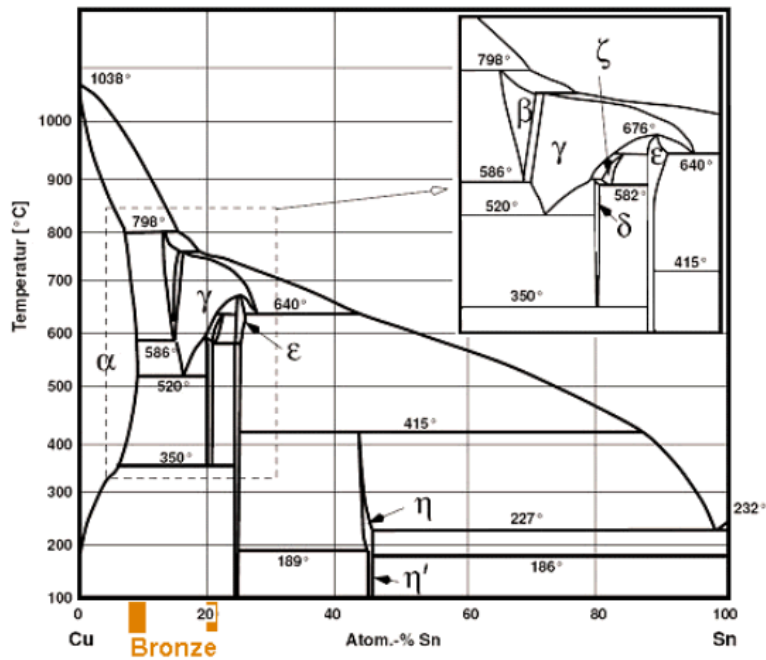


Figure 7.4: Cu-Sn phase diagram

electrical induction). Induction heating of electrically conducting steel through eddy currents produces high power densities and the strip is heated in milliseconds which allows short sintering time at the required temperature, while gas or electric radiant heating furnaces require a longer sintering time. In this study, the electrical induction furnace line speed ranged from 0.8 to 2.0 m/min, and the gas fuelled line speed was between 0.5 to 0.7 m/min. The induction coil length was less than 2 m, and the gas fuelled furnaces were around 9 m in length

7.3 Liquid phase sintering mechanism

As can be seen in the Cu-Sn phase diagram in Figure 7.4, pure Cu-Sn bearing alloys such as CuSn11 have liquid phases above 798°C. Bronze based bearing alloys can contain lead or bismuth low melting point metal, which is distributed in the bronze matrix as second phase.

The finer the particle size and the higher the volume fraction of the liquid phases in the system is, the higher is the densification rate [153]. The three stages in the liquid

phase sintering process are [154, 155]:

1. *Rearrangement*: once the low-melting-point constituent (lead or bismuth) has liquefied, the densification is a result of viscous flow. The liquid formed at this stage flows to the necking areas between powder particles to reduce the surface energy. In the meantime, solid particles are pulled close to each other due to the capillary force of the liquid, leading to the rearrangement of powders. The higher the liquid volume fraction is, the greater is the densification, and above 5-10% volume fraction of liquid, complete densification occurs.
2. *Dissolution-precipitation*: in this stage particles dissolve in the liquid phase and diffusion takes place.
3. *Coalescence*: once the solid skeleton has formed, coalescence takes place that has a similar densification rate to solid particles sintering under comparable conditions.

7.4 Experimental materials and procedures

The manufacturing process described in section 7.2 was used to manufacture the samples that were examined in this study. Sintered bronze bimetal strips comprising of lead-free and leaded bronze alloys sintered onto steel backings from serial production were examined in this study. The dimensional characteristics of the bimetal strips ranged from 1.20 mm to 4.50 mm thickness with input steel thicknesses of 0.75 mm to 4 mm. The strip width ranged from 102 mm to 203 mm. The chemical compositions and mechanical properties of those materials are shown in Table 7.1 for the sintered bronze lining and in Table 7.2 for the low-carbon steel backing. Spherical powder was chosen for the better flow ability and higher packing density when spreading the powder on steel to prevent porosity.

The binary phase microstructure of SB10 comprises of lead pools which are distributed in a homogeneous CuSn matrix is shown in Figure 7.5(a). Figure 7.5(b) shows the CuSnNi homogenous structure of SB20, in which the tin and nickel are completely dissolved in the copper matrix. SB30 is shown in Figure 7.5(c), which has a poly-phase

Chapter 7. Defects, causes and prevention controls in the continuous CuSn/steel bimetal strip sintering process

Table 7.1: Chemical compositions (wt. %) and mechanical properties of SB10, SB20 and SB30

Designation	Cu	Pb	Sn	Ni	Bi	Al ₂ O ₃	Hardness
SB10	Bal.	9.0 - 11.0	9.0 - 11.0	-	-	-	70 - 165 HV ₅
SB20	Bal.	-	7.0 - 9.0	0.7 - 1.3	-	-	95 - 200 HV ₅
SB30	Bal.	-	6.7 - 8.7	0.6 - 1.4	2.6 - 4.0	0.02 - 0.08	95 - 200 HV ₅

Table 7.2: Chemical compositions (wt. %) and mechanical properties of low-carbon steel

Type	Fe	C	Mn	Si	Others total	Hardness
Low-carbon	Bal.	0.13% max.	0.60% max.	0.20% max.	0.20% max.	90 - 150 HV ₁₀

microstructure of homogeneous CuSnNi matrix around particles of free bismuth and alumina. For all bimetal materials it can be seen that the lining to steel bond is free from aligned linear porosity or continuous oxides. The majority of these materials are used in automotive bush applications, and for engine bearing applications the parts may be plated with an overlay of a soft material to produce a tri-metal bearing in order to reduce friction and avoid seizure. This is necessary because, despite the lead or bismuth soft phase, the frictional properties are still too poor in boundary or mixed lubrication conditions for engine bearing applications.

The inspection results (Figure 7.6) from 1,250 km sintered bronze/steel bimetal serial production strips were investigated in this study. Representation of the alloy types varies, i.e. binary phase lead-bronze alloy was 172 km (14%), single-phase lead-free bronze was 1,078 km (86%), which covers the large majority of all strips that were

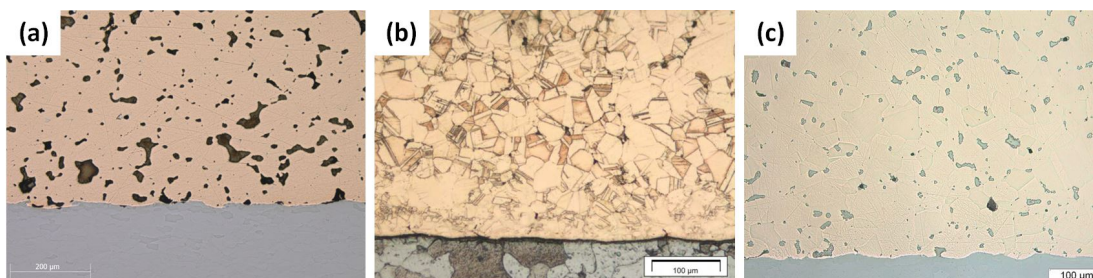


Figure 7.5: Cross sectional view showing typical structures of (a) binary phase SB10 (b) single-phase SB20, (c) binary phase SB30 homogeneous sintered bronze/steel bimetal structure with a continuous lining to steel bond

Chapter 7. Defects, causes and prevention controls in the continuous CuSn/steel bimetal strip sintering process

Total produced km of bronze/steel bi-metal strip	1,250	100%	→	CuPb10Sn10	172	14%
				CuSn8Ni	1,078	86%

Figure 7.6: Distribution of the investigated bronze/steel bimetal strips according to the bronze lining chemical composition

manufactured in the industrial manufacturing facility over three years.

In this study, sheet samples were cut from the beginning and the end of the SB10 and SB20 bimetal coils. Micrographic specimens with 15 mm length were punched from the samples using a flywheel press. The micro samples for assessment were prepared according to the same procedure that was used for Al/Al-Sn/Al/steel specimens and was described in section 5.1.2. The only difference between Al/Al-Sn/Al/steel and CuSn/steel samples preparation was that for CuSn/steel samples, polishing was carried out using increasingly finer polishing suspensions (3 and 1 microns) before non crystallising colloidal silica, 0.04 micron, for 6 minutes was used. CuSn/steel samples were mounted in the transverse direction for examination.

The following techniques were applied for defects quality and quantity measurements. Delamination, degree of sinter, porosity, lead pools size and dimensional defects were evaluated using a microscope. Delamination defects were assessed at x400 magnification, all other defects at x100 magnification. Surface defects were evaluated visually.

Delamination

The bond delamination length ratio used in this study is calculated using Equation 7.1, in which d is the length of individual delamination spots that are measured along the bond line of the sample and l is the length of the sample.

$$\text{Bond delamination length ratio} = \frac{\sum_{i=1}^n d_i}{l} * 100 \quad (7.1)$$

Residual particles and degree of sinter

Following procedure was used to determine the degree of sinter:

1. Calculation of the area of the section under examination (A_s)

Chapter 7. Defects, causes and prevention controls in the continuous CuSn/steel bimetal strip sintering process

2. Measurement of the diameter of five undersintered residual particles with less than 50% of its surface bonded within the section
3. Calculation of the mean diameter of these residual particles
4. Calculation of the average area of the residual particles within the area under examination (A_a)
5. Counting of the number of residual particle within the section (n)
6. Calculation of the percentage of residual particles according to Equation 7.2

$$\text{Percentage of residual particles} = \frac{n * A_a}{A_s} * 100 \quad (7.2)$$

Porosity

Following image analysis procedure was used to determine the degree of porosity using the Zeiss KS300 image analysis software:

1. 10 random fields of view from each prepared micro sample were captured (Figure 7.7(a))
2. Setting the threshold until the porosity is the only feature selected for measurement (Figure 7.7(b))
3. Image changes in appearance, the areas selected for porosity measurement are highlighted in colour (Figure 7.7(c))
4. Confirmation of areas selected for measurement results in the mean porosity value

Lead pools size

Following procedure was used to determine the size range of lead pools:

1. Measurement of the length and width of five large lead pools within the selected section

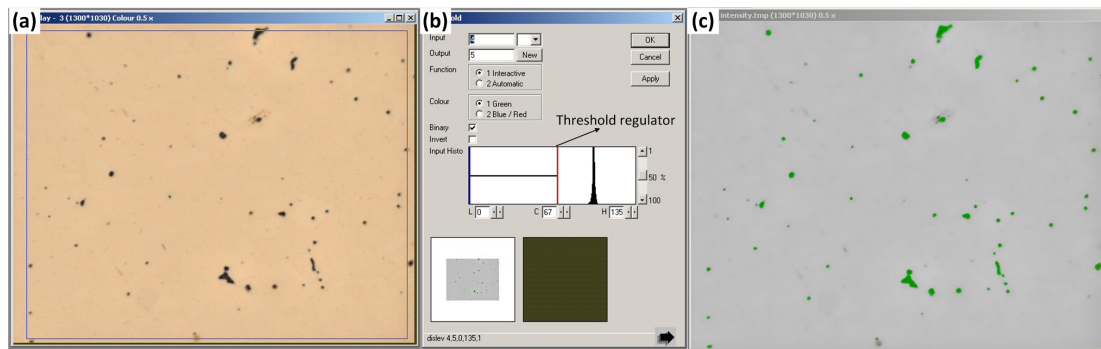


Figure 7.7: Technique applied for porosity measurement: (a) capture of section, (b) threshold setting, (c) areas selected for porosity measurement highlighted in colour

2. Measurement of the length and width of five small lead pools within the selected section
3. Calculation of the average size of the small and large lead pools results in the range between the average size of the small and large lead pools

7.5 Results and discussion

The main causes that lead to defects in bronze/steel bimetal strips for plain bearings are numerous, and often multiple causes can simultaneously contribute to the defect. The results of this study summarised in Figure 7.8(a) show that the types of defects which occurred most frequently in the examined samples were porosity (app. 46%), poor bond (28%), and incorrect microstructure (coarse bronze grains and coarse or non-homogenously distributed lead or bismuth pools) (app. 13%), while other types of defects were much less common such as residual particles (3%), out of specification bronze hardness (app. 3%), excessive lead movement (app. 3%), out of specification dimensional characteristics (app. 2%), lining cracks (app. 2%), blow holes (< 1%) and particle inclusions (< 1%).

In the following analysis all defects related to the sintering of bronze onto a steel backing with their causes and prevention controls are described. Material defects which were detected during the investigation are structured into a fault tree analysis (FTA) for the description of the constructed fault tree root causes. A fault tree is a logical

Chapter 7. Defects, causes and prevention controls in the continuous CuSn/steel bimetal strip sintering process

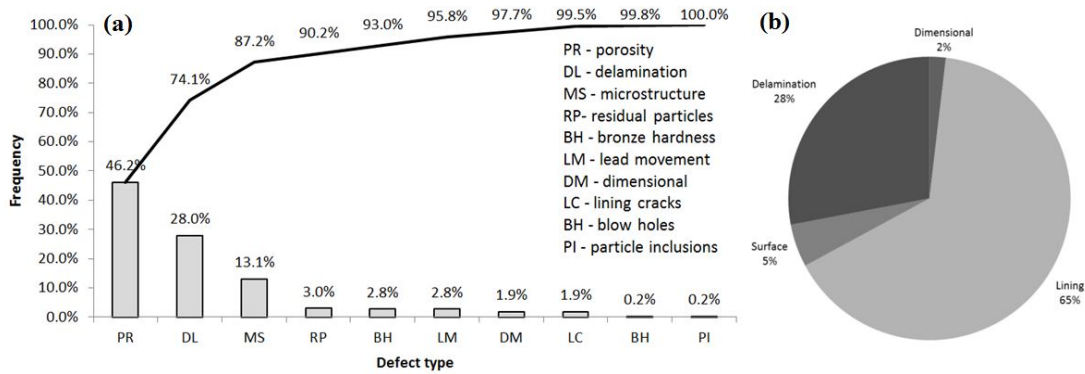


Figure 7.8: Percentage occurrence of (a) different defects, (b) location in bimetal

diagram similar to a family tree, in which possible events lead to a major event. The desired or undesired main event is positioned at the top of the diagram and is called top event [156]. In this study, the top event is titled sintered bronze/steel bimetal strip defect. The defect types were categorised according to their location of occurrence: (1) bond line defect (delamination), (2) bronze lining structure defect, (3) bronze lining surface defect and (4) bimetal (dimensional) defects. Figure 7.8(b) summarises the occurrence of defects according to their location in the bimetal. Delamination defects (28%) are buried below the surface and therefore not detectable. All lining defects (65%) require examination under the microscope in the laboratory to get detected. Dimensional defects (2%) require in-line measurements with gages and additionally lining to steel thickness ratio measurement under the microscope for inspection. Only surface defects (2%) can be detected with the naked eye. This shows the importance to prevent defects from happening in the first place. The FTA diagram in Figure 7.9 for material defects in sintered bronze/steel bimetal strips can be used by manufacturing engineers in practice for problem solving.

7.5.1 Delamination

Characterisation

Delamination can result in failure of a bearing in service. In an ideal process, the material would be made with zero bond line defects.

Figure 7.10 shows SB10 and SB20 with different degrees of bond delamination. An

Chapter 7. Defects, causes and prevention controls in the continuous CuSn/steel bimetal strip sintering process

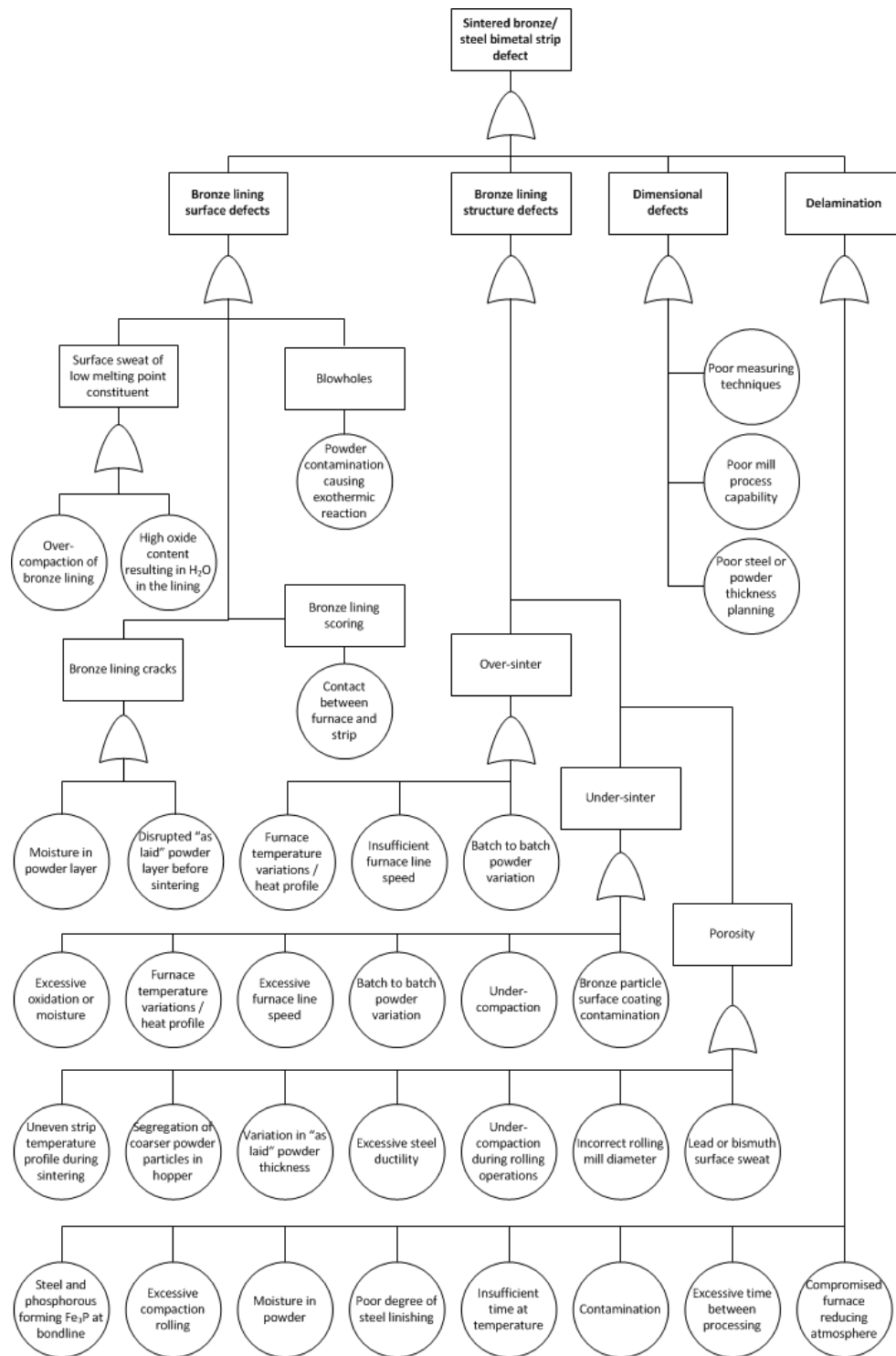


Figure 7.9: Fault tree analysis (FTA) of sintered bronze/steel bimetal strip defects

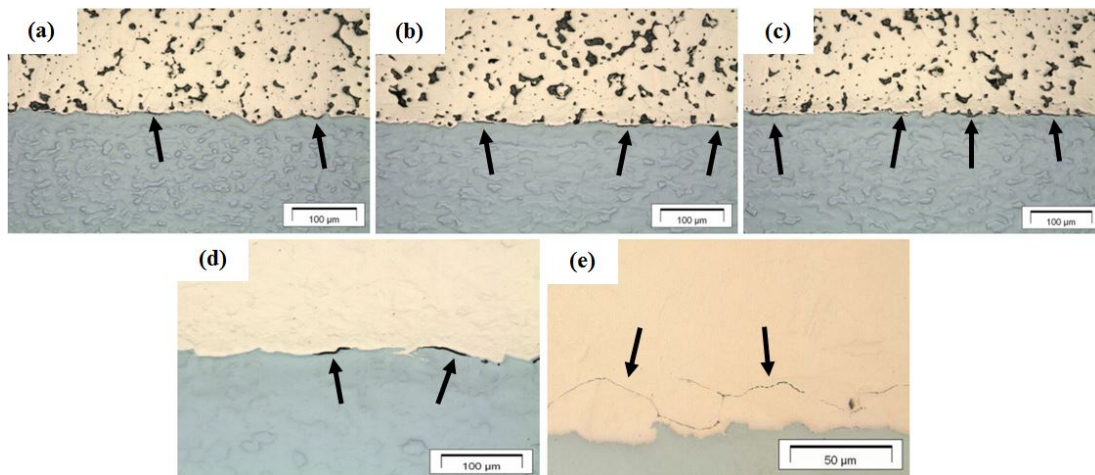


Figure 7.10: SB10 with different lining to steel bond delamination length ratios (a) > 5 and $\leq 10\%$, (b) > 10 and $\leq 20\%$, (c) $> 20\%$, (d) SB20 lining to steel bond delamination length ratio $> 20\%$, (e) SB20 lining shear plane delamination ratio $> 20\%$ in the field of view of the micro sample

ideal bond delamination length would be zero. Figure 7.10(a) shows no continuous delamination longer than 1 mm and a bond delamination ratio between 5 and 10% for SB10. Figure 7.10(b) shows a bond delamination length ratio for SB10 between 10 and 20% and Figure 7.10(c) above 20%, in which the continuous delamination is less than 1 mm length. Figure 7.10(d) shows a bond delamination length ratio above 20% in SB20 material. Sometimes the delamination can occur just above the bronze to steel interface and this is known as shear plane delamination and is shown in Figure 7.10(e) for SB20 with a delamination length ratio above 20%.

Causes and prevention controls

Delamination can be caused by insufficient sintering time and temperature, which is required for the diffusion between powder particles, and the powder particles to the steel backing. Insufficient cleaning of the steel before finishing may leave a layer of contamination and preservative oil between powder and steel which prevents bond. Poor degree of finishing can lead to reduced surface area for bonding and the presence of a thin oxidised skin on the steel surface. Excessive time between finishing and powdering, as well as between sintering and resintering, compounds the oxidised steel

Chapter 7. Defects, causes and prevention controls in the continuous CuSn/steel bimetal strip sintering process

surface. Moisture in the powder can lead to oxidation which can be the root cause for delamination. Excessive stretch at compaction rolling operation can lead to shear at the bondline resulting in delamination. Damaged integrity of the furnace can lead to air ingress with O_2 and H_2O which compromises the reducing atmosphere and can act as oxidising agents for the steel and powder. Direct contact between iron in the steel and phosphorous in the powder can form Fe_3P at the bond line, which can also result in delamination.

7.5.2 Bronze lining structure defects

It is important for optimum structural properties to ensure the material is correctly sintered, which can be monitored by examining the microstructure. Undesirable characteristics in the sinter structure are porosity, coarse grain structure, large lead or bismuth pools and residual bronze particles.

Porosity

Characterisation Porosity can lead to early fatigue failures as pores may act as crack initiation sites. This is further exacerbated if the pores are joined or adjacent. For bearing applications where overlay plating is required, porosity can retain moisture during the plating process which can result in blistering and early failure of the plated overlay. Porosity assessment in this study was carried out using image analysis. The maximum acceptable porosity depends on bronze alloy type and engine application. Figure 7.11(a) shows porosity for SB10 below 1%. Figure 7.11(b) shows 3% porosity, and 5% porosity is shown in Figure 7.11(c). Low porosity with only 0.4% for SB20 is shown in Figure 7.11(d). Figure 7.11(e) shows 2.0% porosity and Figure 7.11(f) 3.0% respectively.

Causes and prevention controls A porosity higher than expected level can be the result of numerous reasons, among them the most important ones are input material characteristics (powder particle size and distribution), rolling related parameters (stress, roll size, speed), temperature stability that results in a variation in degree of

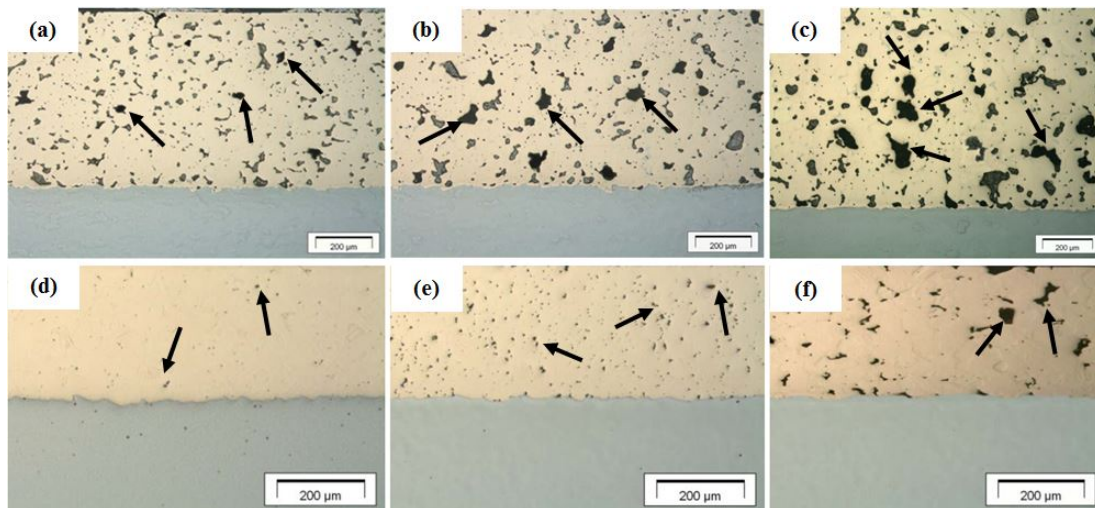


Figure 7.11: Different porosity SB10 (a) 1%, (b) 3%, (c) 5% and SB20 (d) 0.4%, (e) 2.0% and (f) 3.0%

sinter and shrinkage, lead or bismuth sweat if it remains on the surface and is not pulled back into the lining by capillary action. Excessive steel ductility can cause porosity, if the bronze layer work hardens more than the steel, and the steel stretches before the bronze reaches a desired density. Under-compaction during inter-sinter rolling operations will result in porosity. Taper or variation in the as laid powder layer thickness can result in porosity at the strip positions with a thinner powder layer. It was found that if these influencing factors are not controlled, excessive steel stretch and porosity can occur in all material dimensions.

Over-sinter

Characterisation Over sinter is due to excessive time at temperature or excessive temperature at given time. It is characterised by excessive growth of bronze grains and coarse lead or bismuth pools. Macro examination of the surface can often show a crazed or cracked surface on the bronze lining. In this study, the lead grain size is measured along the longest cross section. The maximum allowed lead grain size (long axis) is based on empirical testing in engine applications. Figure 7.12 shows SB10 with lead pools in different sizes within the CuSn matrix. The ideal size of free lead pools is between 5-50 μm , shown in Figure 11(a). Lead pools up to a size of 120 μm are shown

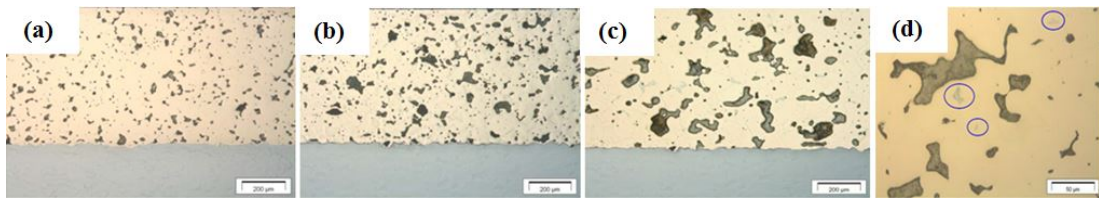


Figure 7.12: SB10 Dual phase structure with CuSn matrix surrounding lead pools with different sizes (a) 5-50 μm , (b) up to 120 μm , (c) up to 150 μm and (d) eutectoid phase

in Figure 7.12(b). Figure 7.12(c) shows free lead pools up to 150 μm size. Coarse lead pools can often be accompanied by porosity as shown in Figure 7.12(c). Figure 7.12(c) also shows a silvery blue eutectoid phase, which is relatively hard and brittle and not ideal in sintered bronze bearing materials. An enlargement of the eutectoid phase is shown in Figure 7.12(d). Although all eutectic phases (α , β , γ , δ , ϵ and ζ) can be formed at any temperature above 798°C according to the Cu-Sn phase diagram in Figure 7.4, they usually occur together with excessive growth of bronze grains and coarse lead or bismuth pools.

Causes and prevention controls Slower than planned line speed at correct temperature in furnace leads to over-sintering. Variation in temperature in the furnace can lead to over-sintering. In gas furnaces, this might be caused by gas burners switching on and off. In induction furnaces, the heat profile across the width of the strips can be uneven. Down strip temperature variation can be caused by manual control of potentiometer settings and the use of non-contact temperature measurements. Furthermore batch to batch powder variation particularly for phosphorous or tin content and variation in particle size can lead to over-sintering.

Under-sinter

Characterisation An under-sintered structure is when examination under the microscope still shows evidence of the original spherical structure of the bronze particles prior to sintering. At the extreme end of the under-sintered range, residual particles (RP) may be present which are defined as particles with less than 50% of their surface bonded. Ideally a sintered structure would have zero incidences of RPs, but some par-

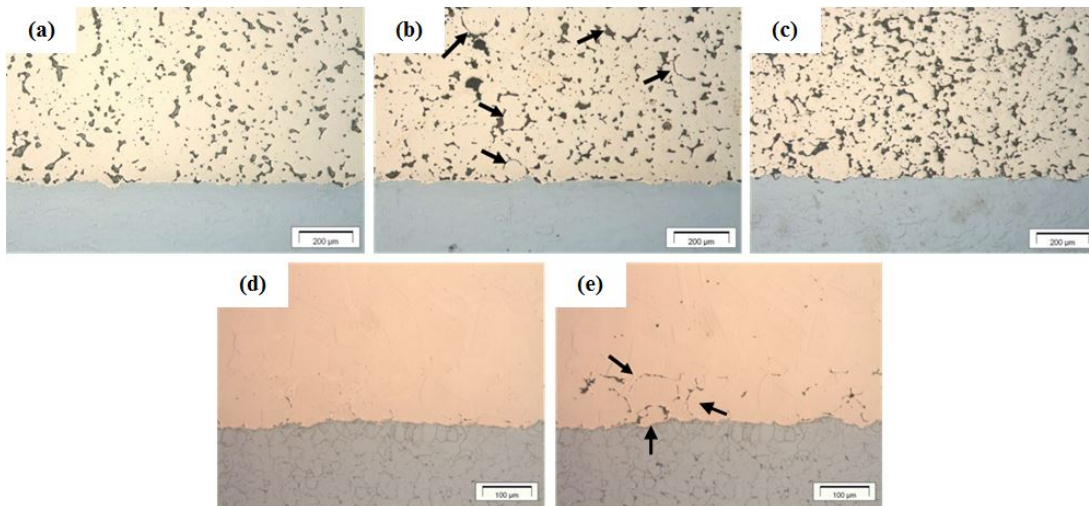


Figure 7.13: SB10 with $< 50\%$ of their particle surface bonded (a) 0 RPs, (b) 5 RPs, (c) > 5 RPs and SB20 with different number of particles (d) 0 RPs, e) > 3 RPs

ticles in a field of view of a sintered microstructure may be allowable. The number of RPs for sintered bronze is determined by counting their occurrence on the field of view in a defined length of a micro sample. Figure 7.13 shows SB10 and SB20 with different numbers of RPs. Ideal SB10 microstructure with no RPs is shown in Figure 7.13(a), while in Figure 7.13(b) 5 RPs and in Figure 7.13(c) more than 5 RPs as a result of under-sintering are visible. Figure 7.13(d) shows SB20 without RPs and Figure 7.13(e) with more than 3 RPs above the bond line.

Causes and prevention controls Under-sintering can often be caused by the same process variations that lead to over-sintering, if the parameters shift to the opposite extreme. These parameters are excessive line speed at correct temperature, temperature variations in the furnace, uneven heat profile across the width of strips, batch to batch powder variation regarding phosphorous or tin content and variation in particle size that might lead to under-sintering. Furthermore lack of physical contact between particles caused by under-compaction leads to under-sintering. Excessive oxidation or moisture of the powder, which is unable to be fully reduced during the sintering process, as well as powder contamination by compounds that coat the bronze particle surface, might cause under-sintering.

7.5.3 Bronze lining surface defects

Material flaws that result from incorrect processing and can be visually examined are surface sweat of low melting point additives, contamination from furnace debris, blow-holes and lining cracks. Scoring can be caused by any point of contact between material and manufacturing equipment.

Surface sweat of low melting point additives

Characterisation During the resintering operation the low melting point materials, lead or bismuth, melt at 327.5°C and 271.4°C respectively, well below the sintering temperature. These metals can form liquid globules on the surface of the strips. Their presence at the surface can be detrimental to the performance of the material. The assessment of the extent to which lead has come out onto the lining surface during resintering is examined visually. Figure 7.14(a) shows SB10 lining surface without trace of lead on the surface. There are two cases of lead movement. The first case is when lead is remaining on the lining surface after resintering. Figure 7.14(b) shows marginal lead remaining on the surface after resintering, Figure 7.14(c) shows increased lead residue and Figure 7.14(d) shows excessive lead residue on the lining surface after resintering. In ideal circumstances, when the strip remains flat and the cooling rate is slow enough, capillary action pulls the lead back into the lining and leaves only a witness mark on the lining surface, which is the second case. Figure 7.14(e) shows such witness marks on the lining surface. Depending on the severity of lead movement, this can result in porosity, especially in case when lead remains on the surface and is not pulled back into the lining by capillary action.

Causes and prevention controls Lead sweat can be caused by over-compaction of the bronze. Due to the plastic deformation of the bronze during compaction rolling, the lead is under pressure. When the strip is heated during resintering, the lead becomes liquid and expands as a result of the higher volumetric coefficient of liquid metal compared to the solid bronze matrix and therefore sweats out on to the surface of the strip. If the cooling conditions are suitable and the strip has remained flat so that

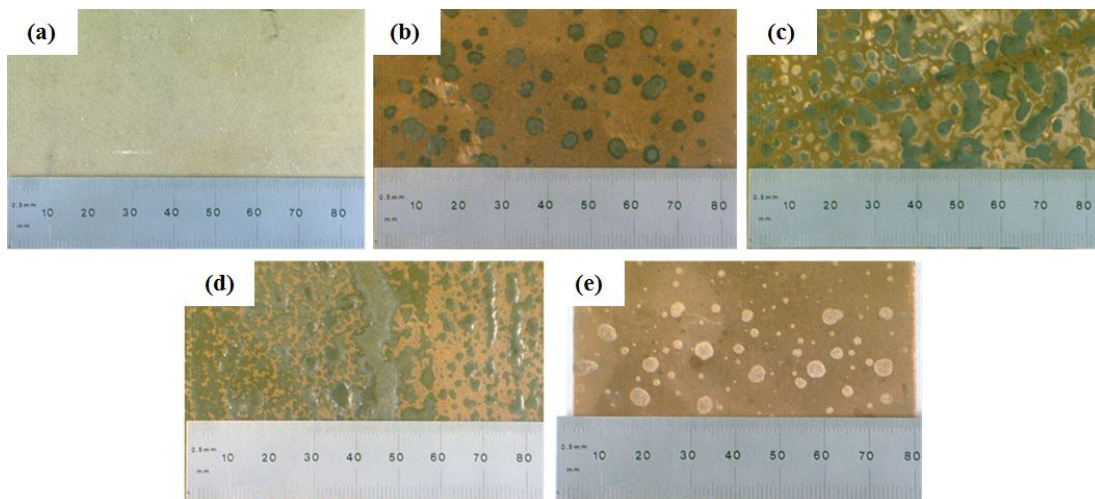


Figure 7.14: Bronze lead movement (a) no lead residue, (b) marginal lead residue, (c) increased lead residue, (d) excessive lead residue, (e) evidence of lead that was drawn back into lining by capillary action

the lead has not run off its original position, then the lead can be pulled back into the original space by capillary action. However, if the strip has moved, then it is not possible to be drawn back in to the lining, leaving the lead exposed on the surface and porosity in the material where the lead vacated. High oxide content of the powder results in excessive lead movement. Oxygen in the powder may react with hydrogen in the furnace atmosphere, resulting in the formation of H_2O gas in the powder lining. This results in vapour pressure, which may push the lead out of the matrix on to the lining surface during the resintering process.

Blowholes

Characterisation Blowholes are defined as smooth-walled cavities with a spherical shape of more than 1 mm in diameter in the sintered bronze lining surface and may be deep enough that an area of bare steel can be visible. Blowholes are often prevalent in leaded bronze, but are normally not found in lead free bronze. Figure 7.15(a) shows a blowhole of approximately 10 mm diameter in SB10 material.

Causes and prevention controls Blowholes are usually caused by particulate contamination in the powder, which can react with lead present resulting in an exothermic



Figure 7.15: Photographs (a) circular blowhole of approx. 10 mm diameter, (b) lining shrinkage cracks (c) scoring

reaction. This can cause a hole to be formed in the bronze lining, which is surrounded by an area of loosely bonded powder. The exothermic reaction can result in the contaminant particle being ejected from the hole. Sometimes the ejected particle can be found lying loose on the strip surface near to the blowhole. The particles disintegrate into fine powder when a force is applied. Figure 7.16(a) shows a SEM image and Figure 7.16(b) elemental identification and quantitative composition from energy dispersive X-ray analysis (EDAX) that was used to identify and quantify compositional information from the impurity deposits. The presence of various light elements including Si, Ca, Al, Ti, Mg, O and Fe were found in the samples. The chemical footprint was similar to that of the refractory crucibles and cements used in the powder manufacturing process. Molten lead has an aggressive effect on the crucible, creating a ring of erosion of the crucible material around the top of the melt. This can result in particles of the eroded crucible contaminating the final powder. The presence of any moisture associated with the contaminant particles can result in trapped water vapour, which ejects the contaminant particle and leaves a blow hole.

Lining cracks

Characterisation Figure 7.15(b) shows lining surface cracks that exceed more than 10 mm length.

Causes and prevention controls Bronze surface cracks are often caused by over-sintering, or disruption of the powdering or sintering process.

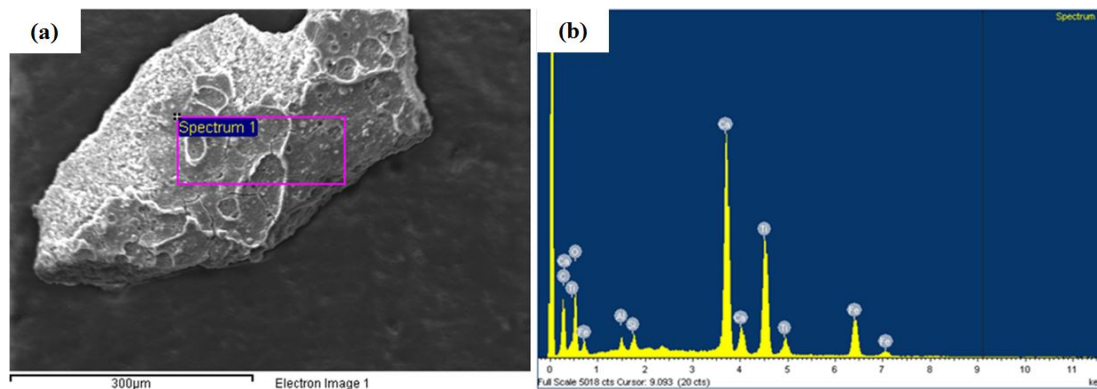


Figure 7.16: (a) SEM image of particle ejected from blowhole, (b) EDAX showing presence of C, Ca, O₂, Ti, Fe, Al, Si

Lining scoring

Characterisation Scoring of the bronze or the steel layers can occur during the strip manufacturing process. An example of scored bronze is shown in Figure 7.15(c). Scoring of the steel can cause poor back contact in the application and localised overheating. Scoring of the bronze layer can cause an initiation site for fatigue, cavitation erosion or flow erosion.

Causes and prevention controls Sinter furnaces are often long, comprising of many different components (flatteners, support rollers, tensioners, hold down rollers, powder dies, weir plates or measuring devices). Any points of contact between the surface of the strip and the furnace components are potential causes of scoring.

7.5.4 Dimensional defects

Characterisation

Bimetal strips are usually planned to customer requirements for manufacturing bushes or half shell bearings. The overall thickness must be correct and within the specified tolerance, typically $\pm 0.05\text{mm}$ for bearing applications and $\pm 0.02\text{mm}$ for bush applications. As well as the bimetal thickness tolerance, it is important that the steel and lining thickness are also correct to their specified tolerances. Typically a maximum steel thickness is specified, since many bearing or bush components are bored, therefore

it is important that there is a minimum specified lining thickness left after the boring operation.

Causes and prevention controls

Dimensional defects can be caused by poor measuring techniques at the compaction rolling or final rolling operations, poor process capability of the rolling mill, poor planning of steel thickness, poor planning of as laid lining thickness or incorrect calculation of the percentage stretch of steel during the compaction and final rolling operations.

7.6 Conclusion

The results obtained by examination of defects established the main defect types that occur in high volume production of serial sintered bronze/steel bimetal strips. Establishment of main defect types facilitated the determination of prevention controls for their reduction or elimination and thus reducing scrap and the risk that components fail in the field. Furthermore, help for process engineers and technicians to determine the root cause for defects in serial production is provided by the fault tree analysis. Based on the obtained results, it can be concluded that most frequent defect types are porosity (app. 46%), delamination (app. 28%) and incorrect microstructure (app. 13%). Therefore these defects are the most important defects that need to be considered in the development of an online NDT technique. Other defects (hardness, lead movement, dimensional, cracks, blowholes, particle inclusions) are less frequent, but can still significantly impair the material performance. The type of bronze lining has an effect on the occurrence of certain defect types under the same or similar manufacturing conditions. Surface sweat of lead and blowholes occur only in leaded bronze, while all other defects were observed in leaded as well as lead-free bronze. The most significant defects porosity and delamination were considered for the NDT feasibility study with the prototype EMAT guided wave inspection system.

Chapter 7. Defects, causes and prevention controls in the continuous CuSn/steel
bimetal strip sintering process

Chapter 8

CuSn/steel bimetal strip online inspection feasibility study

In this chapter, the second project stream to reduce the business risk that CuSn/steel bimetal components fail in the field by 100% volumetric material NDT is described. Early defect detection would allow for the correction of the manufacturing process and thus the reduction of the defective material. The prototype online bond inspection system using guided waves generated with EMATs was employed for CuSn/steel bimetal strip inspection while the strips were processed continuously. Lamb phase and group velocity dispersion curves for CuSn/steel bimetal were calculated in the SAFE method and experimentally verified to identify potential wave modes for inspection. Online inspection trial results of full length defect-free and defective strips were statistically analysed and an alarm threshold for serial inspection was determined. The most important result is that the guided wave inspection system is able to online detect porosity defects above 3.1% and bond defects larger than 10 x 10 mm area or 20% of the bond interface in a harsh serial production environment, which nowadays are only detectable with destructive testing. The content of this chapter is based on the author's journal article *Development of S_1 guided wave mode using EMATs for online inspection of porosity and delamination defects in CuSn/steel bimetal strip production*, which is currently under review in the Journal of Nondestructive Evaluation.

8.1 Introduction

In the previous chapter it was highlighted that there is a need to develop an automated, online inspection technique to examine the quality of bronze/steel bimetal strips produced by the continuous sintering, compaction rolling, and resintering process. The development of the online inspection system for CuSn/steel bimetal is focusing on the detection of porosity and delamination defects, which combined account for about 74% of all defects in serial production. The same online prototype inspection system, which was used for Al/Al-Sn/Al/strips, was used for this case study. This work builds on previous research outcomes and addresses the questions, whether guided waves can be generated in sintered bronze/steel bimetal, which wave modes are most suitable for practical inspection, establish the system sensitivity to detect porosity and delamination defects and if online inspection is feasible.

8.2 Experimental procedure

8.2.1 Guided wave propagation analysis

The inspection experiments were set up in the pitch and catch configuration as shown schematically in Figure 8.1(a). The transducers were positioned at the steel side on opposite sides of the strip. Figure 8.1(b) is a schematic of the EMAT transducer and its interaction with the bimetallic sample. The functional principle of guided waves generated in the material using EMATs is the same as described in chapter 4.

Table 8.1 summarises the material properties considered for the guided wave propagation analysis. Two sample types with the same chemical composition of the bronze lining, but different steel types and dimensional characteristics were considered.

The Lamb phase and group velocity dispersion curves for CuSn8Ni1/steel bimetal in this study were calculated using the SAFE method and identified various wave modes that appeared to be good candidates for inspection. Excitation lines for the employed wavelengths are drawn on the phase velocity dispersion curves. The wave mode at the intersection between the excitation line and the phase velocity dispersion curve will

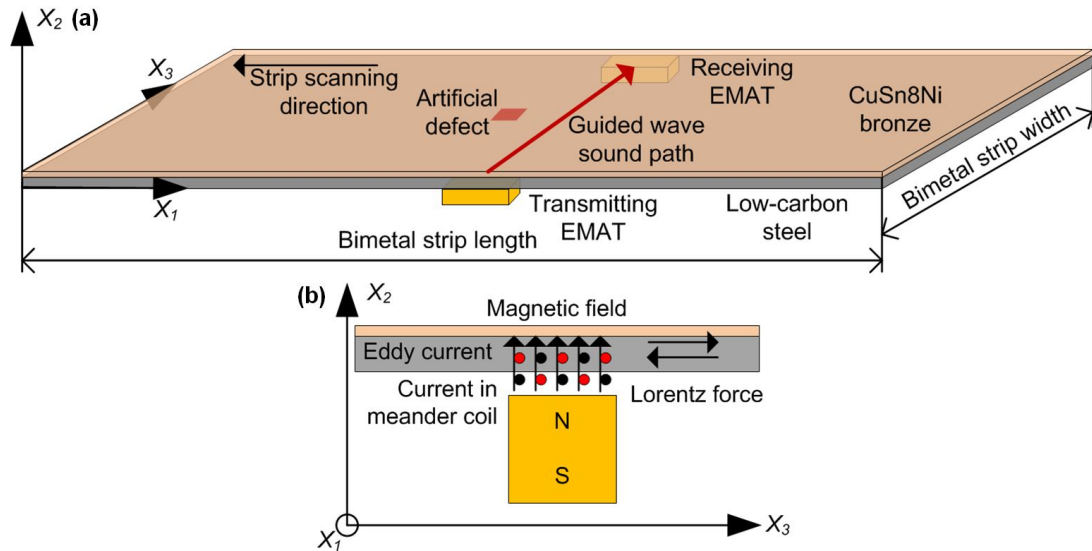


Figure 8.1: Schematic of EMAT transducers generating and receiving guided waves in CuSn8Ni1/steel bimetal plates: (a) sound path; (b) interaction with material

Table 8.1: Material properties of sintered CuSn8Ni bronze/steel bimetal samples

Properties	Sample type I		Sample type II	
	Layer 1	Layer 2	Layer 1	Layer 2
Material	CuSn8Ni1	Medium-carbon steel	CuSn8Ni1	Low-carbon steel
Young's Modulus (GPa)	115	203	115	203
Poisson Ratio	0.35	0.303	0.35	0.303
Density (kg/m ³)	8.8	7.85	8.8	7.85
Width (mm)	136.00	152.00	133.00	159.00
Thickness (mm)	0.55	1.49	1.00	1.07

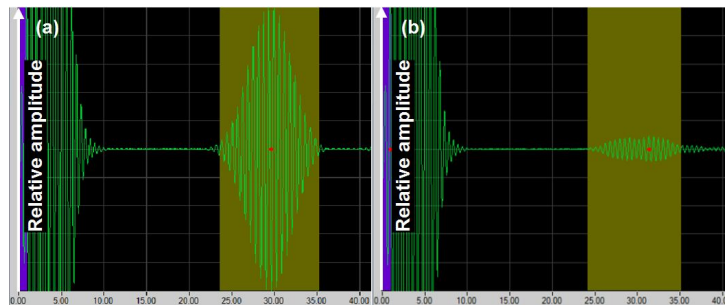


Figure 8.2: A-scan for (a) defect free and (b) defective bronze/steel bimetal plates

be efficiently excited when the corresponding frequency is used. The wavelength was controlled by the period of the meander coil. Since the prototype system discussed in this paper will be industrialised as a commercial product, the wavelengths and frequencies of the employed wave modes are not revealed. Instead, the different wavelengths are described with variables A-C, and used frequencies with letters T-Z. The empirical relationship between defects and guided waves in all experiments is when guided waves encounter a defect, this causes destructive interference, which converts incident wave energy into radiation energy in all directions, which results in attenuation. The remaining wave energy that propagates to the receiving EMAT transducer decreases, which is measured and shown as a lower signal amplitude in the A-scan. Figure 8.2(a) shows an A-scan of a sample with good quality and reference amplitude. Figure 8.2(b) shows how the amplitude drops for a defective sample relative to the reference amplitude for a defect-free sample. During inspection, the maximum amplitude within the TOF filtering gates is used to indicate defective material with the attenuation method.

8.2.2 Experimental set up

The industrial strip processing line and prototype inspection system that was used for the experiments is shown in Figure 8.3. The bronze/steel bimetal strip is under tension between the coiler and uncoiler. The coiler applies a force to pull the strip and the uncoiler continuously provides the strip for inspection and applies back tension. A rolling mill is used to only touch roll and guide the strip to the EMAT probes, which are mounted onto a probe assembly frame directly below the strip. The assembly frame



Figure 8.3: Industrial strip processing line with installed prototype EMAT inspection system

contains remote signal conditioning boxes to connect the probes to the DAQ system, and pneumatic components for passive compliance between the probes and moving strip. Wear plates that are in sliding contact with the steel protect the probe surfaces. The DAQ system has a programmable temate® software installed, which was used for data processing, analysing and presenting. The same temate® software as introduced in section 6.1.2 was used for this feasibility study.

8.2.3 Sample preparation

All sintered bronze/steel bimetal strip samples in this study were produced on the continuous sintering, compaction rolling, and resintering production plant at MAHLE Kilmarnock, Scotland. The sample manufacturing process was the same as described in chapter 7.2. Table 8.2 summarises the samples that were used in this study. GQR-I is a good quality reference plate of sample type I and was produced without altering the process, GQR-II was used as reference for sample type II. Sample AWOL-I had a 60 mm diameter area of a disk without bronze lining, which was vacuumed after the powder layer was spread and before the area of the strip entered the sinter furnace. For sample BS-I, no powder was spread to obtain bare steel, which has the same thickness as in a sample type I bimetal. Various defective type II samples were obtained from production, which contained different degrees of porosity defects. NCS-II-P1 was a non-conformance sample with max. 0.21% porosity in a local area, NCPS-II-P2 had

Table 8.2: Sintered bronze/steel bimetal samples for inspection

Sample #	Sample reference	Sample type	Length (m)	Defect	Size	Sample description / preparation
1	GQR-I	I	1 m	none	-	Good quality reference plate
2	AWOL-I	I	1 m	Circle w/o CuSn8Ni	∅ 60 mm	Area w/o CuSn8Ni lining
3	BS-I	I	1 m	no CuSn8Ni	-	Bare steel
4	GQR-II	II	1 m	none	-	Good quality reference plate
5	NCS-II-P1	II	1 m	Porosity	max. 0.21%	Process deviation resulting in defect
6	NCS-II-P2	II	1 m	Porosity	max. 3.1%	Process deviation resulting in defect
7	NCS-II-P3	II	1 m	Porosity	max. 7.1%	Process deviation resulting in defect
8	ADT-II-100x20	II	1 m	Delamination triangle	100x20 mm	Aluminium hydroxide / titanium dioxide
9	SPS-II-R	II	45	none	-	Good quality serial production strip reference
10	NCS-II-D	II	59	Delamination	20.9-55.6%	Process deviation resulting in defect

max. 3.1% porosity and NCS-II-P3 max 7.11% porosity. In sample ADT-II-100x20, a delamination defect in the shape of a triangle with 100 mm height and 20 mm width was deliberately implanted using a 1-methoxy-2-propanol / aluminium heat resistant liquid. SPS-II-R was a 45 m long strip from serial production without any known defects and was used as good quality serial production reference strip for type II dimensional characteristics. Strip NCS-II-D was 59 m long and was obtained from serial production. It has delamination spots throughout the coil. Micrographs were taken from all samples after non-destructive testing was completed to correlate the results. Figure 8.4 shows photographs of the samples that were used in this study. The defective areas are highlighted.

8.3 Results and discussion

8.3.1 Wave mode selection

For the identification and selection of potential wave modes that are suitable for practical inspection, a comparison study of A_0 , S_0 , A_1 , S_1 , A_2 and S_2 modes for sample type I was done. The phase and group velocity curves shown in Figure 8.5 were calculated in the SAFE method as described in chapter 4.2. The same wavelength λ was used in all experiments, and the excitation line is drawn on the phase velocity dispersion curve. Each wave mode at the intersection between the excitation line and the phase velocity dispersion curve was excited when the corresponding frequency was used. The group velocity curve provided valuable information about dispersion of the

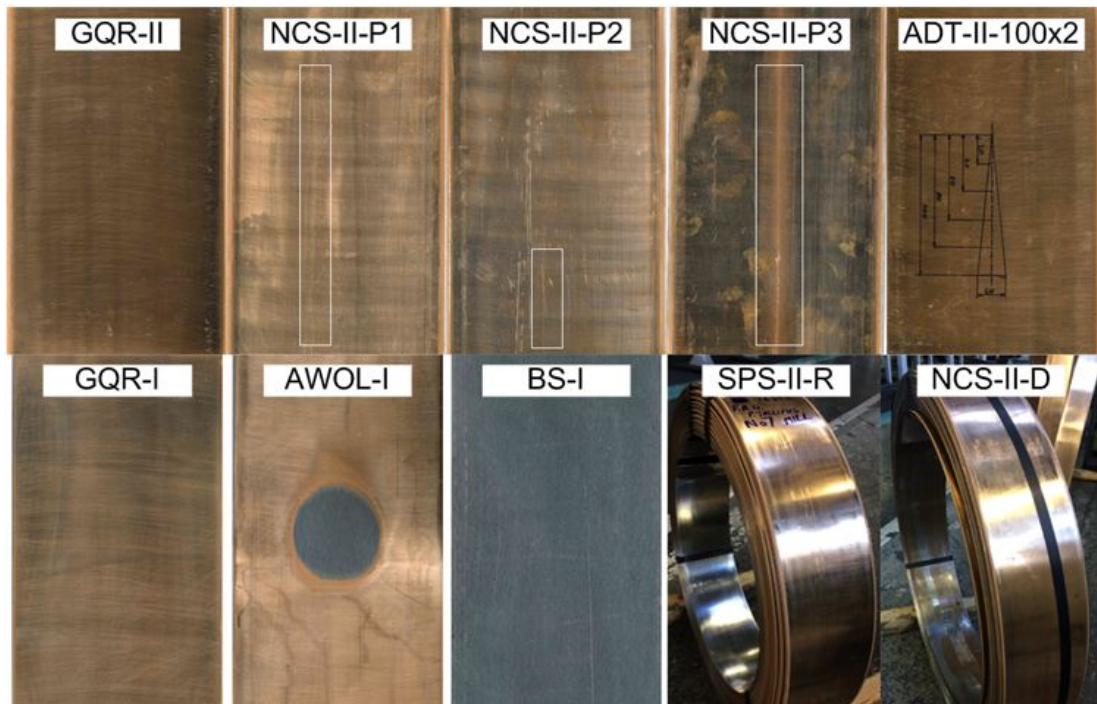


Figure 8.4: Photographs of samples indicating the defective areas

wave mode. For each wave mode, A-scans were obtained and systematically compared for samples GQR-I, AWOL-I and BS-I. The selection of the best candidate was based on the criteria *non-dispersive, low attenuation, high defect sensitivity and good wave mode detectability*.

The phase and group velocities for each frequency and wavelength in bimetal and bare steel for sample type I are summarised in Table 8.3. The group velocity was used to identify wave modes by calculating their time-of-flight and comparing it to the observed time of arrival. Figure 8.6 shows the A-scans for samples GQR-I, AWOL-I and BS-I and modes A_0 , S_0 , A_1 , S_1 , A_2 and S_2 .

It was possible to excite a pure A_0 wave mode in samples GQR-I, AWOL-I and BS-I. Since the A_0 frequency T in bimetal is similar to the A_0 frequency in bare steel (0.651 MHz) for the same wavelength A , and the group velocity in bare steel is 3.16 mm/s compared to 3.03 mm/s in bimetal, the envelope of the ultrasonic pulse in steel arrives earlier than the 32 to 51 s bimetal inspection time gate. Therefore, A_0 is not suitable for inspection, as the signal for bare steel could be easily misinterpreted as flawless bimetal.

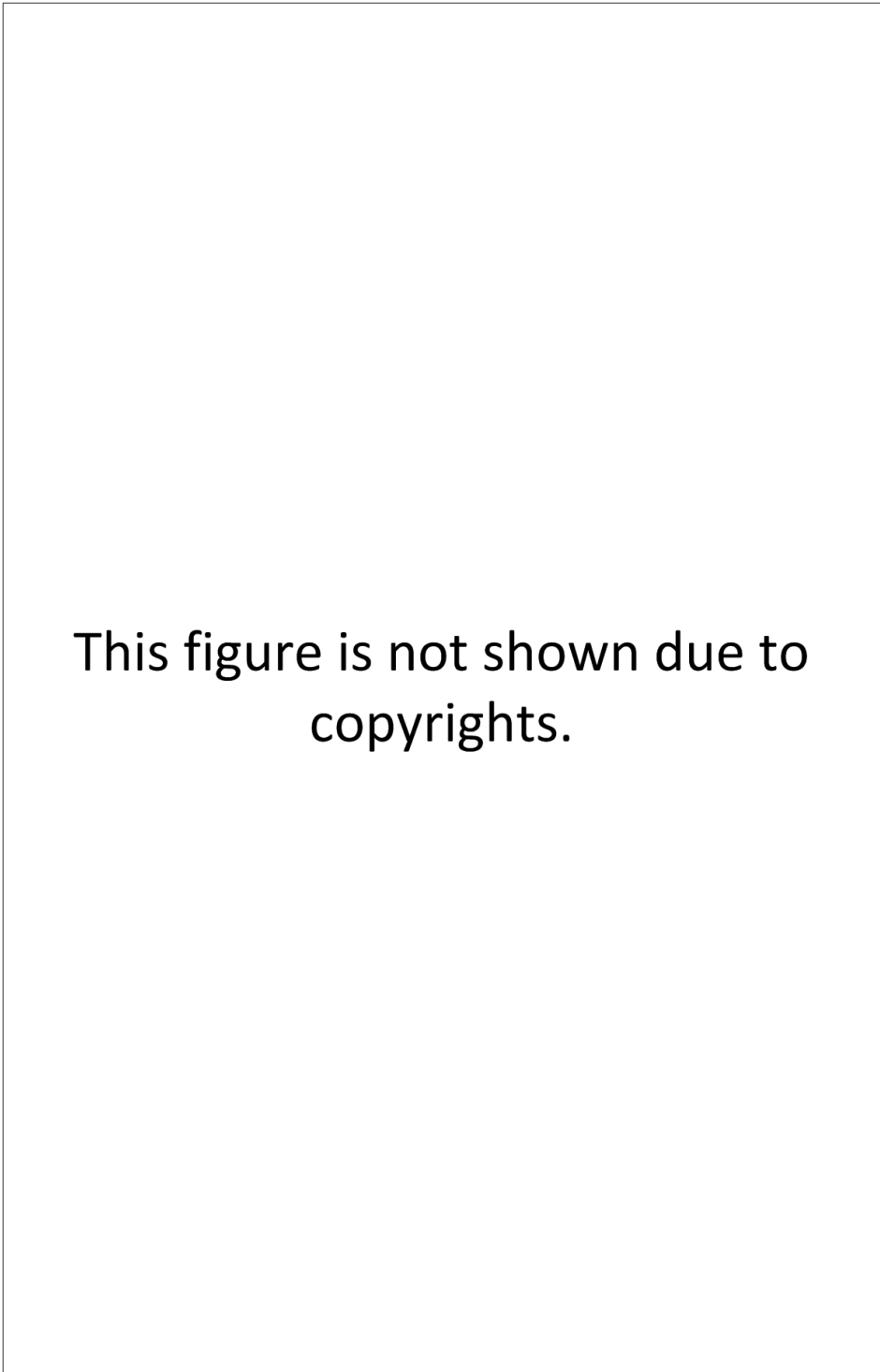


Figure 8.5: Sample type I: (a) sintered bronze/steel bimetal phase velocity curve and (b) group velocity curve, (c) bare steel phase and (d) group velocity curve (supplied by Innerspec)

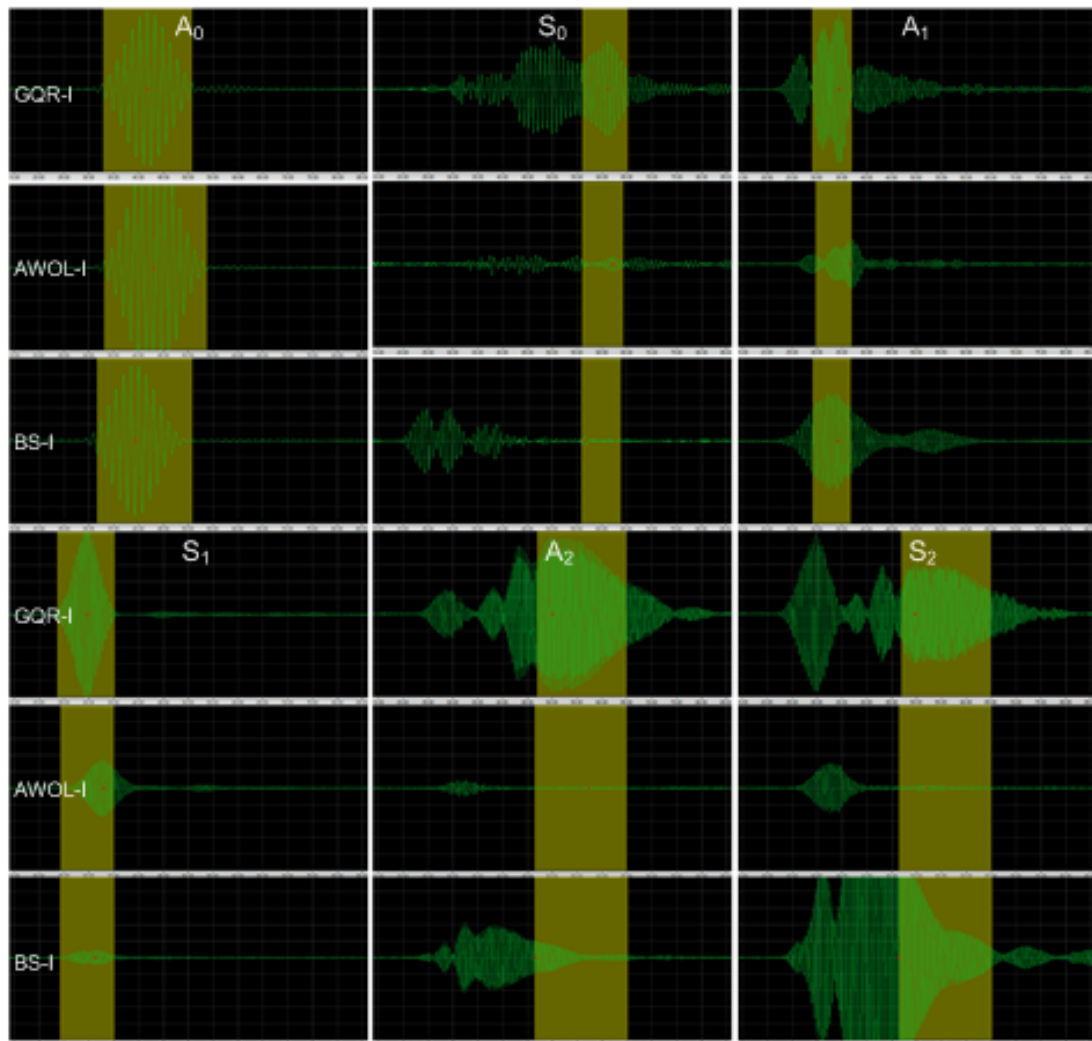


Figure 8.6: Sample type I: A_0 , S_0 , A_1 , S_1 , A_2 and S_2 wave modes in GQR-I, AWOL-I and BS-I samples

Table 8.3: Phase and group velocity for modes A_0 , S_0 , A_1 , S_1 , A_2 , S_2 and wavelength A in sample type I bare steel and sintered bronze/steel bimetal sheets

Material	Mode	Frequency (MHz)	Wavelength (mm)	Phase Velocity (mm/ μ s)	Group Velocity (mm/ μ s)	Gain (dB)
	A0	0.651	A	2.31	3.16	12
	S0	1,359	A	4.83	3.27	30
Low-carbon steel	A1	1,826	A	6.5	3.75	14
	S1	1,943	A	6.89	2.37	-4
	A2	2,815	A	10	3.19	14
	S2	3,228	A	11.5	0.603	14
	A0	T	A	2.37	3.03	12
Sintered bronze/ steel bimetal	S0	V	A	4.03	2.03	30
	A1	W	A	4.77	2.3	14
	S1	X	A	5.87	4.07	-4
	A2	Y	A	8.19	2.64	14
	S2	Z	A	7.48	2.04	14

Modes S_0 and A_1 have similar excitation frequencies V and W in bimetal, therefore interference between the two modes was observed. S_0 and A_1 both have a steep gradient in the group velocity curve, which is explaining that the modes are dispersive. S_0 is sensitive to detect defects, but 30 dB gain was required due to attenuation. Although the bimetal frequency V is similar to the S_0 1,327 MHz frequency in steel, the S_0 group velocity in bare steel is 2.87 mm/s and relatively high compared to 2.03 mm/s for S_0 in bimetal, and therefore S_0 in sample BS-I already arrives between 27 and 33 s, which is out of the 56 and 64 s bimetal inspection time gate. On the contrary, S_0 in bare steel arrives in the same 29 to 33 s time gate for A_1 mode in bimetal, therefore A_1 is not suitable for inspection. S_1 at frequency X offers excellent sensitivity to detect defects, with the lowest attenuation of all tested modes and a used gain of -4 dB. The envelope of the ultrasonic pulse is narrow and allows easy detectability, since the mode is non-dispersive as can be seen in the bimetal group velocity curve. When exciting wave modes A_2 and S_2 in bimetal, interference of multiple modes can be observed since frequencies Y and Z are similar, which makes unambiguous differentiation of the modes difficult. Both modes are sensitive to the defect in sample AWOL-I, but S_2 frequency also excites S_1 in bare steel, and therefore BS-I could be misinterpreted as good quality. A_2 and S_2 are both dispersive in bimetal. The characteristics of wave modes A_0 , S_0 , A_1 , S_1 , A_2 and S_2 were rated between 1 and 3 in the decision matrix shown in Table 8.4 and the result was that wave mode S_1 is most suitable for practical inspection of

Table 8.4: Decision matrix for the selection of the most suitable wave mode for inspection (higher is better)

Characteristic	A ₀	S ₀	A ₁	S ₁	A ₂	S ₂
Non-dispersive	2	1	1	3	1	1
Low attenuation	2	1	2	3	2	2
High sensitivity	1	3	1	2	2	1
Good detectability	3	2	2	3	1	1
Total	8	7	6	11	6	5

Table 8.5: Phase and group velocity for mode S₁ and wavelengths A, B and C in sample type II

Material	Mode	Frequency (MHz)	Wavelength (mm)	Phase Velocity (mm/μs)	Group Velocity (mm/μs)	Gain (dB)
Sintered	S1	T	A	5.64	4.1	-9
bronze/steel	S1	V	B	5.38	3.28	-1
bimetal	S1	W	C	4.91	2.17	25

sintered bronze/steel bimetal.

8.3.2 Wave mode optimisation using non-conformance samples

Sample type I defects were self-evident to detect, and their purpose was to validate that guided wave modes can propagate either in bimetal or steel only. Non-conformance samples of type II with more sophisticated defects were obtained from production to optimise the frequency and wavelength of the selected S₁ inspection mode. Three different wavelengths A, B and C appeared to have suitable inspection points; their excitation line was drawn on the phase velocity dispersion curve in Figure 8.7(a) to mark the intersection with the phase velocity curve. This determined the frequency at which mode S₁ is excited for wavelengths A, B and C. Figure 8.7(b) shows the group velocity curve for mode S₁ and wavelength B in sample type II. For each wavelength, A-scans were obtained and systematically compared for samples GQR-II, NCS-II-P1, NCS-II-P2 and NCS-II-P3. The selection of the best candidate was based on the criteria *non-dispersive*, *low attenuation*, *high defect sensitivity* and *good wave mode detectability*. The calculated phase and group velocities for mode S₁ and wavelengths A, B and C that were used for the mode identification are summarised in Table 8.5.

Figure 8.8 shows the A-scans that were obtained for the various wavelengths and samples. It can be seen that mode S₁ and wavelength A is non-dispersive, has low



Figure 8.7: Sample type II: (a) sintered bronze/steel bimetal velocity curve indicating inspection points for wavelengths A, B and C, (b) group velocity curve for wavelength B (supplied by Innerspec)

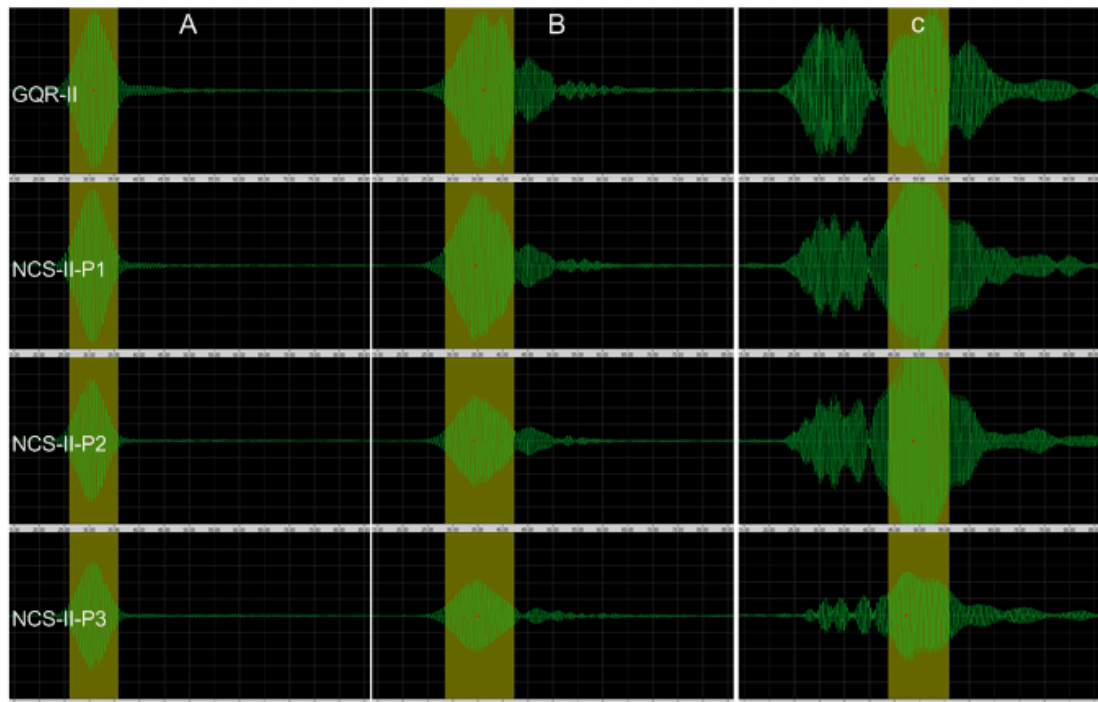


Figure 8.8: Sample type II: S_1 mode with wavelength A, B and C (frequencies T, V and W) for samples GQR-II, NCS-II-P1, NCS-II-P2 and NCS-II-P3

attenuation and good detectability, but sensitivity for the defects is moderate. Mode S_1 and wavelength B in contrary is most sensitive to the defects compared to wavelengths A and C, while attenuation is low (-1 dB) and the wave mode is easily detectable. Wavelength C is dispersive compared to wavelength B, which can be seen by the wider envelope of the ultrasonic pulse. It can be seen that another wave mode, A_2 , gets excited in the samples when wavelength C and frequency V is used, which arrives later than the set inspection gate between 26 and 48 s. When exciting mode S_1 and wavelength C, interference of multiple modes was observed, this makes unambiguous detection of mode S_1 difficult. Furthermore wavelength C is dispersive and has a high attenuation, 25 dB gain had to be used to amplify the signal for sample GQR-II to obtain 100% relative amplitude. Figure 8.9 plots the median and quartiles of the relative amplitudes that were measured in samples GQR-II and the non-conformance porosity defect samples NCS-II-P1, NCS-II-P2 and NCS-II-P3 using the different wavelengths A, B and C (frequencies T, V and W) for wave mode S_1 . Each sample was measured

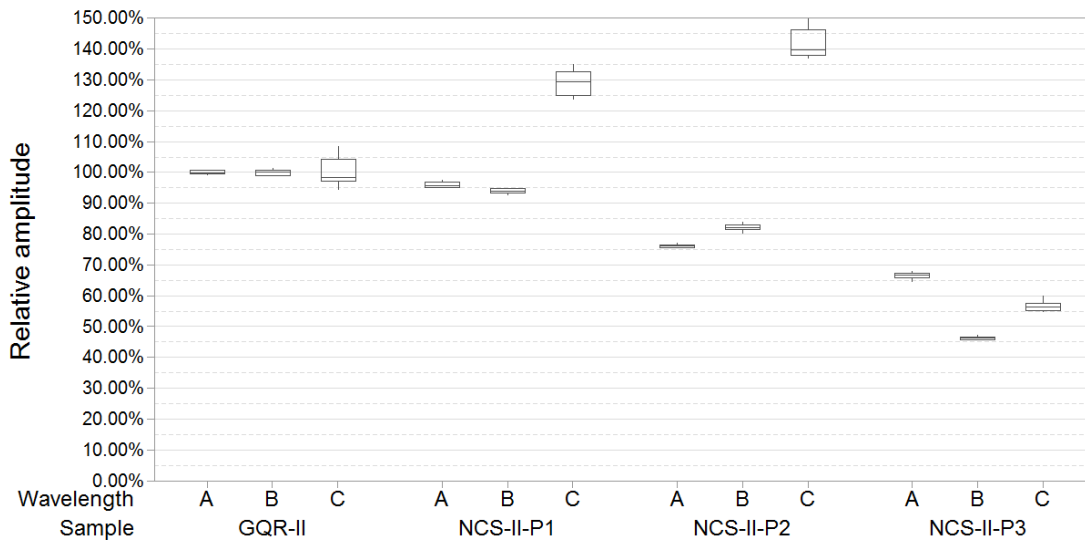


Figure 8.9: Boxplot of measured amplitude for samples GQR-II, NCS-II-P1, NCS-II-P2 and NCS-II-P3 when scanned through the sensors for S_1 mode and different wavelengths A, B and C

ten times. When comparing the relative amplitude per defect for wavelengths A and B, it can be seen that sensitivity for samples NCS-II-P1 and NCS-II-P2 are comparable, but wavelength B is most sensitive to NCS-II-P3, while signal variance due to noise for sample GQR-II is low. The amplitude increase for wavelength C in samples NCS-II-P1 and NCS-II-P2 is likely caused by constructive/deconstructive interference of the different modes caused by the porosity defect and noise due to the high gain. When using only a lower than the reference amplitude alarm threshold, these defects would remain undetected for wavelength C. Therefore wave mode S_1 and wavelength B (and frequency V) is most suitable for practical inspection of porosity defects. The detectability of defects depends on the alarm threshold, which is further discussed in the following sections.

Once non-destructive testing of samples GQR-II, NCS-II-P1, NCS-II-P2, NCS-II-P3 was completed, micrographs were taken to assess the condition of the control sample and percentage of porosity in samples NCS-II-P1, NCS-II-P2, NCS-II-P3. The micrographs are shown in Figure 8.10. In total three micrographs per sample were assessed, one in the centre of the defect, and one to the left and one to the right adjacent to the defective area. The micrographs for sample GQR-II show that the sample is flawless,

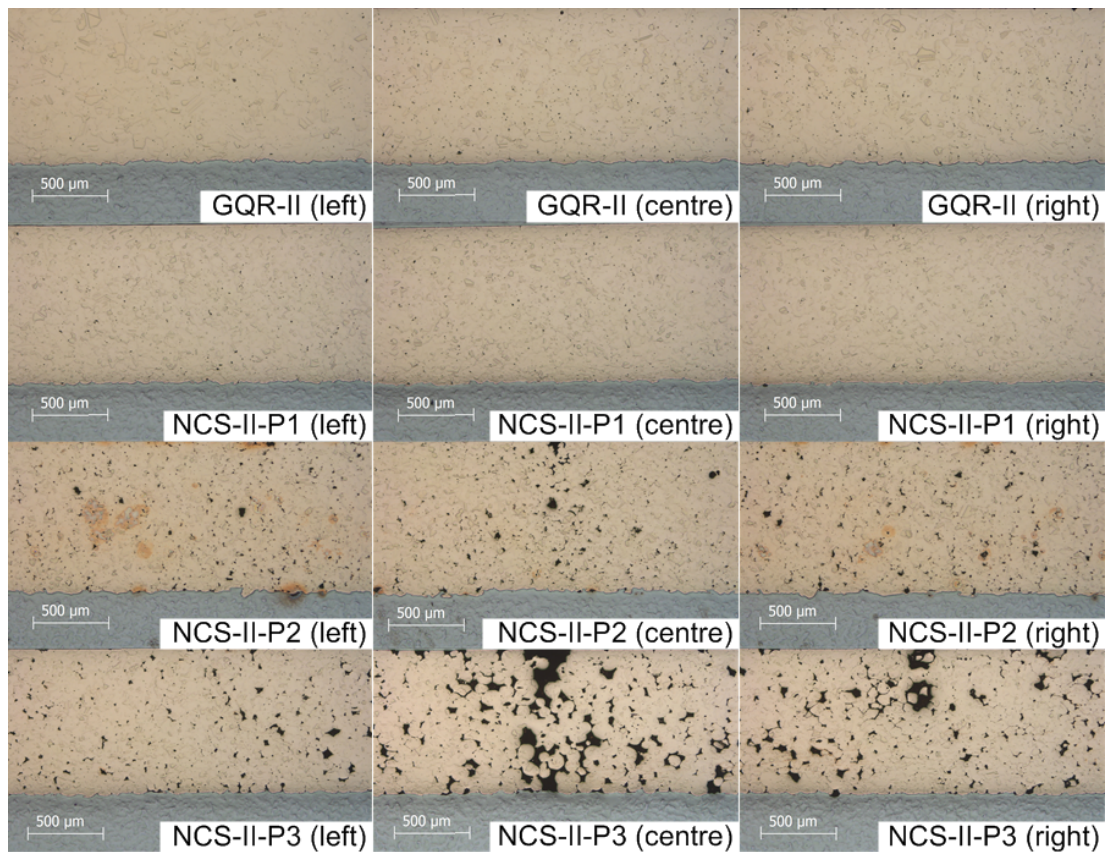


Figure 8.10: GQR-II, NCS-II-P1, NCS-II-P2 and NCS-II-P3 micrographs

and therefore it was suitable as a control sample. The defect shown in Figure 8.4 for sample NCS-II-P1 appeared to be only superficial, as no trace of it was found in the micro sections. This is in line with the measured amplitude in the boxplot, which is not significantly different from sample GQR-II for wavelength B. Sample NCS-II-P2 had max. 3.1% porosity and sample NCS-II-P3 had up to 7.11% porosity.

Since mode S_1 , wavelength B and frequency V performed best for porosity defects, the same mode was employed for further studying of the delamination type defect in sample ADT-I-100x20. Figure 8.11 plots the signal amplitude relative to the distance from the start of the measurement and the theoretical delamination width. The measurement points between 0 to 90 mm were good quality and the amplitude was approximately 100%. Between 90 to 140 mm distance from start of measurement, the theoretical delamination width of the triangle increased to 10 mm, but the measured

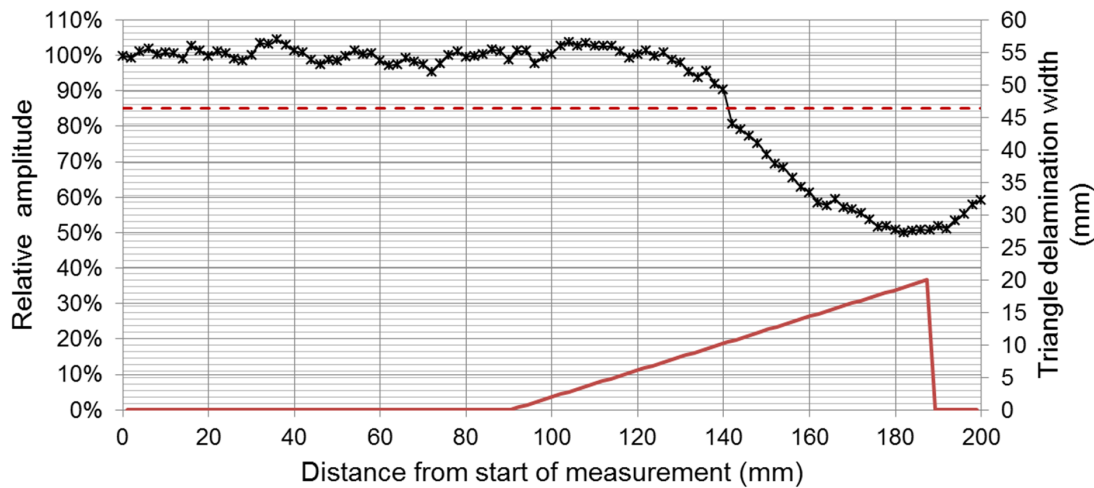


Figure 8.11: Relative amplitude of through transmission guided wave signal for sample ADT-II-100x20, S_1 mode and wavelength B

amplitude was not significantly different, hence delamination defects would remain undetected. For delamination width between 10 and 20 mm, the amplitude drops significantly and there is a correlation between delamination width and amplitude. A debonded interface larger than 10 mm x 10 mm is likely to be detected due to the significant amplitude drop. In order to assess the bond interface, in total 18 micro samples at 0, 20, 40, 60, 80 and 100 mm height of the triangle were taken. Each micro sample measured 20 mm width. The microscope field of view at x50 magnification was about $2400 \mu\text{m}$, and eight micrographs across the width of each micro sample were taken to cover the complete width of the delamination triangle. The micrographs are shown in Figure 8.12. It can be seen that the actual debonded interface width is broadly in line with the theoretical width of the deliberately implanted delamination triangle, and that only starting at $h = 40$ mm the bond interface would not have been acceptable. The step change in delamination between $h = 20$ mm and $h = 40$ mm is also in line with the amplitude drop at this position of the triangle. Furthermore it can be seen, that there are only debonded spots, but the debonded interface is not continuous.

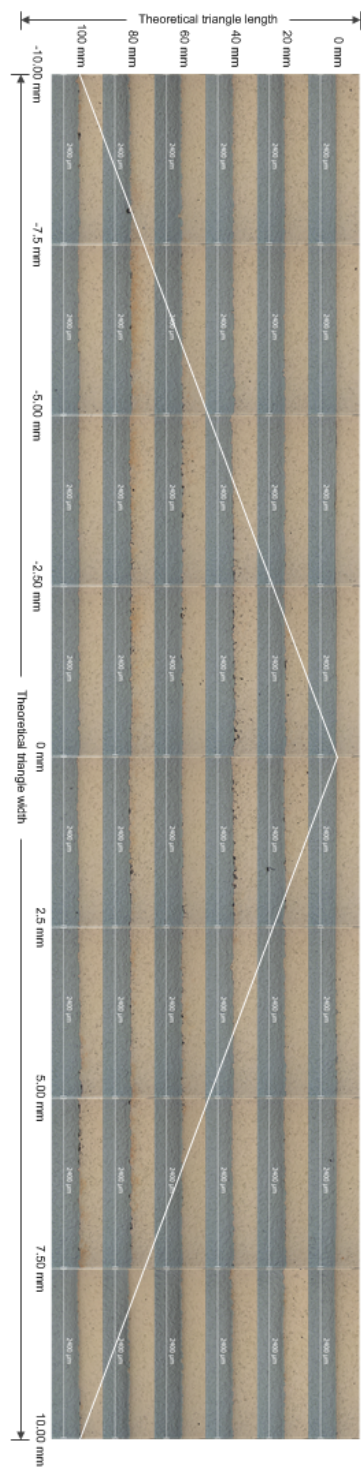


Figure 8.12: Sample ADT-II-100x20 micrographs at $h = 0, 20, 40, 60, 80$ and 100 mm comparing the actual and theoretical delamination width

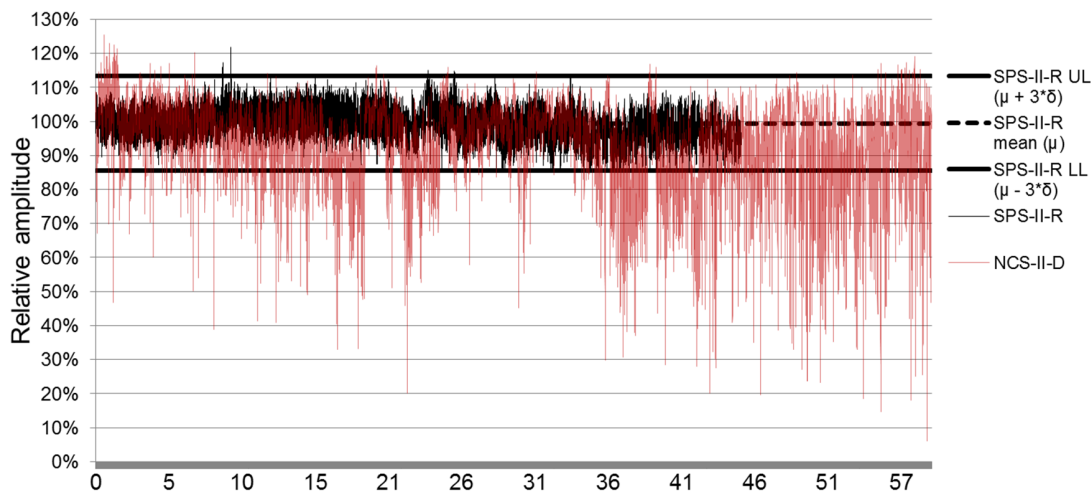


Figure 8.13: Maximum A-scan trace for samples SPS-II-R and NCS-II-D online inspection trials

8.3.3 Online inspection

Wave mode S1, wavelength B and frequency V were employed for online inspection of reference strip SPS-II-R and defective strip SPS-II-D with non-conformance delamination. Figure 8.13 shows the maximum A-scan trace for both samples. For SPS-II-R, the mean $\mu = 99.43\%$ and standard deviation $\delta = 4.65\%$ were calculated. 99.73% of the measured values lie between three standard deviations of the mean. The 113.68% upper limit UL ($\mu + 3\delta$) and 85.48% lower limit LL ($\mu - 3\delta$) are considered as signal variation for good quality due to local material property changes and electrical noise.

Signals below LL are considered as defective; therefore a lower alarm threshold was set at 85.5%. Since the amplitude for NCS-II-D dropped significantly below the alarm threshold, it was expected that there were delamination defects at these positions. Once guided waves inspection of SPS-II-D was completed, in total 33 micro sections at x500 magnification (2,640 fields of views) were assessed to determine the percentage of delamination and plot it relative to the measured signal amplitude. At each down strip position where the amplitude dropped, three samples were cut, one at the left edge, centre and right edge location of the strip. The strip positions where the microsamples were taken were at the relative amplitudes 81%, 70%, 64%, 58%, 54%, 44%, 37%, 29% and 21%. Each micro section showed $l = 20$ mm bond interface, in total 60 mm

bond interface were inspected at each location of h . The delamination percentage was calculated as per Equation 7.1 and as average of in total three samples, one from the left edge, one from the centre and one from the right edge of the sheet.

Figure 8.14 plots the relative amplitude and percentage of delamination. Four quadrants were defined, which are (1) acceptable bond/above threshold, (2) acceptable bond/below threshold, (3) non-conformance bond/below threshold and (4) non-conformance bond/above threshold. According to the current materials standard, the maximum acceptable delamination is 20%. The alarm threshold SPS-R-II LL was 85.5%. These thresholds confine the four quadrants. Sample GWR-II had 2.5% delamination and 100% relative amplitude, and is therefore in quadrant 1. Any data points in quadrant 2 would be false alarm, since the bond quality would be within specification, but the amplitude dropped below the alarm threshold and caused the alarm to scrap material. There were no data points recorded in quadrant 2. All data points from NCS-II-D were plotted in quadrant 3, which means that for samples with non-conformance delamination above 20%, the relative amplitude drops below the threshold and is therefore detectable. However, there was no linear correlation between relative amplitude and delamination percentage observed. Therefore is it not possible to extrapolate the defect size based on the amplitude drop. Gao et al. (2010) observed the phenomenon of cyclic relationship between the guided wave response and the delamination width in guided waves inspection of brass/copper/brass multi-layered sheets, and provided an explanation based on the theory of wave mode decomposition and recombination. It appears that also in CuSn8Ni1 bronze/steel the relation between delamination and signal amplitude has a periodic pattern instead of a monotonic change. There were no data points recorded in quadrant 4. There are two possible explanations for this, either the amplitude for all defective material dropped below the threshold and was therefore plotted in quadrant 3, or due to cyclic behaviour of the amplitude, the defective material was not detected. Further work based on FEM simulation would be necessary to confirm the existence and determine the period of the cyclic behaviour. In this case, a two-channel technique with complementary performance to detect delamination of all sizes could be developed. Based on the inspection results from sample

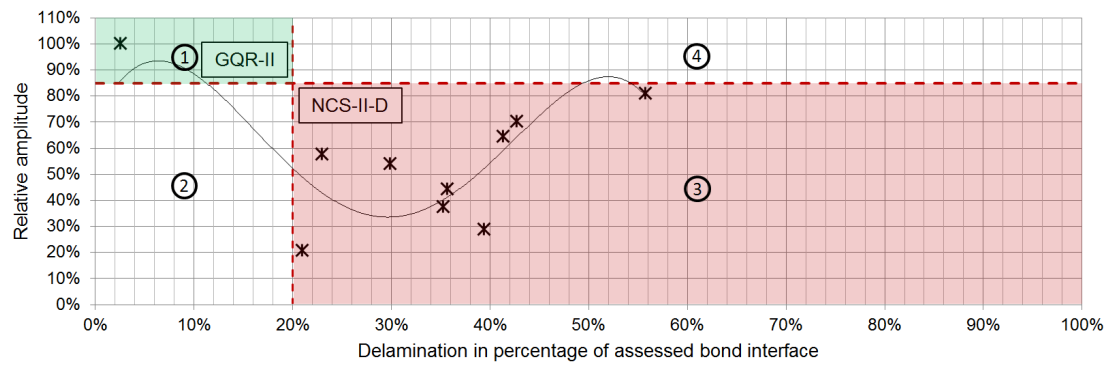


Figure 8.14: Scatter plot diagram of relative amplitude and delamination percentage for samples GQR-II and NCS-II-D

ADT-100x20 and NCS-II-D, the current inspection prototype system is capable to on-line detect delamination larger than 10x10 mm area or 20% delamination across the width of strips.

8.3.4 Serial inspection alarm threshold

The ideal defect alarm threshold as a percentage of good bond reference amplitude is a balancing act between maximising the sensitivity to detect defects and minimising the false alarm rate. The signal variation in defect free strips is due to local material property changes such as thickness variation, porosity or delamination within specification and electrical noise. Based on the signal variation for sample SPS-II-R in Figure 8.13, and the 85.48% LL alarm threshold, the false alarm rate would be 0.27%, which is reasonably low and considered acceptable. Based on this threshold, mode S1, wavelength B and frequency V, porosity defects above 3.1% in a narrow area, delamination spots in a 10x10 mm area, or 20% delamination across the width of strips can be detected. The maximum allowed delamination percentage, without continuous delamination exceeding 0.25 mm, is 20% for the CuSn8Ni bronze/steel bimetals considered in this study. Hence, the system sensitivity for delamination detection is adequate for the application. The threshold could be adjusted depending on the required sensitivity and acceptable false alarm rate.

8.4 Conclusions

The capability of the EMAT guided waves inspection system to detect porosity and delamination defects in sintered bronze CuSn/steel bimetal strips was researched. The technique was successfully employed in the industrial strip processing line for online inspection. This verifies that the developed NDT technique also works for other strip types than Al/Al-Sn/Al/steel bimetal. Micrographs of the samples were assessed and the percentage of porosity and delamination determined. Based on the required defect sensitivity and acceptable false alarm rate, an alarm threshold as percentage of the reference amplitude for good quality was determined. The system is capable to detect delamination and porosity defects that are nowadays only detectable with destructive testing, while 100% material volume is inspected.

Chapter 9

Recommendations for the final inspection system

This chapter summarises the inspection system improvements that were considered in the serial inspection technical machine specification.

9.1 Place of installation

One of the key questions for the industrialisation of the guided waves inspection system is the place of installation. For the industrialisation project in the Kilmarnock plant, three alternatives were considered, which were 1) integration into the A6 continuous CRB line, 2) integration into an existing machine vision final inspection line (SIC or Weybridge line), or 3) design and commissioning of a new, dedicated bond defect final inspection line.

9.1.1 Required inspection line machine components

The minimum required machine components for an inspection line are an uncoiler, inspection DAQ system, scrap marker and upcoiler. In addition there are optional machine components, which are required depending on the inspected product type. For non-silicon containing Al-Sn alloys with high tin content, an interleaf foil coiler is required. This is because liquid tin globules can form on the lining surface during

bimetal annealing due to the low tin melting point (231.9 °C). In order to avoid contact with the steel backing, an interleaf foil is coiled between each layer, which must be removed at final inspection. For Si-containing Al-Sn alloys, which are heat-treated in the fluidised bed process, a lining brush is required. This is because the ceramic beads media can under certain circumstances adhere to the Al-Sn lining and needs to get brushed off. To process coils for export, an oiling station is required to protect the steel from corrosion. A shear is required to cut inspection samples and cut out scrap. The usage of existing machinery must be considered in the design of the NDT inspection system. Furthermore the inspection line must be flexible to inspect different products.

9.1.2 Criteria for selection of industrialisation scenario

The criteria for the selection of an industrialisation scenario were systematically identified, analysed and rated in a decision matrix. The decision criteria were categorised into three categories:

Technological

- Usage of existing machinery
- Difficulty of mechanical integration (access, line speed, vibration, ambient influences)
- Effect of post rolling bimetal annealing on system sensitivity to detect defects
- 100% volumetric material inspection requirement
- Production line capacity utilisation

Cost of implementation and running cost

- Required capital expenditure
- Variable operating costs (consumables, labour, depreciation)

Operating excellence

- Flow of material in production
- Impact of inspection machine technical downtime on production efficiency
- Early detection of defects to avoid further value adding
- Readiness for sintered CuSn/steel bimetal inspection

9.1.3 Industrialisation scenarios

Commissioning of a new bond defect inspection line

The development and commissioning of a new sub surface defect inspection line has the advantage that all machine components could be ideally arranged around the inspection system. The strip guidance system could be designed in such a way to control the gap between strips and sensors to avoid false alarms because of lift-off. However, the required capital expenditure for a complete new line with all required components was too high and would have made the project not economically viable. Furthermore, a dedicated bond inspection line would have added an additional process step and increased manufacturing cost, which could not be passed onto the customer.

Integration into existing CRB line A6

Figure 9.1 shows the continuous CRB line in Kilmarnock that was considered for the in-process installation of the inspection system. The line has a material buffer between the CRB mill exit and coiler, which enables the bonding operation to run continuously. This location was considered for the installation of the inspection system. The main advantages would be 100% volumetric in-process control directly after bonding, which would enable correction of the process in case of defects. Furthermore, no additional inspection operation would be introduced. Disadvantages of this solution are difficult mechanical integration, because the strips are not permanently under tension, line speed variation and vibration. As shown in section 5.2.1, the smallest detectable steel debris defect before bimetal annealing is 5x5 mm compared to 1x1 mm post rolling



Figure 9.1: Continuous CRB line in Kilmarnock

annealing (final inspection). Furthermore, the inspection system set up time of the current inspection system would cause additional downtime with a negative impact on productivity of the continuous CRB line.

Integration into existing machine vision final inspection line SIC

Figure 9.2 shows the SIC machine visual inspection line in Kilmarnock, which was selected for the serial industrialisation of the guided waves inspection system. The line has all required machine components to inspect the complete product portfolio, which minimises the required capital expenditure. The material does not require additional handling because the visual inspection and bond inspection is carried out in the same operation, which also minimises the running cost. Both inspection systems, for surface and bond inspection, will be linked to the scrap marker via a PLC to automatise the marking of defective strips. Disadvantage of the machine vision inspection line is that the capacity is not sufficient to inspect 100% of all the material that is produced in Kilmarnock. However, the modular design of the system will allow that the system



Figure 9.2: SIC machine vision final inspection line in Kilmarnock

can be transferred to the continuous CRB line in future once the inspection system has proven its robustness. The solution to integrate the NDT inspection system into the existing machine vision final inspection line SIC scored highest in the decision matrix. Therefore it was decided to develop the technical machine specification for the integration into the machine visual inspection line.

9.2 EMAT arrays and multi lane scrap marker to improve material yield

Figure 9.3(a) shows a plan view of a pair of EMAT transmitter and receiver that was used in the prototype machine. This configuration was introduced in section 5.1.3. The disadvantage of only one pair of EMATs is that defects across the width of strips cannot be located. This means that when a defect is detected, the full width of the strip has to be scrap marked. However, strips that are manufactured in the CRB line

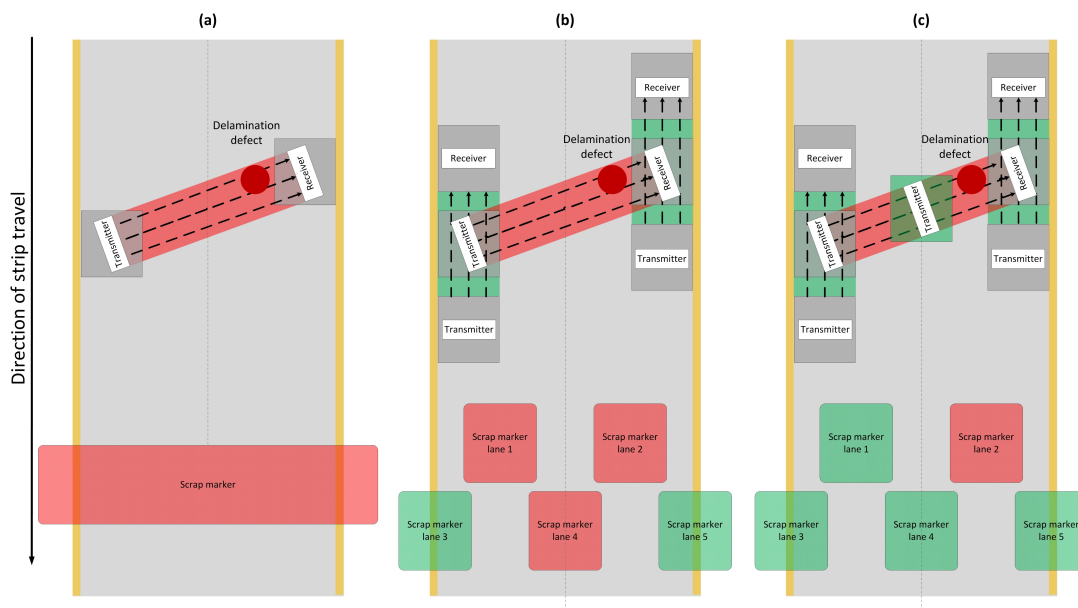


Figure 9.3: EMAT arrays and scrap marker that result in different material yield: (a) 1-channel system and scrap marker with lowest yield in case of a defect, (b) 3-channel system and multi-lane scrap marker with moderate yield and (c) 4-channel system and multi-lane scrap marker optimised yield

are up to 310 mm wide and are slit into multiple, more narrow strands. Depending on the final product, the strip can be slit into three to 15 individual strands. Hence, in the worst case the bond defect affects only one out of 15 strands (6.7%), but 100% of the material must be scrapped, which results in a poor yield. This case is illustrated by the scrap marker that covers the full strip width in Figure 9.3(a).

In order to improve the yield, multiple EMATs could be arranged in a way to cover smaller inspection areas. In combination with a multi-lane scrap marker, only the defects that lie in the smaller inspection area get scrap marked. Figure 9.3(b) shows an EMAT array configuration with two additional inspection channels at the edges. In the example with a bond defect in the central area of the strip, the yield is improved, because the edge sensors indicate that the edges are defect-free and therefore would not get scrap marked.

Figure 9.3(c) shows an additional receiving EMAT in the center line of the strip. In combination with the full width diagonal inspection channel, it is possible to further narrow down the location of the defect. Furthermore the EMAT array and multi-lane

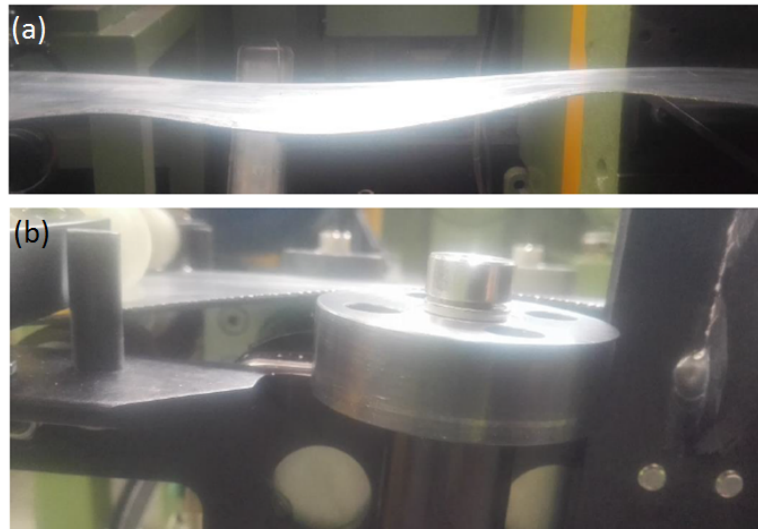


Figure 9.4: Bimetal strip one-side waviness leading to lift-off between material and probe and resulting in false alarms

scrap marker is flexible to inspect different strip widths, since the distance between the edge sensors can be adjusted.

A decision matrix was developed to systematically rate the different EMAT arrays. The considered criteria were required capital expenditure for the different number of sensors, complexity of mechanical integration, scrap/yield percentage and payback time. The 4-channel array design and scrap marker was chosen because of the highest yield, which results in the lowest running cost.

9.3 Robust mechanical integration

Online trials revealed that bimetal strips often have one-side waviness and the shape is not perfectly uniform. Figure 9.4(a) shows an example of strip with one-side waviness. Strip waviness can lead to lift-off between material end EMATs, if the waviness wavelength is too short for the EMAT holder passive compliance to compensate. Figure 9.4(b) shows the resulting lift-off between material and sensor, which causes false alarms.

In order to compensate for strip shape deviations, a robust three-roll steering stand, which applies strip tension, is considered in the serial machine technical specification.

Chapter 9. Recommendations for the final inspection system

When strip irregularities such as clad Al or steel welds passed the prototype inspection system, caution was required to not damage the probes of the system. The serial system will temporarily remove the probes from the strip when the visual system detects welds to prevent any system damage. Since strip 1 m before and 5 m after welds needs to get scrap marked because of oil contamination in the weld in any case, 100% volumetric good material inspection can be guaranteed.

Chapter 10

Summary and final conclusions

In this chapter the main innovations, industrial impact and suggestions for further work are concluded.

10.1 Main innovations

I. Identification of a NDT technique that is capable to detect bond defects in Al/Al-Sn/Al/steel and sintered CuSn/steel bimetal strips

The EngD project was initiated after an incident happened, in which the lining to steel bond of components failed in the field. It was evident that an online bond inspection system at the strip manufacturing plant would significantly reduce the business risk that components fail in the field. In order to identify a NDT technique that is capable to detect bond defects, firstly, the literature was reviewed to narrow down potential techniques. Secondly, a feasibility study using thermography, shearography, ultrasound and guided waves techniques and Al/Al-Sn/Al/steel bimetal samples with artificially implanted defects was conducted. EMATs and guided waves were selected, because the technique allows 100% inspection, is contact-less and does not require a coupling media that would be carried over into the strips. Since no EMAT guided waves inspection system was available on the market, significant research work between MAHLE Engine Systems UK, University of Strathclyde and Innerspec High-performance NDT solutions was undertaken, to develop a prototype machine.

II. Establishing the inspection system sensitivity to detect bond defects and capability for in-process control or final inspection

A sample manufacturing technique was developed to replicate significant defects that occur in serial production. The defects were artificially implanted at known positions and sizes, which enabled comparison of inspection signals and defect type/size. Aluminium oxide was used to create delamination between lining and steel in Al/Al-Sn/Al/steel bimetal. Steel debris was used as foreign particles contamination at the bond line. A brittle intermetallic layer was formed at the bond line by exceeding the solution heat treatment time. It was found that delamination defects with approximately 1x1 mm area can be detected prior and post rolling annealing, embedded steel debris with 1x1 mm area can be detected post annealing and 5x5 mm area embedded steel debris can be detected prior to rolling annealing. The system is not sensitive enough to detect brittle inter-metallic layers. It was shown that the inspection system can be installed either as in-process control or as final inspection.

III. Development and installation of a prototype inspection system

Potential practical inspection wave modes were identified by Innersepec through a numerical model using the SAFE method, which provided phase velocity and group velocity curves for bimetal plates to select suitable wave modes. A Finite Element Model was developed in the commercial software ABAQUS to simulate the interaction of guided waves with defects. It was found that some wave modes are more sensitive to defects than others, which helped to narrow down the list of potential wave modes for inspection experiments and to compare the theory against practical measurements.

IV. Taking measurements on moving bimetal strips with 100% volumetric inspection

A specific holder was designed to keep the EMATs aligned and at a near constant distance from the moving strips to allow online measurements. A system was built, which is capable to inspect bimetal strips online with a high degree of automation and obtain inspection results in real time. The system was installed on an industrial

strip processing line for rigorous online inspection trials of full-length bimetal strips. This work demonstrated that the inspection system is capable to detect defects under harsh industrial conditions. It was found that when inspecting 100% of the material volume, the false alarm rate is about 0.5% to detect all defects that nowadays can only be detected with the destructive peel-off test. In addition, the system is capable to detect 1x1 mm area delamination defects and incorrect thickness reduction, which is not detectable with the peel-off test. The online trials also identified issues in a serial production environment. Improvements were considered in the development of a technical machine specification to build a serial system for serial production.

V. Development of a technical specification for an online EMAT guided wave serial inspection system

The technical specification details the bimetal strip characteristics relevant for inspection, required system performance, criteria for commissioning and final acceptance, design of the mechanical integration to ensure a robust system suitable for the harsh manufacturing environment and how to integrate the system into the existing SIC visual inspection machine. The technical specification was developed in collaboration with Innerspec and a 3rd party mechanical integrator.

VI. Investigation of defects, causes and prevention controls in the continuous CuSn/steel bimetal strip sintering process

Destructive inspection results over a period of three years were collected and analysed to establish which defects occur in CuSn/steel bimetal strips serial production. This work also included a fault tree analysis to understand the root causes for defects and the implementation of prevention controls. It was found that the most frequent defect types are porosity, delamination and incorrect microstructure. Since delamination defects are buried below the surface of strips and are therefore not visible for the operator, it was evident that an online inspection system for sintered CuSn/steel bimetal strip would significantly improve process control and reduce the business risk.

VII. Feasibility study to detect defects in CuSn/steel bimetal strips

The prototype online inspection system was used to inspect CuSn/steel strips with porosity and delamination defects. The system was capable to detect all defects that are nowadays only detectable with destructive testing, while 100% material volume is inspected. This validated the system performance in addition to the Al/Al-Sn/Al/steel inspection results.

10.2 Industrial impact

The motivation for this project was primarily driven from a business (MAHLE) perspective to reduce the risk that components fail in the field and to avoid value adding to defective material. Firstly, the aspiration was to develop a 100% volumetric online inspection technique that is capable to detect critical defects that are buried below the surface of the strips. This work presented a guided waves generated with EMATs inspection technique that has demonstrated its capability to inspect bimetal strips online under the harsh serial production environment. MAHLE Engine Systems UK Ltd. currently plans the industrialisation of the inspection technique in their strategic budget plan for 2019/2020, which demonstrates the high credibility and industrial impact of this work. Secondly, defect root causes in the CuSn/steel bimetal strips production process in Kilmarnock were researched and some prevention controls are already successfully implemented, which is generating significant cost savings for the business due to reduced scrap rates.

10.3 Further work

A challenge in the guided waves inspection application in the Kilmarnock CRB and continuous sintering process is that the product portfolio consists of several hundred different part numbers, which all have different dimensional characteristics (lining thickness, steel thickness, ratio) and material properties (density, Young's modulus, Poisson's ratio) that influence the optimal guided wave mode per product for inspection. Due to experimental work it was possible to cluster products into groups that share the

same inspection wave mode, which significantly reduced the number of different wave modes compared to the initial stage of the project. However, considering the number of product changes in production and the required time to set up the inspection system, there is still a need to further reduce the number of required different wave modes.

During experimental work with CuSn/steel bimetal strips, which had between 0% and 60% delamination across the width of the strip, a cyclic behaviour of wave sensitivity relative to defect size was observed for certain wave modes. Furthermore it was observed that for certain wave modes and porosity defects in CuSn/steel samples, the behaviour of wave sensitivity was constructive interference. Constructive interference could falsely indicate good quality material, although a defect is present. Finite element simulation work for sintered CuSn/steel bimetal could explain the cyclic behaviour and constructive interference of the signal amplitude for these complex defect types. Based on the theoretical analysis, wave modes that have constructive interference and are not suitable for practical inspection, could be identified and avoided.

The method to qualitatively indicate the presence of bond defects was to define an alarm threshold as percentage of the reference amplitude. This is a relatively simple analysis of the captured wave signals and does not identify the defects type or quantify the bond strength or defect size. There exist more sophisticated feature extraction methods to interpret measured wave signals such as time domain analysis, frequency domain analysis or integrated time-frequency domain analysis. The major challenge of these identification techniques are signal contamination from noise, interference with natural vibration and confusion of multiple modes. Future work could focus on the development of a signal processing and identification technique that can cope with the harsh serial production environment. This information would be valuable to better understand defects and make decisions in quality control.

Bibliography

- [1] L. DaSilva, M. El-Sharif, C. Chisholm, and S. Laidlaw, “A review of the cold roll bonding of alsn alloy/steel bimetal strips,” *Metal*, 2014.
- [2] M. Stolbchenko, O. Grydin, F. Nürnberger, A. Samsonenko, and M. Schaper, “Sandwich rolling of twin-roll cast aluminium-steel clad strips,” *Procedia Engineering*, vol. 81, pp. 1541–1546, 2014.
- [3] R. Shuttleworth, “Problems in metallurgical thermodynamics and kinetics: by gs upadhyaya and rk dube. pergamon press, oxford, 1977. international series in materials science and technology, hard cover 15.00, *softcover student edition* 7.50,” 1978.
- [4] L. DaSilva, *A study of cold roll bonded Al/AlSn/Al/Steel bimetallic laminate material: investigation of the bond strength via in situ process optimisation*. PhD thesis, Glasgow Caledonian University, 2016.
- [5] T. B. Massalski and J. Murray, “Binary phase diagrams,” *ASM International*, p. 1096, 1990.
- [6] H. Torabian, J. Pathak, and S. Tiwari, “On wear characteristics of leaded aluminium-silicon alloys,” *Wear*, vol. 177, no. 1, pp. 47 – 54, 1994.
- [7] R. E. Smallman and R. J. Bishop, *Metals and Materials: Science, Processes, Applications*. Elsevier, 2013.

Bibliography

- [8] S. Essex, *Ultrasonic characterisation of rolled aluminium and steel sheet correlated with electron backscatter diffraction measurements*. PhD thesis, University of Warwick, 2009.
- [9] R. W. K. Honeycombe, “Steels—microstructure and properties,” *Edward Arnold Ltd., xi+ 244, 23 x 15 cm, illustrated(8. 50)*, 1981.
- [10] R. E. Reed-Hill and R. Abbaschian, *Physical metallurgy principles*. Brooks/Cole Engineering Division Monterey, Calif, USA, 1973.
- [11] R. Hill, “On uniqueness and stability in the theory of finite elastic strain,” *Journal of the Mechanics and Physics of Solids*, vol. 5, no. 4, pp. 229–241, 1957.
- [12] M. S. Ali, *Microstructural modelling of fatigue in layered bearing architectures*. PhD thesis, University of Southampton, 2007.
- [13] J. F. Nye, *Physical properties of crystals: their representation by tensors and matrices*. Oxford university press, 1985.
- [14] M. Kurrein, *Plasticity of Metals: The Mechanical Behavior and the Changes in Structure of Metals Under Plastic Deformation*. Griffin, 1964.
- [15] C. S. Barrett, *Structure of metals*. McGraw-Hill Book Company, Inc.; New York, 1943.
- [16] D. McLean, “Mechanical properties of metals,(1962),” *John Wiley and Sons*, p. 208, 1981.
- [17] A. D. Rollet and S. I. Wright, *Texture and Anisotropy*. Cambridge University Press, 2000.
- [18] D. Hull and D. Bacon, “Introduction to dislocations, international series on materials science and technology, vol. 37,” 1984.
- [19] E. P. DeGarmo, J. T. Black, R. A. Kohser, and B. E. Klamecki, *Materials and process in manufacturing*. Prentice Hall, 1997.

Bibliography

- [20] U. F. Kocks, C. N. Tomé, and H.-R. Wenk, *Texture and anisotropy: preferred orientations in polycrystals and their effect on materials properties*. Cambridge university press, 2000.
- [21] L. Li, K. Nagai, and F. Yin, “Progress in cold roll bonding of metals,” *Science and Technology of Advanced Materials*, vol. 9, no. 2, p. 023001, 2008.
- [22] J. Cave, “The mechanism of cold pressure welding by rolling,” *J. Inst. Met.*, vol. 101, no. 7, pp. 203–207, 1973.
- [23] D. Pan, K. Gao, and J. Yu, “Cold roll bonding of bimetallic sheets and strips,” *Materials Science and Technology*, vol. 5, no. 9, pp. 934–939, 1989.
- [24] H. Mohamed and J. Washburn, “Mechanism of solid state pressure welding,” *Welding Journal*, vol. 54, pp. 302–310, 1975.
- [25] H. Danesh Manesh and A. Karimi Taheri, “Study of mechanisms of cold roll welding of aluminium alloy to steel strip,” *Materials science and technology*, vol. 20, no. 8, pp. 1064–1068, 2004.
- [26] N. Lukaschkin, A. Borissow, and A. Erlikh, “The system analysis of metal forming technique in welding processes,” *Journal of materials processing technology*, vol. 66, no. 1-3, pp. 264–269, 1997.
- [27] H.-Y. Wu, S. Lee, and J.-Y. Wang, “Solid-state bonding of iron-based alloys, steel-brass, and aluminum alloys,” *Journal of Materials Processing Technology*, vol. 75, no. 1, pp. 173–179, 1998.
- [28] Y. Mitani, R. Vargas, and M. Zavala, “Deformation and diffusion bonding of aluminidecoated steels,” *Thin solid films*, vol. 111, no. 1, pp. 37–42, 1984.
- [29] J. M. Parks, “Recrystallization welding,” *Welding J*, vol. 32, no. 5, pp. 209s–222s, 1953.
- [30] L. Vaidyanath, M. Nicholas, and D. Milner, “Pressure welding by rolling,” *British Welding Jour*, vol. 6, pp. 13–28, 1959.

Bibliography

- [31] C. Clemensen, O. Juelstorp, and N. Bay, “Cold welding. part 3: influence of surface preparation on bond strength,” *n/a*, 1986.
- [32] H. D. Manesh and H. S. Shahabi, “Effective parameters on bonding strength of roll bonded al/st/al multilayer strips,” *Journal of Alloys and Compounds*, vol. 476, no. 1, pp. 292 – 299, 2009.
- [33] M. Sahin, “Effect of surface roughness on weldability in aluminium sheets joined by cold pressure welding,” *Industrial Lubrication and Tribology*, vol. 60, no. 5, pp. 249–254, 2008.
- [34] J. Furnidge, D. Howd, and R. TYLECOTE, “The influence of surface films on the pressure welding of metals,” *British Welding Jour*, vol. 5, no. 1, pp. 21–38, 1958.
- [35] B. Agers and A. Singer, “The mechanism of small tool pressure welding, brit,” *Weld. J., July*, pp. 313–319, 1964.
- [36] M. Alizadeh and M. Paydar, “Study on the effect of presence of TiH_2 particles on the roll bonding behavior of aluminum alloy strips,” *Materials & Design*, vol. 30, no. 1, pp. 82 – 86, 2009.
- [37] R. Jamaati and M. R. Toroghinejad, “Effect of Al_2O_3 nano-particles on the bond strength in crb process,” *Materials Science and Engineering: A*, vol. 527, pp. 4858–4863, 2010.
- [38] M. Movahedi, A. Kokabi, and S. S. Reihani, “Investigation on the bond strength of al-1100/st-12 roll bonded sheets, optimization and characterization,” *Materials & Design*, vol. 32, no. 6, pp. 3143 – 3149, 2011.
- [39] H. D. Manesh and A. K. Taheri, “The effect of annealing treatment on mechanical properties of aluminum clad steel sheet,” *Materials & design*, vol. 24, no. 8, pp. 617–622, 2003.
- [40] C. Lee, W. Hui, and B. Duggan, “Macroscopic shear bands in cross-rolled α brass,” *Scripta Metallurgica et Materialia*, vol. 24, no. 4, pp. 757–762, 1990.

Bibliography

- [41] R. Jamaati and M. R. Toroghinejad, "Effect of friction, annealing conditions and hardness on the bond strength of al/al strips produced by cold roll bonding process," *Materials & Design*, vol. 31, no. 9, pp. 4508–4513, 2010.
- [42] R. Jamaati and M. R. Toroghinejad, "Investigation of the parameters of the cold roll bonding (crb) process," *Materials Science and Engineering: A*, vol. 527, no. 9, pp. 2320–2326, 2010.
- [43] N. Tsuji, T. Toyoda, Y. Minamino, Y. Koizumi, T. Yamane, M. Komatsu, and M. Kiritani, "Microstructural change of ultrafine-grained aluminum during high-speed plastic deformation," *Materials Science and Engineering: A*, vol. 350, no. 1-2, pp. 108–116, 2003.
- [44] H. Madaah-Hosseini and A. Kokabi, "Cold roll bonding of 5754-aluminum strips," *Materials Science and Engineering: A*, vol. 335, no. 1-2, pp. 186–190, 2002.
- [45] M. Buchner, B. Buchner, B. Buchmayr, H. Kilian, and F. Riemelmoser, "Investigation of different parameters on roll bonding quality of aluminium and steel sheets," *International Journal of Material Forming*, vol. 1, no. 1, pp. 1279–1282, 2008.
- [46] H. Yan and J. G. Lenard, "A study of warm and cold roll-bonding of an aluminium alloy," *Materials Science and Engineering: A*, vol. 385, no. 1-2, pp. 419–428, 2004.
- [47] M. Willcox and G. Downes, "A brief description of ndt techniques," tech. rep., Insight NDT, 2003.
- [48] J. Garca-Martn, J. Gmez-Gil, and E. Vzquez-Snchez, "Non-destructive techniques based on eddy current testing," *Sensors*, vol. 11, pp. 2525–2565, 02 2011.
- [49] N. R. Center, "Basic principles of eddy current inspection," 11 2017.
- [50] S. Bagavathiappan, B. Lahiri, T. Saravanan, J. Philip, and T. Jayakumar, "Infrared thermography for condition monitoring a review," *Infrared Physics & Technology*, vol. 60, no. Supplement C, pp. 35 – 55, 2013.

Bibliography

- [51] C. Maierhofer, R. Krankenhagen, M. Röllig, U. Kalisch, and J. Meinhardt, *Development and Application of Active Thermography for Monitoring of Deterioration Processes of Historic Structures*, pp. 1111–1116. Dordrecht: Springer Netherlands, 2013.
- [52] N. Avdelidis, B. Hawtin, and D. Almond, “Transient thermography in the assessment of defects of aircraft composites,” *NDT & E International*, vol. 36, no. 6, pp. 433 – 439, 2003.
- [53] N. Avdelidis, D. Almond, A. Dobbinson, B. Hawtin, C. Ibarra-Castanedo, and X. Maldague, “Aircraft composites assessment by means of transient thermal ndt,” *Progress in Aerospace Sciences*, vol. 40, no. 3, pp. 143 – 162, 2004.
- [54] G. Kim, S. Hong, G. H. Kim, and K.-Y. Jhang, “Evaluation of subsurface defects in fiber glass composite plate using lock-in technique,” *International Journal of Precision Engineering and Manufacturing*, vol. 13, no. 4, pp. 465–470, 2012.
- [55] B. Yang, P. Liaw, M. Morrison, C. Liu, R. Buchanan, J. Huang, R. Kuo, J. Huang, and D. Fielden, “Temperature evolution during fatigue damage,” *Intermetallics*, vol. 13, no. 3, pp. 419–428, 2005.
- [56] M. Omar, M. Hassan, K. Donohue, K. Saito, and R. Alloo, “Infrared thermography for inspecting the adhesion integrity of plastic welded joints,” *NDT & E International*, vol. 39, no. 1, pp. 1–7, 2006.
- [57] S. Marinetti, D. Robba, F. Cernuschi, P. Bison, and E. Grinzato, “Thermographic inspection of tbc coated gas turbine blades: Discrimination between coating over-thicknesses and adhesion defects,” *Infrared physics & technology*, vol. 49, no. 3, pp. 281–285, 2007.
- [58] Y. S. Chen, Y. Y. Hung, S. P. Ng, Y. H. Huang, and L. Liu, “Review and comparison of shearography and active thermography for nondestructive testing and evaluation (ndt&e),” 2009.

Bibliography

- [59] S. M. Shepard and M. F. Beemer, “Advances in thermographic signal reconstruction,” in *Thermosense: Thermal Infrared Applications XXXVII*, vol. 9485, p. 94850R, International Society for Optics and Photonics, 2015.
- [60] Y. Hung and H. Ho, “Shearography: An optical measurement technique and applications,” *Materials science and engineering: R: Reports*, vol. 49, no. 3, pp. 61–87, 2005.
- [61] W. Steinchen, L. Yang, G. Kupfer, and P. Mäckel, “Non-destructive testing of aerospace composite materials using digital shearography,” *Proceedings of the Institution of Mechanical Engineers, Part G: Journal of Aerospace Engineering*, vol. 212, no. 1, pp. 21–30, 1998.
- [62] M. Y. Hung, Y. S. Chen, S. P. Ng, S. M. Shepard, Y. Hou, and J. R. Lhota, “Review and comparison of shearography and pulsed thermography for adhesive bond evaluation,” *Optical engineering*, vol. 46, no. 5, pp. 051007–051007, 2007.
- [63] N. Avdelidis, D. Almond, Z. Marioli-Riga, A. Dobbinson, and B. Hawtin, “Pulsed thermography: philosophy, qualitative & quantitative analysis on aircraft materials & applications,” in *Proc. Vth International Workshop, Advances in Signal Processing for Non Destructive Evaluation of Materials Québec City (Canada)*, pp. 2–4, 2005.
- [64] C. Meola and G. M. Carlomagno, “Recent advances in the use of infrared thermography,” *Measurement science and technology*, vol. 15, no. 9, p. R27, 2004.
- [65] X. Han, Z. Zeng, W. Li, M. S. Islam, J. Lu, V. Loggins, E. Yitamben, L. Favro, G. Newaz, and R. Thomas, “Acoustic chaos for enhanced detectability of cracks by sonic infrared imaging,” *Journal of applied physics*, vol. 95, no. 7, pp. 3792–3797, 2004.
- [66] F. Chen, “Digital shearography: state of the art and some applications,” *Journal of electronic imaging*, vol. 10, no. 1, pp. 240–251, 2001.

Bibliography

- [67] A. Fantin, D. Willemann, M. Benedet, and A. Albertazzi, “Robust method to improve the quality of shearographic phase maps obtained in harsh environments,” *Applied optics*, vol. 55, no. 6, pp. 1318–1323, 2016.
- [68] T. Hasiotis, E. Badogiannis, and N. G. Tsouvalis, “Application of ultrasonic c-scan techniques for tracing defects in laminated composite materials,” *Strojniški vestnik-Journal of Mechanical Engineering*, vol. 57, no. 3, pp. 192–203, 2011.
- [69] B. B. Djordjevic, “Nondestructive test technology for the composites,” in *The 10th International Conference of the Slovenian Society for non-destructive testing*, pp. 259–265, 2009.
- [70] A. H. Volume, “17: Nondestructive evaluation and quality control,” *ASM International*, vol. 795, 1989.
- [71] W. Alobaidi, E. Sandgren, and H. Al-Rizzo, “A survey on benchmark defects encountered in the oil pipe industries,” *International Journal of Scientific & Engineering Research*, vol. 6, no. 2, pp. 844–853, 2015.
- [72] H. Gao, S. Ali, and B. Lopez, “Efficient detection of delamination in multilayered structures using ultrasonic guided wave emats,” *NDT & E International*, vol. 43, no. 4, pp. 316 – 322, 2010.
- [73] X. Wang, Z. Zhou, W. Li, and Y. Li, “Development of an ultrasonic system for composite material inspection,” *International Symposium on Structural Health Monitoring and Nondestructive Testing*, 2018.
- [74] A. Neild, D. Hutchins, T. Robertson, L. Davis, and D. Billson, “The radiated fields of focussing air-coupled ultrasonic phased arrays,” *Ultrasonics*, vol. 43, no. 3, pp. 183–195, 2005.
- [75] C. Brotherhood, B. Drinkwater, and R. Freemantle, “An ultrasonic wheel-array sensor and its application to aerospace structures,” *Insight-Non-Destructive Testing and Condition Monitoring*, vol. 45, no. 11, pp. 729–734, 2003.

Bibliography

- [76] C. Holmes, B. W. Drinkwater, and P. D. Wilcox, “Post-processing of the full matrix of ultrasonic transmit–receive array data for non-destructive evaluation,” *NDT & e International*, vol. 38, no. 8, pp. 701–711, 2005.
- [77] G. P. M. Fierro and M. Meo, “Nonlinear imaging (nim) of flaws in a complex composite stiffened panel using a constructive nonlinear array (cna) technique,” *Ultrasonics*, vol. 74, pp. 30–47, 2017.
- [78] A. Safari, J. Zhang, A. Velichko, and B. W. Drinkwater, “Assessment methodology for defect characterisation using ultrasonic arrays,” *NDT & E International*, vol. 94, pp. 126–136, 2018.
- [79] J. Liu, G. Xu, X. Gu, and G. Zhou, “Ultrasonic test of resistance spot welds based on wavelet package analysis,” *Ultrasonics*, vol. 56, pp. 557–565, 2015.
- [80] C. C. H. Guyott, P. Cawley, and R. Adams, “The non-destructive testing of adhesively bonded structure: a review,” *The Journal of Adhesion*, vol. 20, no. 2, pp. 129–159, 1986.
- [81] M. Ph Papaelias, C. Roberts, and C. Davis, “A review on non-destructive evaluation of rails: state-of-the-art and future development,” *Proceedings of the Institution of Mechanical Engineers, Part F: Journal of Rail and rapid transit*, vol. 222, no. 4, pp. 367–384, 2008.
- [82] J. Krautkrämer and H. Krautkrämer, *Ultrasonic testing of materials*. Springer Science & Business Media, 2013.
- [83] R. Clark, “Rail flaw detection: overview and needs for future developments,” *Ndt & E International*, vol. 37, no. 2, pp. 111–118, 2004.
- [84] H.-M. Thomas, T. Heckel, and G. Hanspach, “Advantage of a combined ultrasonic and eddy current examination for railway inspection trains,” *Insight-Non-Destructive Testing and Condition Monitoring*, vol. 49, no. 6, pp. 341–344, 2007.
- [85] R. Havira, 2016.

Bibliography

- [86] I. Aizpurua, J. Lanzagorta, R. Hidalgo-Gato, and I. Castro, “New ultrasonic inspection strategies for railways,” 2018.
- [87] X. Jian, S. Dixon, R. S. Edwards, and J. Reed, “Coupling mechanism of electromagnetic acoustical transducers for ultrasonic generation,” *The Journal of the Acoustical Society of America*, vol. 119, no. 5, pp. 2693–2701, 2006.
- [88] H.-J. Salzburger, F. Niese, and G. Dobmann, “Emat pipe inspection with guided waves,” *Welding in the world*, vol. 56, no. 5-6, pp. 35–43, 2012.
- [89] P. Petcher, M. Potter, and S. Dixon, “A new electromagnetic acoustic transducer (emat) design for operation on rail,” *Ndt & E International*, vol. 65, pp. 1–7, 2014.
- [90] P. Petcher and S. Dixon, “Weld defect detection using ppm emat generated shear horizontal ultrasound,” *NDT & E International*, vol. 74, pp. 58–65, 2015.
- [91] K. Arun, R. Dhayalan, K. Balasubramaniam, B. Maxfield, P. Peres, and D. Barnoncel, “An emat-based shear horizontal (sh) wave technique for adhesive bond inspection,” in *AIP Conference Proceedings*, vol. 1430, pp. 1268–1275, AIP, 2012.
- [92] S. Huang, Z. Wei, W. Zhao, and S. Wang, “A new omni-directional emat for ultrasonic lamb wave tomography imaging of metallic plate defects,” *Sensors*, vol. 14, no. 2, pp. 3458–3476, 2014.
- [93] S. Dixon, C. Edwards, and S. Palmer, “Recent developments in the characterisation of aluminium sheets using electromagnetic acoustic transducers (emats),” *Insight*, vol. 44, no. 5, pp. 274–278, 2002.
- [94] R. S. Edwards, S. Dixon, and X. Jian, “Characterisation of defects in the railhead using ultrasonic surface waves,” *NDT & e International*, vol. 39, no. 6, pp. 468–475, 2006.

Bibliography

- [95] R. S. Edwards, X. Jian, Y. Fan, and S. Dixon, "Signal enhancement of the in-plane and out-of-plane rayleigh wave components," *Applied Physics Letters*, vol. 87, no. 19, p. 194104, 2005.
- [96] M. Hirao and H. Ogi, "Electromagnetic acoustic resonance and materials characterization," *Ultrasonics*, vol. 35, no. 6, pp. 413–421, 1997.
- [97] M. Hirao and H. Ogi, *EMATs for science and industry: noncontacting ultrasonic measurements*. Springer Science & Business Media, 2013.
- [98] R. B. Thompson, "Physical principles of measurements with emat transducers," *Physical acoustics*, vol. 19, pp. 157–200, 1990.
- [99] K. Kawashima, "Theory and numerical calculation of the acoustic field produced in metal by an electromagnetic ultrasonic transducer," *The Journal of the Acoustical Society of America*, vol. 60, no. 5, pp. 1089–1099, 1976.
- [100] S. Palmer and S. Dixon, "Industrially viable non-contact ultrasound," *Insight-Non-Destructive Testing and Condition Monitoring*, vol. 45, no. 3, pp. 211–217, 2003.
- [101] R. Tylecote, D. Howd, and J. Furnidge, "The influence of surface films on the pressure welding of metals," *British Welding Journal*, vol. 1, pp. 21–38, 1958.
- [102] L. DaSilva, M. El-Sharif, C. Chrisholm, and S. Laidlaw, "A novel adaption of the t-peel bimetal bond test based on the thin film bonding theory using cold roll bonded alsn/steel bimetal laminates," in *Volume 3: Advances in Manufacturing Technology XXX*, pp. 161–166, 2016.
- [103] R. E. Green, "Non-contact ultrasonic techniques," *Ultrasonics*, vol. 42, no. 1, pp. 9 – 16, 2004. Proceedings of Ultrasonics International 2003.
- [104] Z. Su, L. Ye, and Y. Lu, "Guided lamb waves for identification of damage in composite structures: A review," *Journal of sound and vibration*, vol. 295, no. 3, pp. 753–780, 2006.

Bibliography

- [105] J. Achenbach, *Wave propagation in elastic solids*, vol. 16. Elsevier, 2012.
- [106] M. Lemistre and D. Balageas, “Structural health monitoring system based on diffracted lamb wave analysis by multiresolution processing,” *Smart materials and structures*, vol. 10, no. 3, p. 504, 2001.
- [107] Z. Su, L. Ye, and X. Bu, “A damage identification technique for cf/ep composite laminates using distributed piezoelectric transducers,” *Composite structures*, vol. 57, no. 1, pp. 465–471, 2002.
- [108] W. Percival and E. A. Birt, “A study of lamb wave propagation in carbon-fibre composites,” *Insight*, vol. 39, no. 10, pp. 728–735, 1997.
- [109] E. A. Birt, “Damage detection in carbon-fibre composites using ultrasonic lamb waves,” *Insight*, vol. 40, no. 5, pp. 335–339, 1998.
- [110] J. L. Rose, “Ultrasonic waves in solid media,” 2000.
- [111] S. G. Pierce, B. Culshaw, G. Manson, K. Worden, and W. J. Staszewski, “Application of ultrasonic lamb wave techniques to the evaluation of advanced composite structures,” in *Smart Structures and Materials 2000: Sensory Phenomena and Measurement Instrumentation for Smart Structures and Materials*, vol. 3986, pp. 93–104, International Society for Optics and Photonics, 2000.
- [112] Z. A. b. Ahmad, *Numerical simulations of Lamb waves in plates using a semi-analytical finite element method*. PhD thesis, Magdeburg, Universität, Diss., 2011, 2011.
- [113] D. Alleyne and P. Cawley, “A two-dimensional fourier transform method for the measurement of propagating multimode signals,” *The Journal of the Acoustical Society of America*, vol. 89, no. 3, pp. 1159–1168, 1991.
- [114] A. Chakraborty, “Modeling of lamb waves in composite structures,” *Encyclopedia of Structural Health Monitoring*, 2009.

Bibliography

- [115] M. J. S. Lowe, "Matrix techniques for modeling ultrasonic waves in multilayered media," *IEEE Transactions on Ultrasonics, Ferroelectrics, and Frequency Control*, vol. 42, pp. 525–542, July 1995.
- [116] F. Chen and P. D. Wilcox, "The effect of load on guided wave propagation," *Ultrasonics*, vol. 47, no. 1, pp. 111–122, 2007.
- [117] L. Wang and F. Yuan, "Lamb wave propagation in composite laminates using a higher-order plate theory," in *Proc. SPIE*, vol. 6531, p. 65310I, 2007.
- [118] S. Finnveden, "Evaluation of modal density and group velocity by a finite element method," *Journal of Sound and Vibration*, vol. 273, no. 1-2, pp. 51–75, 2004.
- [119] I. Viktorov, "Rayleigh and lamb waves," *New York, Plenum Press.*, 1967.
- [120] M. Chitnis, Y. Desai, A. Shah, and T. Kant, "Comparisons of displacement-based theories for waves and vibrations in laminated and sandwich composite plates," *Journal of sound and vibration*, vol. 263, no. 3, pp. 617–642, 2003.
- [121] P. Wilcox, M. Lowe, and P. Cawley, "Mode and transducer selection for long range lamb wave inspection," *Journal of intelligent material systems and structures*, vol. 12, no. 8, pp. 553–565, 2001.
- [122] P. Wilcox, M. Lowe, and P. Cawley, "The effect of dispersion on long-range inspection using ultrasonic guided waves," *Ndt & E International*, vol. 34, no. 1, pp. 1–9, 2001.
- [123] S. S. Kessler, S. M. Spearing, and C. Soutis, "Optimization of lamb wave methods for damage detection in composite materials," *Technology Laboratory for Advanced Composites Department of Aeronautics and Astronautics Massachusetts Institute of Technology, SHM-2001*, 2001.
- [124] K. Maslov and T. Kundu, "Selection of lamb modes for detecting internal defects in composite laminates," *Ultrasonics*, vol. 35, no. 2, pp. 141–150, 1997.
- [125] T. Kundu and K. Maslov, "Material interface inspection by lamb waves," *International journal of solids and structures*, vol. 34, no. 29, pp. 3885–3901, 1997.

Bibliography

- [126] F. Degertakin and B. Khuri-Yakub, "Lamb wave excitation by hertzian contacts with applications in nde," *ieee transactions on ultrasonics, ferroelectrics, and frequency control*, vol. 44, no. 4, pp. 769–779, 1997.
- [127] R. Monkhouse, P. Wilcox, M. Lowe, R. Dalton, and P. Cawley, "The rapid monitoring of structures using interdigital lamb wave transducers," *Smart Materials and Structures*, vol. 9, no. 3, p. 304, 2000.
- [128] R. Monkhouse, P. Wilcox, and P. Cawley, "Flexible interdigital pvdf transducers for the generation of lamb waves in structures," *Ultrasonics*, vol. 35, no. 7, pp. 489–498, 1997.
- [129] S. S. Kessler, S. M. Spearing, and C. Soutis, "Damage detection in composite materials using lamb wave methods," *Smart materials and structures*, vol. 11, no. 2, p. 269, 2002.
- [130] S. Grondel, C. Paget, C. Delebarre, J. Assaad, and K. Levin, "Design of optimal configuration for generating a 0 lamb mode in a composite plate using piezoceramic transducers," *The Journal of the Acoustical Society of America*, vol. 112, no. 1, pp. 84–90, 2002.
- [131] C. Wang and L. Rose, "Wave reflection and transmission in beams containing delamination and inhomogeneity," *Journal of Sound and Vibration*, vol. 264, no. 4, pp. 851–872, 2003.
- [132] N. Kishore, I. Sridhar, and N. Iyengar, "Finite element modelling of the scattering of ultrasonic waves by isolated flaws," *NDT & E International*, vol. 33, no. 5, pp. 297–305, 2000.
- [133] D. N. Alleyne and P. Cawley, "The interaction of lamb waves with defects," *IEEE transactions on ultrasonics, ferroelectrics, and frequency control*, vol. 39, no. 3, pp. 381–397, 1992.
- [134] D. N. Alleyne and P. Cawley, "Optimization of lamb wave inspection techniques," *Ndt & E International*, vol. 25, no. 1, pp. 11–22, 1992.

Bibliography

- [135] C. Zang and M. Imregun, “Structural damage detection using artificial neural networks and measured frf data reduced via principal component projection,” *Journal of sound and vibration*, vol. 242, no. 5, pp. 813–827, 2001.
- [136] J. Rhim and S. W. Lee, “A neural network approach for damage detection and identification of structures,” *Computational mechanics*, vol. 16, no. 6, pp. 437–443, 1995.
- [137] M. Lowe and P. Cawley, “The applicability of plate wave techniques for the inspection of adhesive and diffusion bonded joints,” *Journal of Nondestructive Evaluation*, vol. 13, no. 4, pp. 185–200, 1994.
- [138] P. A. Games and J. F. Howell, “Pairwise multiple comparison procedures with unequal ns and/or variances: a monte carlo study,” *Journal of Educational Statistics*, vol. 1, no. 2, pp. 113–125, 1976.
- [139] G. C. PRATT, “A review of sintered metal bearings: Their production, properties, and performance,” *Powder Metallurgy*, vol. 12, no. 24, pp. 356–385, 1969.
- [140] H. Wakai, T. Sugitani, H. Nishiuchi, H. Abe, K. Hirose, R. Matsubayashi, T. Maruyama, and T. Kobayashi, “Effect of zn contents on properties of sulfide dispersed lead free copper alloy castings,” in *Proceedings of European Metallurgical Conference*, vol. 4, pp. 2068–2069, 2007.
- [141] B. Challen and R. Baranescu, *Diesel engine reference book*. McFarland, 1999.
- [142] L. O. A. Affonso, *Machinery failure analysis handbook: sustain your operations and maximize uptime*. Elsevier, 2013.
- [143] “Iso 7146-1:2008 plain bearings – appearance and characterization of damage to metallic hydrodynamic bearings – part 1: General.”
- [144] “Iso 7146-2:2008 plain bearings appearance and characterization of damage to metallic hydrodynamic bearings part 2: Cavitation erosion and its countermeasures.”

Bibliography

- [145] P. Mellish, “Failures of automobile plain bearings,” *Tribology*, vol. 2, no. 2, pp. 100–105, 1969.
- [146] Clevite, Ann Arbor, *Engine Bearing Failure Analysis Guide CL77-3-402*, 2002.
- [147] W. Bartz, “The influence of lubricants on failures of bearings and gears,” *TRIBOLOGY international*, vol. 9, no. 5, pp. 213–224, 1976.
- [148] D. Scott, “Bearing failures diagnosis and investigation,” *Wear*, vol. 25, no. 2, pp. 199–213, 1973.
- [149] A. Vencl and A. Rac, “Diesel engine crankshaft journal bearings failures: case study,” *Engineering failure analysis*, vol. 44, pp. 217–228, 2014.
- [150] P. Forrester and J. Beddow, “The continuous sintering of copper-lead to steel,” *Powder Metallurgy*, vol. 3, no. 5, pp. 149–154, 1960.
- [151] O. Katrus, A. Aleshina, V. Gribkov, and V. Ocheretyanskii, “Some properties of thin steel-copper bimetal sheet,” *Soviet Powder Metallurgy and Metal Ceramics*, vol. 23, no. 5, pp. 370–372, 1984.
- [152] G. A. Vinogradov, “Theory and practice of rolling metal powders,” *Powder Metallurgy and Metal Ceramics*, vol. 41, no. 9, pp. 517–525, 2002.
- [153] G. Price, C. Smithells, and S. Williams, “Sintered alloys. part i. copper-nickel-tungsten alloys sintered with a liquid phase present,” *J. Inst. Metals*, vol. 62, pp. 239–264, 1938.
- [154] W. Kingery, “Densification during sintering in the presence of a liquid phase. i. theory,” *Journal of Applied Physics*, vol. 30, no. 3, pp. 301–306, 1959.
- [155] W. Kingery and M. Narasimhan, “Densification during sintering in the presence of a liquid phase. ii. experimental,” *Journal of Applied Physics*, vol. 30, no. 3, pp. 307–310, 1959.
- [156] B. Strauss, “Fault tree analysis of bearing failures,” *Lubrication engineering*, vol. 40, no. 11, pp. 674–680, 1984.

Appendix

MAHLE Engine Systems UK Ltd., Kilmarnock

MAHLE Engine Systems UK Ltd.
Riccarton
Kilmarnock
Ayrshire, KA1 3NA, UK
Phone: +44 (0) 1563 52-1190
Fax: +44 (0) 1563 53-9730
www.mahle.com

Your Reference	Your Message	Contact	Extension	Date
		Charles Lorimer	8256	20 th August 2018
E-Mail:				

To Whom It May Concern:

Bond integrity in Al/Al-Sn/Al/steel and CuSn/steel bimetal strips that are used in the automotive industry to manufacture engine plain bearings, bushes and thrust washers is one of the most critical product characteristics. Delamination between the alloy lining and the steel backing layer can lead to catastrophic failure of engine components in the field, which poses a significant business risk for MAHLE. In some instances, bond defects can be detected in semi-finished half shell bearings, but detection at this point normally results in process yield and value-added manufacturing losses. Creating a sound bond quality consistently is a challenge due to the number of process parameters and their critical interactions with each other in relation to product quality. In order to ensure good quality, operational practice is to use a destructive peel-off test. However, the major disadvantage here is that only a minor proportion of the strip is inspected.

MAHLE initiated a project to address the issue, firstly developing a non-destructive testing (NDT) technique for 100% quality control while strips are processed continuously; then secondly to obtain a thorough understanding about defects and their root causes to implement prevention controls, where possible. The objective here is to achieve both a significant cost and risk reduction. The major challenges however, are the harsh manufacturing environment and that no NDT system is available off-the-shelf.

The MAHLE Project Manager is undertaking this project as part of the Engineering Doctorate programme in Advanced Manufacturing: Forging & Forming at the University of Strathclyde's Department of Design, Manufacture and Engineering Management (DMEM) and the Advanced Forming Research Centre (AFRC). The project has been solely funded by MAHLE Engine Systems UK Ltd. The prototype inspection system that has been installed at the Materials Business Unit in Kilmarnock was developed in collaboration with Innerspec Technologies.

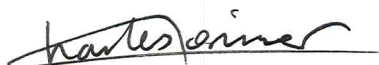
The following project outcomes have been achieved to date:

- In depth study of defects that occur in the CuSn/steel bimetal strip manufacturing process and implementation of prevention controls.
- A feasibility study with different NDT techniques, in which Guided Waves (GW) combined with Electromagnetic Acoustic Transducers (EMATs) technology, was identified to have genuine potential to be developed for online serial inspection.
- Significant experimental research to determine the GW EMATs sensitivity to detect different bond defects and whether the system is capable for either final inspection or in-process control.
- Development of a working prototype EMAT inspection system in collaboration with Innerspec Technologies.
- Installation of the prototype system at an industrial strip processing line and rigorous online inspection trials for both Al/Al-Sn/Al/steel and CuSn/steel materials.
- Development of a technical specification for a turnkey serial inspection system in collaboration with Innerspec Technologies and a 3rd party mechanical integration partner.

The development stage of this project has now been completed and approved for the industrialisation stage. MAHLE is currently planning to invest in a full scale NDT system that will be integrated into a final inspection line in the Kilmarnock plant in 2019/2020.

I can confirm that the project outcomes were all achieved to a consistently high standard, from a metallurgical, engineering and procedural viewpoint. The number of papers that were published in journals and conference proceedings underline the scientific credibility of this work. The progress of the project has exceeded the original scope, and continues to have the full support of MAHLE. This is indeed a credit to the Project Manager, and reflects his high degree of dedication, and commitment to the project and the excellent results to date.

Yours faithfully



Charles Lorimer BSc BEng (hons) MBA MIET
PLANT MANAGER

MAHLE Engine Systems UK Ltd.